# Synthesis and characterisation of metal oxides and metal doped variants

## Thesis

# SYNTHESIS AND CHARACTERISATION OF METAL OXIDES AND METAL DOPED VARIANTS

Stephen John Skinner, BSc

A thesis submitted for the degree of

Doctor of Philosophy

Department of Chemistry
The Open University

January 1997

To

Roslyn

# Contents

# Declaration

The work reported in this thesis was carried out solely by me in the Department of Chemistry, The Open University except were indicated otherwise. No part of this work has been submitted for the award of a degree at any other institution.

The following publications are a direct result of the work contained in this thesis;

"The High Temperature Properties of Tin-Doped Magnetite", F.J.Berry, Ö.Helgason, K.Jónsson and S.J.Skinner, J.Solid State Chem., 1996, 122, 353

"A Study of the Oxidation of Tin-Doped Magnetite by $^{57}Fe$ Mössbauer Spectroscopy", Ö.Helgason, F.J.Berry, K.Jónsson and S.J.Skinner, Conference Proceedings, ICAME 95, I Ortalli, Ed., SIF Bologna, 1996, 59

Stephen Skinner

# Acknowledgements

I would like to thank;

My supervisor, Professor F.J. Berry, for many useful discussions and for his advice throughout this work.

Professor Örn Helgason, Science Institute, University of Iceland, for providing facilities and assistance with high temperature $^{57}Fe$ Mössbauer spectroscopy.

Kristjan Jónsson, Science Institute, University of Iceland, for his patience in adapting the Mössbauer fitting software for my use.

Dr. M.F. Thomas, Department of Physics, University of Liverpool, for providing facilities and assistance with recording applied field $^{57}Fe$ Mössbauer spectra of the $Fe_3O_4$ single crystal and for discussion of the results.

Professor R.J.H. Clark and Dr. I.M. Bell, Department of Chemistry, University College London, for access to the Raman spectrometer and for assistance with collecting the data.

Dr. J.F. Marco, Insituto de Quimica Fisica 'Rocasolano', Madrid, for collecting the XPS data.

Mrs Naomi Williams, Electron Microscopy Suite, Department of Technology, The Open University for instruction and assistance with SEM, EDX and electron diffraction.

Dr. F. Biddlestone, School of Metallurgy and Materials, University of Birmingham for collecting the TGA data.

Members of the research group past and present for many useful discussions and the technical staff of the Chemistry Department.

I would also like to thank EPSRC for funding this work and the ULIRS for providing facilities for Raman spectroscopy.

EX12

# RESEARCH DEGREES CENTRE

# LIBRARY AUTHORISATION FORM

Please return this form to the The Research Degrees Centre with the two bound copies of your thesis to be deposited with the University Library
All students should complete Part 1 Part 2 only applies to PhD students.

Student STEPHEN SKINNER. PI: M7164558.

Degree Ph.D.

Thesis title: SYNTHESIS AND CHARACTERISATION OF METAL OXIDES AND METAL DOPED VARIANTS.

**Part 1 Open University Library Authorisation** [to be completed by all students]

I confirm that I am willing for my thesis to be made available to readers by the Open University Library, and that it may be photocopied, subject to the discretion of the Librarian.

Signed: [signature] Date: 19/5/97

**Part 2 British Library Authorisation** [to be completed by PhD students only]

If you want a copy of your PhD thesis to be available on loan to the British Library Thesis Service as and when it is requested, you must sign a British Library Doctoral Thesis Agreement Form. Please return it to the Research Degrees Centre with this form. The British Library will publicise the details of your thesis and may request a copy on loan from the University Library. Information on the presentation of the thesis is given in the Agreement Form.

The University has agreed that your participation in the British Library Thesis Service should be voluntary. Please tick either (a) or (b) to indicate your intentions.

[a] ☑ I am willing for the Open University to loan the British Library a copy of my thesis. A signed Agreement Form is attached

[b] ☐ I do not wish the Open University to loan the British Library a copy of my thesis.

Signed: [signature] Date: 19/5/97.

# Abstract

The $^{57}Fe$ Mössbauer spectra recorded from inverse spinel related $Fe_3O_4$ below the Verwey transition temperature are best interpreted in terms of tetrahedral A sites and two non-equivalent octahedral B sites. The broadening of the $^{57}Fe$ Mössbauer spectra recorded from $Fe_3O_4$ at 298K is associated with the superposition of the two components arising from the non-equivalent sites as opposed to an electron hopping process.

The unit cell size of the metal-doped ferrite, $Fe_{3-x}Sn_xO_4$, $0 < x < 0.4$, has been shown by X-ray powder diffraction(XRD) to increase linearly as tin content increases. Extended X-ray Absorption Fine Structure(EXAFS) show that the $Sn^{4+}$ ions substitute exclusively on the octahedral B sites of the inverse spinel related $Fe_3O_4$ structure. The amount of $Fe^{2+}$ present in $Fe_3O_4$ increases as the tin content increases in a fashion consistent with charge balance being maintained by reduction of $Fe^{3+}$ on either the A or B sites.

The Curie temperature of $Fe_{3-x}Sn_xO_4$ decreases with increasing tin content. Exsolution of tin from the $Fe_3O_4$ structure after prolonged heating at elevated temperatures *in vacuo* has also been observed. Oxidation of tin-doped magnetite involves a transformation to structurally related tin-doped maghemite before undergoing a structural transformation to tin-doped hematite. A lowering of the Curie temperature for both the tin-doped maghemite and tin-doped hematite has been identified.

Chromium- and gallium- doped magnetite have also been found to have considerably lower Curie temperatures than pure magnetite.

Cubic-, tetragonal- and monoclinic- zirconium(IV) oxides have been produced by boiling zirconium(IV) acetate under reflux and calcining at increasing temperatures. Raman spectroscopy has been used to distinguish between tetragonal- and cubic- zirconia. Addition of HCl to the initial solution suppresses the formation of the tetragonal and cubic phases. Addition of ammonia to the initial solution produces tetragonal zirconia which remains stable to 900°C.

Hydrothermal synthesis of zirconium(IV) oxide from a solution of zirconium(IV) acetate produces a mixture of tetragonal- and monoclinic- zirconia. Increasing calcination temperature induces a transformation to the monoclinic polymorph. Addition of HCl to the initial solution gives monoclinic zirconia via an oxychloride phase. Addition of aqueous ammonia to the initial solution stabilises the tetragonal phase at temperatures up to 900°C.

Tetragonal iron-doped zirconia has been synthesised from iron(II) acetate and zirconium(IV) acetate by boiling under reflux. Increasing calcination temperature induces a transformation to the monoclinic phase. Increasing pH stabilises the tetragonal phase against transformation to monoclinic zirconia. Iron segregates from the zirconia structure at temperatures exceeding 900°C.

Hydrothermal processing of iron(II) acetate and zirconium(IV) acetate produces a mixture of tetragonal- and monoclinic- iron-doped zirconia. Calcination at 900°C

induces the segregation of iron from the zirconia structure. Tetragonal iron-doped zirconia is characterised by a large quadrupole splitting in the $^{57}Fe$ Mössbauer spectrum.

# CHAPTER ONE

# Introduction

## 1.1 Introduction

The aims of the work reported in this thesis have been;

(i) to prepare and characterise compounds of composition $Fe_{3-x}M_xO_4$, M = Sn, Ti, Cr and Ga, ( $0 \leq x \leq 0.4$)

(ii) to investigate the formation of zirconium(IV) oxide and metal doped variants from zirconium(IV) acetate.

## 1.2 Metal doped ferrites

Metal-doped ferrites have found uses in various applications. These include high frequency transformer cores, magnetic memories, and heterogeneous catalysts. Mössbauer spectroscopy, which has been used extensively in the work reported in this thesis, has been used in the past to study the magnetic and electronic properties of cobalt doped magnetite, $Co_xFe_{3-x}O_4$. It was found[1] that for low dopant levels, $x \leq 0.04$, the properties are dictated by the fast electron exchange between $Fe^{2+}$ and $Fe^{3+}$ ions on the B sites of $Fe_3O_4$ (see later). A further study[2] of the cobalt doped system with $x \geq 0.1$ showed that as x increased the Curie temperature decreased, from 856.5K at x = 0.1 to 845.5K at x = 0.3. It was also established that the cation distribution could be estimated from the relative spectral area of the Mössbauer spectra.

Magnetic and electronic properties of many other ferrites have also been examined by Mössbauer spectroscopy. Ni,[3-6] Cr,[7,8] and Al doped[7] ferrites have been the subject of investigation and the results interpreted in terms of the site distribution of the substituting ion and its influence on the magnetic properties of these systems.

Coercivity in a composite cobalt doped magnetite, $(Fe_{0.2}Co_{0.8})_{0.8}[Fe_{2.38}Co_{0.62}O_4]$ in which the $(Fe_{0.2}Co_{0.8})$ component was chemically eliminated to leave only the spinel phase has also been examined.[9] In this phase, $Fe_{2.38}Co_{0.62}O_4$, the coercivity was considerably higher, 3900Oe, than that for the cobalt doped $\gamma$-$Fe_2O_3$, which is used as a magnetic recording material and which has a coercive field of about 1200-1500Oe. The

properties of the spinel phase were compared with the composite material. By comparing the saturation magnetization and coercivity of $(Fe_{0.2}Co_{0.8})_{0.8}[Fe_{2.38}Co_{0.62}O_4]$ and of the individual components, it was established that the magnetization was due to the metallic phase and that coercivity was due to the spinel phase. The composite material possessed both of these properties. High temperature properties of the spinel phase were also investigated, and it was found that at temperatures above 100°C the phase oxidises to cobalt doped $\gamma$-$Fe_2O_3$. On further heating to 800°C, $\alpha$-$Fe_2O_3$ segregated.

Surface area measurements using the BET method have been used to rationalise the catalytic properties of several divalent transition metal doped ferrites.[10] Specific heat measurements have also been used[11] to investigate these systems e.g. Zn doped ferrites. The effects of the dopant ions on the phase transitions at or around the Verwey transition were examined. It was established that deviations away from the exact $Fe_3O_4$ composition in the $0 \leq x \leq 0.036$ range resulted in a depression of the transition temperature.

Hence, although there have been some investigations of metal doped $Fe_3O_4$, the system has not been examined in detail. This work reports on an investigation of $Fe_{3-x}M_xO_4$ (M = Sn, Ti, Cr, Ga) with a view to establishing the site of doping, the influence on magnetic properties and the behaviour of the material at elevated temperatures. The titanium- and tin-doped magnetite structures have been subjected to particular attention.

### 1.2.1. Structure of $Fe_3O_4$

The iron oxide of composition $Fe_3O_4$, which is called magnetite, adopts a spinel related structure.[12-14] In the spinel structure the unit cell consists of a fcc lattice of 32 $O^{2-}$ ions. The cations are located on the interstices, of which 64 are tetrahedrally co-ordinated and 32 octahedrally co-ordinated. In spinel, one eighth of the tetrahedral and one half of the octahedral interstices are occupied. These are known as the A and B sites respectively.

The unit cell can therefore be represented as a combination of 4 A and 4 B octants arranged alternately. To complete the structure these 8 octants are encompassed by a fcc lattice of A ions. This corresponds to a formula of $A_8B_{16}O_{32}$ and is shown in Figure 1.1. This constitutes the normal spinel structure which can be represented empirically as $[A]^{tct}[B]_2^{oct}O_4$, where square brackets represent the cationic sites. The spinel structure requires the size of the metal ions occupying the A and B sites to be between 50 and 100pm,[15] although there is no restriction on valency.

Magnetite, although being of the spinel type, consists of a slightly different cationic distribution which was first proposed by Barth and Posnjak[16] and is known as inverse spinel. In the inverse structure the B ions are distributed over both the tetrahedral and octahedral sites, with the A ions being located solely on the octahedral sites. Empirically this can be represented as $[B]^{tct}[A,B]^{oct}O_4$. In magnetite this means that the A site consists of $Fe^{3+}$ and the B site of both $Fe^{3+}$ and $Fe^{2+}$ ions, Figure 1.2.

The structure of magnetite has been investigated by Mössbauer spectroscopy over a variety of temperature ranges[6,17-25] An early study[18] showed there to be two magnetic components in the $^{57}Fe$ Mössbauer spectrum of $Fe_3O_4$ at both room temperature and below the Verwey transition temperature, 119K. The two components were attributed to iron on the tetrahedral A site and the octahedral B site. It was also observed that the low temperature spectrum contained an extra peak which could not be accounted for. A subsequent study[19] investigated the structure over the temperature range 298-860K and also found only 2 components before the transition to the paramagnetic state at 840K. Kündig and Hargrove[20] observed that the lines in the Mössbauer spectrum were broadened and attributed this to an electron hopping process previously proposed[13, 21] from theoretical calculations.

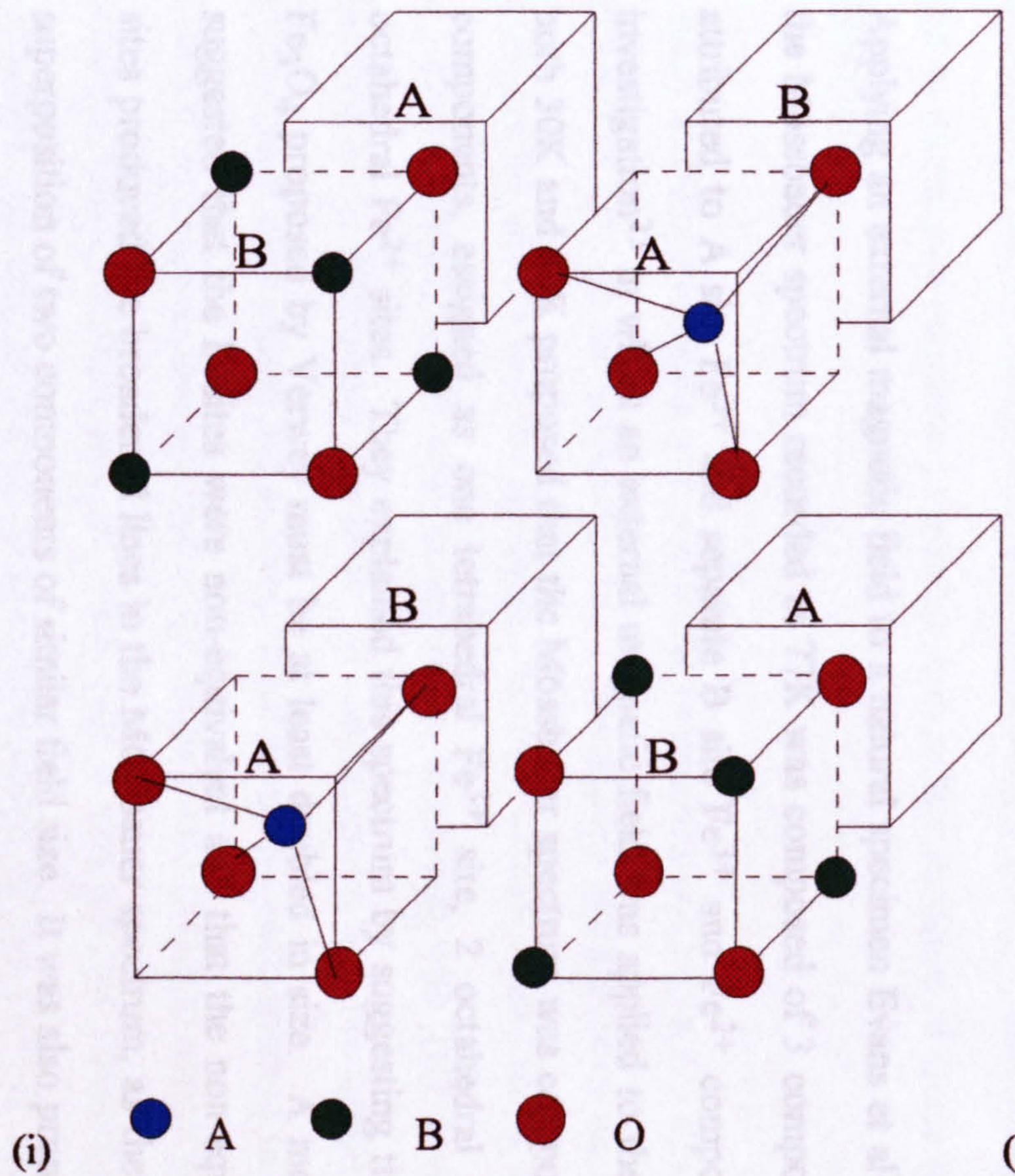


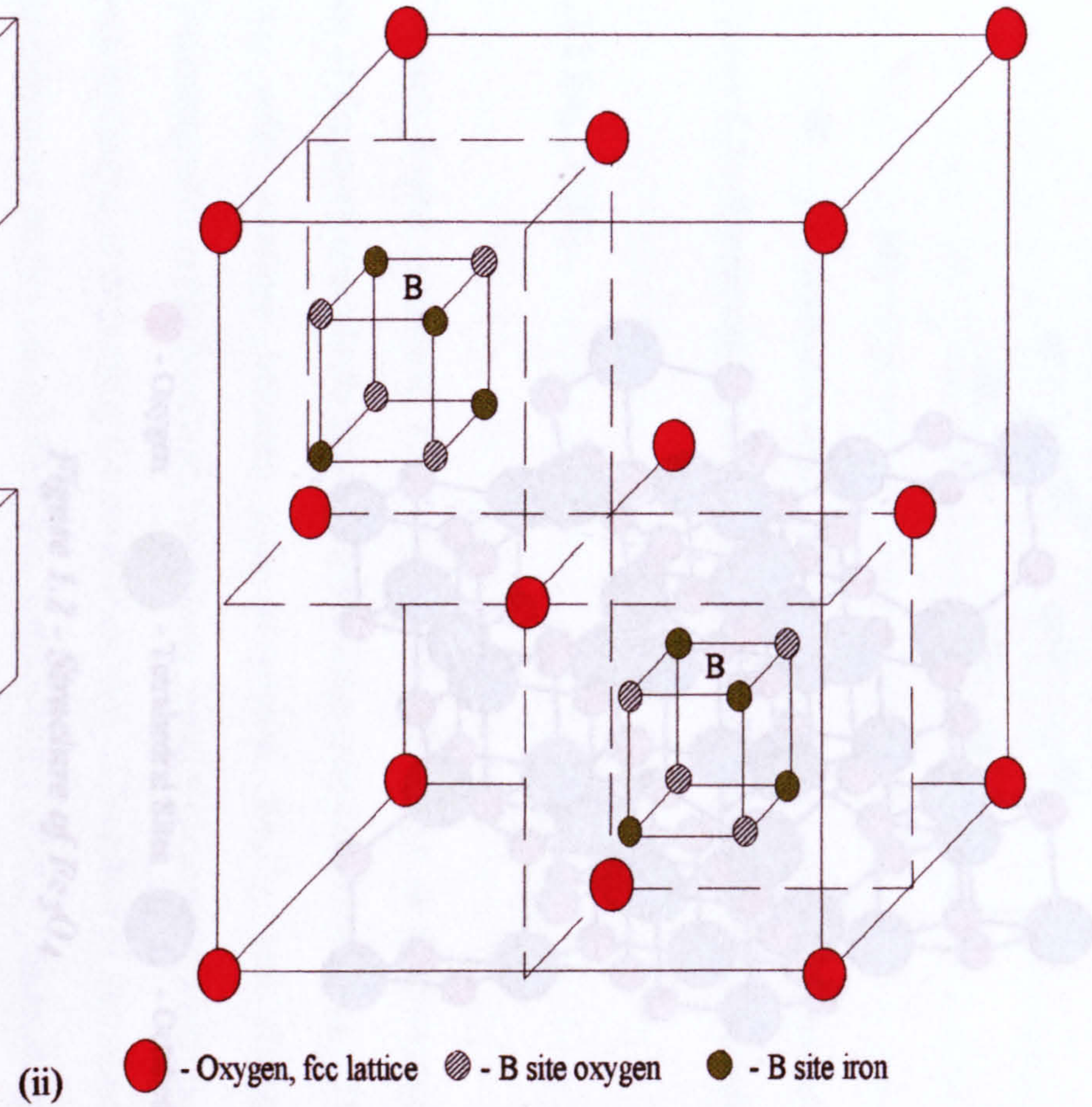


***Figure 1.1 - Representation of the spinel structure showing i) alternating $AO_4$ tetrahedra and $B_4O_4$ cubes and ii) fcc of oxygen with two $B_4O_4$ cubes shown for orientation***

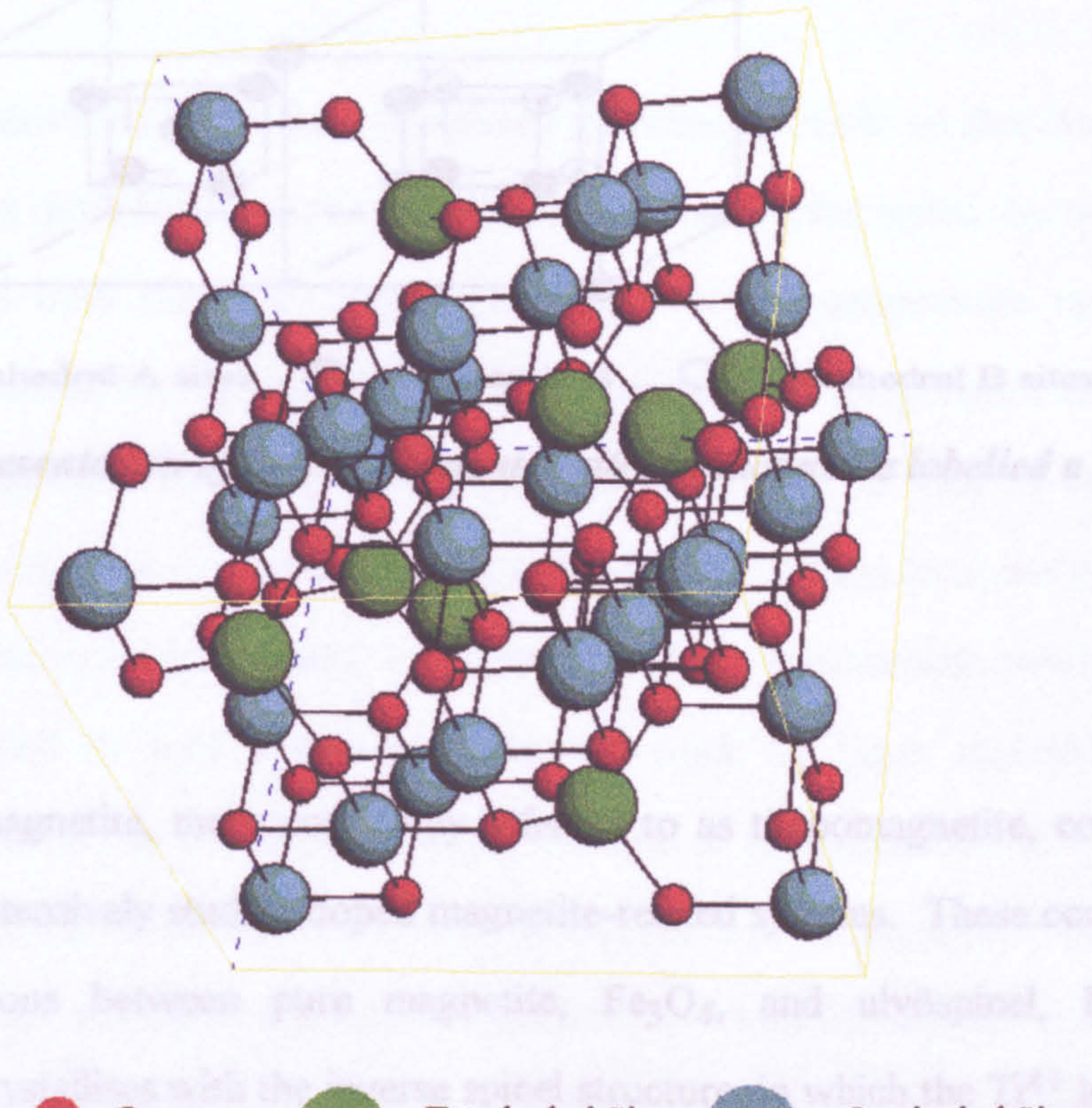


*Figure 1.2 - Structure of $Fe_3O_4$*

Applying an external magnetic field to a natural specimen Evans et al[22] established that the Mössbauer spectrum recorded at 77K was composed of 3 components which were attributed to A site $Fe^{3+}$ and separate B site $Fe^{3+}$ and $Fe^{2+}$ components. A further investigation[23] in which an external magnetic field was applied to the $Fe_3O_4$ sample at both 30K and 82K proposed that the Mössbauer spectrum was composed of 5 magnetic components, assigned as one tetrahedral $Fe^{3+}$ site, 2 octahedral $Fe^{3+}$ sites and 2 octahedral $Fe^{2+}$ sites. They explained this spectrum by suggesting that the unit cell of $Fe_3O_4$ proposed by Verwey must be at least doubled in size. A more recent study[24] suggested that the B sites were non-equivalent and that the non-equivalence of these sites produced the broadened lines in the Mössbauer spectrum, as the result of a partial superposition of two components of similar field size. It was also proposed that the non-equivalent sites had a 3:1 occupation ratio which was confirmed by the experimental results. The non-equivalence is illustrated in Figure 1.3.

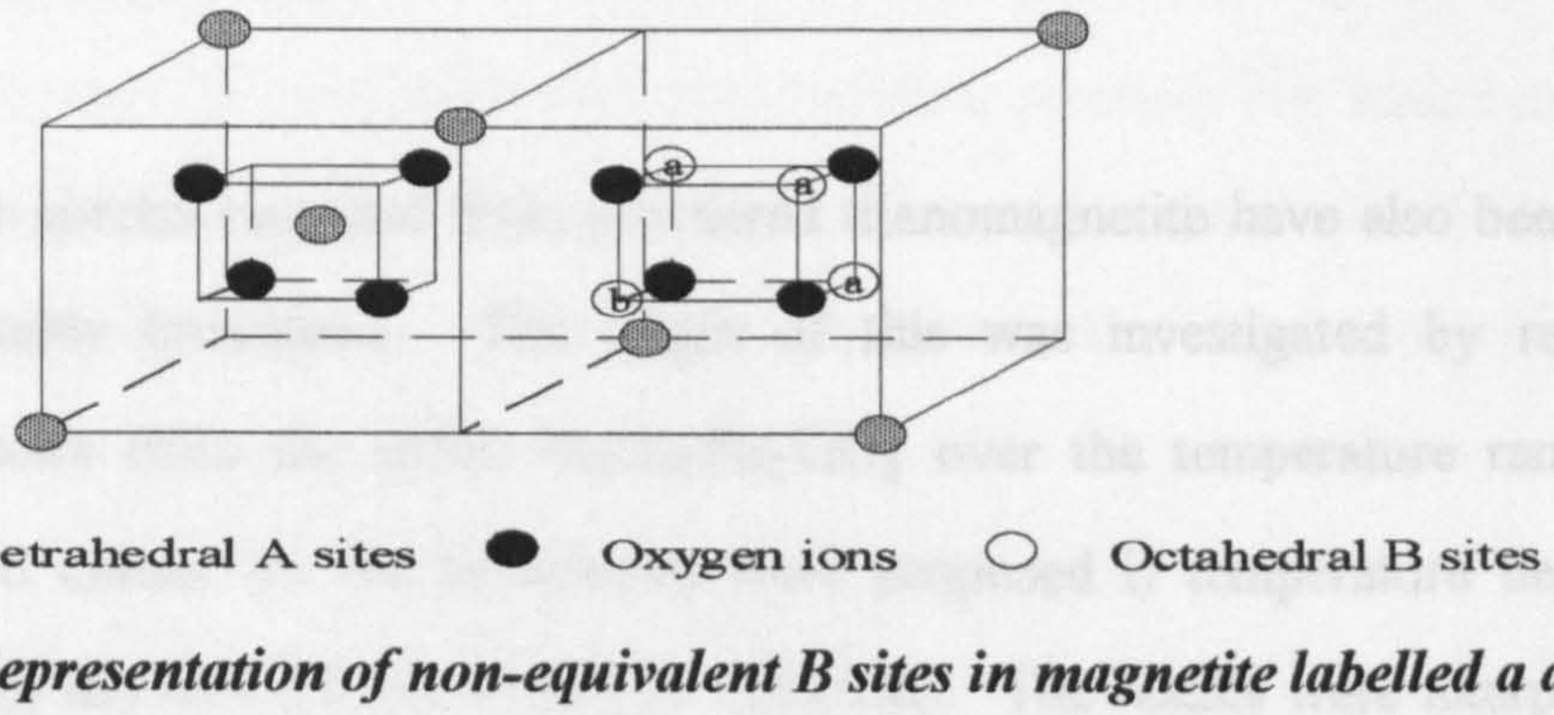


***Figure 1.3 - Representation of non-equivalent B sites in magnetite labelled a and b[24]***

### 1.2.2 $Fe_{3-x}Ti_xO_4$

Titanium doped magnetite, more commonly referred to as titanomagnetite, constitutes one of the more extensively studied doped magnetite-related systems. These compounds form solid solutions between pure magnetite, $Fe_3O_4$, and ulvöspinel, $Fe_2TiO_4$. Titanomagnetite crystallises with the inverse spinel structure, in which the $Ti^{4+}$ ions have been envisaged as occupying the octahedral sites. The effect of this substitution has been the subject of studies using Mössbauer spectroscopy. [26, 27] This technique has also been used to investigate magnetic properties such as the variation of Curie temperature with dopant level.

A study of titanomagnetite with low titanium concentration[28] ($x \leq 0.05$) investigated the influence of $Ti^{4+}$ on the electronic order. Mössbauer spectroscopy was performed on a single crystal sample and the spectrum recorded at 85K found to be very sensitive to $Ti^{4+}$ concentration. Small tails, or shoulders, increasing with $Ti^{4+}$ concentration, were observed in the Mössbauer spectrum. It was proposed that the substitution of iron by $Ti^{4+}$ on the B sites caused the ordering of electrons to break down in the neighbourhood of the $Ti^{4+}$, and it was this process which caused extra peaks to appear in the Mössbauer spectrum. This variation was observed over a very narrow concentration range x = 0.024-0.04 and was attributed to the deformation of the $Fe^{2+}$-II ions, identified by Hargrove and Kündig,[23] to $Fe^{2+}$-I type character (where $Fe^{2+}$-I and $Fe^{2+}$-II represent octahedral $Fe^{2+}$ sites). This deformation was caused by the proximity of the $Fe^{2+}$-II ions

to the $Ti^{4+}$ ions on the B sites.

The Mössbauer spectra recorded from powdered titanomagnetite have also been found to be considerably broadened. The origin of this was investigated by recording Mössbauer spectra from the series $Fe_3O_4$-$Fe_2TiO_4$ over the temperature range 1.3-300K.[25] Two causes for the broadening were proposed i) temperature dependent electron hopping and ii) local site symmetry variations. The results were interpreted in terms of $Fe_3O_4$ undergoing a hopping process, and $Fe_2TiO_4$ having local site symmetry variations. The reason for broadening in the spectra of the intermediate solid solution series was attributed to both processes. Further work by these authors[29] using Mössbauer spectroscopy as a complementary technique to measurements of saturation magnetisation, electrical resistivity, coercivity and unit cell size variation reinforced these findings. It was proposed that the generation of more $Fe^{2+}$ ions through the substitution of $Ti^{4+}$ for $Fe^{3+}$ created a trigonal distortion on the octahedral sites which broadened the Mössbauer spectra of the titanomagnetites, and caused a variation of local symmetry, effectively producing a summation of sextets of varying hyperfine field.

Although titanomagnetite can be prepared relatively easily by standard solid state methods, it is also found as a naturally occurring mineral, particularly in basaltic lavas. This has prompted a great deal of geological interest in the study of titanomagnetite and Mössbauer spectroscopy has been used to investigate the natural material. In contrast to the low temperature studies of synthetic titanomagnetite, Helgason et al[30] studied the high temperature properties of natural basaltic titanomagnetites to determine the Curie temperature. Further measurements were made to examine the oxidation/transformation process in two different basalts. It was found that titanomagnetite undergoes an oxidation process at high temperature forming the structurally similar maghemite, which is followed by a transformation to hematite. Stabilisation of maghemite below the maghemite-hematite transition temperature was also observed.

Oxidation processes have also been the subject of investigation[31] using the variation of lattice constants and Curie temperature. As oxidation proceeds the lattice constants decrease whereas the Curie temperature increases. Using either the above relationship or the ternary phase diagram, Figure 1.4, the ulvöspinel content of natural titanomagnetite was estimated.

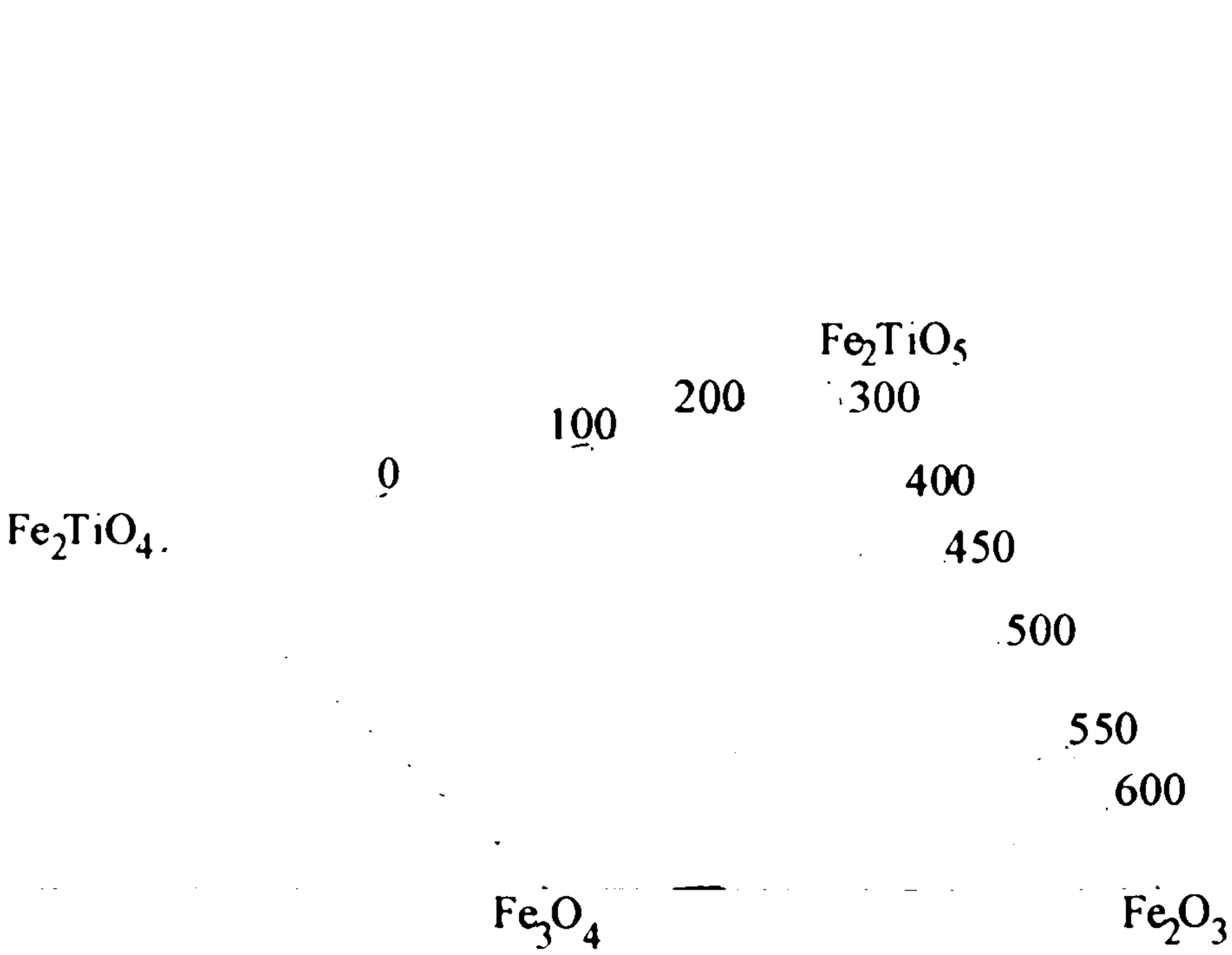


***Figure 1.4 - Ternary phase diagram showing contours of equal Curie point (°C) for the $Fe()$-$Fe_2()_3$-$Ti()_2$ system[31]***

An extensive study of ferrimagnetic oxides[15], especially titanomagnetites, considered several techniques for establishing the cation distribution in these materials. Three main methods were described i) low temperature measurement of saturation magnetisation, ii) X-ray diffraction and iii) neutron diffraction.

The substitution of $Ti^{4+}$ for the $Fe^{3+}$ ions creates a charge imbalance which has to be corrected by either reduction of $Fe^{3+}$ to $Fe^{2+}$ or introduction of an oxygen excess. Many suggestions have been proposed for the cationic distribution to account for both the charge balance and the $Ti^{4+}$ site occupancy. Of these the simplest was proposed by

Akimoto.[32] He suggested that some of the $Fe^{3+}$ on the tetrahedral A site was reduced, allowing the extra charge introduced by the $Ti^{4+}$ to be accommodated;

$$Fe^{3+}_{1-x}Fe^{2+}[Fe^{3+}_{1-x}Fe^{2+}Ti^{4+}_{x}]O^{2-}_{4} \qquad (0 \leq x \leq 1)$$

Akimoto arrived at the above distribution for the cations from a purely hypothetical point of view. It was known that both ulvöspinel and magnetite had inverse spinel structures, and therefore the solid solution series could be expressed empirically as;

$$xFe^{2+}(Ti^{4+}Fe^{2+})O_4\ (1-x)Fe^{3+}(Fe^{2+}Fe^{3+})O_4$$

which on rearrangement gives the previous expression;

$$Fe^{3+}_{1-x}Fe^{2+}[Fe^{3+}_{1-x}Fe^{2+}Ti^{4+}_{x}]O^{2-}_{4}$$

Subsequent studies have questioned the Akimoto model and more complex distributions have been proposed. Chevallier[33] and Néel[34] have described different situations occurring above and below a dopant level of $x = 0.5$;

$$Fe^{3+}[Fe^{3+}_{1-2x}Fe^{2+}_{1+x}Ti^{4+}_{x}]O^{2-}_{4} \qquad (0 \leq x \leq 0.5)$$

$$Fe^{3+}_{2-2x}Fe^{2+}_{2x-1}[Fe^{2+}_{2-x}Ti^{4+}_{x}]O^{2-}_{4} \qquad (0.5 \leq x \leq 1.0)$$

The derivation of the Chevallier model is based, as in the Akimoto case, on the known structure of the end members of the solid solution series. Chevallier then introduced Verwey's[13] rules of cation localisation which state that the most stable arrangement occurs where the highest charged cations occupy the sites with the highest coordination number. In the case of titanomagnetite this means that i) $Ti^{4+}$ ions prefer to occupy octahedral sites, ii) $Fe^{3+}$ ions prefer to occupy tetrahedral sites, and iii) $Fe^{2+}$ ions will occupy the remaining sites after the preceding rules have been obeyed. The Akimoto

model does not conform to these rules.

Lack of experimental evidence for the Néel-Chevallier model prompted a further refinement by O'Reilly and Banerjee.[35] The O'Reilly-Banerjee model was similar to the Chevallier model in the $0 \leq x \leq 0.2$ and $0.8 \leq x$ 1.0 ranges. Variation from the Néel-Chevallier model was observed in the $0.2 \leq x \leq 0.8$ range. Experimental observations led O'Reilly and Banerjee to conclude that the variation was due to the preference of the $Fe^{3+}$ ion for tetrahedral sites.

$$Fe^{3+}[Fe^{3+}_{1-2x}Fe^{2+}_{1+x}Ti^{4+}_{x}]O^{2-}_{4} \qquad (0 \leq x \leq 0.2)$$

$$Fe^{3+}_{1.2-x}Fe^{2+}_{x-0.2}[Fe^{3+}_{0.8-x}Fe^{2+}_{1.2}Ti^{4+}_{x}]O^{2-}_{4} \qquad (0.2 \leq x \leq 0.8)$$

$$Fe^{3+}_{2-2x}Fe^{2+}_{2x-1}[Fe^{2+}_{2-x}Ti^{4+}_{x}]O^{2-}_{4} \qquad (0.8 \leq x \leq 1.0)$$

Saturation magnetisation was measured[36] for a range of samples. The results indicated that as $Fe_2TiO_4$ content increased the magnetisation decreased. O'Reilly et al[35] plotted the saturation magnetisation data collected by Akimoto[36] together with their conductivity data against composition to determine any variation in the cation distribution, Figure 1.5.

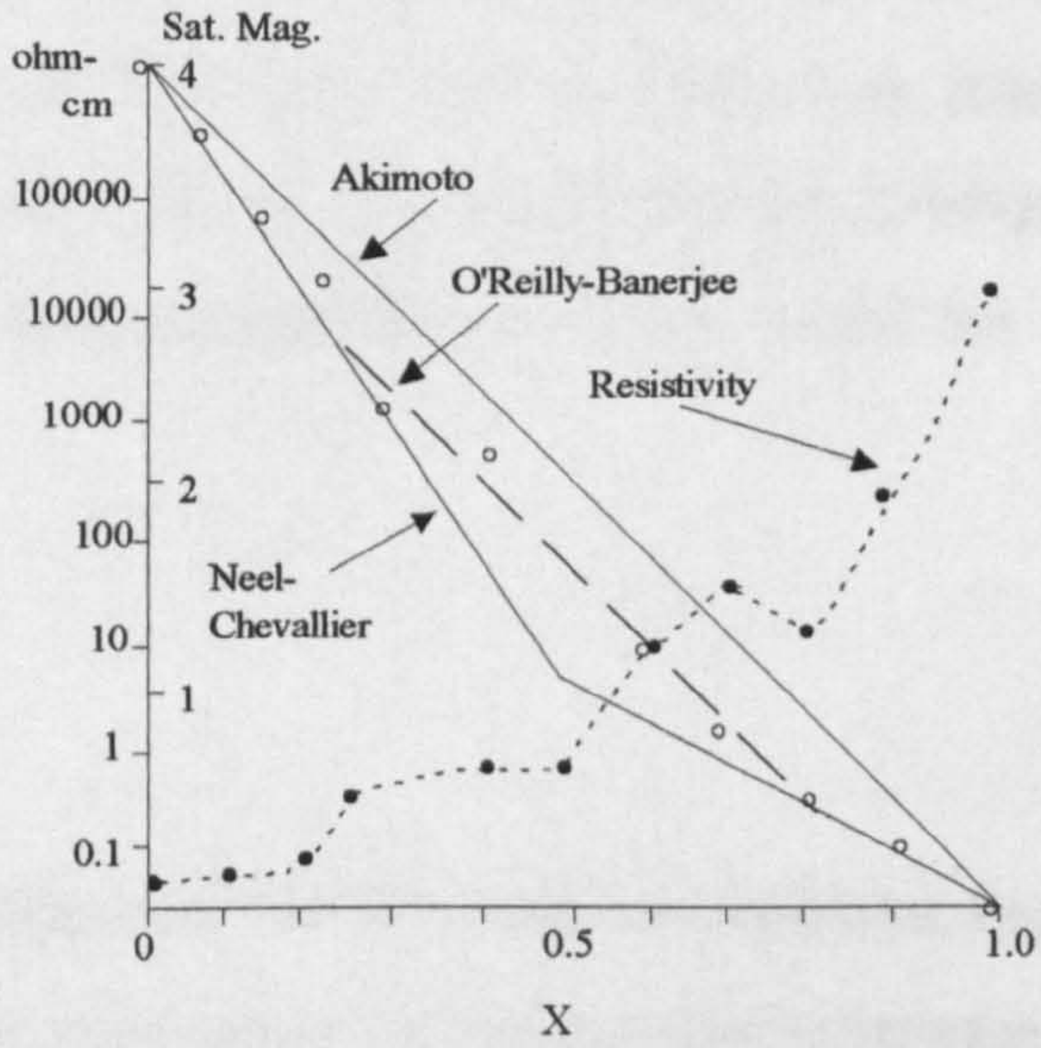


***Figure 1.5 - Saturation magnetisation and resistivity data versus titanium content, X, for the Akimoto, Néel-Chevallier and O'Reilly-Banerjee models[35]***

Despite the similarity between these models agreement on detail has been difficult to establish. All models agreed on the octahedral site for the titanium ion, as proposed by Blasse.[37]

More recently Wechsler,[38] after attributing the differences in the Néel-Chevallier and O'Reilly models as being due to inhomogeneities in the samples, has favoured the original Akimoto model. The cation distribution suggested by the Akimoto model may, according to Wechsler, be a low temperature distribution, whereas Tanaka[27] claimed that cation distribution was not temperature dependent in titanomagnetite. From the Mössbauer spectroscopy studies Tanaka rewrote the Akimoto model as;

$$Fe^{3+}_{1-x}Fe^{2+}_{x}[(Fe^{3+}_{1-2x}Fe^{2+}_{1-2x})(Fe^{3+}_{x}Fe^{2+}_{2x}Ti^{4+}_{x})]O^{2-}_{4}$$

The main difference is that only the $Fe^{3+}$-$Fe^{2+}$ pair in the first parenthesis participate in the electron hopping process. This conclusion was reached by determining the relative fractional areas of the subspectra of the Mössbauer spectra of $Fe_{3-x}Ti_xO_4$ ($0 \leq x \leq 1$).

Hence, in conclusion, titanomagnetite has been studied by a variety of techniques. Much information has been gathered on the behaviour of the material over a large temperature range. Many models for the cation distribution have been proposed, and Mössbauer spectroscopy has shown itself to be a useful tool for investigating the models. In contrast to this, very few investigations have been carried out on the analogous tin-doped magnetite.

### 1.2.3 $Fe_{3-x}Sn_xO_4$

Although $Sn^{4+}$ is of similar size[39] to $Ti^{4+}$ tin-doped magnetite, $Fe_{3-x}Sn_xO_4$, has not been subjected to substantial examination. Indeed the analogy between $Ti^{4+}$ and $Sn^{4+}$ seems to be restricted to a $^{57}Fe$ Mössbauer spectroscopy study[40] of the titanomagnetite solid

solution series end member, $Fe_2TiO_4$, which showed broadened spectral lines. The Mössbauer spectrum of $Fe_2SnO_4$ was also found[40] to have broadened lines and so the effect was attributed to the type of structure rather than the particular compound. Of the work carried out on the tin-doped system this would appear to be the only one which mentions both the tin and titanium analogues.

The existence of $Fe_2SnO_4$ was questioned by Djega-Mariadassou et al[41] after a substantial study found evidence for a solubility limit in $Fe_{3-x}Sn_xO_4$ of $x = 0.58$. It was claimed that if the compound did exist it would most probably be metastable. The solubility limit was established by Curie temperature measurements. As x increased, $T_c$ decreased until a minimum was reached at $x = 0.58$. By measuring the intensity of lines in the X-ray powder diffraction pattern and comparing these with a theoretical model, the $Sn^{4+}$ ions were associated with the octahedral sites.

In contrast to the claim of Djega-Mariadassou,[41] a subsequent study by Panek[42] claimed the existence of $Fe_2SnO_4$. The material, identified by X-ray powder diffraction measurements, was described as coexisting with tin and FeO in an electrical cell.

A further investigation[43] of saturation magnetisation proposed that the substitution of the $Fe^{3+}$ ions by the $Sn^{4+}$ ions on the octahedral sites produced $Fe^{2+}$ ions on the tetrahedral sites, which destabilised other $Fe^{2+}$ ions on the octahedral sites. The following formulation was proposed;

$$(Fe^{2+}_{1-y}Fe^{3+}_{y})[Sn_xFe^{2+}_{x+y}Fe^{3+}_{2-2x-y}]O^{2-}_4$$

where ( ) represents the tetrahedral site, [ ] represents the octahedral site. The value of y was determined from the saturation magnetisation measurements and the known size of the magnetic moment for both the divalent and trivalent iron ions;

$$a[2 - 2x - 2y] + b[-1 + x + 2y] = \sigma_{o,\infty}$$

where a = $\mu Fe^{3+}$, b = $\mu Fe^{2+}$, $\sigma_{o,\infty}$ = the magnetic moment of the solid solution. This was used to determine the site occupation for the A and B sites, Table 1.1. It was also suggested that use could be made of Mössbauer spectroscopy to obtain more information on the magnetic properties of the solid solution series.

| x | $Fe_A^{2+} = 1-y$ | $Fe_A^{3+} = y$ | $Fe_B^{2+} = x + y$ | $Fe_B^{3+} = 2 - 2x - y$ |
|---|---|---|---|---|
| 0.00 | 0 | 1 | 1 | 1 |
| 0.12 | 0.052±0.016 | 0.948 | 1.068 | 0.812 |
| 0.20 | 0.083±0.038 | 0.917 | 1.117 | 0.683 |
| 0.30 | 0.157±0.024 | 0.843 | 1.143 | 0.557 |
| 0.40 | 0.248±0.022 | 0.752 | 1.152 | 0.448 |
| 0.50 | 0.402±0.027 | 0.598 | 1.098 | 0.402 |

***Table 1.1 - Average distribution as a function of x[43]***

A further study by these authors[44] of the magnetic interactions related to the substitution mechanism examined the situation that occurs above $T_c$ and from these paramagnetic measurements the molecular field coefficients were deduced. The magnetisation vs. temperature curves agreed well with the experimental results. It was found that as the concentration of $Fe^{2+}$ ions on the B site increased, the $Fe^{2.5+}$ concentration decreased, inferring a decrease in the hopping process. The importance of A - A site interactions in the $0 \leq x \leq 0.2$ range was considered to discount the possibility of substitution directly onto the A site.

The first study of the system by Mössbauer spectroscopy[45] reported that, as tin is incorporated within the lattice, the $Fe^{2+}/Fe^{3+}$ ratio alters, and that the $Fe^{2+}$ content on the A site increases. The $^{119}Sn$ Mössbauer spectrum recorded from $Fe_{2.9}Sn_{0.1}O_4$ at 77K, showed a $Sn^{2+}$ doublet. This was attributed to a localisation of conduction electrons on the tin sites below the Verwey transition temperature of magnetite 119K.

Further investigation by Mössbauer spectroscopy[46] produced results similar to those of

Evans,[45] indicating an increase in the $Fe^{2+}$ A site concentration as $Sn^{4+}$ is substituted onto the B site. Two separate cation distributions were proposed, dependent on the value of x;

$$Fe^{3+}[Fe^{3+}_{1-2x}Fe^{2+}_{1+x}Sn^{4+}_{x}]O^{2-}_{4} \qquad x < 0.1$$

$$Fe^{3+}_{1-y}Fe^{2+}_{y}[Fe^{3+}_{1-2x+y}Fe^{2+}_{1+x-y}Sn^{4+}_{x}]O^{2-}_{4} \qquad x \geq 0.2$$

The value of y was estimated by the probability of finding $Fe^{2+}$ on the A site. From this, y was determined as 0.35 for x = 0.2, and 0.5 for x = 0.3. This constitutes a considerable difference in the final cation distribution when compared to the findings of Basile;[43]

$$Fe^{3+}_{0.65}Fe^{2+}_{0.35}[Fe^{3+}_{0.95}Fe^{2+}_{0.45}Sn^{4+}_{0.2}]O^{2-}_{4} \qquad \text{- Melzer}^{46}$$

$$Fe^{3+}_{0.917}Fe^{2+}_{0.083}[Fe^{3+}_{0.683}Fe^{2+}_{1.117}Sn^{4+}_{0.2}]O^{2-}_{4} \qquad \text{- Basile}^{43}$$

A more recent study[47] has investigated the oxidation process of magnetite to maghemite by studying the tin substituted magnetite, $Fe_{3-x}Sn_xO_4$ where $x < 0.20$, by both X-ray powder diffraction and $^{119}Sn$ Mössbauer spectroscopy. The oxidation was found to be a two step process involving i) diffusion of $\frac{1}{6}$ of the iron atoms from the B site to the surface ii) oxidation of the $Fe^{2+}$ to $Fe^{3+}$ at the B site.

Hence, in contrast to the titanomagnetites, very little has been reported on the tin-doped magnetite solid solution series. There appears to be little agreement over the cation distributions, other than that $Fe^{2+}$ ions should be present on the A site.

## 1.3 Zirconium (IV) oxide

Zirconium dioxide is commonly referred to as zirconia. Most commercial applications of $ZrO_2$ make use of stabilised polymorphs which are good ionic conductors and also have important thermal properties.

### 1.3.1 Crystalline phases of zirconia

Zirconium dioxide exists as four polymorphs, Figure 1.6. The stable room temperature phase is the monoclinic polymorph and is often called after its mineral name baddeleyite. The crystal structure[48] showed that monoclinic $ZrO_2$ has a 7 co-ordinate structure, Figure 1.7. Bond distance measurements have indicated a large variation in the 7 Zr-O bonds in the unit cell, with distances in the range 2.05Å - 2.28Å. This variation may indicate the presence of multiple bonds in the monoclinic structure, but it was found from infra red spectroscopy[49] that multiple bonds do not exist since any metal-oxygen double bonds would be expected to absorb in the 900 - 1100$cm^{-1}$ range. Also the Zr-O-Zr bond absorbs in the 850$cm^{-1}$ region. An electrostatic imbalance in the 7 co-ordinate structure is thought to be responsible for the difference in the bond lengths.

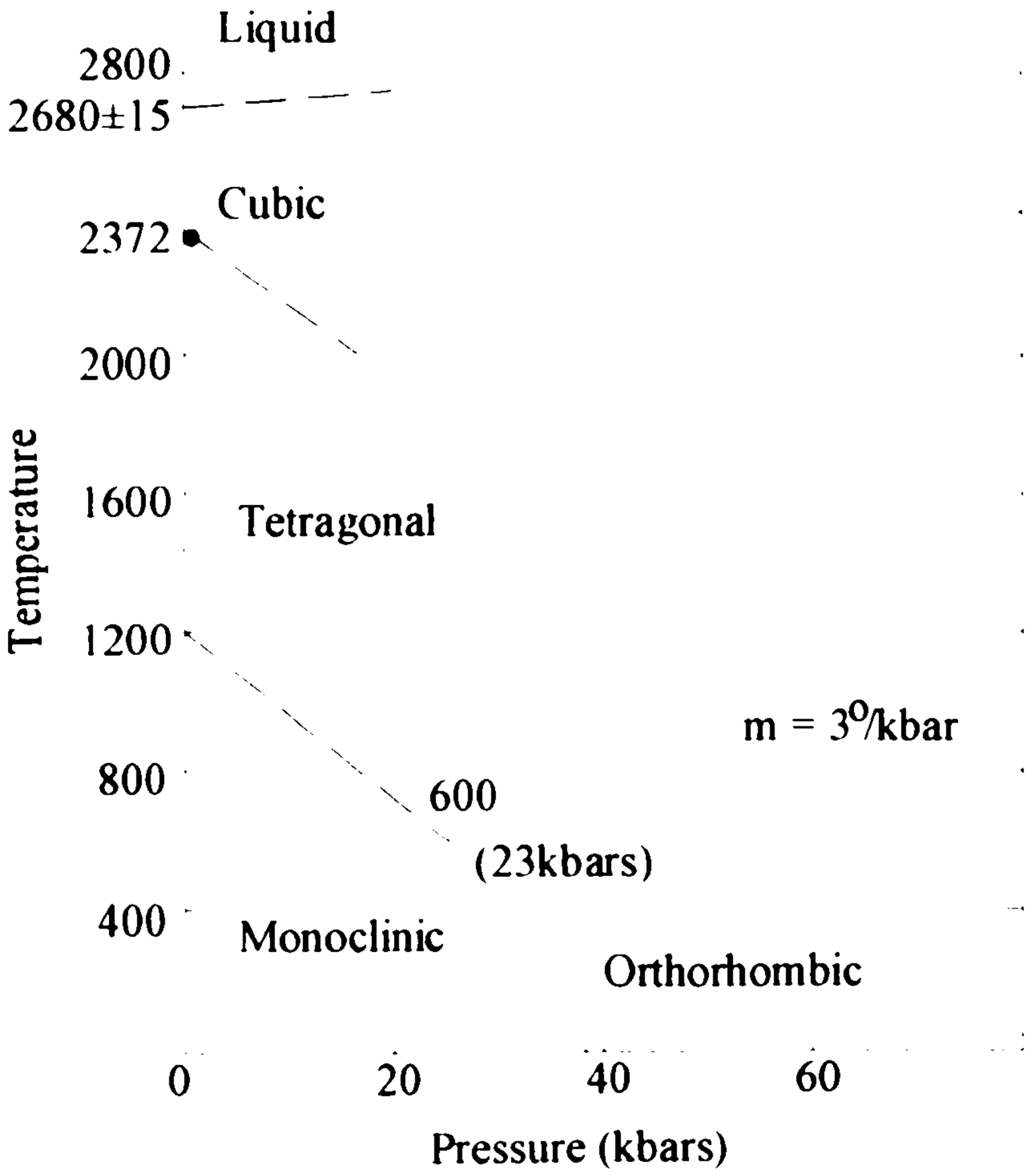


***Figure 1.6 - Phase diagram of $Zr()_2$ showing 4 different polymorphs[50]***

### 1.3.1 Crystalline phases of zirconia

Zirconium dioxide exists as four polymorphs, Figure 1.6. The stable room temperature phase is the monoclinic polymorph and is often called after its mineral name baddeleyite. The crystal structure[48] showed that monoclinic $ZrO_2$ has a 7 co-ordinate structure, Figure 1.7. Bond distance measurements have indicated a large variation in the 7 Zr-O bonds in the unit cell, with distances in the range 2.05Å - 2.28Å. This variation may indicate the presence of multiple bonds in the monoclinic structure, but it was found from infra red spectroscopy[49] that multiple bonds do not exist since any metal-oxygen double bonds would be expected to absorb in the 900 - 1100$cm^{-1}$ range. Also the Zr-O-Zr bond absorbs in the 850$cm^{-1}$ region. An electrostatic imbalance in the 7 co-ordinate structure is thought to be responsible for the difference in the bond lengths.

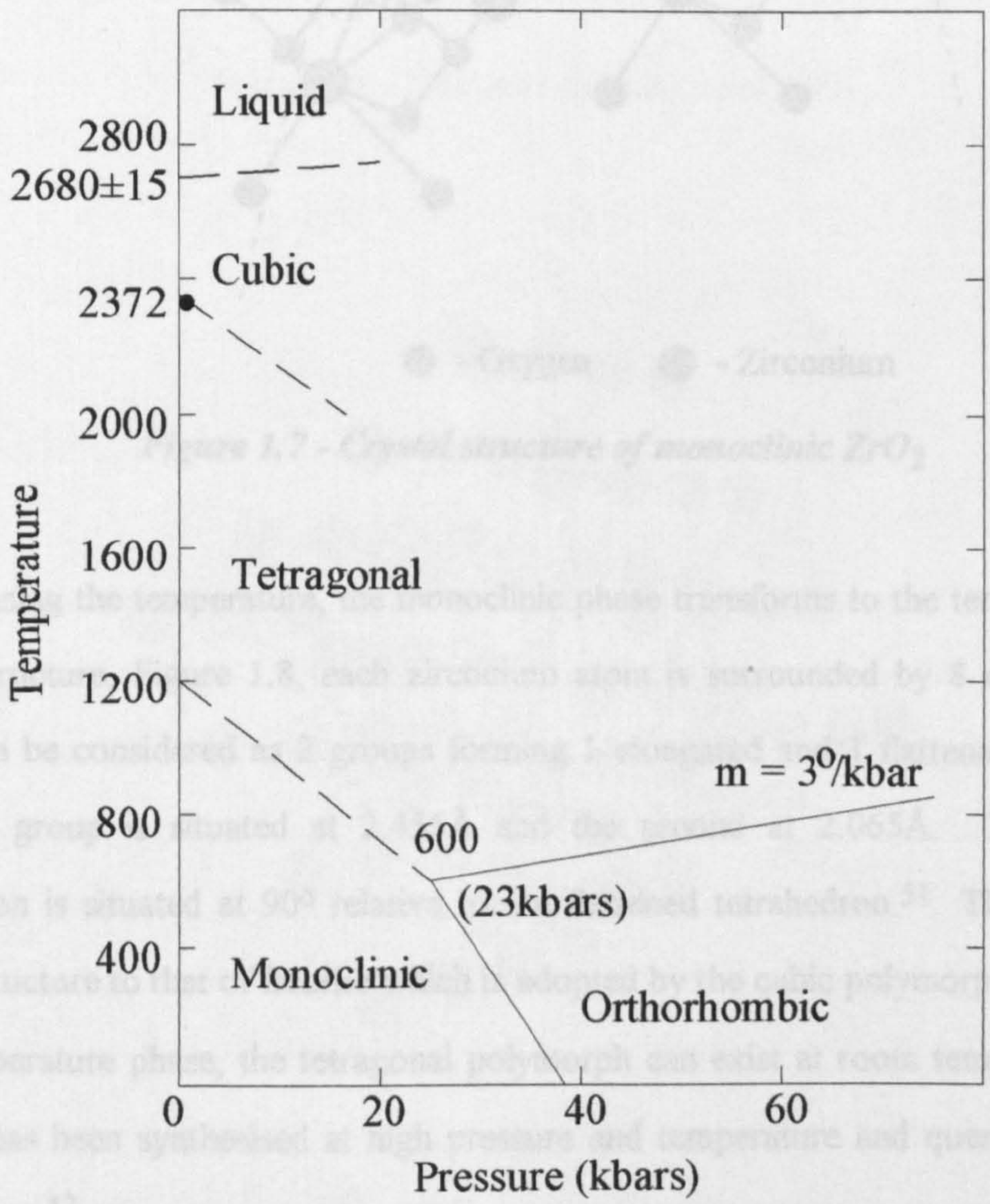


***Figure 1.6 - Phase diagram of $ZrO_2$ showing 4 different polymorphs[50]***

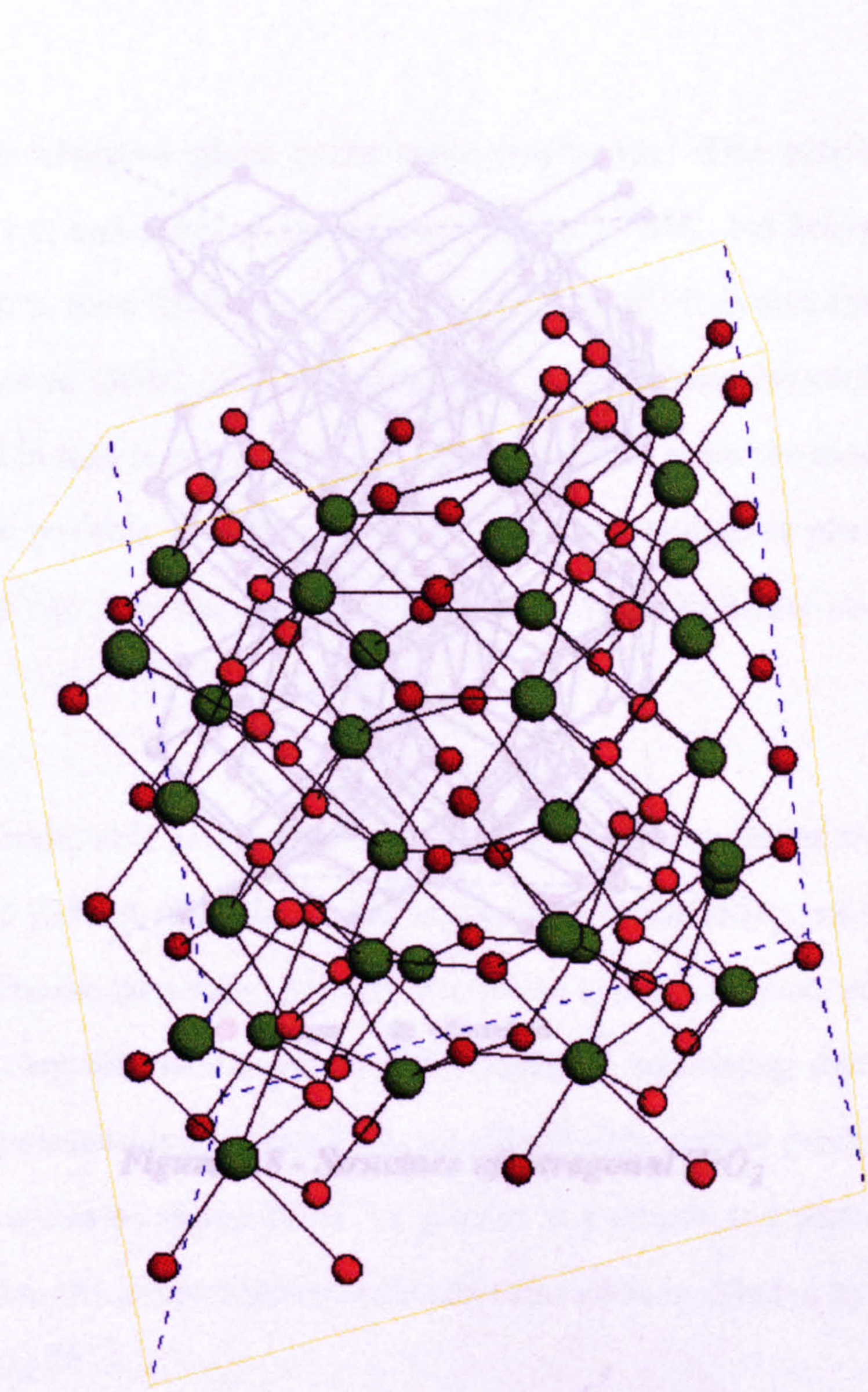


***Figure 1.7 - Crystal structure of monoclinic $ZrO_2$***

On increasing the temperature, the monoclinic phase transforms to the tetragonal phase. In this structure, Figure 1.8, each zirconium atom is surrounded by 8 oxygen atoms. These can be considered as 2 groups forming 1 elongated and 1 flattened tetrahedron. The first group is situated at 2.455Å and the second at 2.065Å. The elongated tetrahedron is situated at 90° relative to the flattened tetrahedron.[51] This produces a similar structure to that of fluorite which is adopted by the cubic polymorph. Although a high temperature phase, the tetragonal polymorph can exist at room temperature if the material has been synthesised at high pressure and temperature and quenched to room temperature.[52]

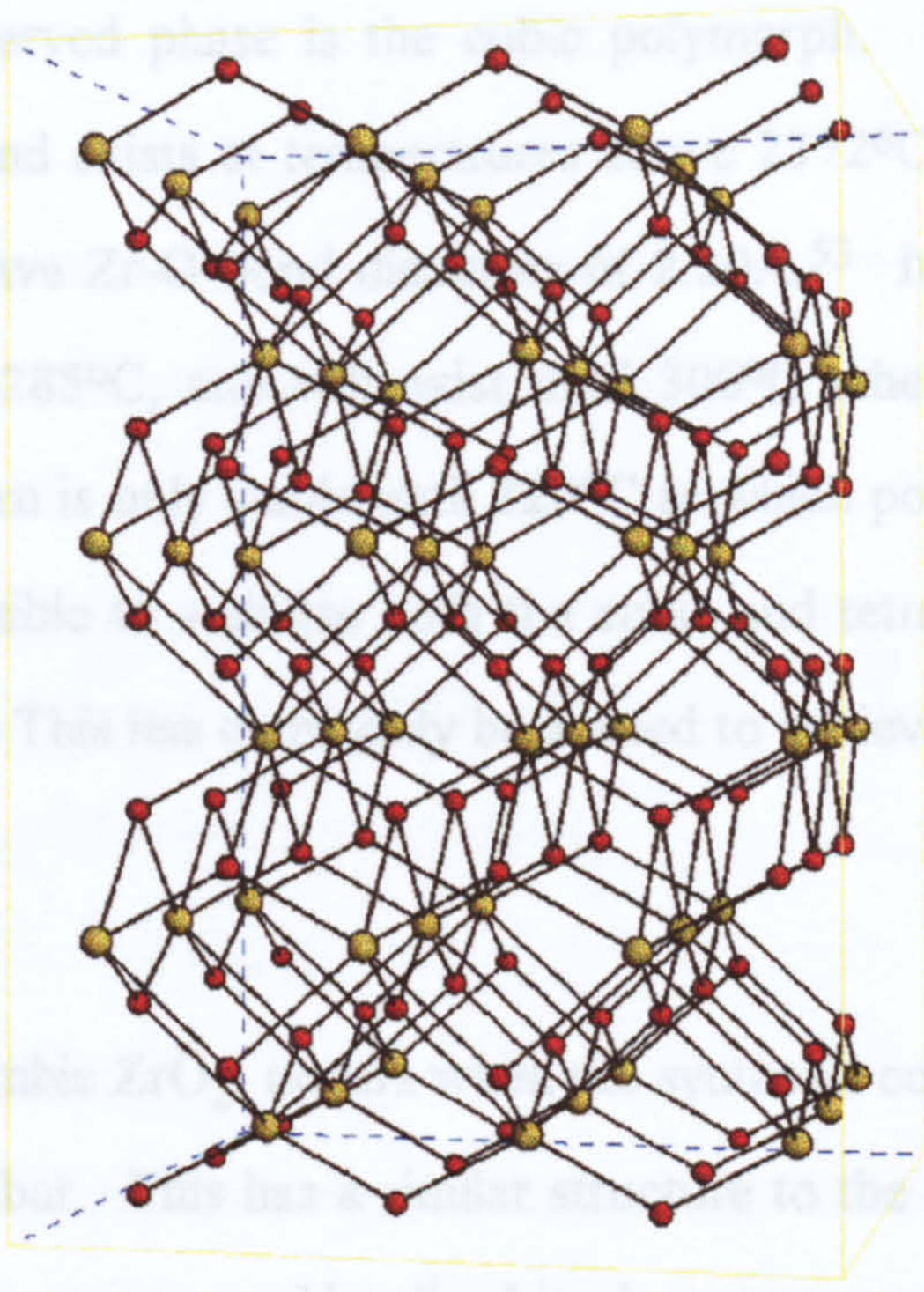


***Figure 1.8 - Structure of tetragonal $ZrO_2$***

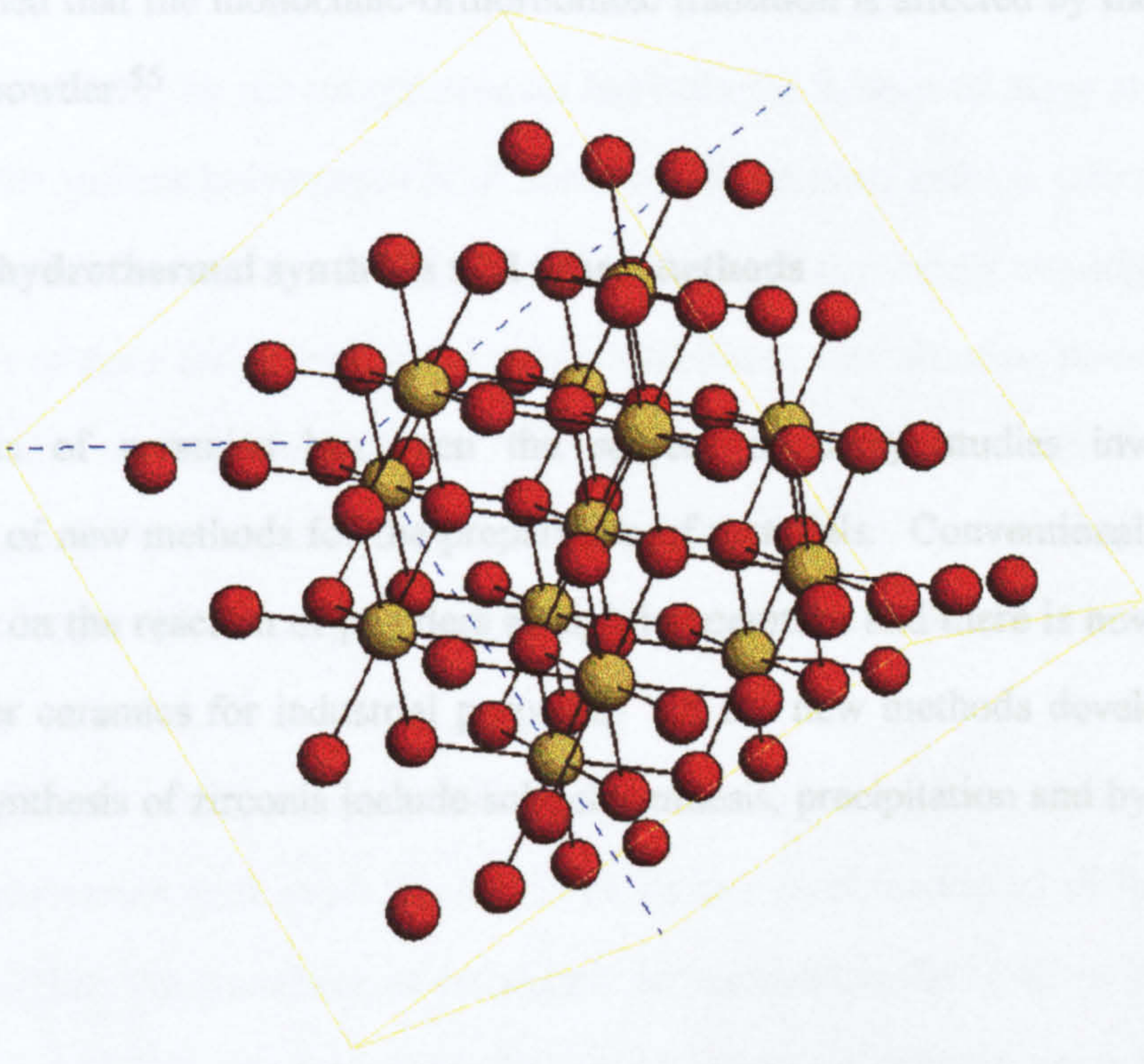


***Figure 1.9 - Fluorite structure adopted by cubic $ZrO_2$***

A third commonly observed phase is the cubic polymorph. This adopts the fluorite structure, Figure 1.9, and exists at temperatures above 2372°C, but below 2700°C. It has been reported to have Zr-O bond distances of 2.20Å.[53] It is also known that this phase is metastable at 285°C, and will exist until 300°C where metastable tetragonal $ZrO_2$ forms. This in turn is only stable until 320°C at which point the monoclinic phase appears. It is also possible to stabilise both the cubic and tetragonal phases by doping with another metal ion. This has commonly been used to achieve better materials for use in industry.

A final phase, orthorhombic $ZrO_2$, occurs when the synthesis conditions are increased to at least 600°C and 23Kbar. This has a similar structure to the tetragonal $ZrO_2$, as both have a distorted fluorite structure. Usually this phase appears only on quenching from high temperature, but this will leave a small amount of co-existing monoclinic phase unless the starting material is fine, wet $ZrO_2$ powder.[54] This method produces a product that is stable unless heated above 300°C or ground in a mortar and pestle. It has also been established that the monoclinic-orthorhombic transition is affected by the grain size of the $ZrO_2$ powder.[55]

### 1.3.2 Use of hydrothermal synthesis and other methods

The synthesis of ceramics has been the subject of many studies involving the development of new methods for the preparation of materials. Conventional solid state methods rely on the reaction of powders at high temperature and there is now a need to provide better ceramics for industrial purposes. Of the new methods developed those used in the synthesis of zirconia include sol-gel synthesis, precipitation and hydrothermal synthesis.

### 1.3.2.1 Sol gel processing

Sol-gel processing involves two steps - hydrolysis followed by a condensation process. In the case of the preparation of zirconia this may be explained by the following set of equations;[56]

$$Zr(OR)_4 \xrightarrow{H_2O,\ -ROH} Zr(OH)_2(OR)_2 \xrightarrow{H_2O,\ -ROH} Zr(OH)_4 \qquad (1)$$

$$Zr(OH)_2(OR)_2 \xrightarrow{-H_2O} ZrO(OR)_2 \qquad (2)$$

$$Zr(OH)_4 \xrightarrow{-H_2O} ZrO_2 \qquad (3)$$

Equation 1 represents the hydrolysis stage of the process, where (OR) represents either a carboxide, an inorganic salt or a salt of an organic acid, equations 2 & 3 represent the different polycondensation routes. These processes may occur simultaneously. Some of the advantages of this process are that it produces excellent chemical purity, homogeneity and nanosized particles.

The formation of $ZrO_2$ by the sol-gel process has been the subject of many studies. The evolution of the various polymorphs is of considerable interest, and the effect of doping zirconia to produce stabilised materials is one of the most commonly investigated areas. A comparison of pure and stabilised $ZrO_2$ has established that ultrafine powders can be produced at relatively low temperatures[57] via an initially amorphous phase. At 773K the pure monoclinic $ZrO_2$ phase crystallised. In the yttrium doped system, the cubic phase crystallised at 726K. All of the particles produced were of small size, (< 25nm).

Tetragonal zirconia can also be synthesised by the sol-gel process, involving partial zirconium replacement with either Al, Nb, Si or Ta or a combination of all four.[58] This study showed that the transition of tetragonal to monoclinic $ZrO_2$ is martensitic and occurs at around 1573K. As tetragonal $ZrO_2$ is an important ceramic, production of the material at room temperature is significant. Hence doping with other metals may be

required; the sol-gel process provides a good method for this, forming homogeneous oxides.

Further study has established that non-aggregated crystalline particles can be produced via a hydrolysis/condensation reaction of zirconium alkoxides.[59] These alkoxides were chemically modified by organic compounds such as paratoluene sulfonic acid. It has been reported[59] that the control of the condensation depends on the hydrolysis reaction leading to the condensation process, and the complexation of the alkoxides by nucleophilic species.

### 1.3.2.2 Precipitation technique

The production of zirconia at low temperature has also been achieved by precipitation methods. This involves precipitating a hydrous zirconium oxide by adding a base to a zirconium chloride or nitrate solution. The influence of pH and ageing of the precipitate on crystal polymorph has been of interest.[60] Not only does the final pH of the precipitate influence the phase produced, but time of addition of the base has dramatically influenced the phase obtained. The effect of pH and synthesis conditions are illustrated in Figure 1.10.

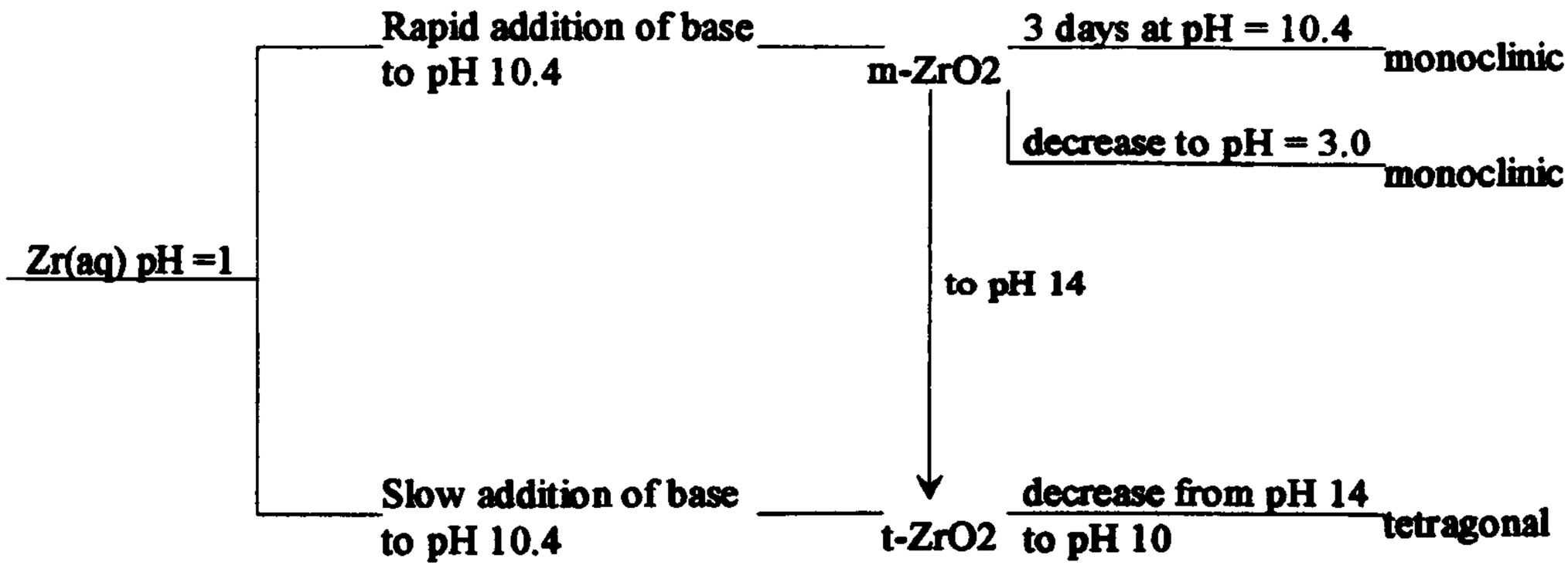


***Figure 1.10 - Flow diagram showing the effect of variation of synthesis conditions on phase composition of $ZrO_2$[60] where m = monoclinic and t = tetragonal***

A further investigation[61] established that ultrafine zirconia powder can be prepared by precipitation but, if the precipitate is rinsed with distilled water, then aggregation of the powder prevails. The formation of the tetragonal phase was found to be influenced by the structural similarity between the precursor material and the tetragonal phase.

### 1.3.2.3 Hydrothermal processing

The method of greater interest in this work is hydrothermal processing. The definition of the hydrothermal process has been proposed by several workers.[62-65] A general definition is that the reaction has to take place in aqueous media, above 100°C and 1 bar.[64] A slightly more detailed definition is that the hydrothermal process is a chemical interaction between precursor materials and water either directly or catalytically under hyperatmospheric pressure at temperatures above the boiling point of water to produce oxides.[65]

This process was first used to produce quartz crystals from silica gel and water. Since then, the hydrothermal technique has been used to induce processes such as precipitation, crystallisation, oxidation, decomposition, synthesis, and anodic oxidation.[66] The work reported in this thesis has been concerned with the hydrothermal synthesis of zirconia.

Hydrothermal synthesis has many advantages over conventional synthesis,[62] Table 1.2.

| | Conventional | Sol-gel | Coprecipitation | Hydrothermal |
|---|---|---|---|---|
| Cost | Low-moderate | High | Moderate | Moderate |
| State of Development | Commercial | R & D | Commercial/ demonstration | Demonstration |
| Compositional Control | Poor | Excellent | Good | Good-excellent |
| Morphology Control | Poor | Moderate | Moderate | Good |
| Powder reactivity | Poor | Good | Good | Good |
| Purity (%) | <99.5 | >99.9 | >99.5 | >99.5 |
| Calcination step | Yes | Yes | Yes | No |
| Milling step | Yes | Yes | Yes | No |

*Table 1.2 - Comparison of Oxide Powder Processes[62]*

Products which are normally difficult to produce such as the metastable subiodides of tellurium, $Te_2I$ and β-TeI, can be synthesised quite easily. It is also possible to produce low temperature phases such as γ-CuI, and also compounds with unusual oxidation states, such as $CrO_2$. This is formed from the common oxides e.g.

$$Cr_2O_3 + CrO_3 \xrightarrow{623K,\ 440bar,\ H_2O} 3CrO_2 \quad \text{and}$$

$$CrO_3 \xrightarrow{623K,\ 440bar,\ H_2O} CrO_2 + \tfrac{1}{2}\ O_2$$

In this reaction the decomposition of $CrO_2$ leads to a build up of $O_2$ which stabilises the $CrO_2$.

The production of ultrafine monoclinic $ZrO_2$ has been achieved by processing precipitated hydrated zirconia with $NH_4OH$ and a mineralizer.[67] Particles less than 30nm have been produced, the crystallite size being calculated using the Scherrer formula (see Chapter 2). Other studies have also used the hydrothermal method.[68] In this the amorphous $ZrO_2$ undergoes a slight rearrangement to produce the cubic phase. With an increase in the concentration of the base used, NaOH, the cubic crystallite size increased. It is also thought that the $Na^+$ ions may have some role in the formation of needlelike crystals of cubic zirconia. Further processing allows both the monoclinic and tetragonal polymorphs to be formed.

Interest in tetragonal $ZrO_2$ has fuelled speculation about the mechanism of formation of this phase. Tani et al[69] investigated the relationship between particle size and impurities on the stabilisation of the tetragonal phase. They proposed that these factors did not influence the stabilisation of the tetragonal phase, but that the formation of tetragonal zirconia is closely related to the existence of amorphous $ZrO_2$. The formation of the tetragonal phase was attributed to a topotactic crystallisation on the nuclei of the amorphous material.

The transformation of tetragonal $ZrO_2$ to monoclinic $ZrO_2$, and the effect of variables on this process have been studied extensively, as has the mechanism of crystallisation.[70, 71] It was also found that the pH of the reaction medium has a large influence on the crystallisation process. A generalised mechanism for the crystallisation of tetragonal and monoclinic zirconia has been proposed,[71] Figure 1.11.

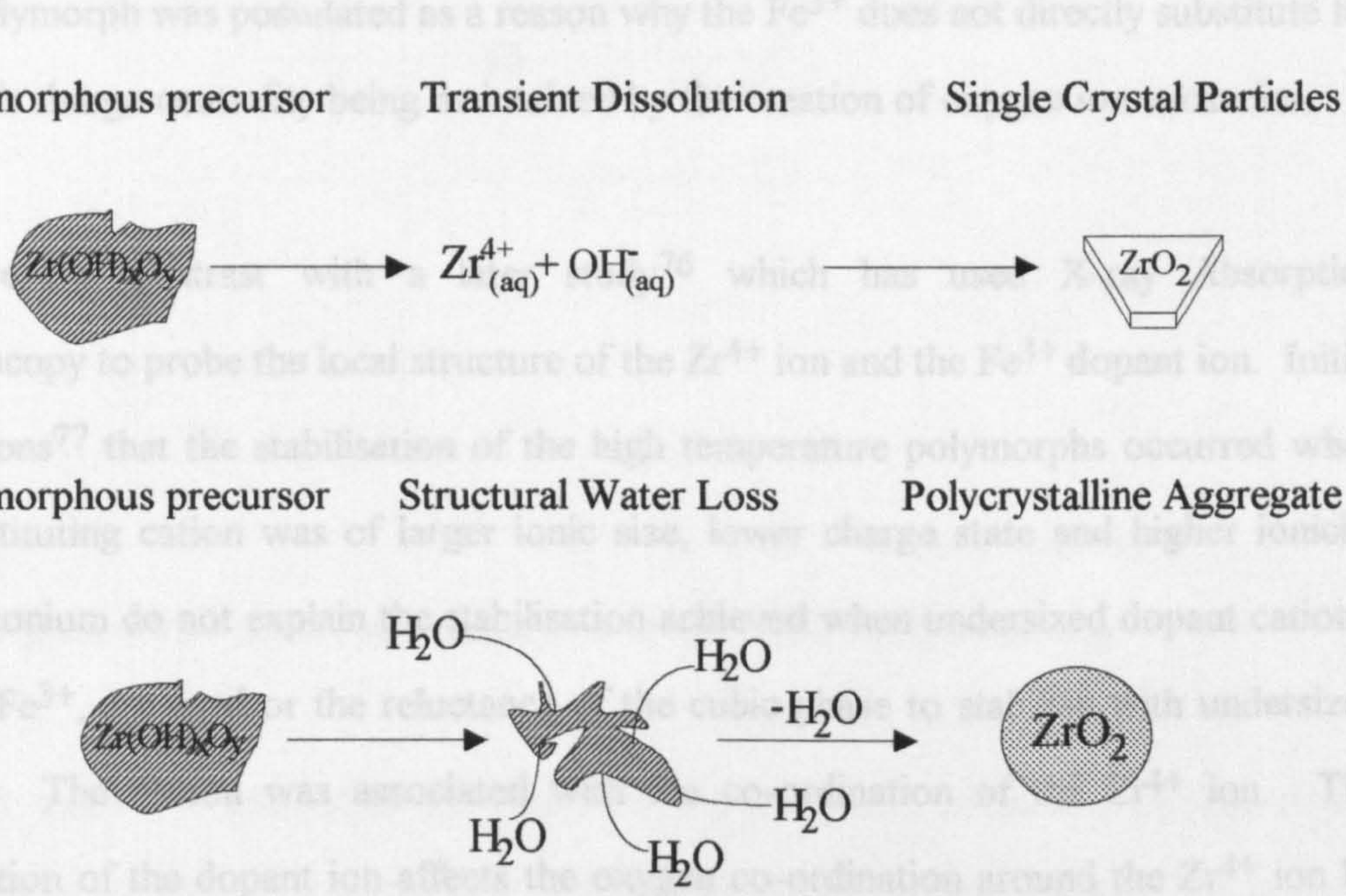


***Figure 1.11 - (a) Proposed mechanism of formation for m-$ZrO_2$ from acidic solution and (b) Proposed mechanism of formation of t-$ZrO_2$ from amorphous $Zr(OH)_xO_y$ precursors[71] where m = monoclinic and t = tetragonal***

Zirconium metal has also been used in a different type of hydrothermal reaction. The metal was reacted with supercritical water which produced the monoclinic phase.[72]

Finally the use of the hydrothermal process has been described[73] as a method to produce ultrafine $ZrO_2$ from a zirconium acetate/glacial acetic acid mixture. This is an advantageous method as very fine crystallites of high purity with controllable morphology are produced.

### 1.3.3 Iron-doped zirconium(IV) oxide

There is general agreement[74, 75] that the solubility limit of iron in monoclinic zirconia is less than 20 mol %. It was also observed that the cubic $ZrO_2$ converts to the monoclinic form with segregation of $\alpha$-$Fe_2O_3$. This was observed in both the Mössbauer spectra and the XRD patterns. The reluctance of iron to adopt eightfold co-ordination in the cubic polymorph was postulated as a reason why the $Fe^{3+}$ does not directly substitute for $Zr^{4+}$ with charge neutrality being maintained by the creation of oxygen ion vacancies.

These results contrast with a later study[76] which has used X-ray Absorption Spectroscopy to probe the local structure of the $Zr^{4+}$ ion and the $Fe^{3+}$ dopant ion. Initial suggestions[77] that the stabilisation of the high temperature polymorphs occurred when the substituting cation was of larger ionic size, lower charge state and higher ionicity than zirconium do not explain the stabilisation achieved when undersized dopant cations, such as $Fe^{3+}$, are used or the reluctance of the cubic phase to stabilise with undersized dopants. The reason was associated with the co-ordination of the $Zr^{4+}$ ion. The introduction of the dopant ion affects the oxygen co-ordination around the $Zr^{4+}$ ion by introducing oxygen vacancies to maintain charge balance. This alters the $ZrO_7/ZrO_8$ ratio. Only when this ratio reaches 1 does the minimum concentration for stabilisation occur. For oversized dopants this level was found[76] to be 11 mol % of $Fe_2O_3$, but for undersized dopants the level was found to be 20 mol %. Hence, it is twice as difficult to form cubic stabilised zirconia with undersized dopants, as the minimum level of dopant required is twice that required for stabilisation with oversized dopants.

In the case of the tetragonal phase the presence of the dopant ion increases the $ZrO_7$ content as oxygen vacancies are introduced to maintain charge balance. As $ZrO_7$ content increases the structure undergoes a transformation to the monoclinic phase. Undersized trivalent dopants provide half as much $ZrO_7$ as oversized dopants and therefore have less effect on tetragonality and so stabilise the tetragonal phase. From

these results,[76] a model for the doping of zirconia with undersized dopants where one dopant ion is associated with two oxygen vacancies has been proposed, Figure 1.12.

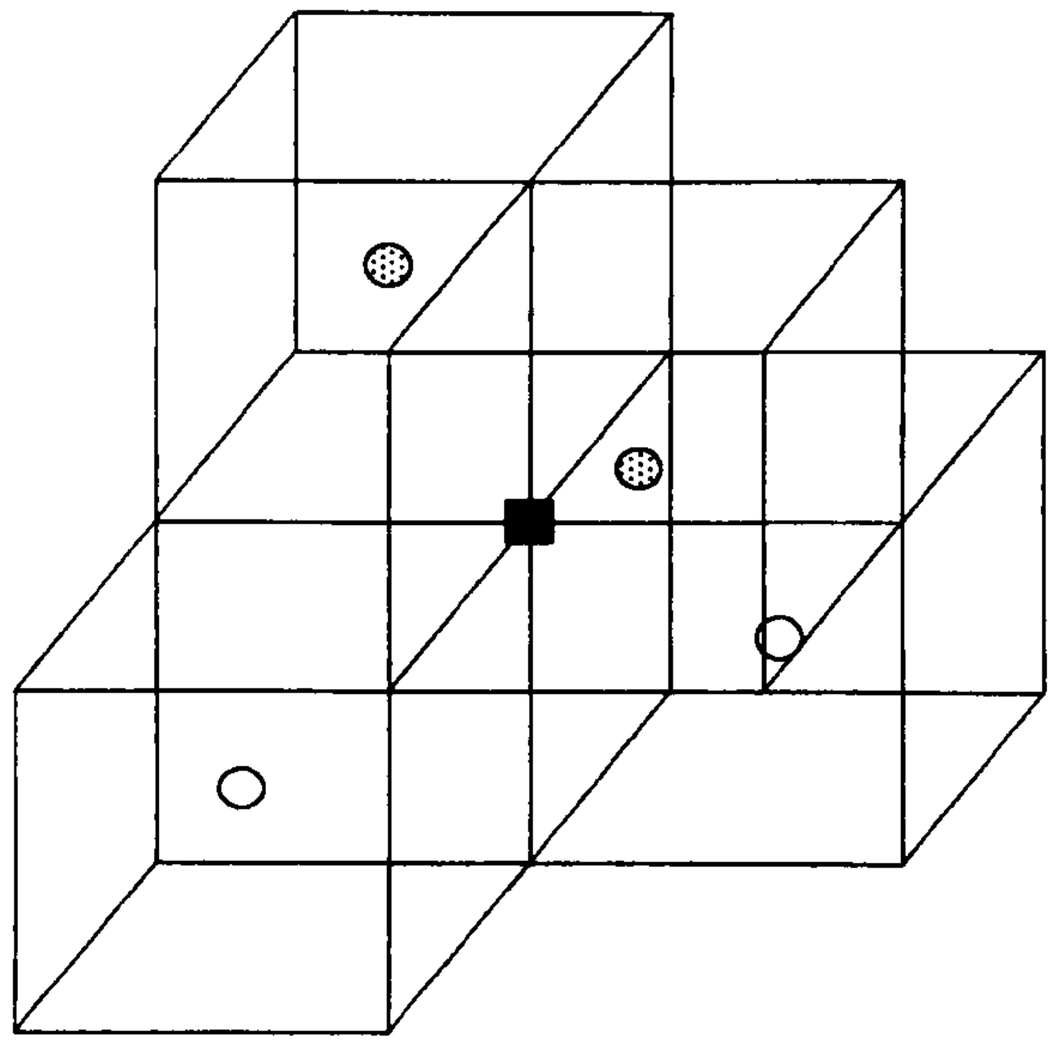


***Figure 1.12 - Model of substitution of $M^{3+}$ into $ZrO_2$ where $r_M < r_{Zr}$[76]***

A recent study[78] investigated the structure and reduction behaviour of iron-doped zirconium(IV) oxide. $^{57}Fe$ Mössbauer spectra were recorded at 298K and 77K in order to study the variation of the zirconia structure with increasing iron content. A segregation of $\alpha$-$Fe_2O_3$ was observed as the dopant level was increased to 38 at%. It was proposed that for iron contents of 38 at% and above the $Fe^{3+}$ ions dope the zirconia as expected and also the $Zr^{4+}$ ions dope the $\alpha$-$Fe_2O_3$ phase. This was indicated by a decrease in the hyperfine field of the $\alpha$-$Fe_2O_3$ component in the $^{57}Fe$ Mössbauer spectrum to 49.8T from an expected value of *ca.* 52.5T for pure $\alpha$-$Fe_2O_3$. A phase transformation from the cubic iron doped zirconia to zirconium doped $\alpha$-$Fe_2O_3$ was observed to occur on increasing the dopant level to 79 at%. At very high iron contents (>70 at%) the $Zr^{4+}$ ions were found to dope the $\alpha$-$Fe_2O_3$ phase exclusively.

# References


1 E.De Grave, R.M.Persoons, R.E.Vandenberghe and P.M.A.De Bakker, Phys.Rev.B, 1993, 47, 5881

2 R.M.Persoons, E.De Grave, P.M.A.De Bakker and R.E.Vandenberghe, Phys.Rev.B, 1993, 47, 5894

3 G.A.Sawatzky, F.van der Woude and A.H.Morrish, Phys.Rev., 1969, 187, 747

4 T.Kodama, Y.Wadu, T.Yamamoto M.Tsuji and Y.Tamaura, J.Mater.Chem., 1995, 5, 1413

5 C.J.Nistor, G.A.Sawatzky, C.Boekema and F.van der Woude, Int.Conf.Mössbauer Spec. 5th Nucl.Int. Conf., Prague, Czech., 1975.

6 R.Bauminger, S.G.Cohen, A.Marinov, S.Ofer and E.Segal, Phys.Rev., 1961, 122, 1447

7 M.J.Rossiter, J.Phys.Chem.Solids, 1965, 26, 775

8 M.Robbins, G.K.Wentheim, R.C.Sherwood and D.N.E.Buchannan, J.Phys.Chem. Solids, 1971, 32, 717

9 A.Malets i Riera, G.Pourroy and P.Poix, J.Magn.Mag.Mater., 1994, B4, 195

10 P.Lahiri and S.K.Sengupta, Can.J.Chem., 1991, 69, 33

11 A.Kozlowski, Z.Kakel, R.Zalecki and J.M.Honig, J.Magn.Mag.Mat., 1995, 140-144, 2083

12 R.J.Hill, J.R.Craig and G.V.Gibbs, Phys.Chem.Minerals, 1979, 4, 317

13 E.J.W.Verwey and E.L.Heilmann, J.Chem.Phys., 1947, 15, 174

14 H.St.C.O'Neill and A.Navrotsky, Amer.Miner., 1983, 68, 181

15 E.W.Gorter, Adv.Phys., 1957, 6, 336

16 T.F.W.Barth and E.Posnjak, Z.Krist., 1932, 82, 325

17 C.Boekema, Philisophical Magazine, 1980, B42, 409

18 A.Ito, K.Ono and Y.Ishikawa, J.Phys.Soc.Jpn., 1963,18,1465

19 F.van der Woude, G.A.Sawatzky and A.H.Morrish, Phys.Rev., 1968, 167, 533

20 W.Kündig and R.S.Hargrove, Solid State Comm., 1969,7,223

21 E.J.W.Verwey, P.W.Haayman and F.C.Romeijn, J.Chem.Phys., 1947, 15, 181

22 B.J.Evans and S.S.Hafner, J.Appl.Phys., 1969, 40, 1411

23 R.S.Hargrove and W.Kündig, Solid State Comm., 1970, 8, 303

24 L.Häggström, H.Annerstein, T.Ericsson, R.Wäppling, W.Karner and S.Bjarman, Hyp.Int., 1978, 5, 201

25 S.K.Banerjee, W.O'Reilly and C.E.Johnson, J.Appl.Phys., 1967, 38, 1289

26 S.Mitra, "Applied Mössbauer Spectroscopy - Theory and Practice for Geochemists and Archeologists", Pergamon Press, Oxford

27 H.Tanaka and M.Kono, J.Geomag.Geoelectr., 1987, 39, 463

28 S.Umemura and S.Iida, J.Phys.Soc.Jpn., 1978, 44, 341

29 S.K.Banerjee, W.O'Reilly, N.N.Greenwood and T.C.Gibb, J.Phys.Chem.Solids, 1967, 28, 1323

30 Ö.Helgason, H.P.Gunnlaugsson, K.Jónsson and S.Steinhórsson, Hyp.Int., 1994, 91, 595

31 T.Nishitani and M.Kono, Geophys.J.R.astr.Soc., 1983, 74, 585

32 S.Akimoto, J.Geomag.Geoelectr., 1954, 6, 1

33 R.Chevallier, J.Bolfa and S.Mathieu, Bull.Soc.Franc.Min.Crist., 1955, 78, 307

34 L. Néel, Adv.Phys., 1955, 4, 191

35 W.O'Reilly and S.K.Banerjee, Phys.Lett., 1965, 17, 237

36 S.Akimoto, T.Hatsura and M.Yoshida, J.Geomagn.Geoelectr., 1957, 9, 165

37 G. Blasse, Philips Res.Repts.Suppl., 1964, 3, 1

38 B.A.Wechsler, D.H.Lindsley and C.T.Prewitt, Amer.Miner., 1984, 69, 754

39 R.D.Shannon and C.T.Prewitt, Acta Crystallogr., 1969, B25, 925

40 S.K.Banerjee, W.O'Reilly, N.N.Greenwood and T.C.Gibb, Phys.Lett., 1966, 20, 455

41 C.Djega-Mariadassou, F.Basile, P.Poix and A.Michel, Ann.Chim., 1973, 8, 15

42 Z.Panek and K.Fitzner, Thermochim.Acta, 1984, 78, 261

43 F.Basile, C.Djega-Mariadassou and P.Poix, Mat.Res.Bull., 1973, 8, 619

44 F.Basile, C.Djega-Mariadassou and P.Poix, J.Phys.Chem.Solids, 1974, 35, 1067

45 B.J.Evans, L.S.Pan and R.H.Vogel, AIP Conf.Proc.(MMM Intermag Conf.), 1975, 29, 390

46 K.Melzer, G.Dehe and H.Mehner, J.Phys., Colloq.(Orsay, Fr.), 1980, C-1, 181

47 K.Yamada, S.Tobashi and S.Ichiba, Chem.Lett., 1990, 8, 1327

48 D.K.Smith, H.W.Newkirk, Acta Crystallogr., 1965, 18, 983

49 C.G.Barraclough, J.Lewis and R.S.Nyholm, J.Chem.Soc., 1959, 59, 3552

50 E.M.Levin and H.F.McMurdie, Phase Diagrams for Ceramists, 1975 Supplement, The American Ceramic Sociey, INC.

51 T.E.Macdermott, Coord.Chem.Rev., 1973, 11, 1

52 G.Katz, J.Am.Ceram.Soc., 1971, 54, 531

53 F.W.Vahldiek, L.B.Robinson and C.T.Lynch, Science, 1963, 142, 1059

54 R.Suyama, T.Ashida and S.Kume, J.Am.Ceram.Soc., 1985, 68, C314

55 S.Kawasaki and T.Yamanaka, J.Mater.Sci.Lett., 1994, 13, 514

56 C.Wolf and C. Russell, J.Mater.Sci., 1992, 27, 3749

57 T.Okubo and H.Nagamoto, J.Mater.Sci., 1995, 30, 749

58 H.Asaoko, Mater.Lett., 1994, 19, 213

59 M.Chatry, M.Henry and J.Livage, Mat.Res.Bull., 1994, 29, 517

60 R.Srinivasan, M.B.Harris, B.H.Davis, S.F.Simpson and R.J.De Angelis, J.Mat.Res., 1988, 3, 787

61 Feng-Chau Wu, Shu-Cheng Yu, J.Mater.Sci., 1990, 25, 970

62 A.Rabenau, Angew.Chem.Int.Ed.Engl., 1985, 24, 1026

63 W.J.Dawson, Ceram.Bull., 1988, 67, 1673

64 S.Hirano, Am.Ceram.Soc.Bull., 1987, 66, 1342

65 C.B.Ponton, P.M.Brownie, M.R.Piremoon and P.M.Marquis, Prop. Appl. Met. Ceram. Mater. Process Eng. Mater. Adv. Serv., Wardy, UK 1992, 2, 1099

66 S.Somiya, T.Kumaki, Z.Nakai, K.Hishimura, T.Akiba and Y.Suwa, Prog. Crystal Growth & Charact., 1990, 21, 195

67 E.Tani, M.Yoshimura and S.Somiya, J.Am.Ceram.Soc., 1981, 64, C181

68 H.Nishizawa, N.Yamasaki, K.Matsuoka and H.Mitsushio, J.Am.Ceram.Soc., 1982, 65, 343

69 E.Tani, M.Yoshimura and S.Somiya, J.Am.Ceram.Soc., 1983, 66, 11

70 J.H.Adair, R.P.Denkewicz, F.J.Arriagada and K.Osseo-asare, Ceram.Trans., 1, 135-145

71 R.P.Denkewicz, K.S.Ton Huisen and J.H.Adair, J. Mater.Res., 1990, 5, 2698

72 M.Yoshimura and S.Somiya, Adv. in Ceramics, 3, 455

73 S.A.Matchett, U.S. Patent No. 5,037,579 1991

74 F.J.Berry, M.H.Loretto and M.R.Smith, J.Solid State Chem., 1989, 83, 91

75 J.F.Collins and I.F.Ferguson, J.Chem.Soc. A, 1968, 4,

76 P.Li, I-Wei Chen and J.E.Penner-Hahn, J.Am.Ceram.Soc., 1994, 77, 118

77 S.M.Ho, "On the Structural Chemistry of Zirconium Oxide," Mater.Sci.Eng., 1982, 54, 23

78 K.Chen, Y.Fan, Z.Hu and Q.Yan, J.Mater.Chem., 1996, 6, 1041

# CHAPTER TWO

# Theory of Experimental Methods

## 2.1 X-ray Powder Diffraction

The use of X-ray powder diffraction as a tool for the structural characterisation of crystalline solids is well known and has been extensively used since its discovery in the early 20th Century. A description of the theory and techniques has been reported in the literature.[1-3]

### 2.1.1 Theory

Laue and his colleagues discovered in 1912 that crystalline solids diffract X-rays when a crystal of copper sulphate was irradiated by X-rays. Although this demonstrated the principle of X-ray diffraction, it was Bragg in 1913 who actually performed the first structural analysis using a single crystal, proving that ZnS had a face centred cubic structure.

The behaviour of X-rays is such that when a beam strikes an atom there is an interaction with the electrons of the atom resulting in the X-rays being emitted in all directions. As the atoms of a crystal structure are periodically arranged, both constructive and destructive interference can occur if certain conditions are met. If the diffracted X-rays are in phase then constructive interference will occur, but if the diffracted beam is out of phase then destructive interference will occur. The necessary conditions for diffraction of an incident X-ray beam by a crystal, from which Bragg's Law is derived, is illustrated in Figure 2.1.

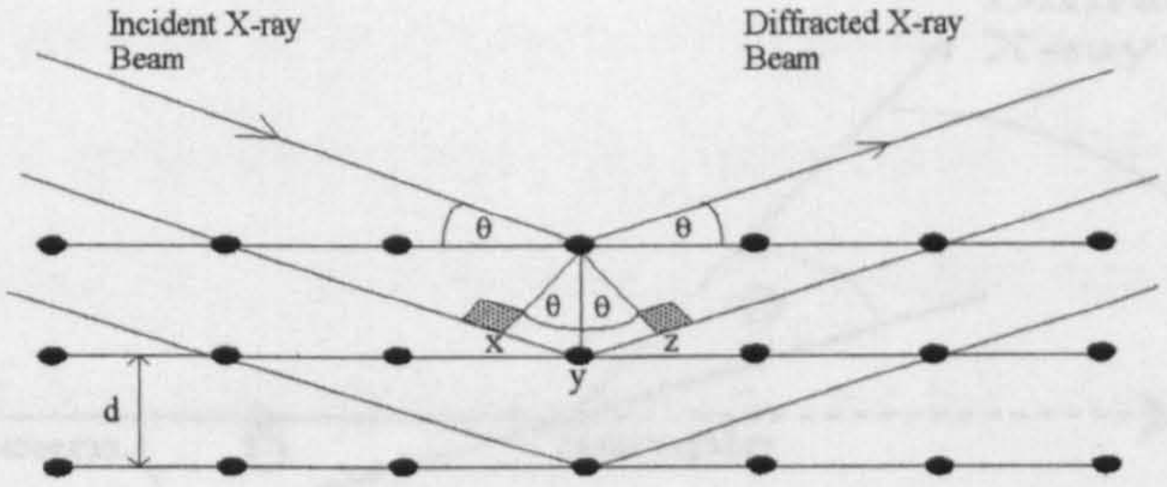


***Figure 2.1 - Schematic representation of the diffraction of an X-ray beam incident at the Bragg angle to parallel planes***

The difference between the path of the X-rays diffracted from successive planes is xy + yz. d is known as the interplanar spacing and θ is the Bragg angle, that is the angle at which the incident beam impacts with a particular crystal plane. So, applying trigonometry;

$$xy = yz = d \sin\theta \qquad (1)$$

$$xy + yz = 2d \sin\theta \qquad (2)$$

If the wavelength of the incident X-ray beam is termed λ and n is called the order of reflection, then for the reflected beam to be in phase;

$$xy + yz = n\lambda \qquad (3)$$

Then, by substituting equation 2 into the above, the equation known as Bragg's Law is obtained.

$$n\lambda = 2d \sin\theta \qquad (4)$$

In a crystalline powder sample there are a variety of randomly orientated crystals. On passing an X-ray beam through a powder sample a fraction of the crystals will be orientated so that their lattice planes satisfy the Bragg equation. This is illustrated in Figure 2.2;

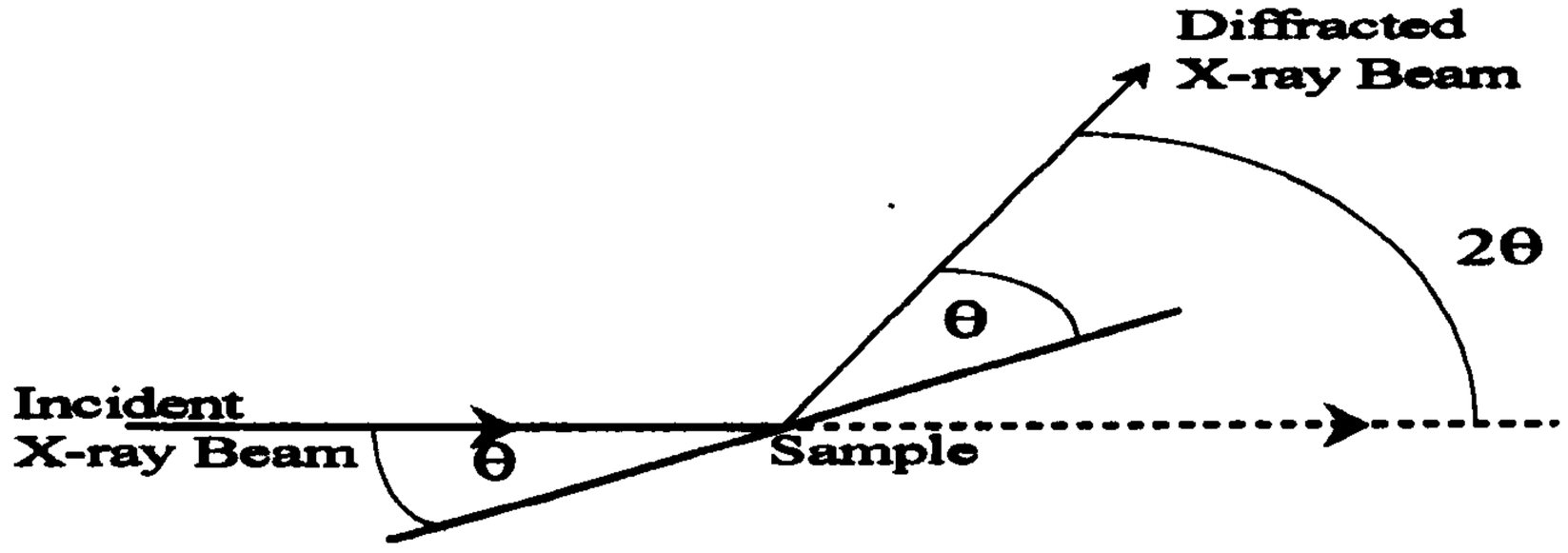


***Figure 2.2 - Schematic representation of diffraction from a powder***

As the sample will contain particles in all rotational positions about the incident beam axis, the diffracted X-ray beam will form a diffraction cone with the locus of the beam at the surface of the cone. For each set of differently spaced lattice planes a separate diffraction cone is produced, Figure 2.3. So, diffracted beams for the set of planes $d_1$ generate a cone with semi apex angle $2\theta_1$, the set of planes $d_2$ generates a cone with semi apex angle $2\theta_2$. These cones can be recorded as a set of concentric circles by placing a photographic film about the sample. This allows angles of $0^o < 2\theta < 180^o$ to be measured.

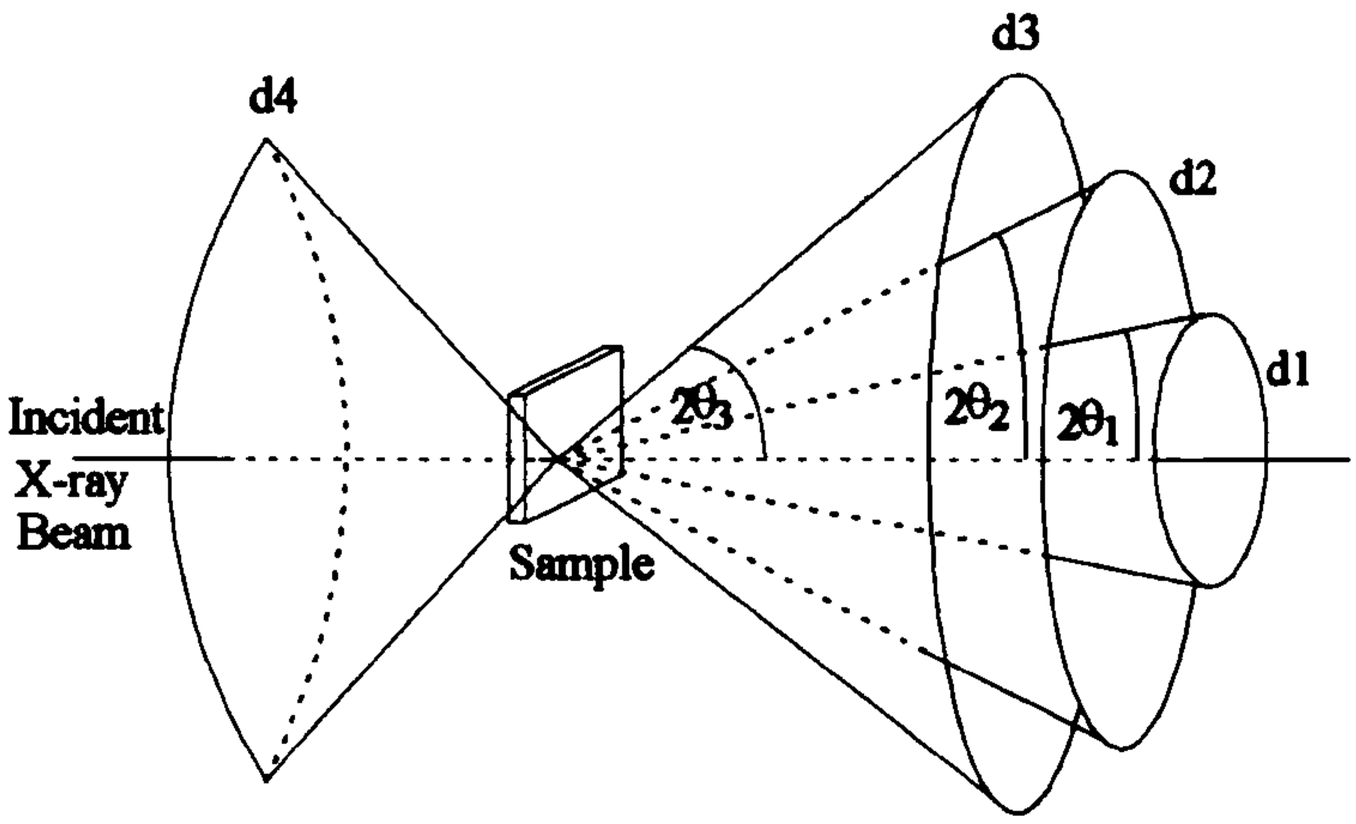


*Figure 2.3 - Formation of a diffraction cone*

Having recorded the $2\theta$ values the next stage is to interpret the data in terms of crystal structures. Crystalline solids can be regarded as a number of repeating blocks called the unit cell. All unit cells contain an array of points, known as lattice points, which represent equivalent positions in the structure, that is an atom or a point in the unit cell which has an identical environment to all other lattice points. This produces a limited number of arrangements, the simplest of which is the primitive arrangement, P. In this the lattice points are situated at the 8 corners of the unit cell. Other arrangements are body centred (I), face centred (F) and side centred (A,B,C) where only two opposite faces out of six are occupied, Figure 2.4.

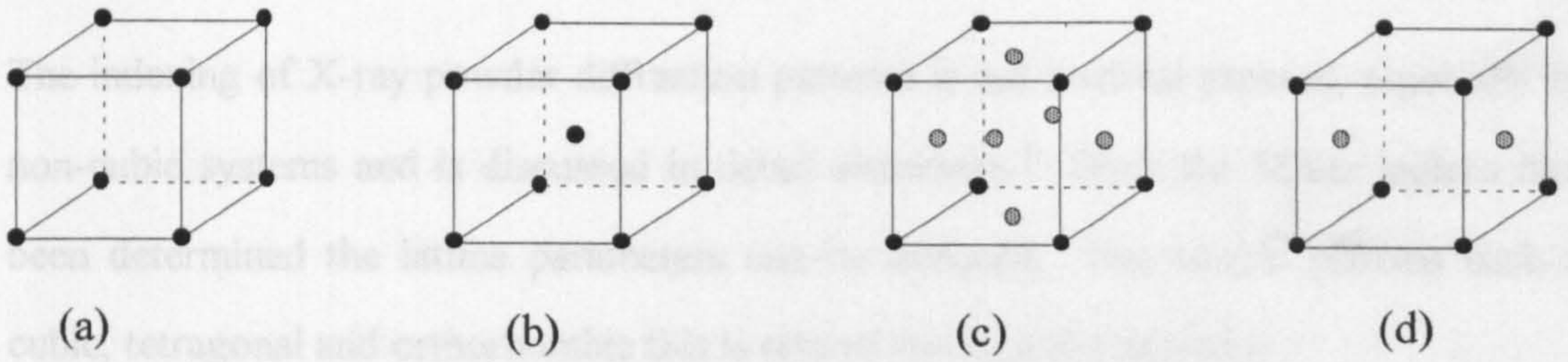


***Figure 2.4 - (a) primitive unit cell, (b) body centred, (c) face centred and (d) side centred***

There is a limit to the number of different unit cells that are possible, known as crystal systems. These are cubic, tetragonal, orthorhombic, hexagonal, trigonal, monoclinic and triclinic which have different geometries and shapes.

Combining the crystal system with lattice type gives a structure known as the Bravais lattice, of which there are a total of 14. This arises because certain combinations of lattice type and crystal system can violate the symmetry of the crystal system or be represented by a smaller unit cell.

To use the diffraction data it is necessary to identify the lattice planes so that Bragg's Law can be implemented. Lattice planes are regarded as layers of atoms stacked to form a three dimensional structure. Miller indices are used to define the planes. A Miller index is described by 3 numbers, (h, k, l), which are the reciprocal of the coordinates where the lattice plane cuts the unit cell axes. The coordinates are expressed as fractions of the unit cell, between 0 and 1. If a plane runs parallel to the axis then the intercept is infinity which gives a Miller index of zero.

The Miller indices can be associated with a Bragg angle, $\theta$, for a line which can then be converted into an interplanar spacing. The spacing depends only on the lattice dimensions and crystal system, and therefore any two crystals with the same type of unit cell will produce a similar X-ray powder diffraction pattern in terms of peak position.

The indexing of X-ray powder diffraction patterns is not a trivial process, especially for non-cubic systems and is discussed in detail elsewhere.[1] Once the Miller indices have been determined the lattice parameters can be deduced. For simple systems such as cubic, tetragonal and orthorhombic this is related through the equation;

$$\frac{1}{d^2} = \frac{h^2}{a^2} + \frac{k^2}{b^2} + \frac{l^2}{c^2}$$

For the less symmetric systems more complicated relationships exist and as these are different for each system calculating lattice parameters for non-cubic systems is not a trivial process, and is dealt with in detail elsewhere.[1]

Another characteristic feature of the X-ray powder diffraction pattern is the intensity of the reflections. This depends on a number of factors, detailed by Klug and Alexander.[1] One of the major influences is the scattering factor, or form factor (f). The form factor depends on the number of electrons in an atom, and the reflected X-ray beam is therefore the result of the X-ray beams scattered by each of the electrons.

Scattering by two electrons in an atom at some angle $2\theta$ to the incident beam results in a phase difference between the resultant reflected beams, Figure 2.5. As distances between electrons in an atom are so small, the phase difference is usually less than one wavelength. Therefore only partial destructive interference occurs, causing a general decrease in the scattered intensity with decreasing X-ray wavelength, so the form factor decreases as $\sin\theta/\lambda$ increases. A summation of all the scattering factors in the unit cell gives the structure factor for the hkl reflection. The structure factor can be defined as the ratio of the amplitude scattered by the plane hkl relative to the amplitude scattered by a single electron.

The intensity of the diffraction lines is further affected by the superposition of the reflected X-ray beams from several planes. In this case the effect will be additive and the

multiplicity factor, j, is introduced to account for this in the intensity formula. In the powder diffraction technique the value of j is dependent on the symmetry of the crystalline material. From the Bragg equation it follows that, with monochromatic radiation, planes of the same interplanar spacing d will reflect the X-rays at the same angle $\theta$. Therefore they will all contribute to the same diffraction line. This can be illustrated by considering the equation for d in the cubic system;

$$d_{(hkl)} = \frac{a}{\sqrt{h^2 + k^2 + l^2}}$$

From this it is clear that (1 1 1) and ($\bar{1}$ $\bar{1}$ $\bar{1}$) will have the same spacing as will all other combinations of positive and negative unit indices. So all eight planes contribute to the line designated as (1 1 1) and therefore the line is eight times as strong as if only the (1 1 1) plane was responsible for the reflection. This treatment can be extended to examine the set of planes (2 1 3), (1 2 3) and (3 2 1) which also give the same spacing. For this set of planes there are six further permutations and for each of these there are eight permutations of sign meaning that 48 reflections contribute to this line in the powder pattern. It is clear that the multiplicity factor is totally dependent on the symmetry of the crystal. Values for the 32 crystal classes have been calculated and tabulated[1] for use in the powder method.

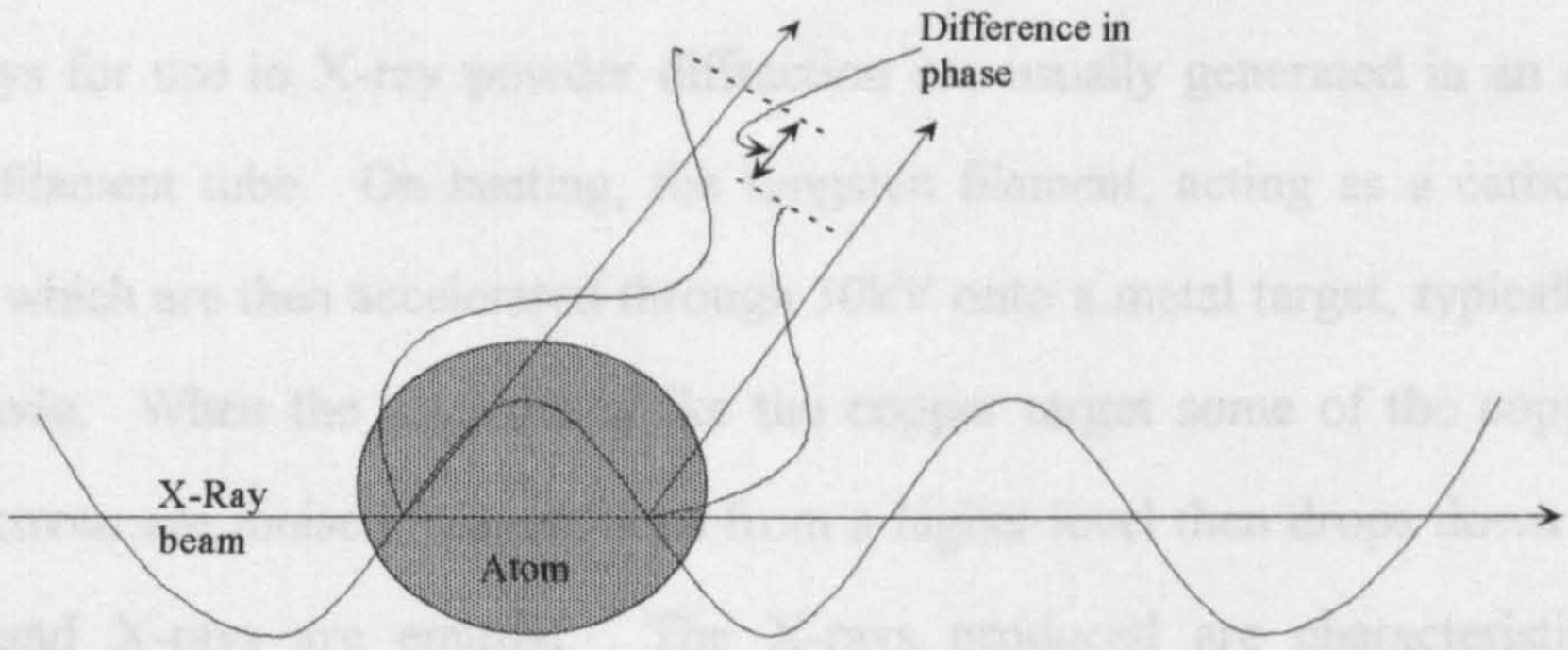


***Figure 2.5 - Phase difference in scattering from electrons in different parts of an atom***

It is known that small particles can cause line broadening in the X-ray powder diffraction pattern and the relationship between particle size and line broadening was determined by Scherrer[4] and is described in detail by Klug and Alexander.[1] Scherrer related the mean dimension, D, of the crystallite to the pure diffraction broadening, β, by the equation

$$D = \frac{K\lambda}{\beta Cos\theta}$$

where K is a constant approximately equal to unity, θ is the diffraction angle and λ is the diffraction wavelength.

This provides a useful method for determining approximate crystallite sizes from powder diffraction patterns, but should not be used as an absolute method. Any crystallite sizes determined in this way should be confirmed using other methods.

X-ray powder diffraction can be used to determine and characterise crystal structures. A powder pattern is generated by a particular set of X-ray reflections which are unique to that particular crystal structure. Therefore X-ray powder diffraction is a useful technique for the identification of crystal structures.

### 2.1.2 Instrumentation

The X-rays for use in X-ray powder diffraction are usually generated in an evacuated tungsten filament tube. On heating, the tungsten filament, acting as a cathode, emits electrons which are then accelerated through 30kV onto a metal target, typically copper, at the anode. When the electrons strike the copper target some of the copper 1s (K shell) electrons are ionised. An electron from a higher level then drops down to fill the vacancy and X-rays are emitted. The X-rays produced are characteristic of that particular target metal, and the wavelength of the X-ray produced is dependent on the electronic transition involved, Table 2.1.

| | | |
|---|---|---|
| $K_{\alpha 1}$ | $2p \rightarrow 1s$ | 1.54050Å |
| $K_{\alpha 2}$ | $2p \rightarrow 1s$ | 1.54434Å |
| $K_{\beta}$ | $3p \rightarrow 1s$ | 1.39217Å |

***Table 2.1 - The characteristic X-rays produced by copper***

For X-ray diffraction the $K_{\beta}$ X-rays are of no use and are typically removed with a nickel filter. The $2p \rightarrow 1s$ transition produces 2 characteristic wavelengths, $K_{\alpha 1}$ and $K_{\alpha 2}$ because the transition has slightly different energies for the two total angular momentum states of the 2p electron. As the angle $2\theta$ increases the existence of these two peaks becomes more obvious.

Early X-ray powder diffraction patterns were recorded using a Debye-Scherrer camera, illustrated schematically in Figure 2.6.

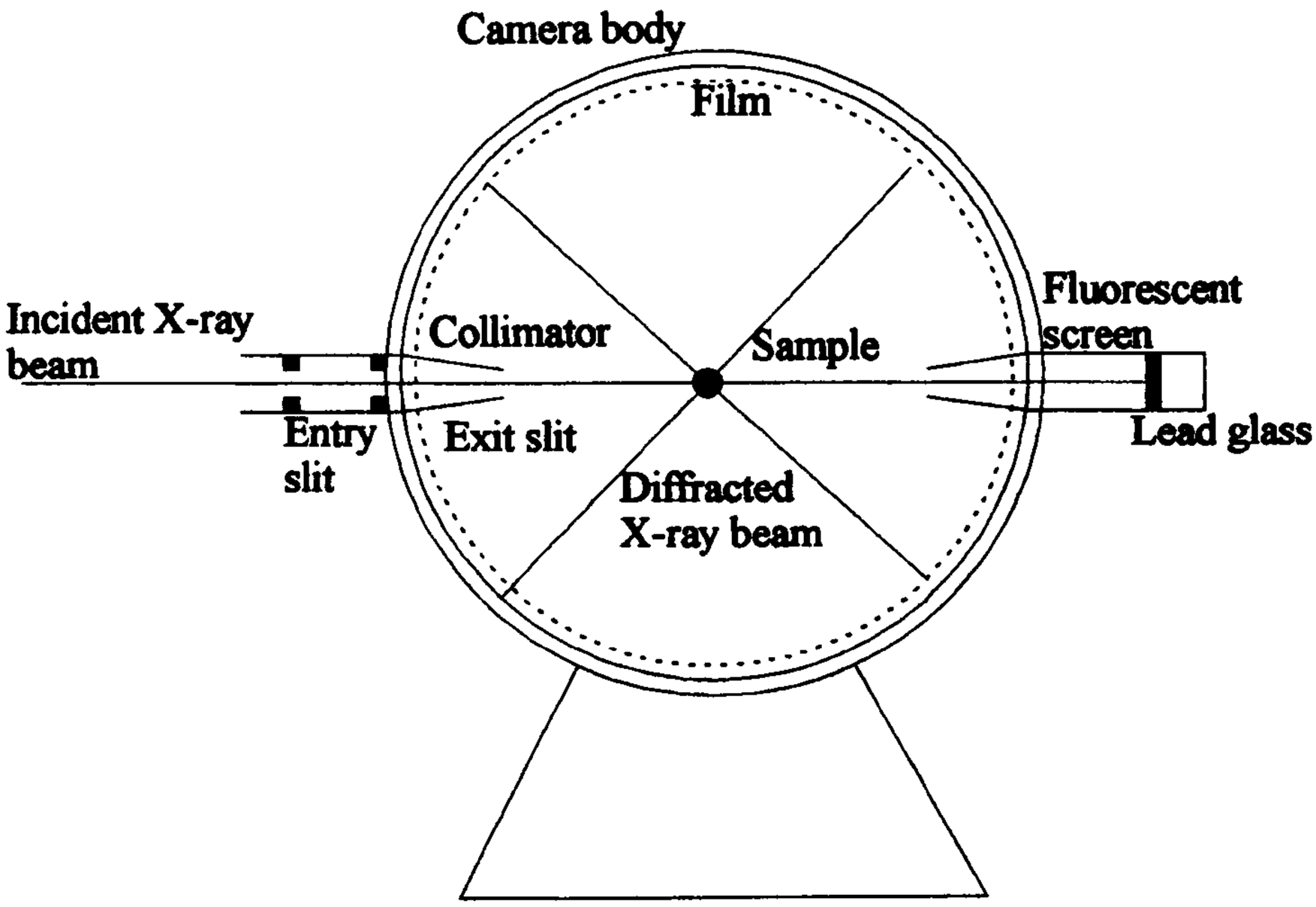


***Figure 2.6 - Schematic representation of a Debye-Scherrer camera***

A Debye-Scherrer camera consists of a light tight cylinder with the sample mounted in the centre. The incident X-ray beam is introduced at one side of the cylinder through a collimator and exits directly opposite, being stopped by a lead glass stop. The diffracted beam is detected on a photographic film held on the inside of the cylinder, and the diffraction pattern is seen as a series of arcs on the film, Figure 2.7.

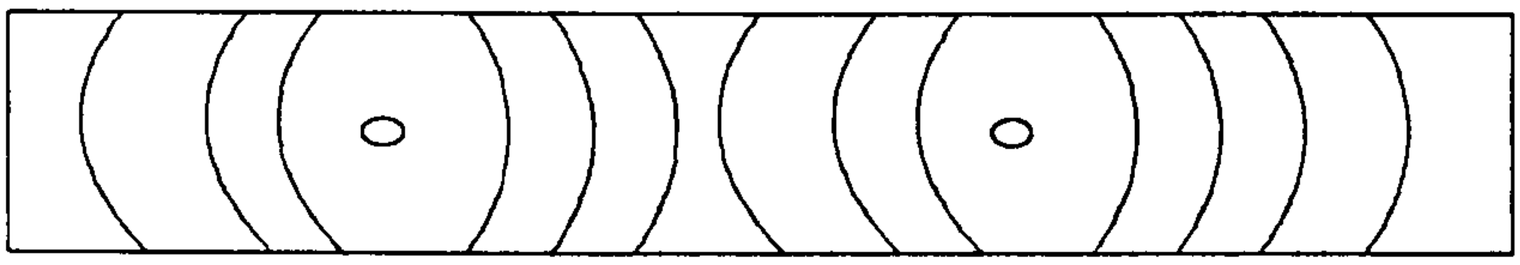

*Figure 2.7 - Example of a Debye-Scherrer film*

These arcs are parts of the diffraction cones discussed in 2.1.1 with the distance between the entrance and exit holes being exactly $180^{o}$ ($2\pi$ radians), which allows the radius of the film to be calculated. Diffraction angles for each of the cones can then be calculated from the diameter of the cones;

$$2\theta = \frac{AB}{R}$$

where $2\theta$ is the cone angle radius, AB is the cone diameter and R is the radius of the film.

More recently X-ray diffraction patterns have been recorded using a diffractometer. A typical diffractometer is depicted in Figure 2.8. The X-ray beam emitted by the X-ray tube passes through the nickel filter and collimating slits before striking the sample. This is usually pressed flat onto a plate which is rotated through $\theta^{o}$ accompanied by the detector moving through $2\theta^{o}$. Therefore only the crystal planes which satisfy the Bragg equation will be diffracted towards the detector. The detector will then record the number of X-ray counts and plot this against the $2\theta$ values. Bragg's equation can be used to determine the d values and the recorded patterns can be matched against existing

powder patterns using the Joint Committee on Powder Diffraction Standards (JCPDS) file.

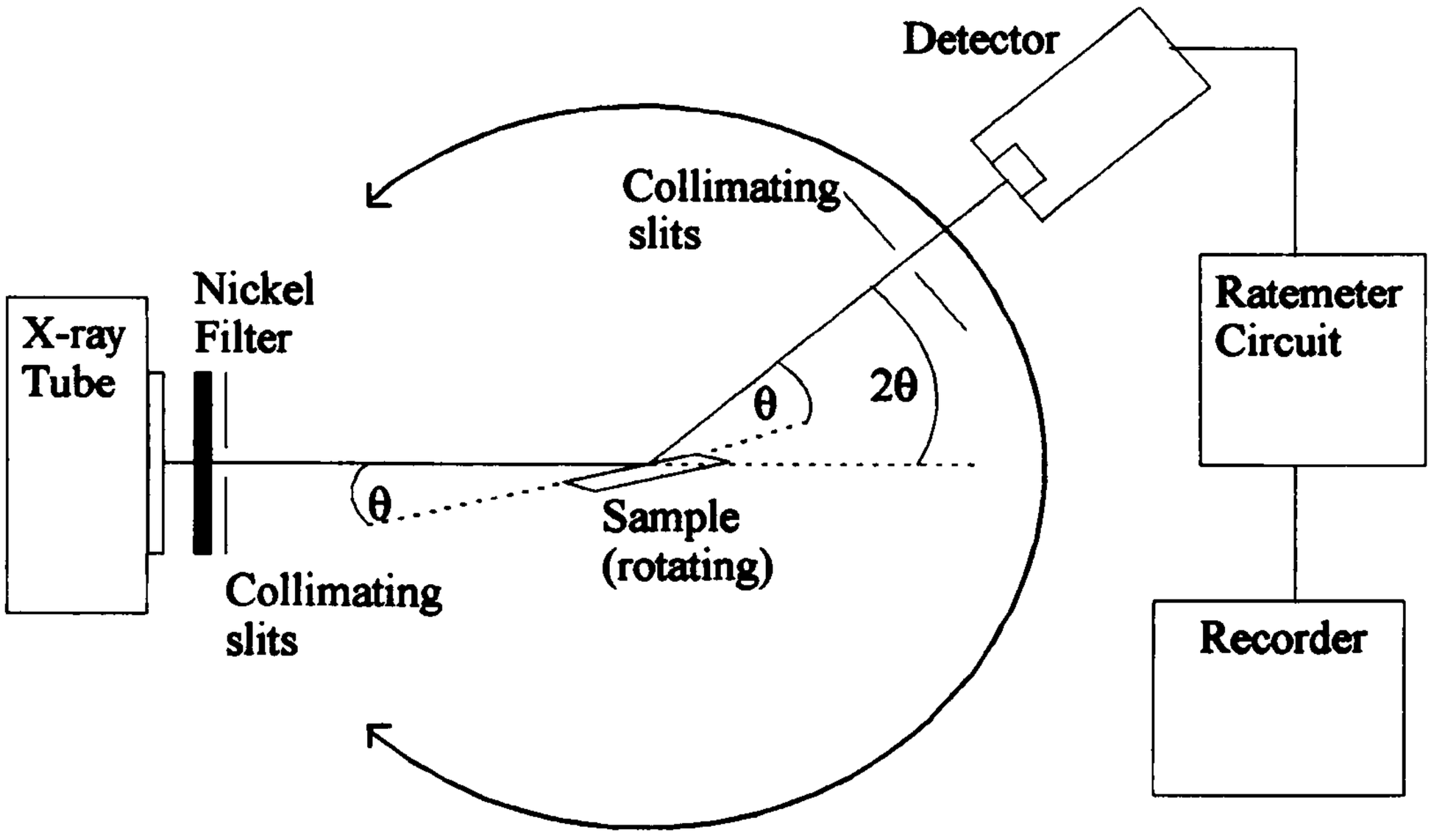


***Figure 2.8 - Schematic representation of a powder X-ray diffractometer***

## 2.2 Mössbauer Spectroscopy

### 2.2.1 Theory

Mössbauer spectroscopy is a technique which involves the resonant absorption and emission of gamma rays by nuclei. This phenomenon was first observed by Rudolf Mössbauer in $^{158}Ir$ in 1958, and led to the development of the technique which now bears his name. Many detailed accounts of the theory and instrumentation of Mössbauer spectroscopy can be found in the literature.[5-7]

In Mössbauer spectroscopy the source of the γ-rays usually consists of a solid matrix in which a radioactive isotope is embedded. This will decay into the Mössbauer isotope in an excited state, which then relaxes with the emission of a γ-ray. For resonant absorption the energy of the γ-ray must not be influenced by nuclear recoil. To achieve

this the Mössbauer nuclei are held in a rigid crystal lattice. If the energy of the nuclear recoil associated with the absorption and emission of γ-rays is small in comparison to the lowest quantised lattice vibration, recoil free transitions suitable for a Mössbauer experiment can occur. In the case of $^{57}Fe$ and $^{119}Sn$ the γ-ray energies are small (14.4keV and 23.8keV respectively), and thus the recoil effects are small.

The energy of the transition between the excited and ground state of the Mössbauer nucleus is usually slightly different in the source and absorber. Therefore, rarely does the energy of the incident γ-ray correspond to the energy transition of the absorber Mössbauer atom. The γ-ray energy is modified by the Doppler effect, achieved by vibrating the source at a velocity of millimetres per second. So, a Mössbauer spectrum consists of a plot of γ-ray counts against the velocity of the source, Figure 2.9. A typical Mössbauer spectrum obtained from a sample in which the Mössbauer atoms are in the same cubic environment in both source and absorber is presented in Figure 2.9.

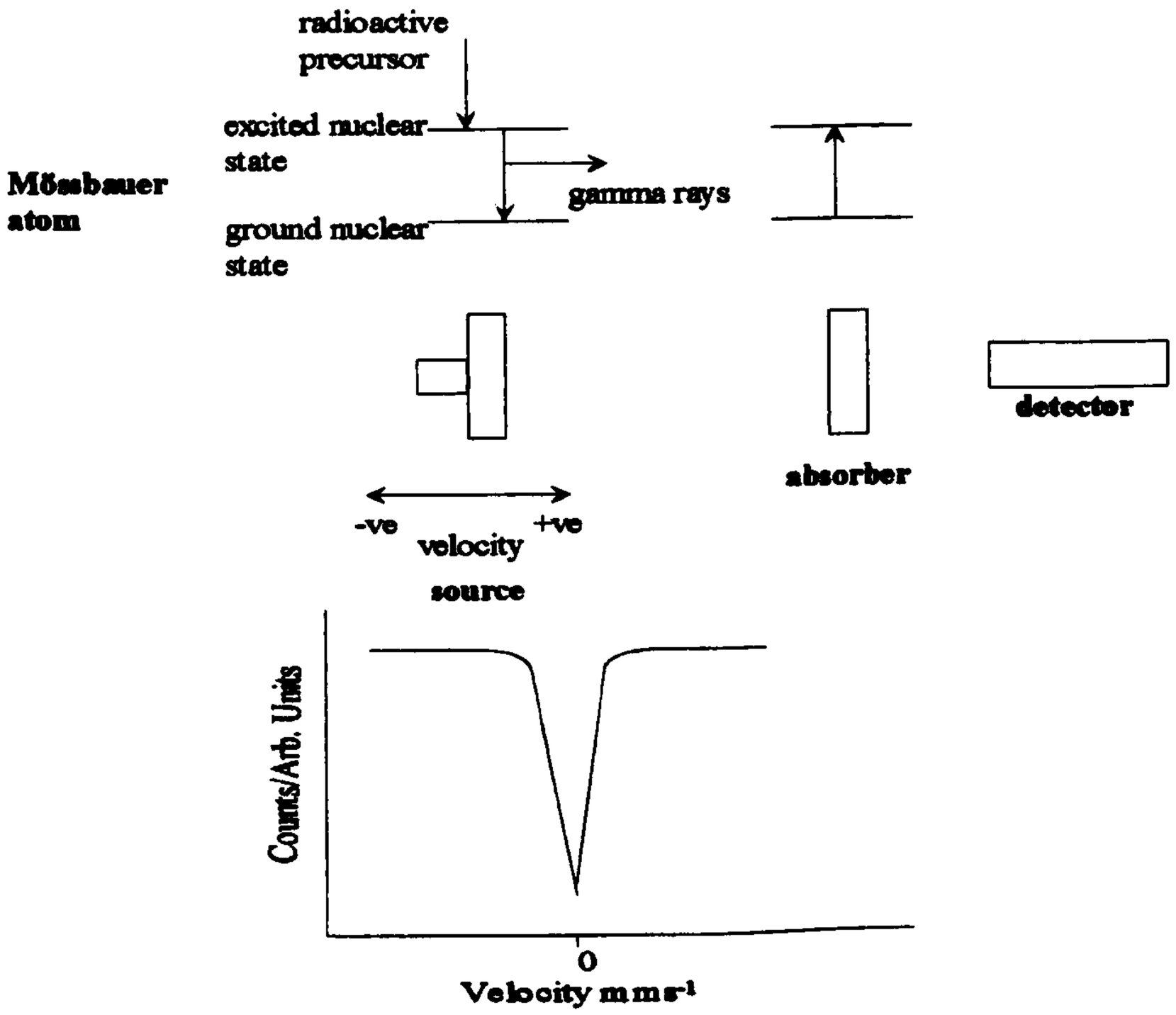


***Figure 2.9 - Schematic representation of the recording of a Mössbauer spectrum, and a spectrum recorded with source and absorber nuclei in the same cubic environments***

The various environments about the nucleus in the absorber atom give rise to hyperfine interactions which are quoted as the Mössbauer parameters known as isomer shift, quadrupole splitting and magnetic hyperfine splitting. These arise because of the electric monopole interaction, electric quadrupole interaction and magnetic monopole interaction respectively.

### 2.2.2 Isomer Shift

To understand the origin of the isomer shift it is useful to consider a nucleus stripped of its electrons. In this nucleus the energy of the transition between ground and excited states may be represented as E, Figure 2.10(a).

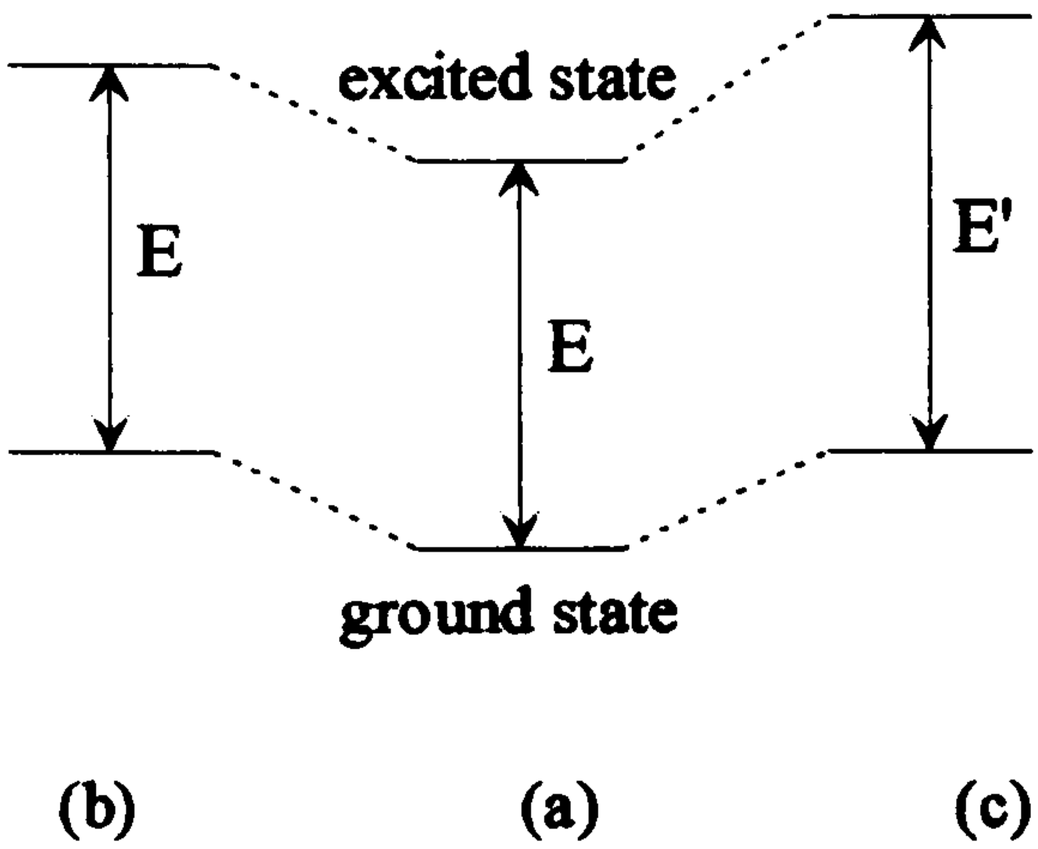


***Figure 2.10 - Nuclear energy level of (a) a bare nucleus, and a nucleus for which the nuclear excited and ground states are (b) the same and (c) different***

If the nucleus is surrounded by electrons a Coulombic attraction between the nuclear- and the electronic- charges occurs which will modify the nuclear energy levels. If in both the excited and ground states the size of the nucleus is the same, then the interaction of these states with the electrons will be the same. Hence the energy levels will be changed by the same amount, as will the energy of the transition E, Figure 2.10(b). If, on the otherhand, the size of the nucleus of the two states are different, as usually arises, the energies of the ground and excited states will be modified to a different extent. The

energy of the transition will be modified, but will be of some new value E', Figure 2.10(c).

The nuclear energy levels depend upon the electronic environment. Therefore if the source and absorber nuclei are in different electronic environments then the nuclear energy levels will be modified to differing degrees, Figure 2.11a. So the energy of the emitted γ-ray is modified by the Doppler effect and the Mössbauer spectrum will exhibit a resonant absorption shifted from zero velocity, Figure 2.11b. This is known as the isomer- or chemical isomer- shift, δ.

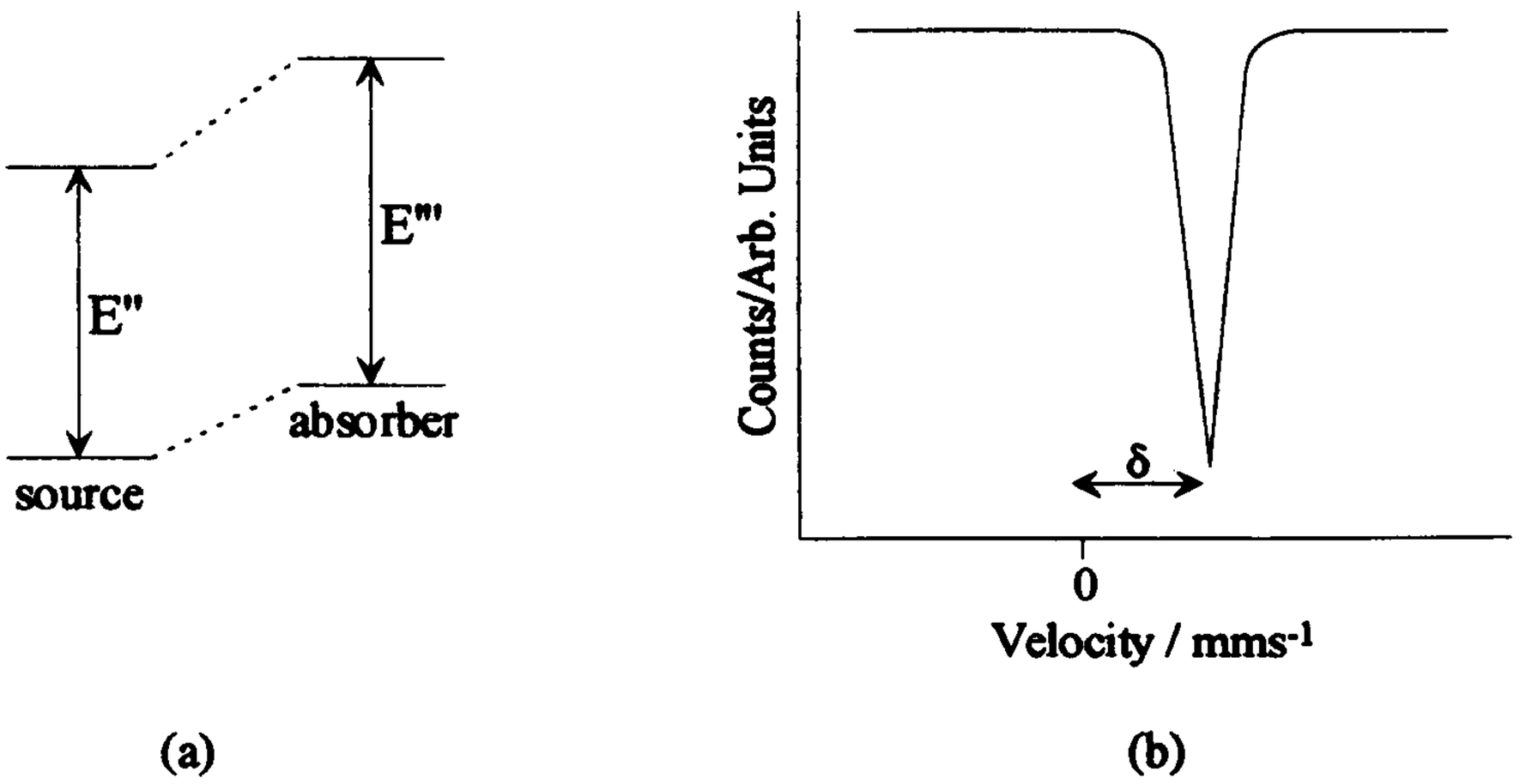


***Figure 2.11 - (a) Nuclear energy levels of source and absorber atoms in different electronic environments and, (b) the resulting Mössbauer spectrum***

The isomer shift can be related to the electronic properties by the equation

$$\delta = \text{constant}\frac{\Delta R}{R}(\Psi_o^2(o)_A - \Psi_s^2(o)_S)$$

where $\Delta R/R$ is $(R_e - R_g)/R_g$ and $R_e$ and $R_g$ are the radii of the excited and ground state nuclei respectively. $\Psi_s^2(o)_A$ and $\Psi_s^2(o)_S$ are the s-electron densities at the absorber and source respectively. $\Psi_s^2(o)$ is dependent primarily on the population of the s-orbitals, but will also be influenced by the occupation of other types of orbitals. This is because the outer electrons can shield the interaction of the s-electrons with the nucleus. For any particular source the value of $\Psi_s^2(o)_S$ will be constant, and therefore any change in the

isomer shift will reflect changes in $\Psi_s^2(o)_A$. Therefore information about the electronic environment of the absorber is obtained, which can then be used as a probe of oxidation state.

For $^{119}Sn$ the sign of $\Delta R/R$ is positive, which means that the excited nucleus is larger than the ground state nucleus, and so higher s-electron densities at the tin nuclei in the absorber are reflected in a more positive isomer shift value. Tin(II) compounds give a value of between +2.9 and +4.5 $mms^{-1}$ relative to $SnO_2$ whereas tin(IV) compounds give values in the range of -0.5 to +2.0 $mms^{-1}$.

For $^{57}Fe$ Mössbauer spectroscopy the value of $\Delta R/R$ is negative. Hence higher s-electron densities at iron nuclei in the absorber are reflected by a decrease in isomer shift. Another influence on the isomer shift in iron compounds is the effect of shielding. As d electron removal effectively increases the s-electron density at the iron nuclei, iron(II) species with a $d^6$ configuration have a more positive isomer shift than iron(III) species with a $d^5$ configuration.

In both $^{57}Fe$ and $^{119}Sn$ nuclei the magnitude of $\Delta R/R$ is sufficiently large for a range of isomer shifts to exist, compared to the natural line width of the absorber.

### 2.2.3 Quadrupole Splitting

If a nucleus has a spin I greater than $\frac{1}{2}$ then it will have an asymmetric charge distribution, which gives rise to a nuclear quadrupole moment. It is then possible for the nuclear quadrupole moment to interact with an asymmetric electric field represented by an electric field gradient tensor. This results in the partial or complete splitting of the nuclear energy levels. As more than one nuclear transition may occur, a multi-line Mössbauer spectrum results. For nuclear transitions the selection rule is $\Delta M = 0, \pm 1$. Both $^{57}Fe$ and $^{119}Sn$ excited and ground states have spins of $\frac{3}{2}$ and $\frac{1}{2}$ respectively,

which for these isotopes means that the presence of an electric field gradient gives rise to a two line spectrum, Figure 2.12. The distance between the peaks is the quadrupole splitting, Δ.

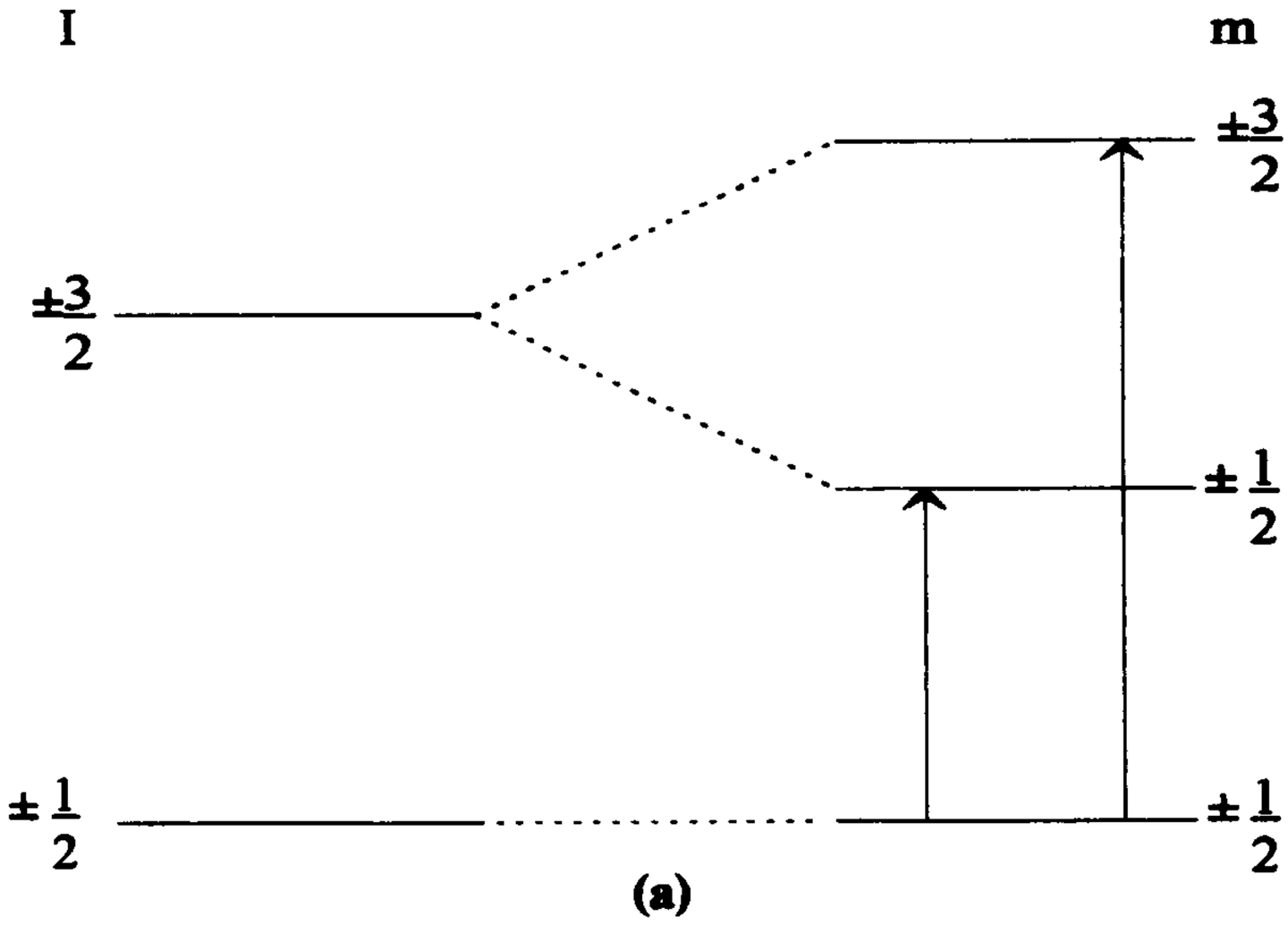


***Figure 2.12 - (a) Splitting of nuclear energy levels for both $^{57}Fe$ and $^{119}Sn$ nuclei by the presence of an electric field gradient and, (b) the resulting Mössbauer spectrum***

The quadrupole splitting is calculated as $\Delta = eQV_{zz}/2$ which is half the quadrupole coupling constant for the I = 3/2 state, where $V_{zz} = \frac{1}{4\pi\varepsilon_o}\sum q_i r_i^{-3}\left(3\cos^2\theta_i - 1\right)$.[8] In a system with a charge distribution about the nucleus of cubic symmetry the $3\cos^2\theta - 1$ term becomes zero resulting in a zero quadrupole splitting.

Several different components contribute to the electric field gradient. One contribution is from the electronic environment about the nucleus, and is called the valence term.

This can be envisaged as arising from the valence electrons of the Mössbauer atom and originates from asymmetry in the electronic structure which may derive from the unfilled or partially filled electron shells occupied by the valence electrons. The main contribution to the valence term is the asymmetric p- and d- electron populations, as the s electron density is principally symmetric about the nuclear volume. A lattice contribution, arising from the surrounding charged entities also contributes to the electric field gradient. This arises from the asymmetry in the arrangement of atoms around the Mössbauer nuclei. Further contributions to the electric field gradient include the effects of molecular orbitals and any polarisation of the core electrons of the Mössbauer atom.

Hence the quadrupole splitting reflects the symmetry of the bonding environment and local structure in the vicinity of the Mössbauer atom. In high spin iron(III) compounds the iron nucleus is in a nearly symmetric $d^5$ configuration, and consequently such compounds have small quadrupole splittings. In contrast, high spin iron(II) compounds frequently show large quadrupole splittings because of the asymmetric $d^6$ electronic environment. Tin(II) compounds typically have a splitting of 0.5 to 2.0 $mms^{-1}$ due to the stereo chemically active lone pair, whereas inorganic tin(IV) compounds show quadrupole splittings of up to about 1 $mms^{-1}$

When used in conjunction with chemical isomer shift data, the quadrupole splitting can be used to elucidate the oxidation states, electronic configurations and ligand arrays.

### 2.2.4 Magnetic Splitting

A nucleus of spin $I > 0$ has a magnetic moment which may interact with a magnetic field via a magnetic dipole interaction. This magnetic interaction induces the splitting of the nuclear energy levels. The degeneracy of the nuclear states is removed by the interaction of the nucleus with the magnetic field, and the levels then split into $2I + 1$ substates. In $^{57}Fe$ the ground state with $I = \frac{1}{2}$ splits into two substates, and the excited state with $I =$

$\frac{3}{2}$ splits into four substates. For these spin states the selection rules $\Delta M = 0, \pm 1$ give rise to a symmetric six line Mössbauer spectrum. In this spectrum the isomer shift is given as the centre of gravity of the six peaks. The magnetic splitting of the ground and excited states for $^{57}Fe$ is illustrated in Figure 2.13a, and the resultant spectrum in Figure 2.13b.

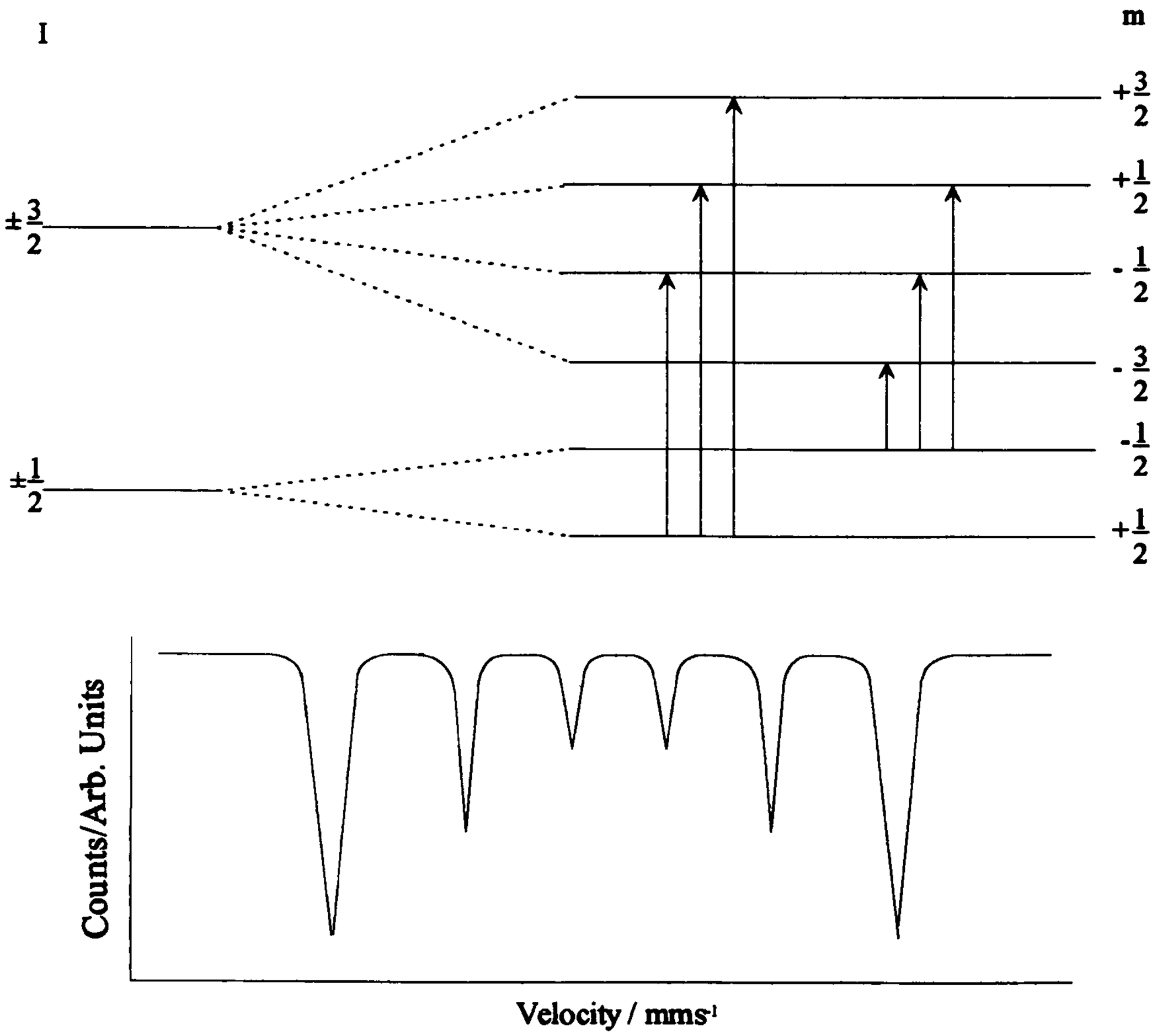


***Figure 2.13 - (a) Splitting of nuclear energy levels of a $^{57}Fe$ nucleus by the presence of a magnetic field, and (b) the resultant Mössbauer spectrum***

The total magnetic field experienced by the nucleus is a vector sum of the magnetic hyperfine field and any external applied field. The magnetic hyperfine field arises from the spin of any unpaired electrons and is dependent on the oxidation state and spin state of that atom. Hence, interpretation of the magnetically split Mössbauer spectrum can give information on the magnetic properties arising from the electronic structure. It is also possible to modify the hyperfine field by application of an external factor, which

distinguishes the hyperfine field from the other Mössbauer hyperfine interactions. Altering the applied field can change the appearance of the spectrum and aid interpretation.

A magnetic field applied to a sample has different effects depending on whether the field is applied parallel or perpendicular to the gamma ray direction. When the field is applied parallel to the gamma ray direction the spins are aligned along that direction and causes the 2nd and 5th lines of the magnetically split spectrum to disappear. The disappearance of these lines occurs because the angle between the spins and the gamma ray direction is zero. This results in the ratio of the peak intensities becoming 3:0:1:1:0:3. When a field is applied perpendicular to the gamma ray direction the angle between the gamma ray direction and the spins is $90^{o}$. This causes the peak intensity ratio to become 3:4:1:1:4:3.

Application of an external magnetic field can also cause the quadrupole splitting in a magnetically split spectrum to disappear. If a field is applied along a particular axis in a single crystal sample then the spins will be directed along that axis. If that material has a quadrupole splitting then the angle between $V_{zz}$ and the direction of the magnetisation deviates from $\cos^{-1}\left(1/\sqrt{3}\right)$ which results in $3\cos^{2}\theta-1$ becoming non-zero. When a field is applied the spins are directed along the axis of choice making the angle $\theta = \cos^{-1}\left(1/\sqrt{3}\right)$ to $V_{zz}$. This in turn results in $3\cos^{2}\theta-1$ becoming zero and hence the quadrupole interaction becomes zero.

The occurrence of magnetically split $^{57}Fe$ Mössbauer spectra is common among ferro- and antiferro- magnetic materials. Paramagnetic materials cooled to below their Curie temperatures also exhibit a magnetically split Mössbauer spectrum. A less common occurrence is the magnetically split $^{119}Sn$ Mössbauer spectrum, which arises through a superexchange interaction with magnetic ions.

### 2.2.5 Instrumentation

A typical Mössbauer spectrometer is shown schematically in Figure 2.14. The spectrometer consists of a constant velocity drive connected to a γ-ray source, detector and a microprocessor. For recording spectra at temperatures down to liquid helium temperatures, a cryostat may be used which can improve the recoil free fraction and consequently the resolution of the spectrum.

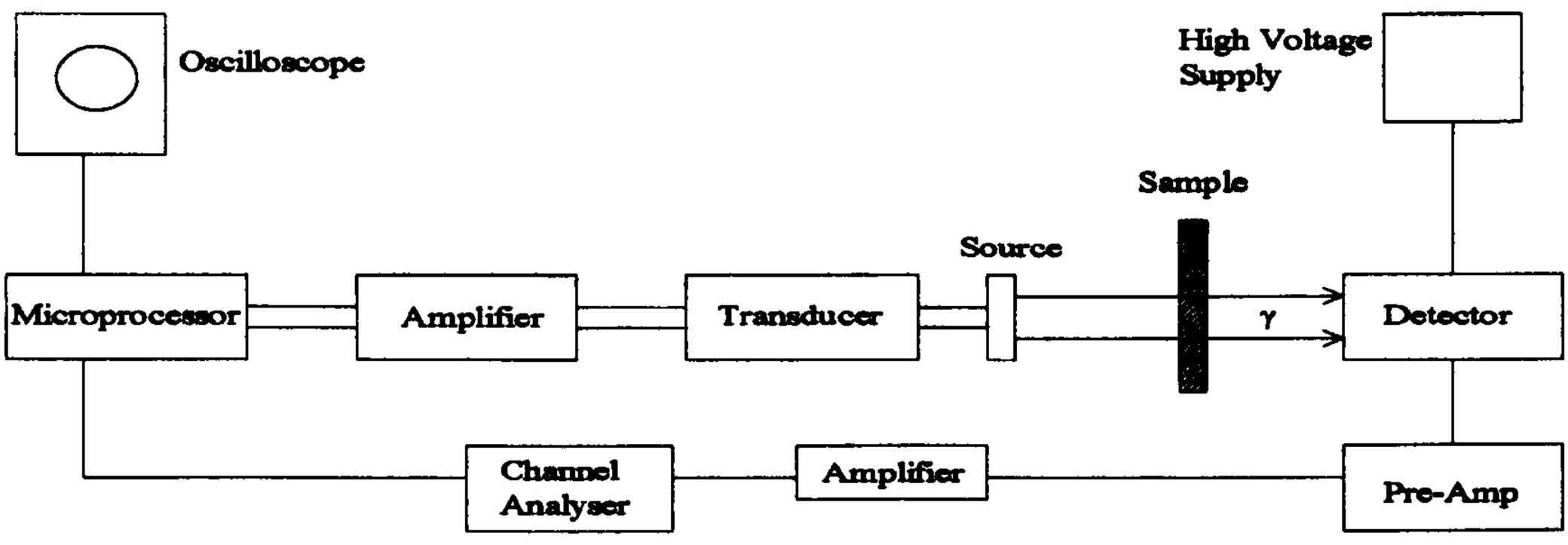


***Figure 2.14 - Schematic diagram of a Mössbauer Spectrometer***

The detector for isotopes such as $^{57}Fe$ and $^{119}Sn$ is commonly an $Ar/CO_2$ filled proportional counter which is placed in line with the source and sample. The γ-radiation ionises the Ar gas in the detector producing electrons which are accelerated towards an anode in the centre of the detector. This produces an electric current proportional to the γ-ray energy. The presence of the $CO_2$ acts as a quenching gas to prevent continuous electrical discharge. The resultant signal is then amplified and passed to a multichannel analyser.

### 2.2.6 High Temperature Mössbauer Spectroscopy

The measurement of Mössbauer spectra at elevated temperatures up to 900K can be performed in a furnace which has been specially designed for such purposes.[8,9] The central part of the furnace consists of a highly polished aluminium elliptical cylinder. The heat source is a 250 W halogen lamp placed at one focal point of the ellipse with a

cylindrical black painted copper tube, the heat absorber, at the other focal point. The main features are illustrated in Figure 2.15. The sample is placed between two beryllium oxide disks and held in the copper tube. Aluminised mylar windows allow gamma rays to enter and leave the chamber. The temperature of the tube is monitored by a thermocouple with electronic zero-point reference. The signal from the thermocouple controls the temperature by modulating the power of the lamp and maintains the sample at a temperature within $\pm 0.3$K over 24 hours.

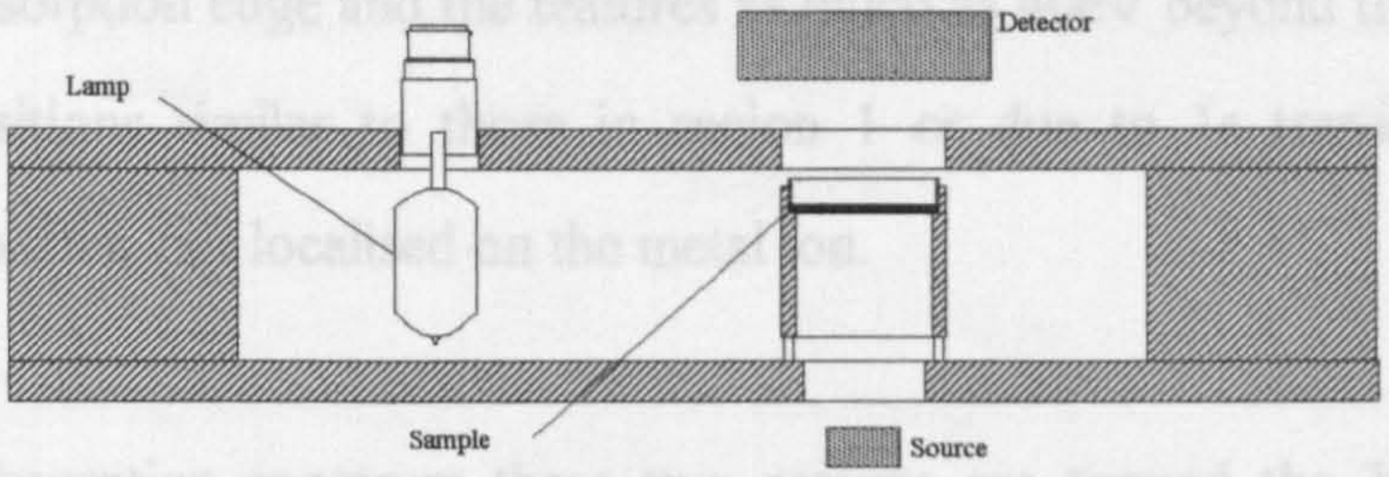


***Figure 2.15 - Schematic representation of the furnace used for high temperature Mössbauer spectroscopy***

## 2.3 Extended X-Ray Absorption Fine Structure (EXAFS)

The use of X-ray absorption spectroscopy for structural determination has been known of for about sixty years but only in the last 20 years, with the development of synchrotron radiation sources, has EXAFS been developed as a powerful tool for the chemist. The technique allows structural information to be derived from solids, whether crystalline or amorphous, liquids, gases and fluid-solid interfaces. Detailed descriptions of the theory, instrumentation and applications of EXAFS have been published.[10-16]

### 2.3.1 Theory

In X-ray absorption spectroscopy the excitation of core electrons of the atom under investigation gives rise to an X-ray absorption spectrum which exhibits sharp edges. The

X-ray absorption spectrum obtained from transition metals can be separated into 3 distinct regions.

1) Pre-edge absorption features which occur a few eV below the steep absorption edge. These appear to be associated with electronic transitions from the 1s core orbital to the molecular orbitals, Figure 2.16.

2) The steep absorption edge and the features as much as 40eV beyond the edge may be due to 1s transitions similar to those in region 1 or due to 1s transitions to more continuum like states, not localised on the metal ion.

In the X-ray absorption spectrum these two regions are termed the XANES (X-ray Absorption Near Edge Structure) region. XANES may be used to probe a specific ion environment. Oxidation states and co-ordination environment of the element are known to cause shifts in the position of the edge. Unfortunately XANES suffers from a current weakness in theory to explain spectral features.

3) The absorption cross section of the region from 40eV to 1000eV or more, is known as the post edge region, which is observed to oscillate. These oscillations are termed the Extended X-ray Absorption Fine Structure, or EXAFS. This is also known as the Kronig structure, Figure 2.16.

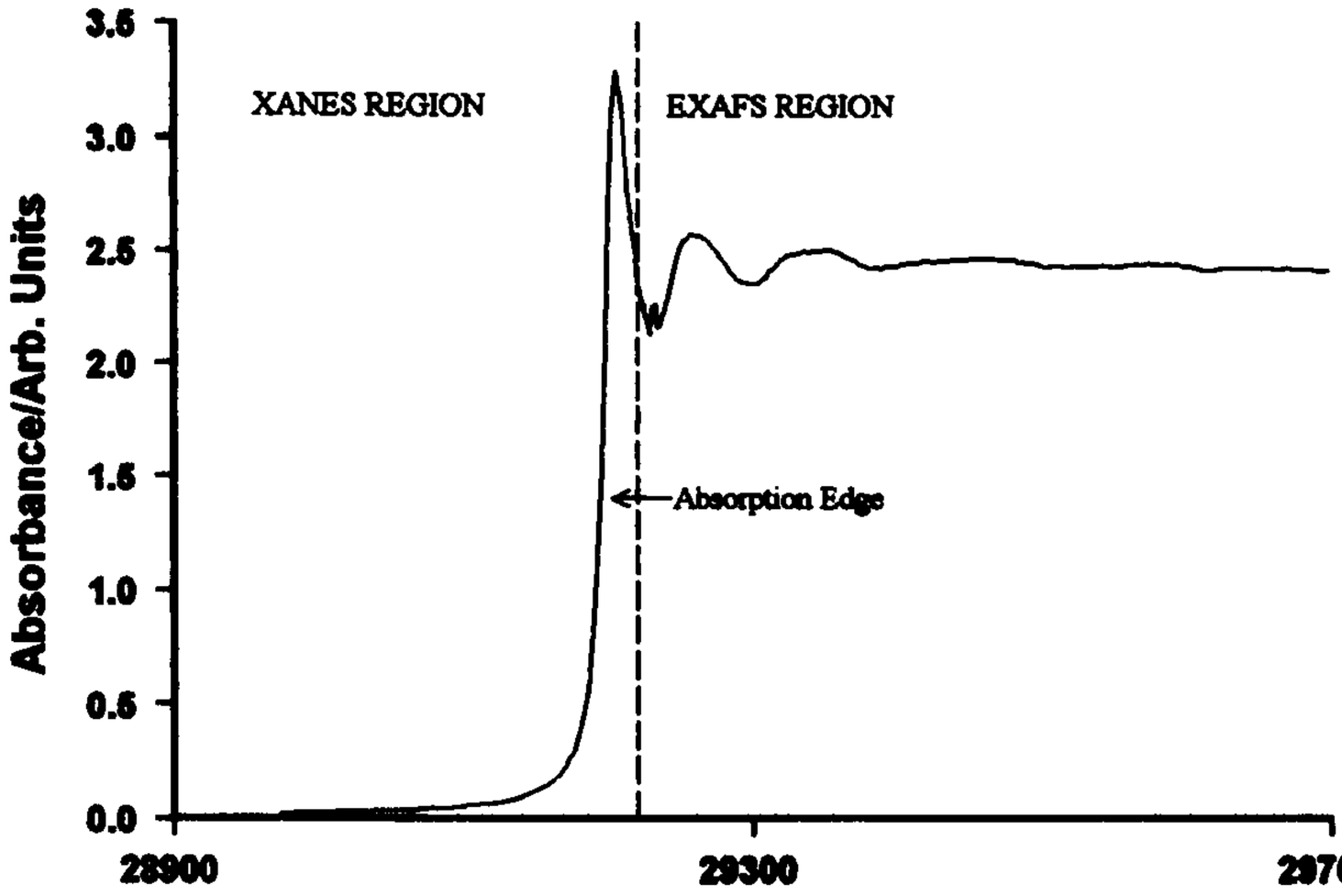


***Figure 2.16 -Plot showing the regions containing the XANES and EXAFS information and the position of the absorption edge***

## 2.3.2 EXAFS

EXAFS, normally expressed in terms of absorption coefficient, μ, can be determined from a measurement of the attenuation of X-rays during their passage through a material, by measurement of the incident and the transmitted X-ray intensities. The absorbance is given by Beer's Law;

$$\mu x = \ln \frac{I_o}{I}$$

where x is the thickness of the material and $I_0$ and I are the incident and the emergent X-ray intensities respectively. When the energy of the X-ray photon, E, of the monochromatic beam is tuned to the binding energy of a core electronic level of an atom in the material, an increase in the absorption coefficient is observed, known as the absorption edge. At the edge the energy is sufficient to cause an electron to be ejected from the sample atom. This electron will be from either the K or L shells and the X-ray energies will be 1-40keV. If there is any further increase in the X-ray energy, this will be translated into the kinetic energy of the ejected photoelectron. Beyond the absorption

edge for isolated atoms such as those in a monoatomic gas the energy of the edge resumes a steady decrease, Figure 2.17.

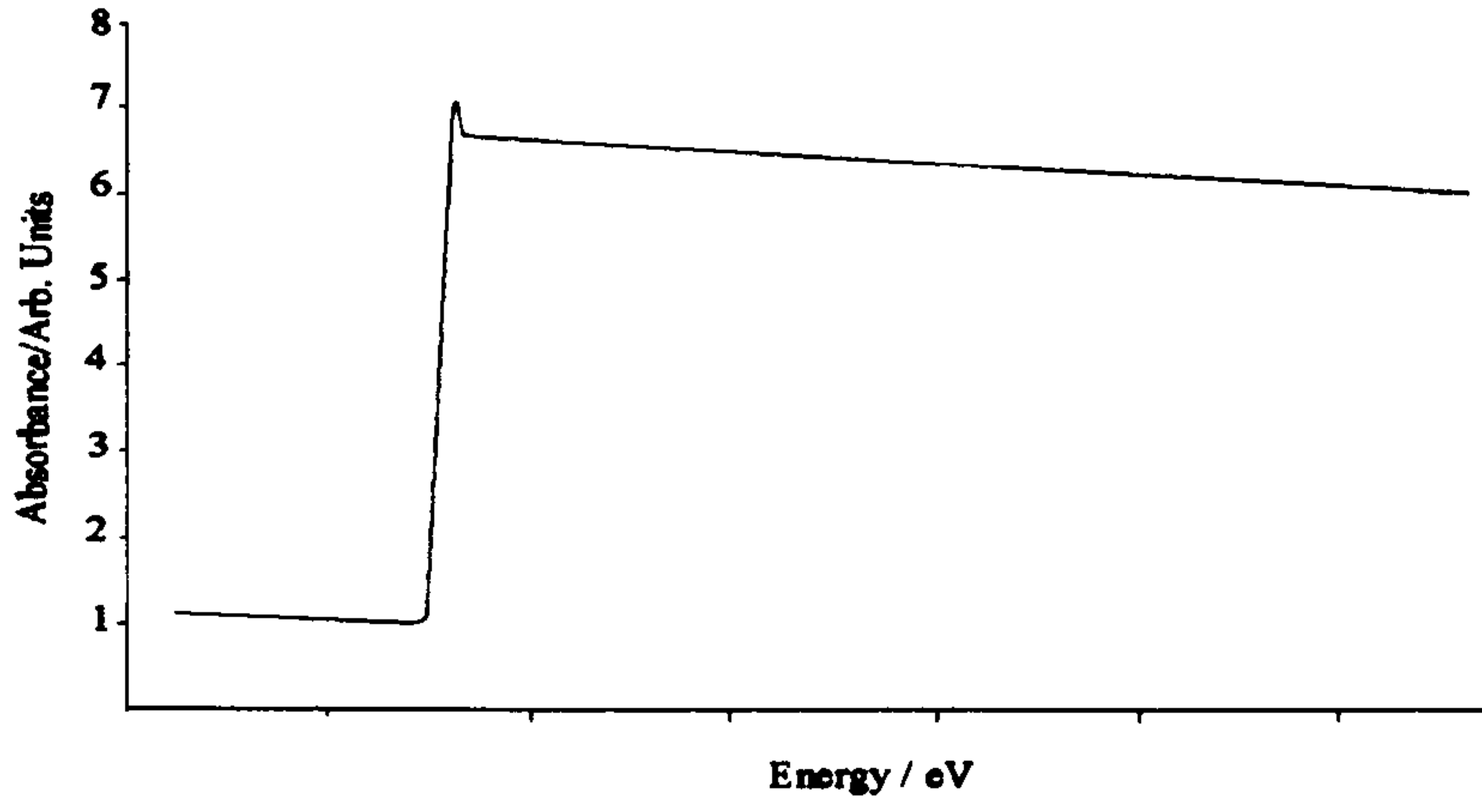


***Figure 2.17 - Schematic representation of the X-ray absorption spectrum for a monoatomic gas***

The EXAFS can be explained by considering the outgoing photoelectron as a spherical wave originating from the absorbing atom. When an excited atom is surrounded by other atoms the outgoing spherical wave is reflected back towards the origin by the surrounding scatterers. The wavelength of the photoelectron and the atomic number of the scatterers determines the phase of the reflected wave. This reflected wave undergoes self-interference with the outgoing wave, Figure 2.18, and depending on the wavelength of the photoelectron, outgoing and back-scattered waves may interfere constructively or destructively. A sinusoidal variation of the absorption coefficient, $\mu$, as a function of photon energy results from the interference. Quantum mechanically the photoelectron interference effect in the final state modifies the absorption cross-section and results in modulations of the transmitted X-ray intensity beyond the absorbing edge.

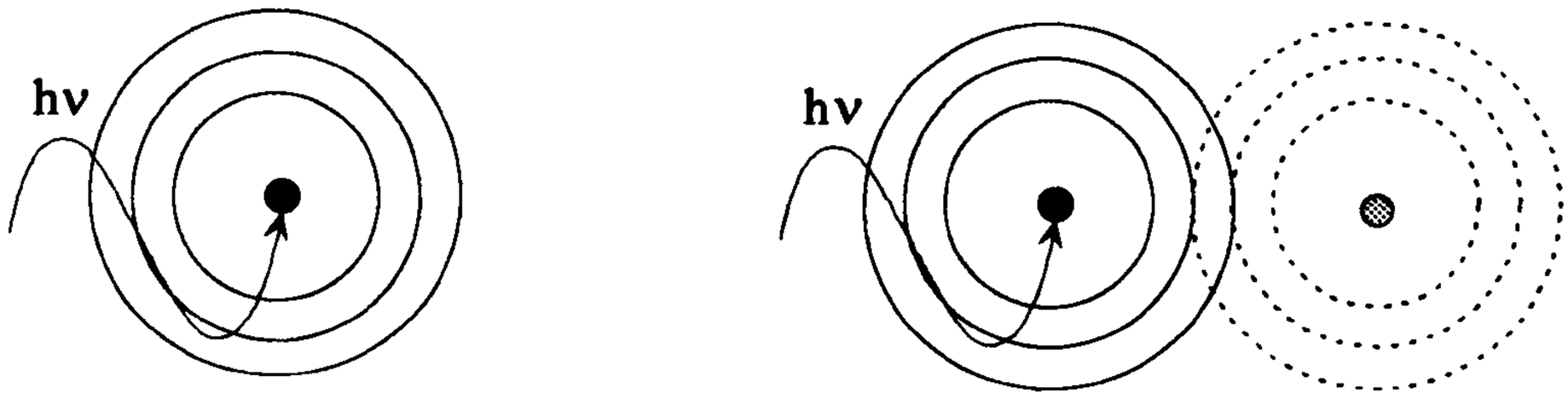


An outgoing photoelectron wave caused by the absorption of an X-ray photon.

Outgoing photoelectron waves (solid line) and backscattered waves (dashed line) from neighbouring atoms, interacting a) constructively, and b) destructively.

***Figure 2.18 - Diagram illustrating constructive and destructive interference of an outgoing wave***

The frequency of the EXAFS oscillations depends on the distance between the absorbing atom and the scattering atoms, since the wave travels from the absorber to the scatterer and returns. During this period the photoelectron undergoes a phase shift. If the phase shift can be determined either from model compounds such as standards of known structure with atoms in similar electronic and structural environments or by calculation, then interatomic distances can be calculated for the immediate vicinity of the absorber atom from the frequency of the oscillation. The amplitude of each modulation depends on several factors; the atomic number, back scattering power of the neighbouring atoms, as well as their number and bonding distance from the absorber. Bond distance and co-ordination number can be determined from this amplitude.

Having recorded a set of EXAFS data, several mathematical procedures may be followed in order to extract the structural information, such as inter-atomic distance, co-ordination number and the Debye-Waller factor. These procedures are determined by the mathematical theory of EXAFS as detailed in the literature.[12,14]

Initially the data should be normalised so that the EXAFS modulation $\chi(E)$ can be observed. It is therefore necessary to subtract the background spectrum leaving the EXAFS oscillations. This consists of several stages.

1) Firstly, the position of the absorption edge $E_0$ is found which is then used as a standard against which the EXAFS oscillations can be based. This value is not fixed but allowed to iterate to provide more accurate inter-atomic distance determination.

2) The pre-edge absorption is fitted to a linear polynomial function and extrapolated across the EXAFS region.

3) The post-edge absorption is fitted to a set of polynomials which model $\mu_o$, the atomic absorption factor. This passes smoothly through the EXAFS oscillations, which effectively models the post-edge as it would appear without the EXAFS oscillations. This procedure then produces isolated EXAFS oscillations.

Having carried out the pre- and post- edge subtractions, the x-axis is converted from energy space, E, into photoelectron wave vector space, k. Finally a Fourier transformation using a $k^3$ weighting factor is carried out. This results in a radial distribution function being produced, with peaks appearing at certain distances away from the core atom, Figure 2.19. Further manipulation is carried out using window functions. At this stage the structural information is obtained by producing a theoretical model which is iterated to match the experimental data using a series of curve fitting routines.

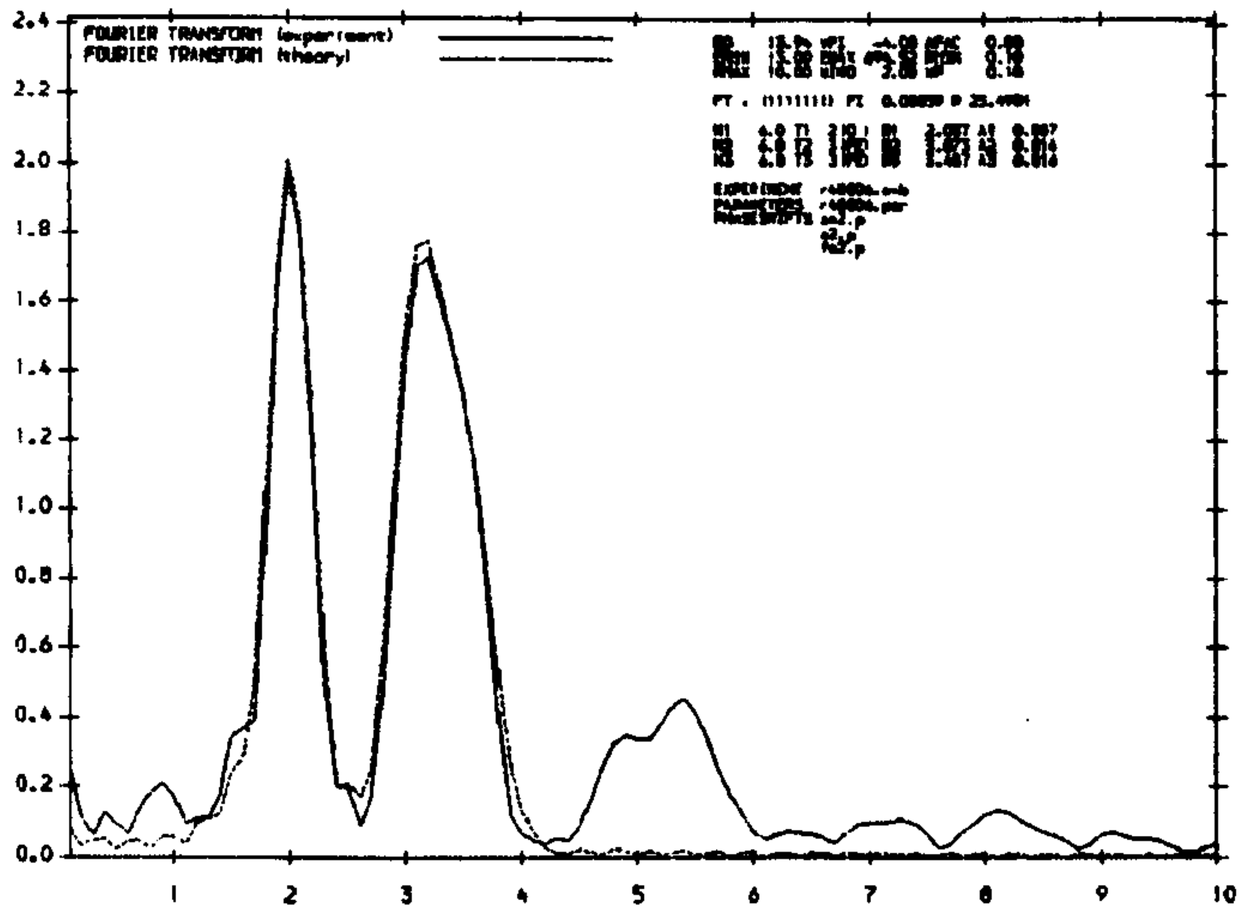


***Figure 2.19 - Fourier transformed EXAFS data showing experimental data (solid line) and modelled data (dashed line)***

### 2.3.3 Instrumentation

Many methods for measuring EXAFS have been developed. These differ mainly in the detection technique employed, sample geometry and choice of X-ray detectors. The transmission mode directly measures the incident and transmitted X-rays and gives a direct measurement of the absorption coefficient. As the absorption of X-rays is limited to the creation of an electron vacancy it is possible to determine the absorption coefficient. The vacancy can be filled by an outer shell electron which is accompanied by emission of fluorescence radiation or Auger electrons, both of which can yield EXAFS information. In the fluorescence mode, the fluorescence yield increases with increasing atomic number. The advantage of this method is that background radiation can be measured with suitable filters, increasing the sensitivity of the method. If the fluorescence method fails, then the Auger method may be useful, which is particularly good in the analysis of surfaces (SEXAFS). In EXAFS the most commonly used source is the synchrotron. Synchrotron radiation has many advantages. The energy spectrum of X-rays generated by synchrotron radiation is smooth and continuous and extends from the end of the infra-red to the hard X-ray region. This allows all of the desired X-ray

energies to be investigated. Also the beam is intense, and the flux can be as high as $10^{12}$ photons per second, allowing the EXAFS spectrum to be collected in a short time.

Synchrotrons are particle accelerators. Charged particles, usually electrons, are accelerated to high velocities, then stored in a storage ring. Whilst in this ring they are subjected to a magnetic field which maintains the electrons in an orbit, but places accelerating forces upon them. As a result of this the electrons emit intense white electromagnetic radiation covering all frequencies.

A monochromator allows the X-ray beam to be separated into its component frequencies. The monochromator consists of two single crystals of silicon aligned along defined planes. These crystals can be rotated so that the path length between them changes and allows differing energies of X-rays to be scanned. The single crystals are slightly offset to allow rejection of the harmonics which are detrimental to the data quality. The monochromator is enclosed in a helium filled chamber with beryllium windows. A typical transmission EXAFS configuration is shown in Figure 2.20.

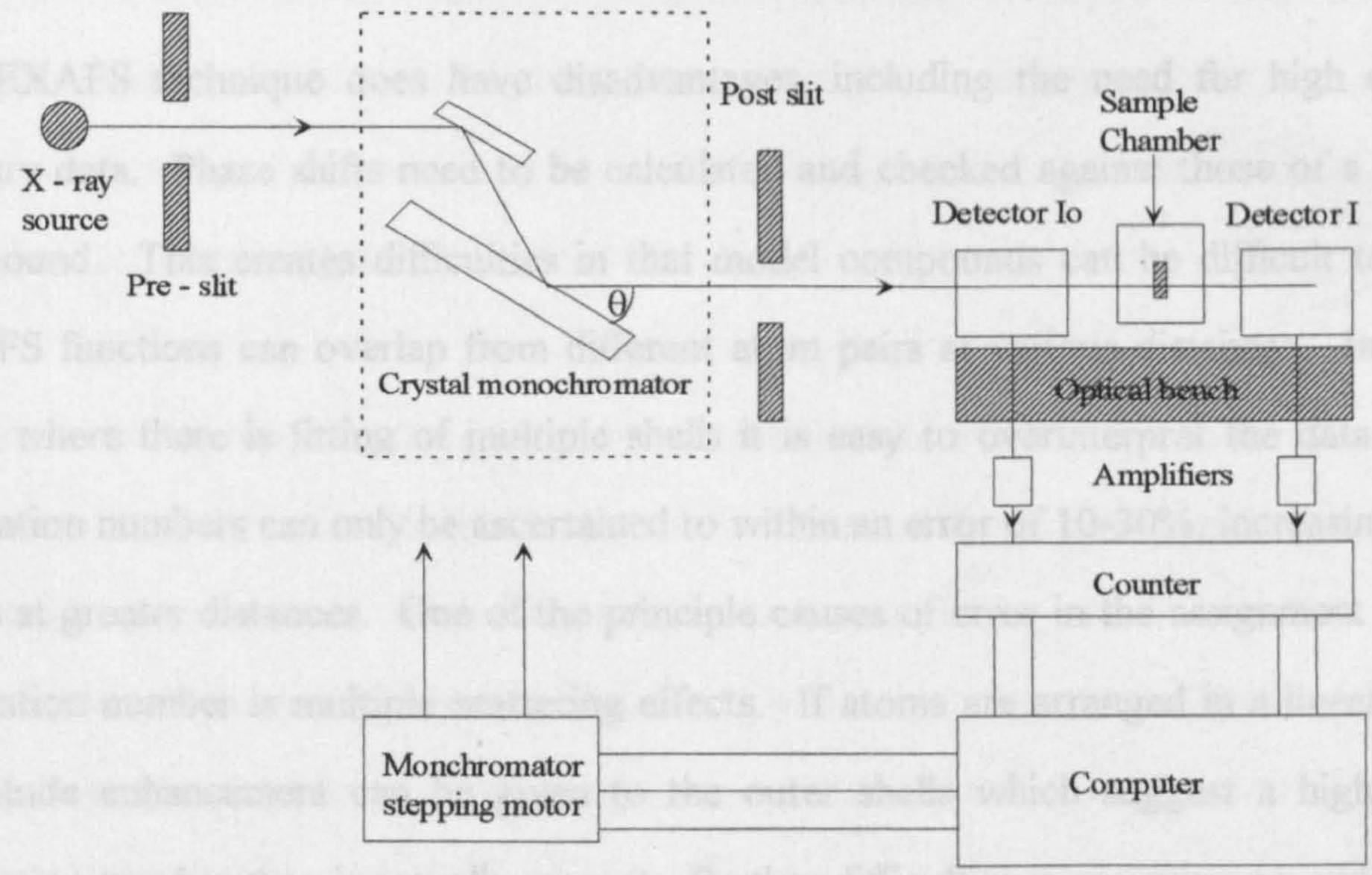


***Figure 2.20 - Typical experimental configuration of a transmission EXAFS experiment***

Samples can be located in ovens, pressure chambers and vacuum chambers during measurement. One of the requirements for the sample is that it is uniformly thin and homogeneous. Ion chambers are used as detectors in the transmission mode as only a small fraction of the incident intensity is depleted by them. The ion chambers work on the principle of measuring the photoion current. Ion chambers have a gas mixture in them which can be readily adjusted to achieve the optimum detector absorption for the atom under investigation. The measured photo-currents are converted into voltages which are recorded by a computer which also controls the stepping motor movement for the monochromator. EXAFS are typically recorded up to between 800 and 1000eV above the absorption edge.

EXAFS has many advantages over conventional X-ray diffraction techniques. The local structure of each individual atomic species can be determined, and provides short range order information about the absorbing species up to a distance of 6Å with accuracy of *ca* 0.01-0.03Å although the accuracy with outer shells is diminished. It is also particularly useful in situations where conventional diffraction methods cannot be used.

The EXAFS technique does have disadvantages, including the need for high quality primary data. Phase shifts need to be calculated and checked against those of a model compound. This creates difficulties in that model compounds can be difficult to find. EXAFS functions can overlap from different atom pairs at various distances. In these cases where there is fitting of multiple shells it is easy to overinterpret the data. Co-ordination numbers can only be ascertained to within an error of 10-30%, increasing with shells at greater distances. One of the principle causes of error in the assignment of co-ordination number is multiple scattering effects. If atoms are arranged in a linear array amplitude enhancement can be given to the outer shells which suggest a higher co-ordination number than is actually present. Further difficulties in assigning co-ordination number come from differentiating between a reduction in co-ordination number and an increase in thermal disorder, the Debye-Waller factor. For these reasons EXAFS should

be used to complement other structural data and not used as the sole structural determination technique.

## 2.4 Scanning Electron Microscopy

### 2.4.1 Theory

The principle of SEM involves the irradiation of a sample by a finely focused electron beam, which may be either static or swept across the sample in a raster scan. When electrons with energies of 1-50keV impinge on the surface of a solid sample they exhibit very complex behaviour. Two primary effects are observed, elastic and inelastic scattering.

In inelastic collisions between loosely bound electrons and the incoming beam, energy is lost from the beam, and loosely bound electrons are ejected. These ejected electrons typically have energies less than 50eV and are known as secondary electrons. Inelastic collisions can also result in a variety of ionisation processes which are responsible for the production of the majority of signals from a sample, including secondary electrons, Auger electrons and characteristic X-rays. The primary electron beam loses energy equivalent to the binding energies of the K, L and M shells.

Elastic scattering may be thought of as a process occurring in two parts i) a single scattering act resulting in a large change of direction and ii) multiple scattering which is composed of many small angle scattering events, which may result in a large angle change for the impinging electron beam. Elastic scattering is responsible for the production of backscattered electrons which leave with reduced energy.

Therefore the difference between the two types of scattering is that inelastically scattered electrons undergo an energy loss with a negligible change in direction whereas elastically

scattered electrons undergo a change of direction with a negligible energy loss. In SEM it is the secondary and backscattered electrons which are of most interest, as these vary with differences in surface topography, allowing study of the surface characteristics of the sample.

The detail obtained by SEM imaging is dependent on which signal is used in the imaging process. The various signals have quite different ranges and spatial resolution. Therefore examination of a surface by SEM is very versatile. The theory of SEM imaging involves much more detail of electron optics and beam-specimen interactions than detailed here and has been extensively discussed in the literature.[17-19]

### 2.4.2 SEM Instrumentation

In principle a scanning electron microscope is very similar to an optical microscope. The electron optical column consists of an electron gun with two or more electron lenses, Figure 2.21. The lenses in the microscope use magnetic fields to focus the electron beam, which is kept under a vacuum of *ca* $1.33 \times 10^{-2}$ Pa. This is necessary to prevent the interaction of the beam with the atmosphere. Typically the electron gun used is a tungsten filament cathode, which consists of a 0.01cm diameter wire bent in the shape of a hairpin with a V shaped tip 100μm in radius. The cathode is then heated directly as the filament current is passed through it, reaching a temperature of 2700K, allowing the electrons to become sufficiently energetic to escape, forming the beam. This process is known as thermionic emission.

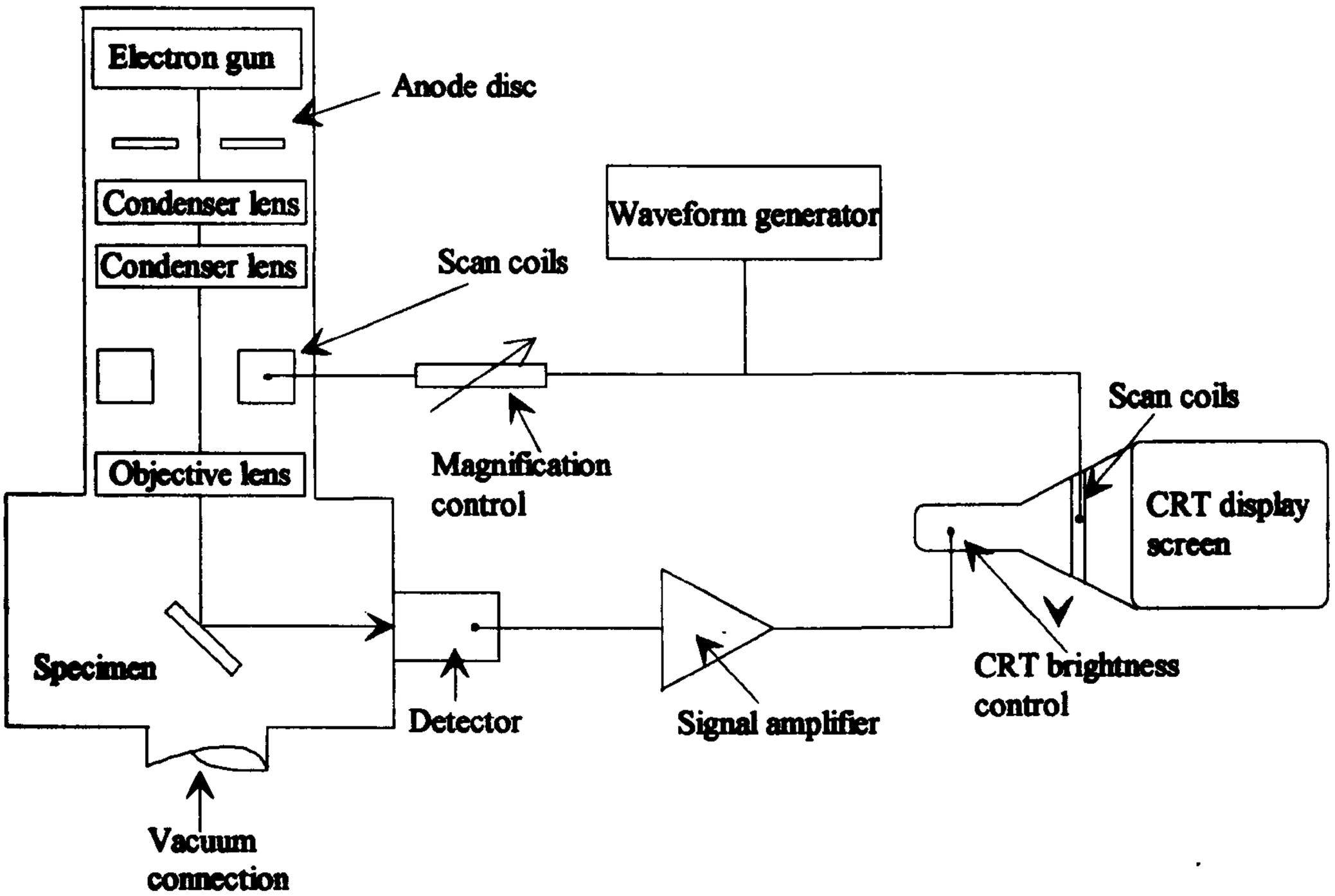


***Figure 2.21 - Schematic diagram of a Scanning Electron Microscope***

Different detectors are then connected to the column and the facility for obtaining photographic images is also attached. The sample sits in a holder which can be tilted in the beam to allow viewing of the surface topography.

### 2.4.3 Energy Dispersive X-Ray Microanalysis (EDX)

As stated in Section 2.4.1 one of the effects of an electron beam interacting with a specimen is the production of characteristic X-rays. This X-ray beam may then be used to provide information on the chemical composition of the samples. As the electron beam strikes the specimen an electron from an inner shell of an atom may be ejected, leaving the atom in an excited state. As a vacancy has been left, for example, in the K shell, at a higher energy than the outer shells, an electron from one of these outer shells falls into the vacancy. This returns the atom to its ground state. It is this relaxation stage which causes an amount of energy to be released as a photon, and if the ejected electron is from the inner shells then the photon will be an X-ray.

To detect the characteristic X-rays a silicon-lithium detector is used. The X-ray signal passes through a thin beryllium window into the cooled detector. Each individual X-ray produces a charge pulse which is converted into a voltage pulse by a preamplifier. The signal is then further processed and passed to a multichannel analyser where the signal is sorted by voltage. Once sorted the signal can be displayed as an X-ray intensity versus energy plot using a computer or quantitative analysis can be carried out. Quantitative analysis has to take into account many factors including atomic number, absorption within the sample and detector and X-ray induced fluorescence within the sample. A typical EDX system is depicted in Figure 2.22.

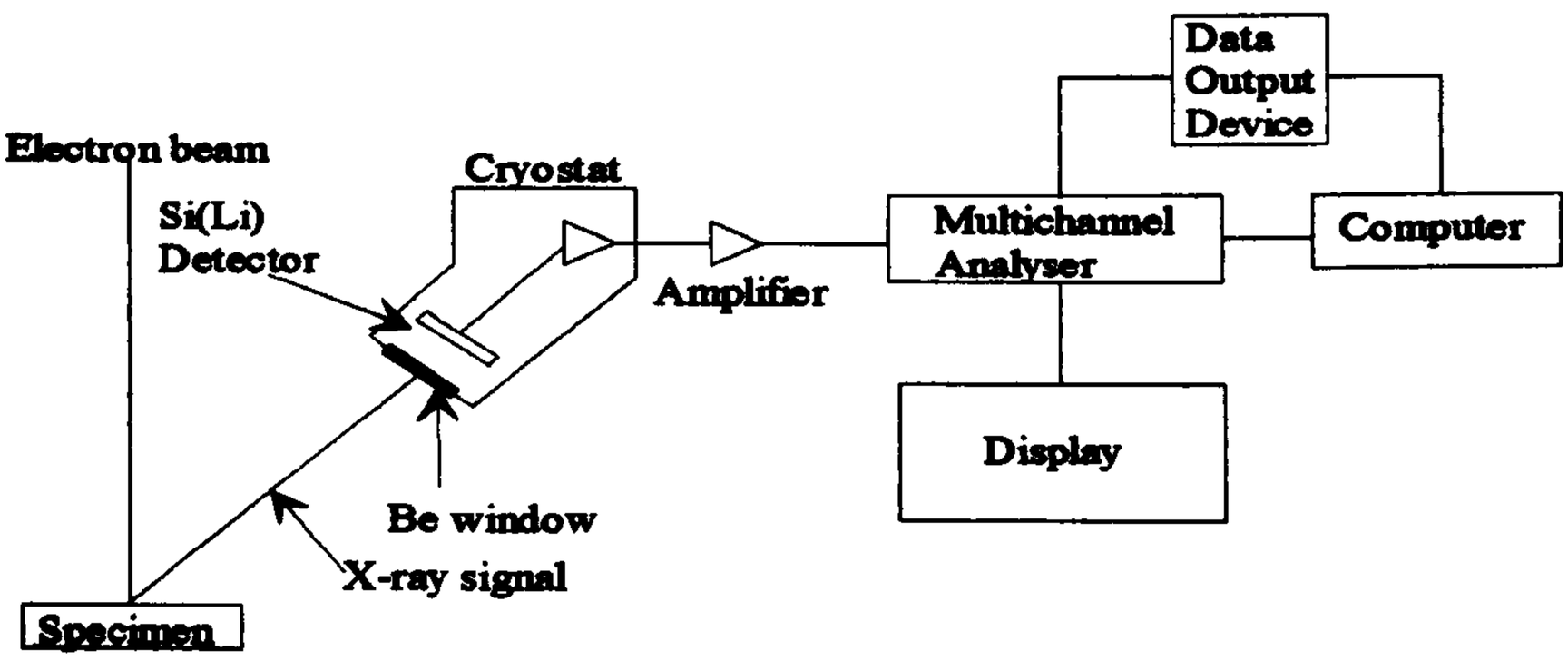


***Figure 2.22 - Schematic representation of an EDX system***

# References


1 H.P.Klug and L.E.Alexander, "X-ray Diffraction Procedures", 2nd Edition, John Wiley & Sons, New York, 1974

2 J.Wormald, "Diffraction Methods", Clarendon Press, Oxford, 1973

3 L.V.Azároff and M.J.Buerger, "The Powder Method in X-ray Crystallography", McGraw-Hill, New York, 1958

4 P.Scherrer, Göttinger Nachtricthen, 1918 2 98

5 N.N.Greenwood and T.C.Gibb, "Mössbauer Spectroscopy", Chapman and Hall, London, 1971.

6 "Mössbauer Spectroscopy", Editors D.P.E.Dickson and F.J.Berry, Cambridge University Press, Great Britain, 1986

7 R.V.Parish, "NMR, NQR, EPR and Mössbauer Spectroscopy In Inorganic Chemistry", Ellis Howard, London, 1990, p.128

8 Ö.Helgason, H.P.Gunnlaugsson, S.Steinflórsson and S.Mørup, Hyp. Int., 1992 70 981

9 F.J.Berry, Ö.Helgason, K.Jónsson and S.J.Skinner, J.Solid State Chem., 1996 122 353

10 G.A.Waychunas, G.E.Brown and M.J.Apted, Phys.Chem.Minerals 1986 13 31

11 J.C.J.Bart and G.Vlaic, Adv.Catalysis Vol 35, Academic Press 1987 1

12 D.G.Stearns and M.B.Stearns "Extended X-ray Absorption Fine Structure" in Microscopic Methods in Metals, U.Gonser, Topics in Current Physics, Vol 40, Springer-Verlag, Berlin-Heidelberg, 1986 p.153

13 G.A.Waychunas, M.J.Apted and G.E.Brown, Phys.Chem.Minerals 1983 10 1

14 P.A.Lee, P.H.Citrin, P.Eisenberger and B.M.Kincaid, Reviews of Modern Physics 1981 53 769

15 B.K.Teo and D.C.Joy in "EXAFS Spectroscopy:Techniques and Applications" Proceedings of 1979 meeting of the Materials Research Society, November 26-30, 1979, Boston, Massachusetts, B.K.Teo and D.C.Joy, Plenum Press, New York, 1981

16 B.K.Teo "EXAFS : Basic Principles and Data Analysis", Springer-Verlag, Berlin-Heidelberg,

17 J.I.Goldstein, D.E.Newbury, P.Echlin, D.C.Joy, C.Finini and E.Lifshin "Scanning Electron Microscopy and X-ray Microanalysis", Plenum Press, New York, 1981

18 J.I.Goldstein, H.Yakowitz, D.E.Newbury, E.Lifshin, J.W.Colby and J.R.Coleman in "Practical Scanning Electron Microscopy", Editors J.I.Goldstein and H.Yakowitz, Plenum Press, New York, 1975

19 G.Lawes "Scanning Electron Microscopy and X-ray Microanalysis", J.Wiley & Sons, Chichester, 1987

# CHAPTER THREE

# Experimental

## 3.1 Preparation of metal-doped $Fe_3O_4$

### 3.1.1 Preparation of $Fe_{3-x}Sn_xO_4$

Materials of composition $Fe_{3-x}Sn_xO_4$, where $0.05 \leq x \leq 0.5$, were prepared by mixing stoichiometric amounts of $\alpha$-$Fe_2O_3$, Fe powder and $SnO_2$ intimately in an agate mortar and pestle. The mixture was then transferred to a quartz ampoule which was evacuated, sealed and heated at 900°C for 24 hours. It was necessary to heat the oxide of composition $Fe_{2.7}Sn_{0.3}O_4$ for 48 hours to obtain a monophasic product.

### 3.1.2 Synthesis of $Fe_{3-x}M_xO_4$ where M = Cr, Ga, or Ti

Materials of composition $Fe_{3-x}M_xO_4$, where $0.1 \leq x \leq 0.2$ and M = Cr, Ga, or Ti, were prepared by mixing stoichiometric amounts of $\alpha$-$Fe_2O_3$, Fe powder and $Cr_2O_3$, $Ga_2O_3$ or $TiO_2$ intimately in a mortar and pestle. The samples were then placed in quartz ampoules, evacuated, sealed and heated at 900°C for 24 hours.

### 3.1.3 Mössbauer spectroscopy of a $Fe_3O_4$ single crystal

A single crystal of $Fe_3O_4$, supplied by The British Museum, was cut perpendicular to the [1 1 1] axis, previously identified by Laue diffraction, with a diamond tipped saw. The sections were approximately 1mm thick by 1cm square. One section was mounted in low temperature Araldite glue using a mould illustrated in Figure 3.1. This was allowed to set for 24 hours. Once hardened the thickness of the sample was reduced by sanding until it was possible to detect a 14.4keV Mössbauer signal in transmission geometry. A seal of Araldite was placed over the exposed surface. A lead jacket was cut to the shape of the crystal and placed around it to prevent $\gamma$-radiation passing through the Araldite mount.

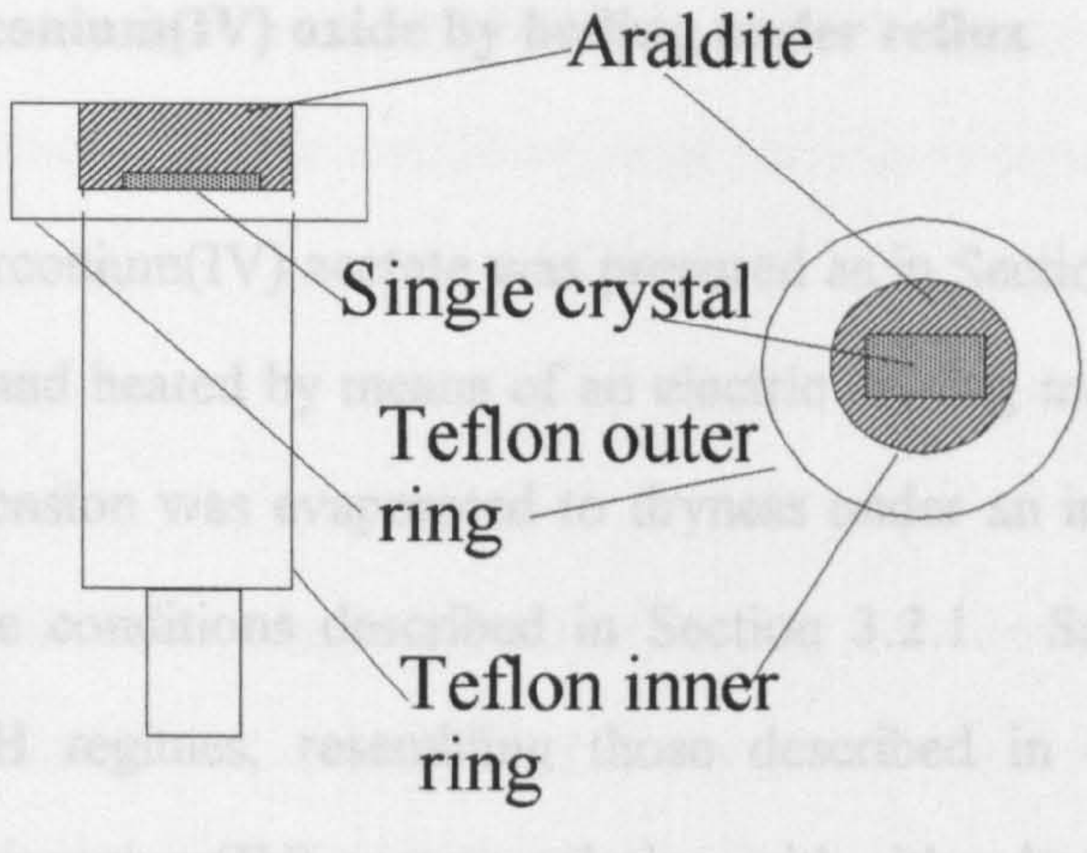


***Figure 3.1 - Illustration of mould used to mount single crystal sample for low temperature Mössbauer spectroscopy***

## 3.2 Preparation of zirconium(IV) oxide

### 3.2.1 Preparation of zirconium(IV) oxide by hydrothermal synthesis

Zirconium(IV) acetate powder (4g) was dissolved in deionised water (200ml) producing a 0.12 mol solution. Some solutions of zirconium acetate at pH 1 were prepared by addition of hydrochloric acid. To achieve high pH conditions a solution of aqueous ammonia was added until pH 10 was reached. Intermediate pHs' were achieved by adjusting the pH of the initial solution with either acetic acid or trimethylamine, $(CH_3)_3N$. The solutions were then transferred to a Berghof Teflon lined autoclave and heated to 220°C under the autogeneous pressure of the autoclave for 2½ hours. The cooled product was transferred to a glass beaker and heated to dryness under an infra red lamp. The products were subsequently calcined at 200°C, 500°C, 900°C and 1400°C for 3 hours and allowed to cool in the furnace to room temperature.

### 3.2.2 Preparation of zirconium(IV) oxide by boiling under reflux

A 0.12 mol solution of zirconium(IV) acetate was prepared as in Section 3.2.1, placed in a round bottomed flask, and heated by means of an electric heating mantle under reflux for 2½ hours. The suspension was evaporated to dryness under an infra red lamp and calcined according to the conditions described in Section 3.2.1. Samples were also produced in different pH regimes, resembling those described in Section 3.2.1 by adjusting the pH of the zirconium(IV) acetate solution with either hydrochloric acid or aqueous ammonia. These products were dried under an infrared lamp and then calcined as described in Section 3.2.1.

### 3.2.3 Preparation of iron-doped zirconium(IV) oxide

A solution of zirconium acetate was prepared by the method described in Section 3.2.1. To this solution iron(II) acetate was added to produce 5 or 10 wt% iron-doped zirconia. The effect of variation of pH on both the 5 and 10 wt% doped samples was studied by adding either hydrochloric acid or aqueous ammonia to the initial iron(II) acetate/zirconium(IV) acetate solution, adjusting the pH to 1 and 10 respectively. The iron(II) acetate/zirconium(IV) acetate solution was treated by both hydrothermal synthesis and by boiling under reflux for 2½ hours according to the conditions described in Section 3.2.1. On cooling the samples were dried under the infrared lamp. Further treatment of the samples was carried out as described in Section 3.2.1.

## 3.3 Instrumental Techniques

### 3.3.1 X-Ray Powder Diffraction

The X-ray powder diffraction patterns were recorded with a Siemens D5000 X-ray diffractometer using Ni filtered Cu $K_\alpha$ radiation. All patterns were matched using the

Joint Committee on Powder Standards (JCPDS) database. Lattice parameters were calculated using the Win Metric, Louer and Dicvol least squares computer programs.

### 3.3.2 Laue Diffraction

Laue diffraction patterns from the single crystal of $Fe_3O_4$ were recorded in reflection mode using a diffractometer based on a Philips X-ray generator. A goniometer and photographic plate mounting designed and built by The University of Liverpool was used to collect the data.

### 3.3.3 Mössbauer Spectroscopy

$^{57}Fe$ Mössbauer spectra were recorded using a microprocessor controlled Mössbauer spectrometer with a 25mCi $^{57}Co/Rh$ source at 298K. $^{119}Sn$ Mössbauer spectra were recorded with a 5mCi $Ca^{119m}SnO_3$ source and a gas filled proportional counter at 298K. The spectrometer was calibrated using a $^{57}Co/Rh$ source and a natural iron foil. All $^{57}Fe$ chemical isomer shift data are quoted relative to metallic iron and $^{119}Sn$ data are quoted relative to $SnO_2$. In situ high temperature $^{57}Fe$ Mössbauer spectra were recorded using the furnace described in Chapter 2. All Mössbauer spectra were computer fitted to Lorentzian lines using the Mfit software produced by Kristjan Jónsson, Science Institute, University of Iceland.

The $^{57}Fe$ Mössbauer spectra of the single crystal of $Fe_3O_4$ were recorded at 4.2K using a microprocessor controlled Mössbauer spectrometer, based on an AERE(Harwell) design with a $^{57}Co/Rh$ source of original strength 100mCi and actual strength about 60mCi. Magnetic fields of up to 13 Tesla were applied using a superconducting magnet supplied by Cryogenic Consultants. This consisted of 5 concentric cylindrical coils connected in series. The inner coils were of Nb/Sn wire and the outer coils made from Nb/Ti wire.

The applied field was proportional to the current in the coils and reached a maximum of 14 Tesla with a current of 95.7A.

### 3.3.4 Extended X-Ray Absorption Fine Structure (EXAFS)

EXAFS data were recorded on beamlines 7.1 and 9.2 at the Synchrotron Radiation Source at Daresbury Laboratory using a beam with energy of 200mA and 2GeV. The data were fitted with the EXCALIB, EXBACK and EXCURV92 programs supplied by Daresbury Laboratory with radial distribution data obtained from the ICSD and MDF databases.

### 3.3.5 Scanning Electron Microscopy and Energy Dispersive X-Ray Microanalysis (SEM and EDX)

Scanning electron micrographs were recorded from finely ground powder samples attached to carbon coated metal stubs using a JEOL JSM820 microscope with an accelerating voltage of 15keV. The samples were coated with a thin layer of gold. EDX data were recorded from non-gold coated samples in the scanning electron microscope using a Kevex X-ray detector and quantex analysis software.

### 3.3.6 Raman Spectroscopy

Raman spectra were recorded using a Dilor XY spectrometer with excitation at 514.5nm provided by a coherent I70 $Ar^+$ laser. Radiation power at the sample was varied between 5 and 15mW.

### 3.3.7 X-ray Photoelectron Spectroscopy

X-ray photoelectron spectra were recorded by Dr. J.F. Marco at the Instituto de Quimica Fisica 'Rocasolano', Madrid, Spain with a Leybold LHS-10 spectrometer using Al $K_\alpha$ radiation under an operating vacuum better than 1 x $10^{-8}$ mbar. The powdered samples were pressed on double sided adhesive conductive carbon tape. The energy scale was calibrated with the C 1s signal at 284.6eV.

# CHAPTER FOUR

# Investigation of $Fe_{3-x}M_xO_4$

## 4.1 Mössbauer spectroscopy examination of a single crystal of $Fe_3O_4$

Mössbauer spectra were recorded from a single crystal of $Fe_3O_4$, cut perpendicular to the [1 1 1] axis, in applied fields of 0, 2, 5, 9 and 13 Tesla at 4.2K. Initial inspection of the spectrum recorded in zero applied field, Figure 4.1, indicated that there were 5 magnetic components. The $^{57}Fe$ Mössbauer parameters from this spectrum, Table 4.1, indicated one component characteristic of $Fe^{3+}$ ions situated in the tetrahedral (A) sites together with four components indicative of a mixture of $Fe^{3+}$ and $Fe^{2+}$ ions situated on the octahedral (B) sites. One of these components, Oct. $Fe^{2+}$-II, had a particularly large quadrupole splitting, Table 4.1, involving the unusual peak at ~3.8mms$^{-1}$ which has also been observed by Ito[1] and Sawatzky.[2] Although Ito was unable to account for this peak Sawatzky accounted for the peak with a second $Fe^{2+}$ magnetic component with a large quadrupole splitting.

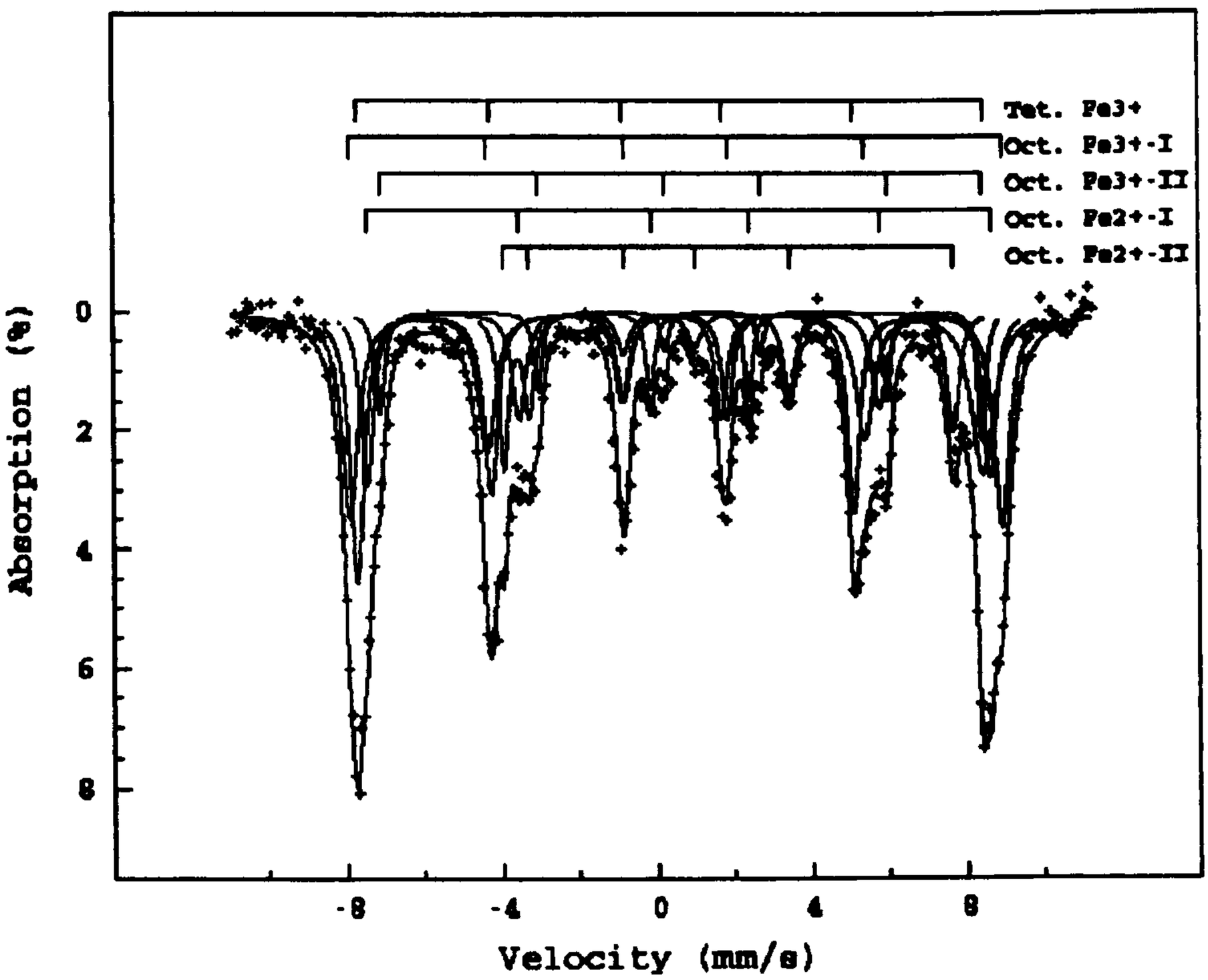


***Figure 4.1 - $^{57}Fe$ Mössbauer spectrum recorded from an $Fe_3O_4$ single crystal in zero applied field at 4.2K***

From an examination of the local symmetry around the iron ions in $Fe_3O_4$ Häggström et al[3] calculated that the B site component in the $^{57}Fe$ Mössbauer spectrum recorded from

| Field/ Tesla | Tet. $Fe^{3+}$ | | | Oct. $Fe^{3+}$ I | | | Oct. $Fe^{3+}$ II | | | Oct. $Fe^{2+}$ I | | | Oct. $Fe^{2+}$ II | | |
|---|---|---|---|---|---|---|---|---|---|---|---|---|---|---|---|
| | δ/$mms^{-1}$ ±0.03 | Δ/$mms^{-1}$ ±0.05 | H/Tesla ±0.2 | δ/$mms^{-1}$ ±0.03 | Δ/$mms^{-1}$ ±0.05 | H/Tesla ±0.2 | δ/$mms^{-1}$ ±0.03 | Δ/$mms^{-1}$ ±0.05 | H/Tesla ±0.2 | δ/$mms^{-1}$ ±0.03 | Δ/$mms^{-1}$ ±0.05 | H/Tesla ±0.2 | δ/$mms^{-1}$ ±0.03 | Δ/$mms^{-1}$ ±0.05 | H/Tesla ±0.2 |
| 0 | 0.37 | -0.02 | 50.1 | 0.49 | 0.00 | 52.2 | 0.83 | -0.27 | 49.8 | 1.03 | -0.41 | 48.2 | 0.96 | 0.89 | 35.9 |
| 2 | 0.42 | 0.00 | 52.3 | 0.53 | -0.03 | 50.8 | 0.89 | -0.16 | 48.6 | 0.78 | 0.32 | 39.3 | 1.15 | 0.12 | 40.6 |
| 5 | 0.39 | -0.02 | 55.1 | 0.70 | -0.29 | 47.4 | 0.69 | 0.17 | 46.7 | 0.85 | -0.06 | 40.7 | 1.15 | 0.09 | 38.7 |
| 9 | 0.39 | -0.02 | 58.9 | 0.74 | -0.37 | 43.8 | 0.72 | 0.11 | 42.9 | 0.82 | -0.03 | 37.7 | 1.16 | 0.01 | 35.4 |
| 13 | 0.39 | -0.01 | 62.8 | 0.75 | -0.40 | 40.0 | 0.74 | 0.11 | 39.3 | 0.82 | -0.09 | 34.2 | 1.11 | -0.05 | 32.4 |

***Table 4.1 - $^{57}$ Fe Mössbauer parameters of single crystal $Fe_3O_4$ oriented parallel to the [1 1 1] axis recorded at 4.2K***

$Fe_3O_4$ at 300K was a superposition of two components arising from non-equivalence in the B site. It was calculated that the occupation ratio of the non-equivalent sites should be 3:1. Having proposed this model they then proceeded to record Mössbauer spectra from $Fe_3O_4$ over the temperature range 120K-880K and found the experimental data to agree well with the proposed model. Assuming that there is a non-equivalence in the B site of $Fe_3O_4$ it would be reasonable to expect that below the Verwey transition temperature, 119K, the $^{57}Fe$ Mössbauer spectrum of the B site should consist of 4 components as a result of the termination of the electron hopping process. The cessation of the hopping process would then be expected to produce distinct $Fe^{2+}$ and $Fe^{3+}$ components in the Mössbauer spectrum. Hence the success here in fitting the spectrum recorded at 0 Tesla to five components from the crystal at 4.2K is consistent with the findings of both Sawatzky et al[2] and Häggström et al.[3] Further, the four B site components would be expected to have relative area ratios of 25:25:8:8 ($Fe^{3+}$:$Fe^{2+}$:$Fe^{3+}$:$Fe^{2+}$) as is observed here since the ratio of the non-equivalence on the B sites is 3:1.

To attempt to separate out these components a field of 2 Tesla was applied to the sample along the [1 1 1] axis. This has the advantage of separating the individual components and simplifying the spectrum as the 2nd and 5th peaks in the Mössbauer spectrum disappear when this geometry is used, Section 2.2.4. The spectrum recorded in a 2 Tesla applied field, Figure 4.2, was similar to that recorded in zero applied field with two exceptions. Firstly, the 2nd and 5th peaks had virtually disappeared as expected and, secondly, the peak at ~3.8mms$^{-1}$ had vanished. The disappearance of this peak correlates with it being the 5th peak of the Oct $Fe^{2+}$-II component, but the fitting, with parameters listed in Table 4.1, also showed the quadrupole splitting to be reduced to a near zero value. In $Fe_3O_4$ the spins are not aligned along the [1 1 1] axis , but are directed more along the [0 0 1] axis which is taken as the direction of $V_{zz}$ for this site. This arises because at temperatures below the Verwey transition temperature the structure of magnetite changes from cubic to orthorhombic symmetry. In the cubic

structure the electric field gradient(efg) is zero but in the lower symmetry case the efg is non-zero. It would then be expected that $V_{zz}$ would lie along the axis of highest symmetry which itself depends on the distortion but, if nearly tetragonal, would be along the c axis, [0 0 1]. Applying a field parallel to the [1 1 1] axis aligns the spins along that axis thereby swinging the spins by approximately 50°. This realignment causes the angle between $V_{zz}$ and the axis to become $\cos^{-1}(1/\sqrt{3})$ and so $3\cos^2\theta-1$ becomes 0 with the consequent disappearance of the quadrupole splitting, as discussed in Section 2.2.3.

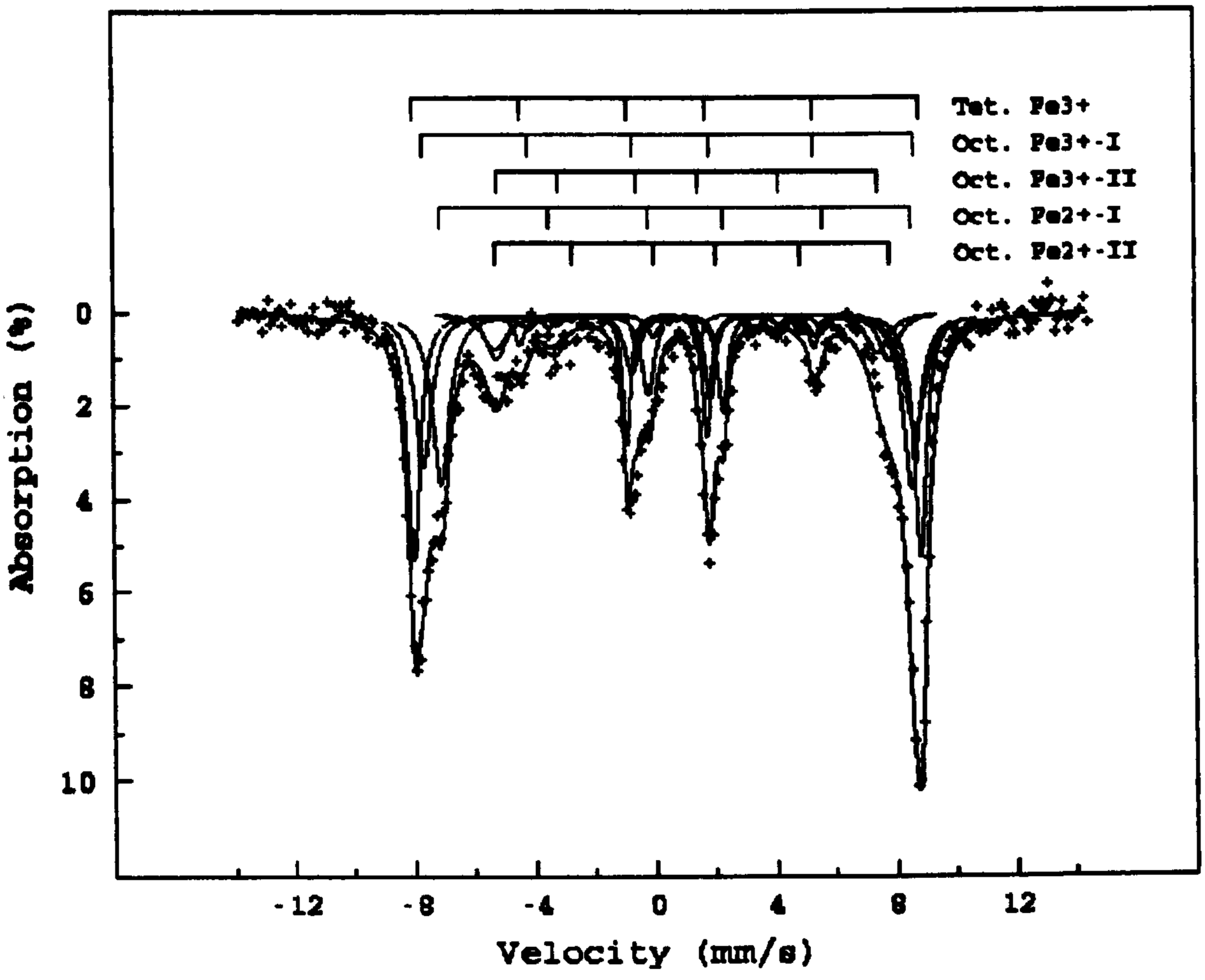


***Figure 4.2 - $^{57}Fe$ Mössbauer spectrum recorded from a single crystal of $Fe_3O_4$ in an applied field of 2 Tesla at 4.2K***

Further examination of the parameters from the spectrum recorded at 2T, Table 4.1, indicated the 4 B sites to be in the ratio of 24.5:27.7:9.3:8.7, in reasonable agreement with that expected if there is a magnetically non-equivalent B site.

As the applied field was increased to 5, 9 and 13 Tesla the distinction between the A and B sites became more apparent, Figure 4.3. As with the earlier spectra, fits to 5

components generally agreed well with the expected peak areas. Differences in the relative area ratios may be attributed to variations in the thickness of the sample used. The alignment of the spins in $Fe_3O_4$ is such that when a field is applied along the [1 1 1] axis the effect on the components due to the A and B sites is completely opposite. With the A site the applied field has an additive effect but with the B sites the observed field is seen to decrease.

On examining the parameters for the A site in each spectrum, Table 4.1, the size of the field was observed to increase to 62.8 Tesla in an applied field of 13 Tesla. This is as expected when we consider that the spectrum recorded at 0 Tesla had a field of 50.1 Tesla, i.e. the hyperfine field due to the A site in $Fe_3O_4$ is 50.1 Tesla. Further, the parameters are consistent to within $\pm 0.05 mms^{-1}$ for $\delta$ and to within $\pm 0.03 mms^{-1}$ for $\Delta$ for the A site. For the B sites the parameters are less consistent on progressing through the series although the 4 different B site components do show reasonable agreement in the spectra recorded at 5, 9 and 13 Tesla.

Hence, the Mössbauer spectra recorded at low temperature in applied fields provide the first direct evidence from low temperature spectra to support the model proposed by Häggström et al.[3] The spectra clearly indicated that the octahedral sites in $Fe_3O_4$ are composed of two non-equivalent sites and therefore that the broadening of the room temperature spectrum of $Fe_3O_4$ is indeed due to a superposition of components rather than to an electron hopping process.

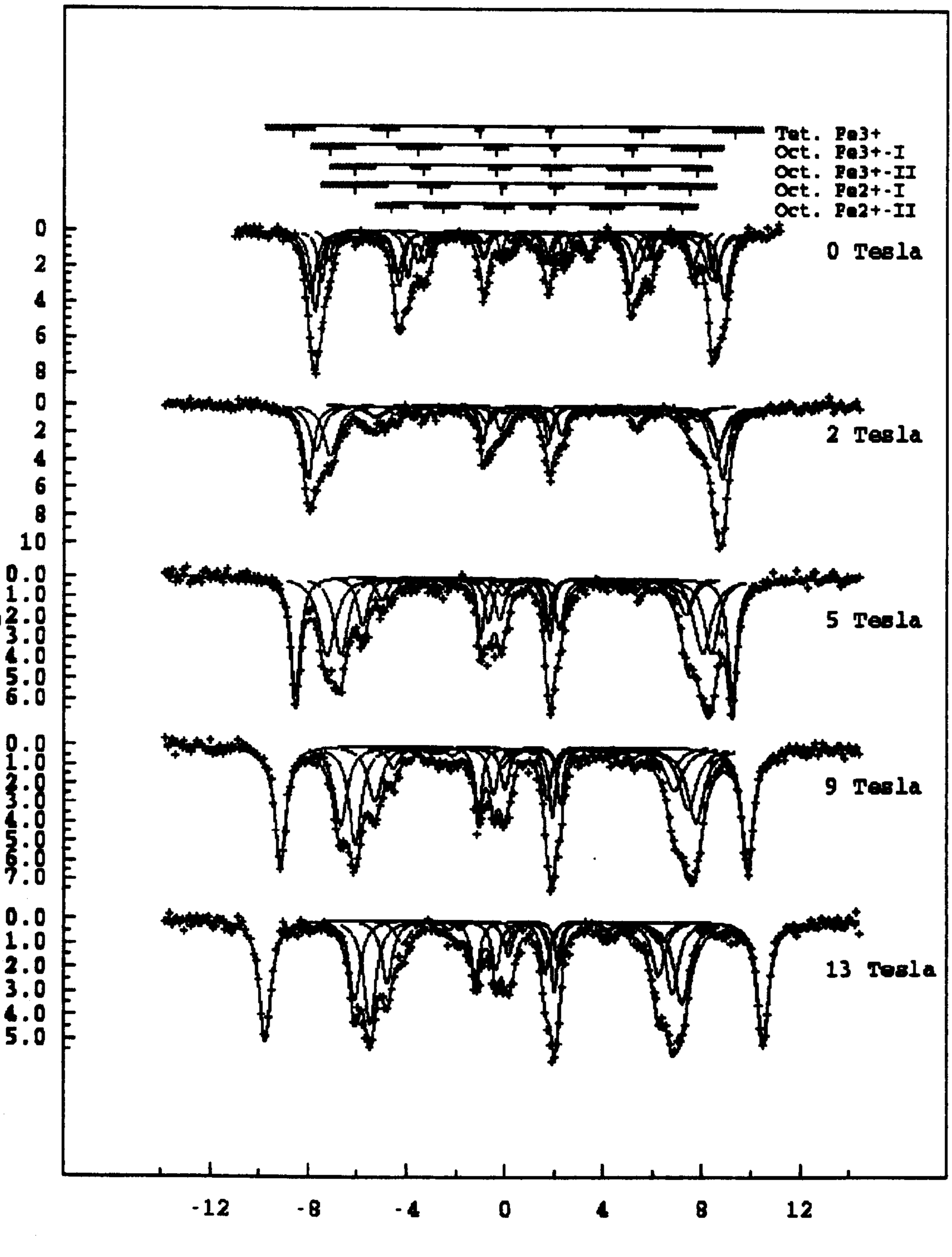


***Figure 4.3 - $^{57}Fe$ Mössbauer spectra recorded from a single crystal of $Fe_3O_4$ in varying applied fields at 4.2K***

## 4.2 Investigation of $Fe_{3-x}Sn_xO_4$

Tin-doped magnetite has been investigated with the aim of gaining a further understanding of the effect of tin on the magnetic properties of $Fe_3O_4$ and to establishing the stability of the materials at elevated temperature both in air and *in vacuo*. The relationship between this system and the analogous titanium doped magnetite has also been of interest as the similarity between the tin and titanium species means that any insight gained using tin may be related to the titanium system. Using tin has the advantage that it is a Mössbauer isotope, hence the phase transformation, from $Fe_3O_4$ to $\gamma$-$Fe_2O_3$, and the magnetic properties are amenable to examination by both $^{119}Sn$ and $^{57}Fe$ Mössbauer spectroscopy. This may give some indication of the processes involved in the substitution of $Fe^{3+}$ by $Sn^{4+}$ and which may also be applicable to the titanium-doped $Fe_3O_4$.

### 4.2.1 Energy Dispersive X-ray Microanalysis of $Fe_{3-x}Sn_xO_4$

Energy Dispersive X-ray Microanalysis (EDX) was used to determine the amount of tin present in the samples. For this technique to be valid the material under investigation must be single phase as EDX determines the total amount of each of the ions present. Measurements were recorded from the tin-doped magnetite samples, $Fe_{3-x}Sn_xO_4$ where $0.05 \leq x \leq 0.4$, which were shown, by XRD, Section 4.2.2., to be single phase. The results, Figure 4.4, showed the tin content to be similar to the nominal tin content. The variation between the determined and nominal values at high tin contents is due to the errors in the technique (±25%) when a standardless analysis of metal oxides is performed.

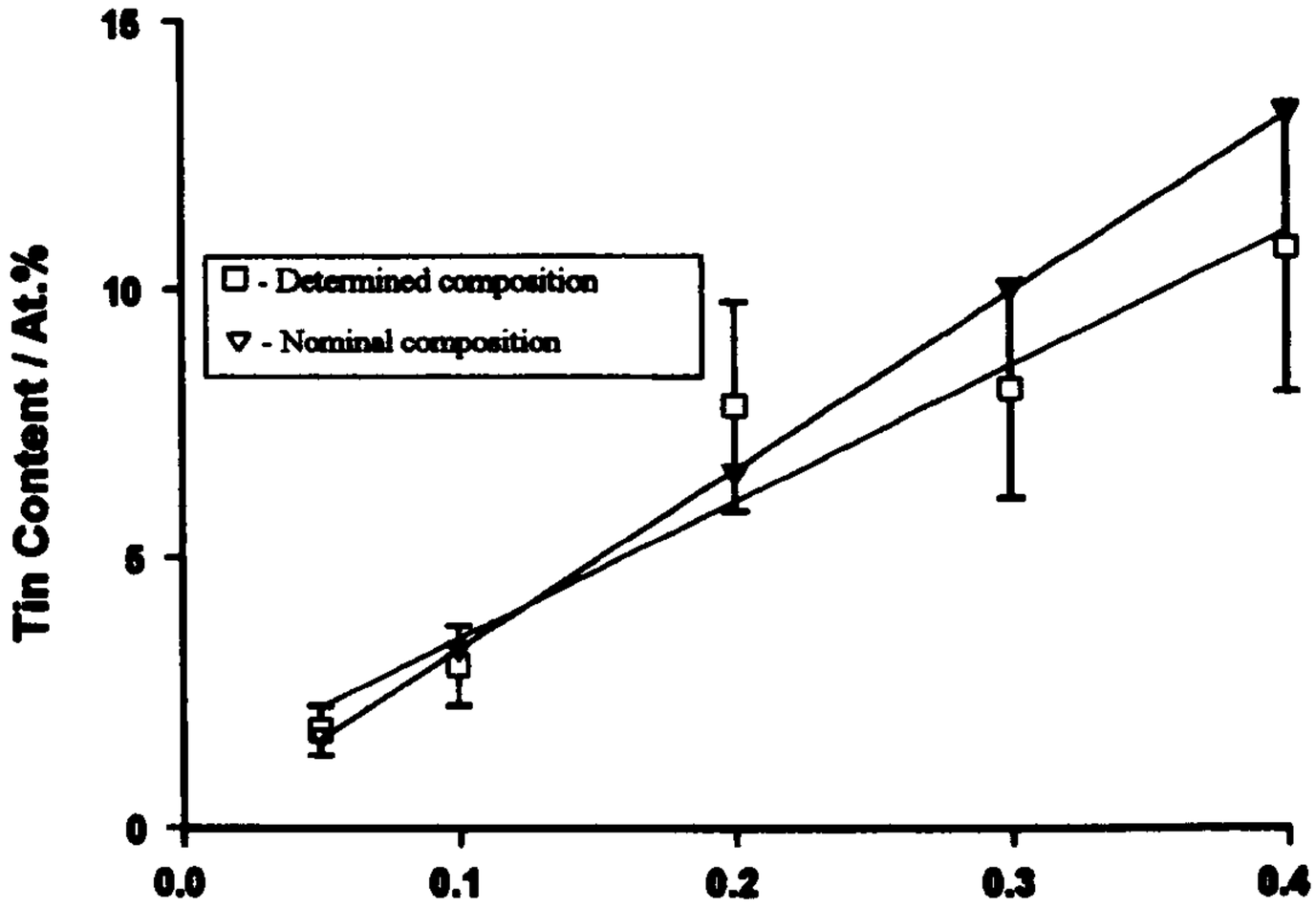


***Figure 4.4 - Tin content in $Fe_{3-x}Sn_xO_4$ as determined by Energy Dispersive X-ray Microanalysis***

### 4.2.2 X-ray powder diffraction data recorded from $Fe_{3-x}Sn_xO_4$

The X-ray powder diffraction pattern recorded from $Fe_{2.8}Sn_{0.2}O_4$, Figure 4.5, was similar to that reported[5] in the literature for stoichiometric $Fe_3O_4$ but with peak positions which had shifted to slightly lower 2θ values indicating an increase in the unit cell size of the tin-doped magnetite. The increasing shift in peak position with dopant level is shown in Figure 4.6. Peaks which could not be attributed to the magnetite phase were identified as an impurity phase of $Fe_2SiO_4$ at about the 5% level. The presence of a silicate phase is not surprising given the use of a quartz ampoule in the reaction. It is likely that the iron powder in the reaction mixture reacted with the surface layer of silica. This was confirmed by a further reaction where $SnO_2$ and $Fe_2O_3$ were placed in a quartz ampoule and heated at 900°C for 24 hours. In this case there was no coating on the inside surface of the ampoule and the X-ray powder diffraction pattern gave no evidence of $Fe_2SiO_4$, indicating that the presence of iron powder is required to induce reaction with the $SiO_2$ surface. Lattice parameters for solid solutions of composition $Fe_{3-x}Sn_xO_4$ ($0.05 \leq x \leq 0.4$) are collected in Table 4.2.

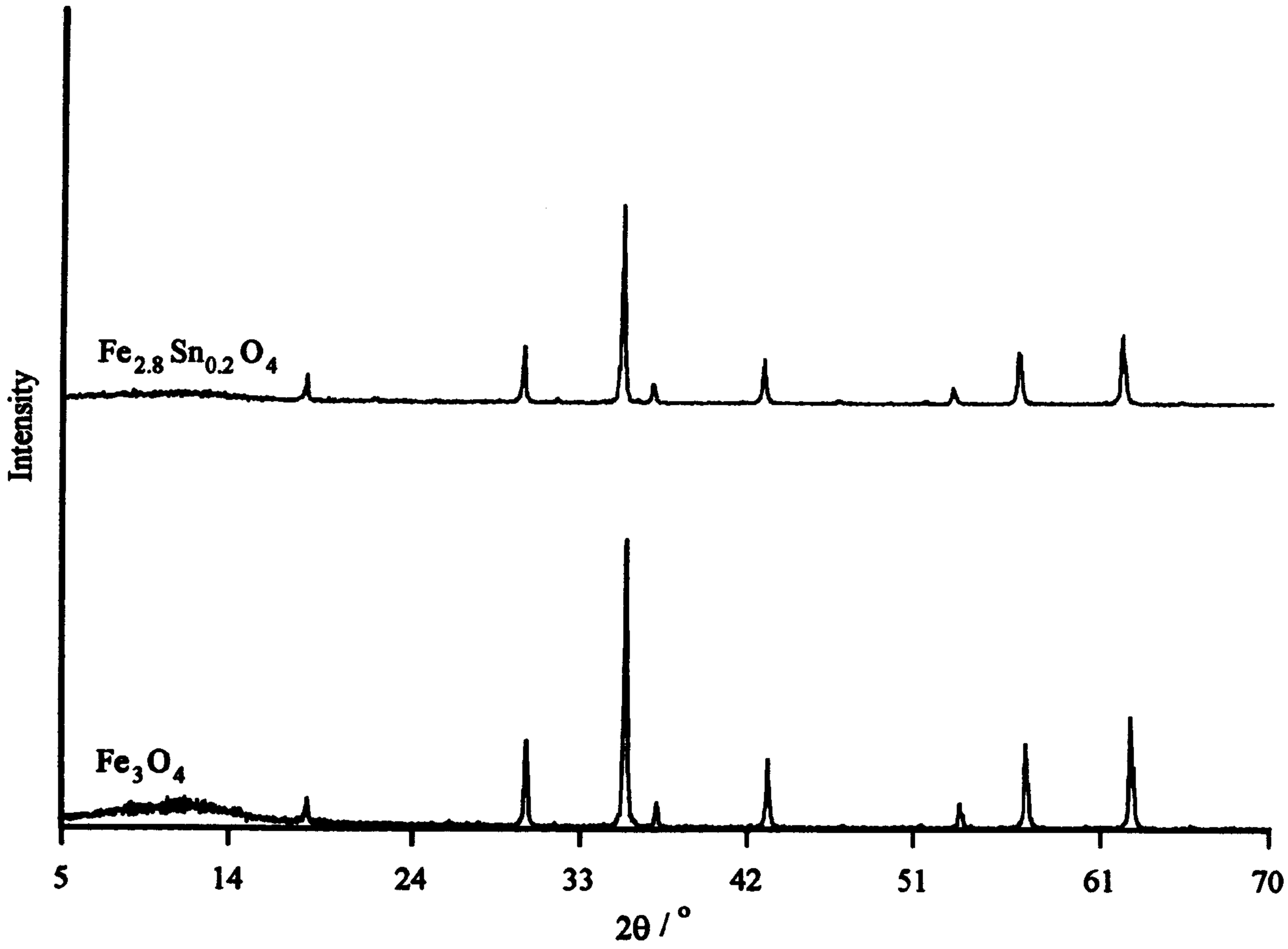


***Figure 4.5 - Comparison of X-ray powder diffraction patterns for $Fe_3O_4$ and $Fe_{2.8}Sn_{0.2}O_4$***

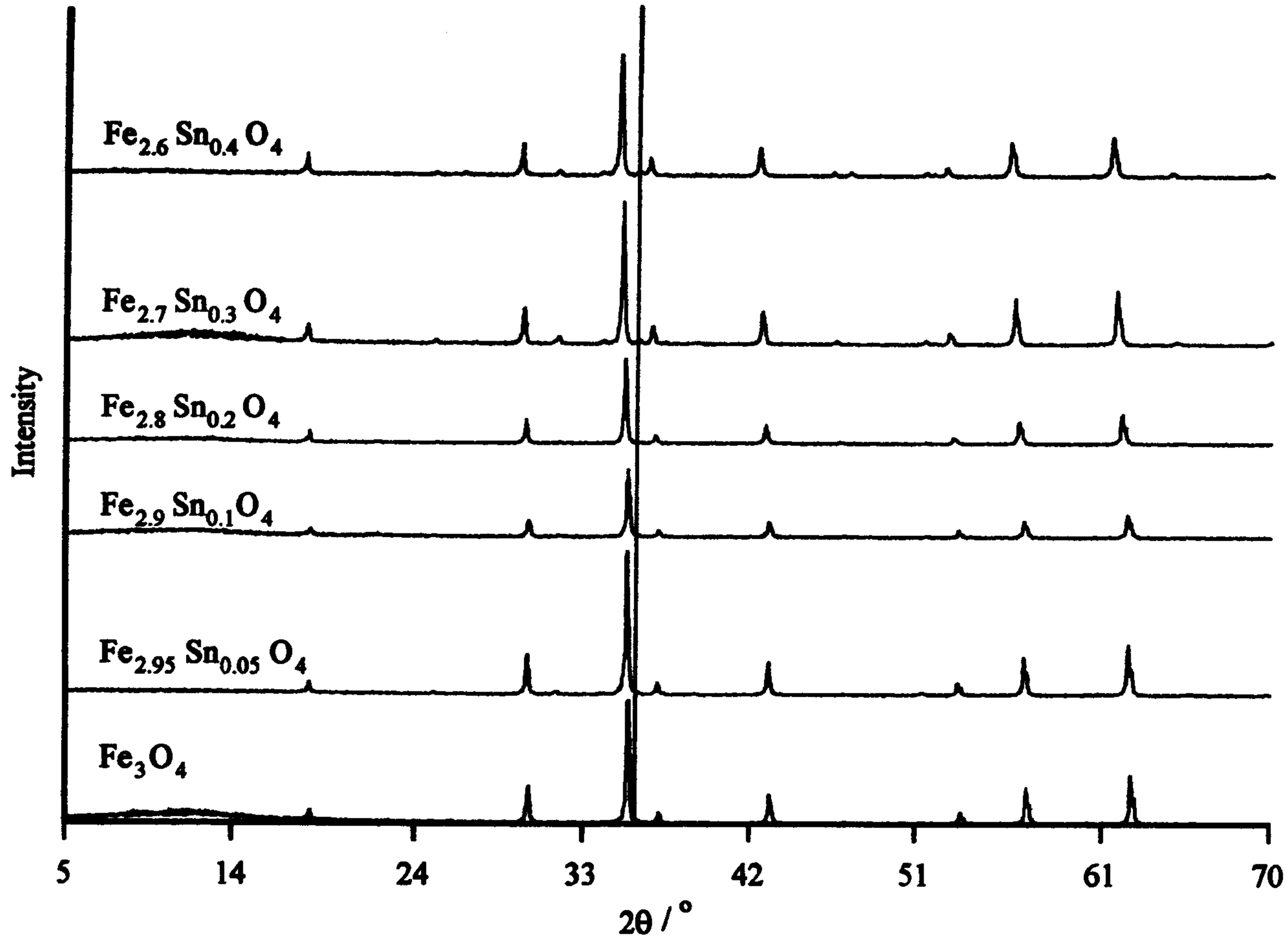


***Figure 4.6 - X-ray powder diffraction patterns for a series of tin-doped magnetites***

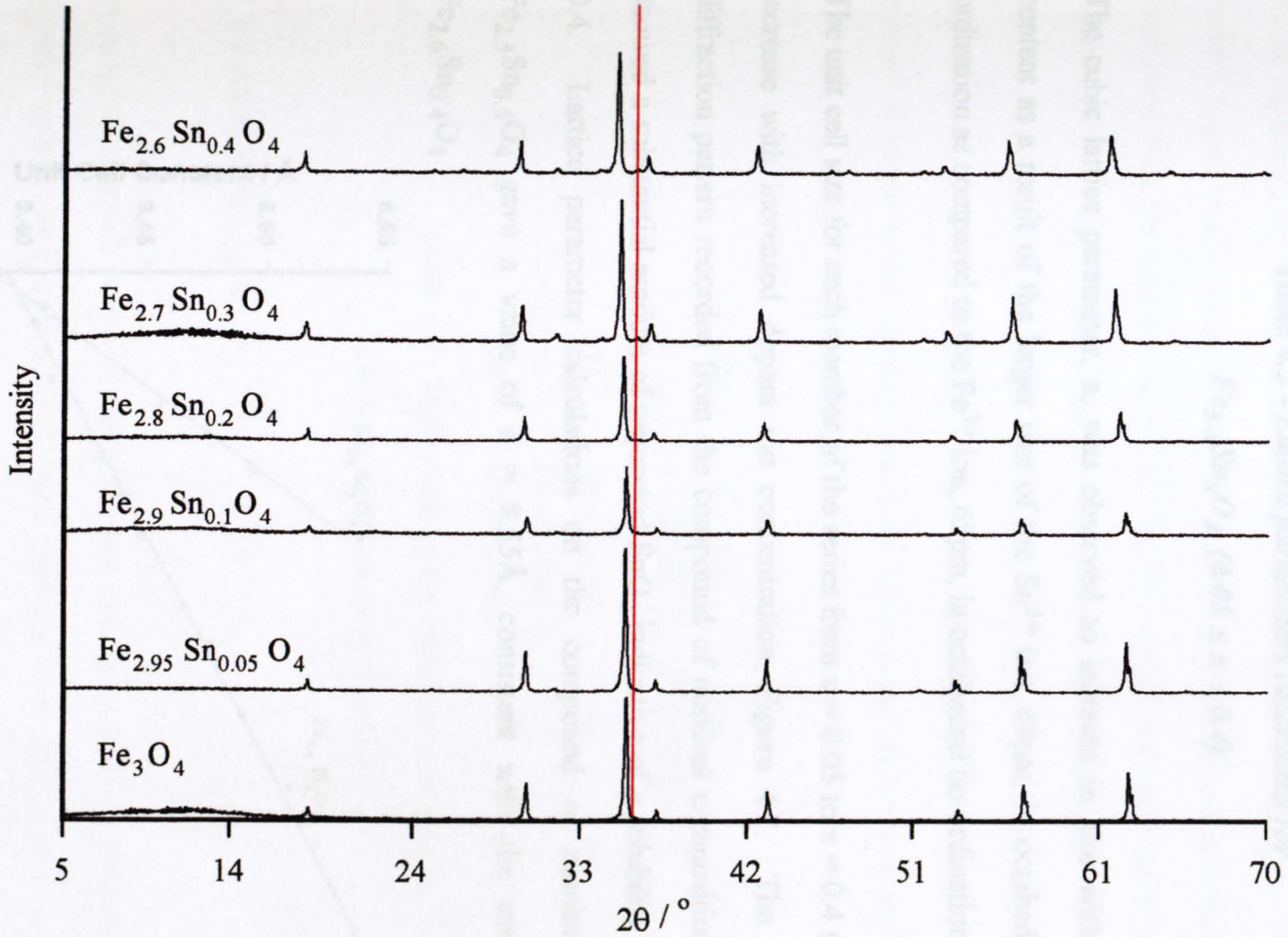


***Figure 4.6 - X-ray powder diffraction patterns for a series of tin-doped magnetites***

| x | a (Å) |
|---|---|
| 0.05 | 8.41 |
| 0.10 | 8.42 |
| 0.20 | 8.46 |
| 0.30 | 8.50 |
| 0.40 | 8.54 |

***Table 4.2 - Lattice parameters calculated for $Fe_{3-x}Sn_xO_4$ ($0.05 \leq x \leq 0.4$)***

The cubic lattice parameter, a, was observed to increase in size with increasing tin content as a result of the larger size of the $Sn^{4+}$ ion, 69pm, in octahedral oxygen co-ordination as compared to the $Fe^{3+}$ ion, 65pm, in octahedral co-ordination.[6]

The unit cell size for each member of the series from x = 0.05 to x = 0.4 showed a linear increase with increased dopant ion concentration, Figure 4.7. The X-ray powder diffraction pattern recorded from the compound of nominal composition $Fe_{2.5}Sn_{0.5}O_4$ showed a substantial amount of unreacted $SnO_2$ indicative of a solubility limit at *ca.* x = 0.4. Lattice parameter calculations on the compound of nominal composition $Fe_{2.5}Sn_{0.5}O_4$ gave a value of a = 8.55Å, consistent with the unit cell size of $Fe_{2.6}Sn_{0.4}O_4$.

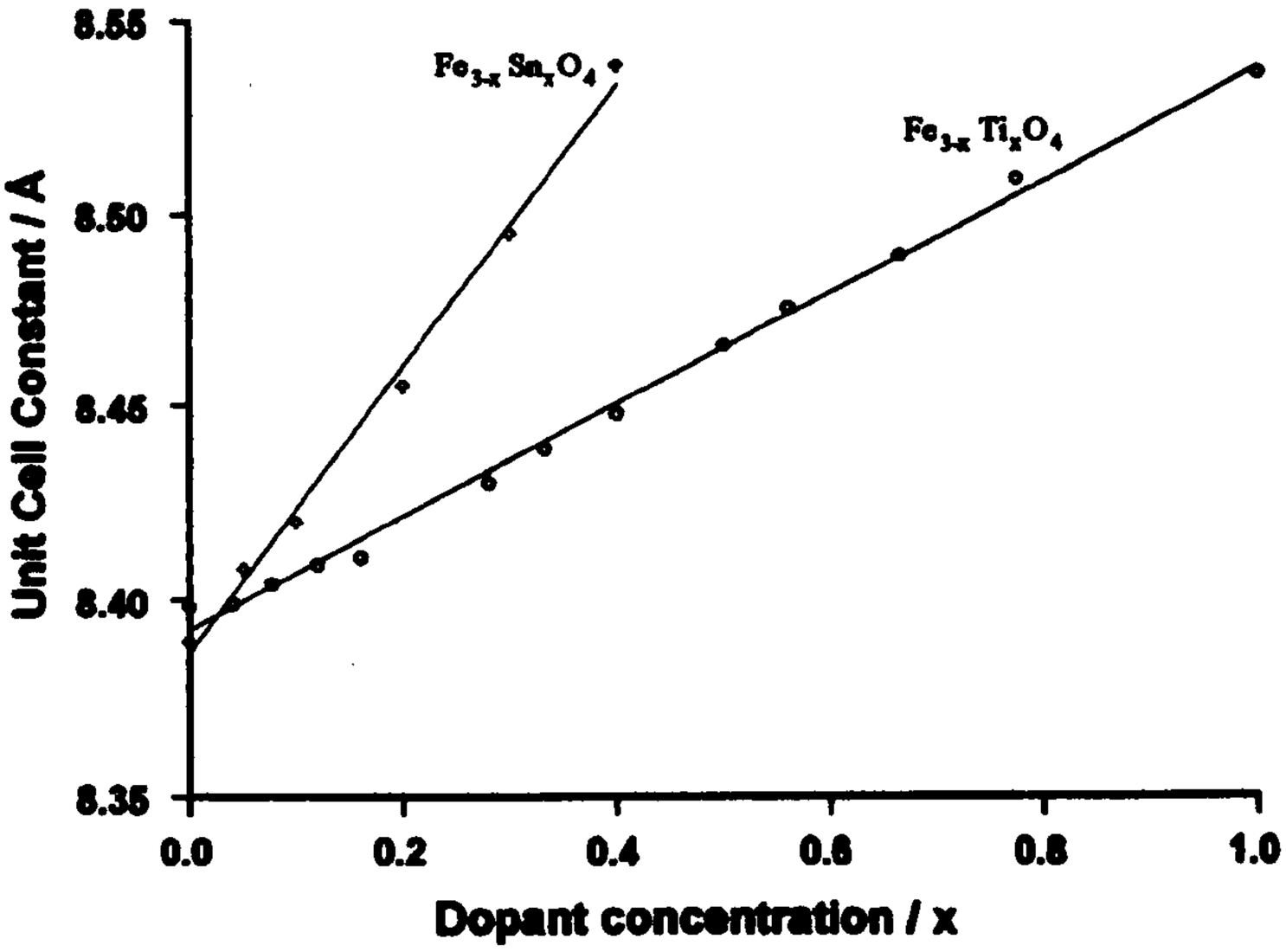


***Figure 4.7 - Variation of lattice parameters with dopant concentration for tin-doped magnetite and titanomagnetite[7]***

Similar variations in lattice parameters have been observed[7,8] in the titanomagnetites, $Fe_{3-x}Ti_xO_4$. A linear increase in the unit cell size was also observed for the titanomagnetites but, as can be seen from Figure 4.7, the increase for the tin-doped magnetite is far greater than for the titanium-containing analogue. This can be attributed to the difference in the size of the cations. In the case of $Fe_{3-x}Ti_xO_4$, $Ti^{4+}$ has an ionic radius[6], 61pm, smaller than that of $Fe^{3+}$ in octahedral oxygen co-ordination. This can be associated with the substitution of $Fe^{3+}$ by $Ti^{4+}$ which has been assumed to require the maintenance of charge balance by $Fe^{3+}$ being reduced to the larger $Fe^{2+}$ species, Table 4.3, as represented by the relationship[9] $2Fe^{3+} = Ti^{4+} + Fe^{2+}$. As will be shown later, substitution of $Fe^{3+}$ by $Sn^{4+}$ also involves the reduction of $Fe^{3+}$ to $Fe^{2+}$. The observed increase is larger in $Fe_{3-x}Sn_xO_4$ than in the titanomagnetite because $Sn^{4+}$ is larger than $Ti^{4+}$ and because $Fe^{2+}$ is also formed.

| Ion | Oxygen co-ordination | Ionic Radius/pm |
|---|---|---|
| $Sn^{4+}$ | Octahedral | 69 |
| $Ti^{4+}$ | Octahedral | 61 |
| $Fe^{3+}$ | Octahedral | 65 |
| $Fe^{2+}$ | Octahedral | 77 |

***Table 4.3 - Ionic radii of tin, titanium and iron in octahedral oxygen co-ordination[6]***

### 4.2.3 EXAFS of $Fe_{3-x}Sn_xO_4$

In order to establish which of the structural sites is occupied by the $Sn^{4+}$ ions in tin-doped magnetite tin K-edge EXAFS were recorded from samples of $Fe_{3-x}Sn_xO_4$ where x = 0.1, 0.3. For $Fe_{2.9}Sn_{0.1}O_4$, Figure 4.8, the first shell was fitted to six oxygen atoms at a Sn-O distance of 2.039Å with the subsequent shells being fitted to iron atoms with distances and co-ordination environments in good agreement with those reported[10] for stoichiometric $Fe_3O_4$, Table 4.4.

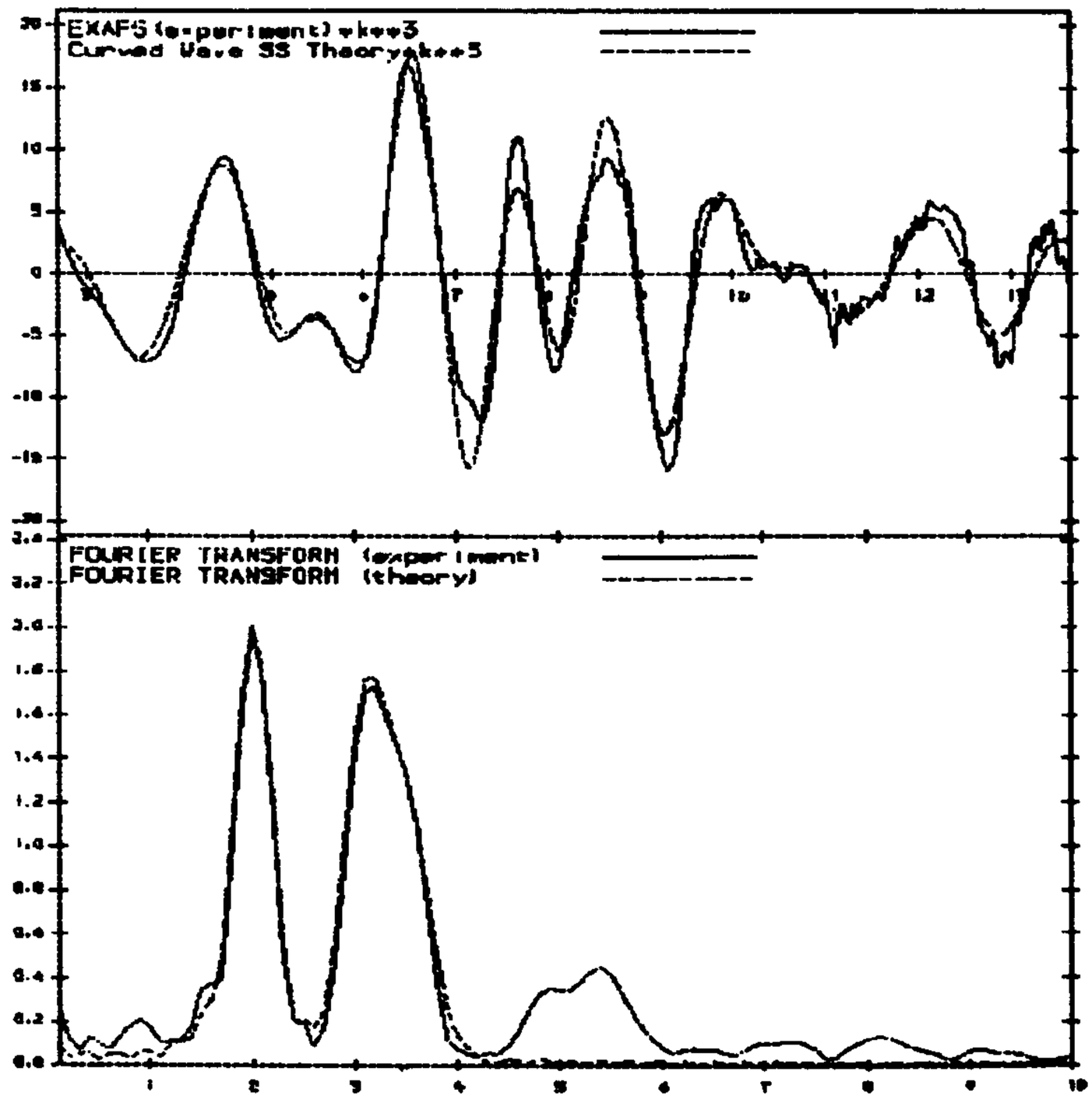


***Figure 4.8 - Fourier transform of tin K-edge EXAFS recorded from $Fe_{2.9}Sn_{0.1}O_4$***

| Compound | Atom Type | R (Å) | $2\sigma^2$ (Å$^2$) |
|---|---|---|---|
| $Fe_{2.9}Sn_{0.1}O_4$ | 6O | 2.039 | 0.007 |
| | 6Fe | 3.073 | 0.014 |
| | 6Fe | 3.487 | 0.016 |
| $Fe_{2.7}Sn_{0.3}O_4$ | 6O | 2.040 | 0.007 |
| | 6Fe | 3.071 | 0.015 |
| | 6Fe | 3.506 | 0.022 |
| $Fe_{2.8}Ti_{0.2}O_4$ | 6O | 1.937 | 0.017 |
| | 6Fe | 3.011 | 0.024 |
| | 6Fe | 3.465 | 0.024 |
| $SnO_2$ | 6O | 2.041 | 0.005 |
| | 2Sn | 3.17 | 0.006 |
| | 4O | 3.628 | 0.021 |

***Table 4.4 - Best fit parameters for tin K-edge and titanium K-edge EXAFS***

For $Fe_{2.7}Sn_{0.3}O_4$, Figure 4.9, a shell of six oxygen atoms at a Sn-O distance of 2.040Å gave the best fit. The calculated Sn-O distances for these samples were in excellent

agreement with the Sn-O distance of 2.041Å deduced from the EXAFS of a $SnO_2$ standard, Figure 4.10, Table 4.4, and also with that reported in the literature.[11] The data indicated that the $Sn^{4+}$ ions occupy the octahedral B sites in the magnetite structure, as opposed to the tetrahedral A sites. The results agree with predictions[12] that the $Sn^{4+}$ ions substitute exclusively onto the octahedral B sites.

The EXAFS results recorded from $Fe_{3-x}Sn_xO_4$ also contradict the findings of Aksenova et al[13] who proposed a cation distribution of;

$$(Fe^{3+}_{1-y}Sn^{4+}_{y})[Fe^{2+}Fe^{3+}_{1-4x/3+y}Sn^{4+}_{x-y}\square_{x/3}]O_4$$

where the brackets represent the tetrahedral and octahedral sites respectively. From the EXAFS there is no evidence for the substitution of the $Sn^{4+}$ ions onto both the tetrahedral A sites and the octahedral B sites.

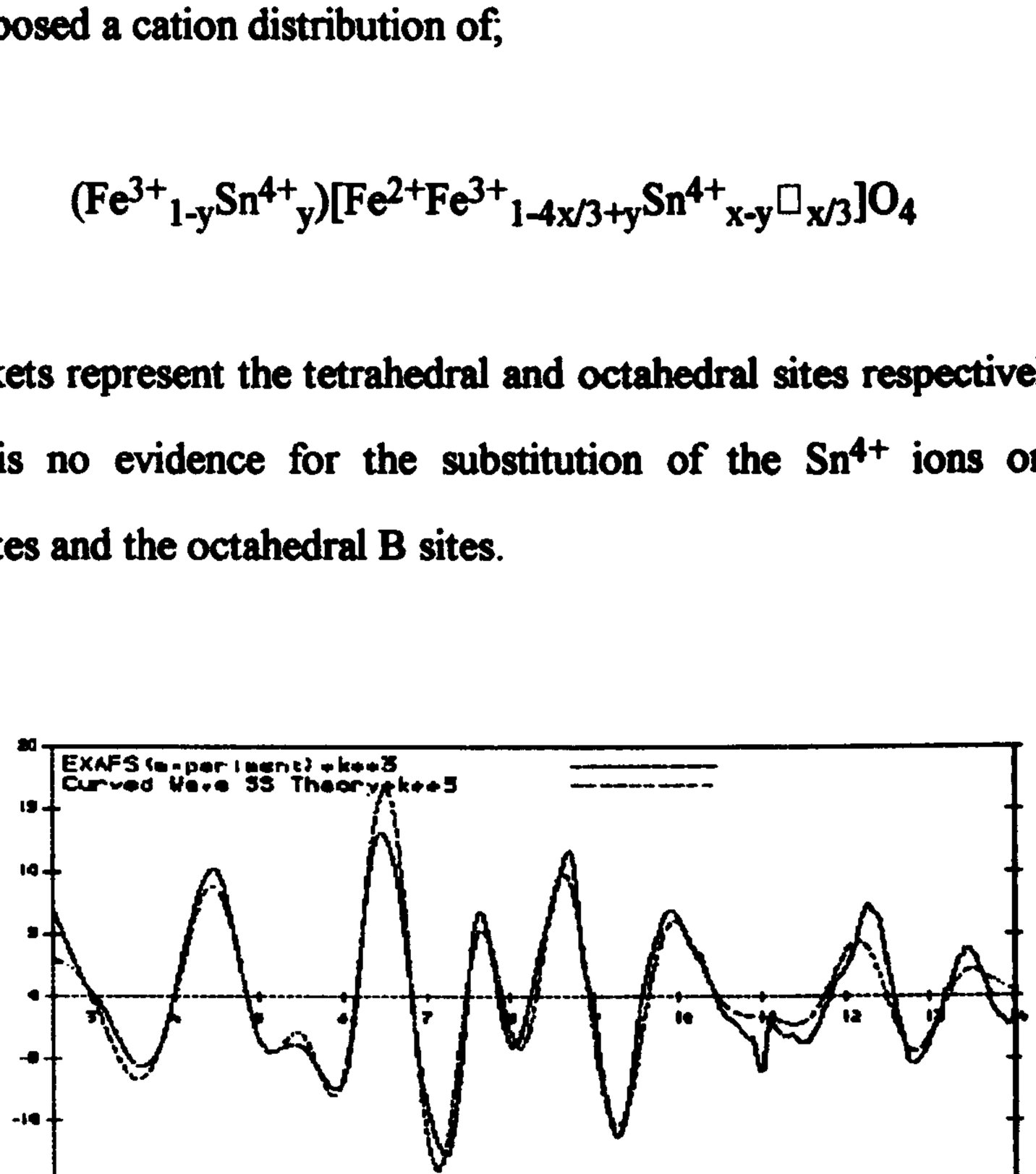


***Figure 4.9 - Fourier transform of tin K-edge EXAFS recorded from $Fe_{2.7}Sn_{0.3}O_4$***

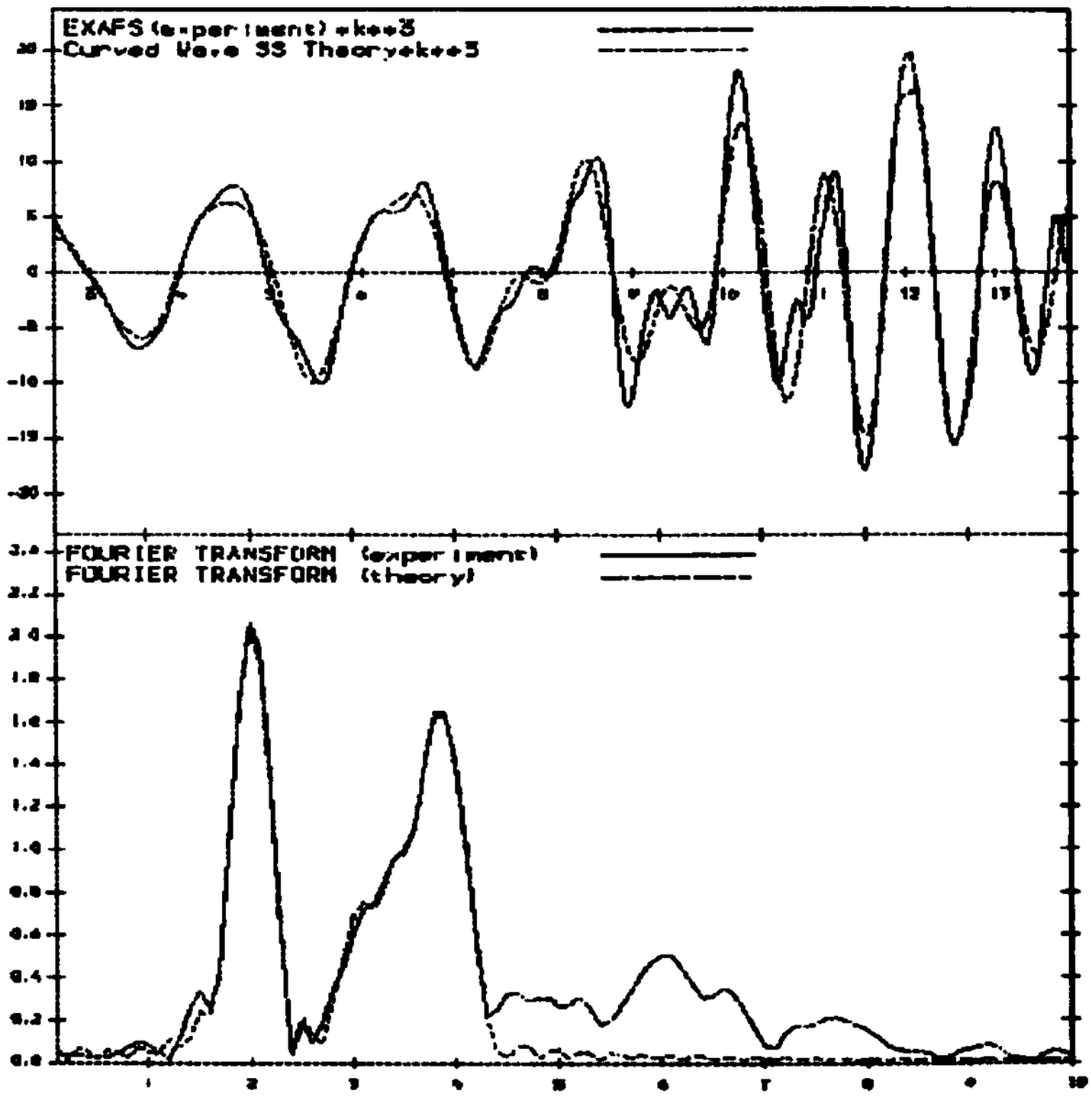


***Figure 4.10 - Fourier transform of tin K-edge EXAFS recorded from $SnO_2$***

### 4.2.3.1 EXAFS of $Fe_{3-x}Ti_xO_4$

The EXAFS recorded from $Fe_{2.8}Ti_{0.2}O_4$, Figure 4.11, showed that the $Ti^{4+}$ ion also substitutes onto the octahedral sites in preference to the tetrahedral site. This confirms earlier predictions[14] and is also in agreement with models which have been proposed for cation distribution discussed in Chapter 1. The first shell of six oxygen atoms was fitted at a distance of 1.937Å in very good agreement with the Ti-O bond distance in rutile,[16,17] $TiO_2$. This provides further justification for drawing a comparison between the tin-doped and titanium-doped magnetites. The best fit parameters are shown in Table 4.4.

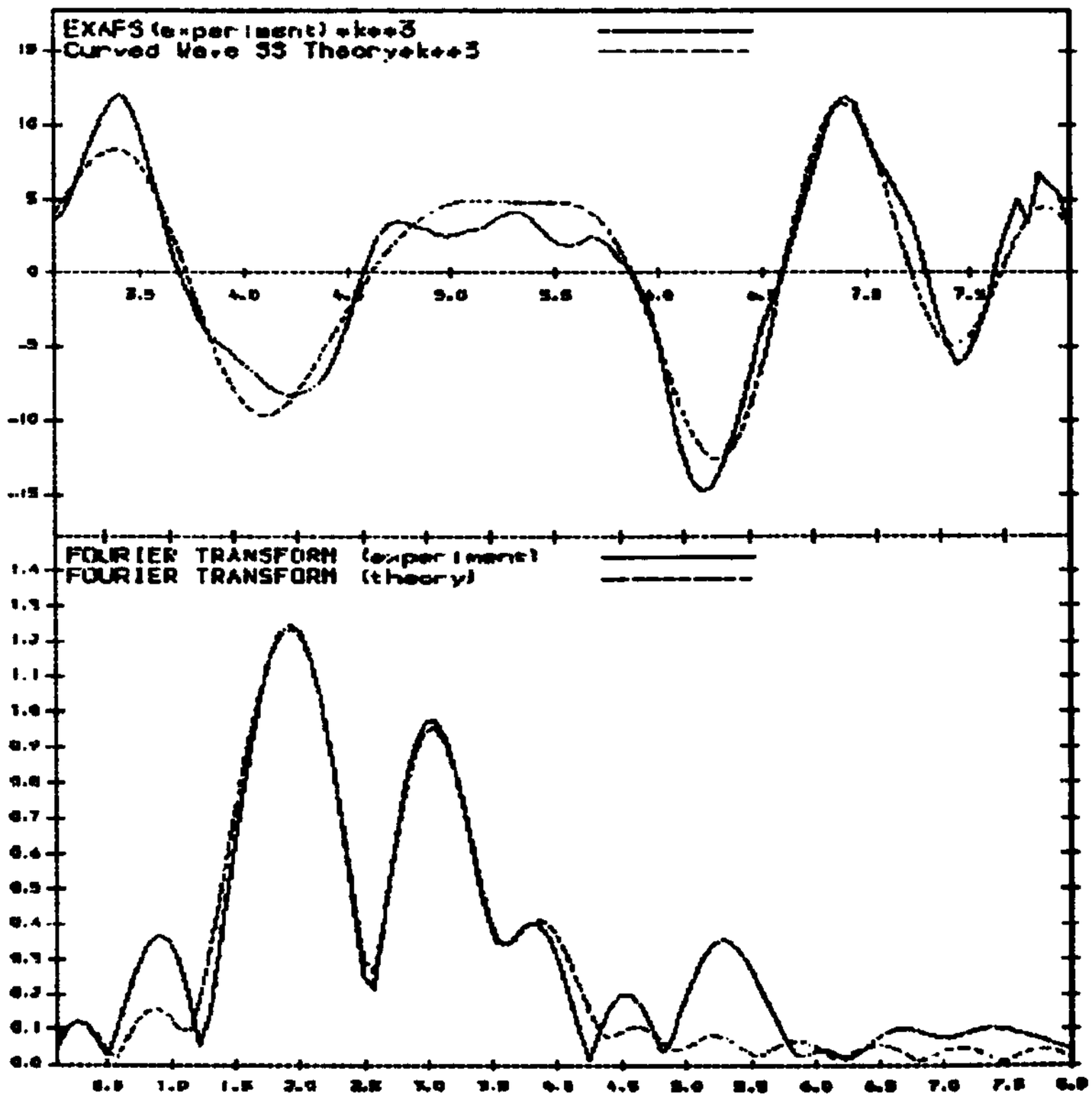


***Figure 4.11 - Fourier transform of titanium K-edge EXAFS recorded from $Fe_{2.8}Ti_{0.2}O_4$***

### 4.2.4 X-ray photoelectron spectroscopy of $Fe_{3-x}Sn_xO_4$ where $0 < x < 0.2$

The Fe 2p X-ray photoelectron spectrum recorded from $Fe_3O_4$, Figure 4.12a, and the Fe $2p_{3/2}$ binding energy of 710.9eV were in good agreement with the data reported in the literature.[17,18] The peaks in the Fe 2p spectra recorded from $Fe_{2.9}Sn_{0.1}O_4$ and $Fe_{2.8}Sn_{0.2}O_4$, Figure 4.12b and c, were slightly broader than those observed in the spectrum recorded from $Fe_3O_4$ with the binding energy maxima shifted to lower values, 710.4eV and 710.0eV respectively. A peak at 715.4eV which was attributed to the Sn $2p_{3/2}$ core level was visible in both spectra. It was also observed that there was a peak at 714eV in addition to the Sn $2p_{3/2}$ peak at 715.4eV which was indicative of an $Fe^{2+}$ satellite peak.[18,19] The Fe $2p_{3/2}$ peak of $Fe_3O_4$ indicated that only the $Fe^{3+}$ species were present although $Fe_3O_4$ contains both $Fe^{2+}$ and $Fe^{3+}$ species. This has been associated[20,21] with surface oxidation of the $Fe^{2+}$ species which generally leaves only

$Fe^{3+}$ species on the surface. In contrast the spectra recorded from $Fe_{2.9}Sn_{0.1}O_4$ and $Fe_{2.8}Sn_{0.2}O_4$ were deconvoluted to four peaks. The peak at 710.7eV corresponded to $Fe^{3+}$ species and those at 709.2 and 714eV were characteristic of the $Fe^{2+}$ contribution[18,19] and, as stated previously, the peak at 715.4eV was due to the Sn $2p_{3/2}$ level.

It was also found that the peaks due to the $Fe^{2+}$ contribution increased as the tin content increased, Table 4.5, indicating that $Fe^{3+}$ species were reduced to $Fe^{2+}$ on incorporation of $Sn^{4+}$ into the $Fe_3O_4$ structure, as suggested in Section 4.2.2. The Fe 3p spectra recorded from $Fe_{2.9}Sn_{0.1}O_4$ and $Fe_{2.8}Sn_{0.2}O_4$, Figure 4.13, showed a contribution at 56.2eV characteristic of $Fe^{3+}$ together with a second peak at 54.3eV characteristic of $Fe^{2+}$ species. It was also found that, as with the Fe 2p spectra, the $Fe^{2+}$ contribution increased with increasing tin content, Table 4.6. The Sn 3d spectrum contained a peak at 486.1eV, Figure 4.14, indicative of the Sn $3d_{5/2}$ level. The $Sn^{2+}$ and $Sn^{4+}$ binding energies are very similar,[22] but as the tin K-edge EXAFS, Section 4.2.3, indicated a Sn-O bond distance similar to that in $SnO_2$ the Sn $3d_{5/2}$ peak was attributed to the $Sn^{4+}$ species.

| Compound | Binding Energy / eV | Relative Intensity / % | Assignment |
|---|---|---|---|
| $Fe_3O_4$ | 710.9 | 100 | $Fe^{3+}$ |
| $Fe_{2.9}Sn_{0.1}O_4$ | 709.2 | 43 | $Fe^{2+}$ |
| | 710.7 | 57 | $Fe^{3+}$ |
| $Fe_{2.8}Sn_{0.2}O_4$ | 709.1 | 66 | $Fe^{2+}$ |
| | 710.7 | 34 | $Fe^{3+}$ |

***Table 4.5 - Fe $2p_{3/2}$ binding energy values and assignments for $Fe_3O_4$, $Fe_{2.9}Sn_{0.1}O_4$ and $Fe_{2.8}Sn_{0.2}O_4$***

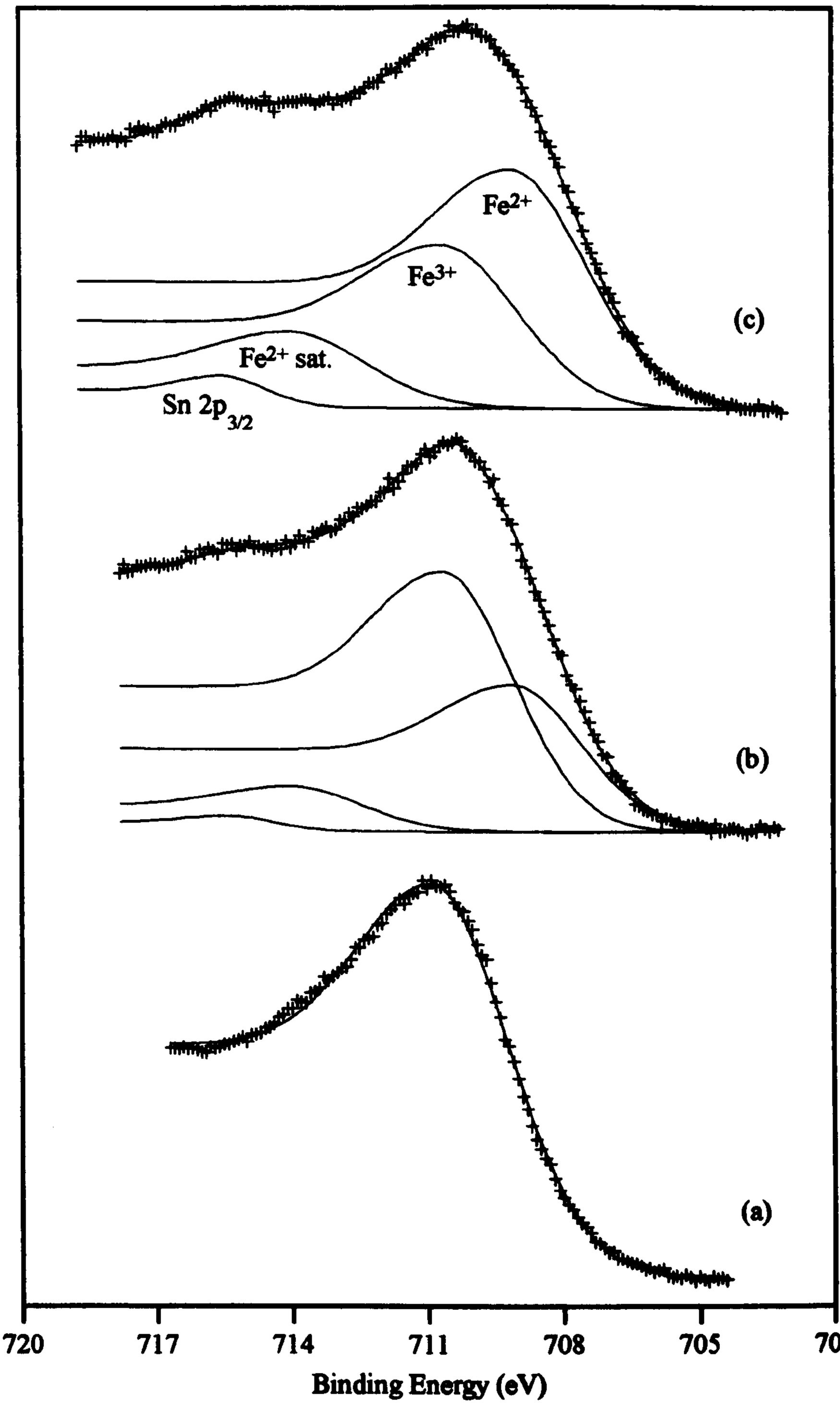


***Figure 4.12 - Deconvolution of the Fe $2p_{3/2}$ spectra recorded from (a) $Fe_3O_4$ (b) $Fe_{2.9}Sn_{0.1}O_4$ and (c) $Fe_{2.8}Sn_{0.2}O_4$ $Fe^{2+}$ sat indicates a satellite peak***

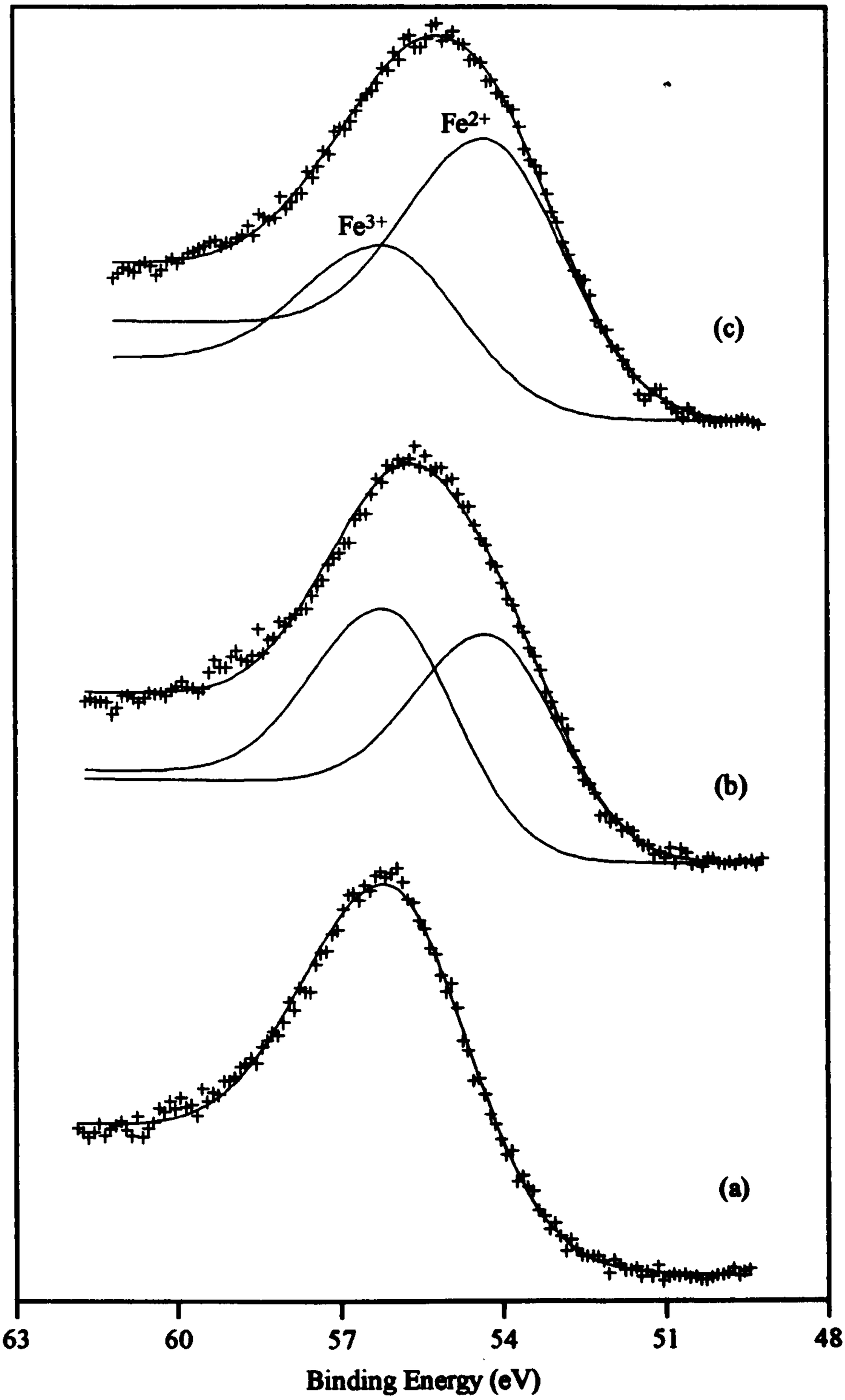


***Figure 4.13 - Deconvolution of the Fe 3p spectra recorded from (a) $Fe_3O_4$ (b) $Fe_{2.9}Sn_{0.1}O_4$ and (c) $Fe_{2.8}Sn_{0.2}O_4$***

| Compound | Binding Energy / eV | Relative Intensity / % | Assignment |
|---|---|---|---|
| $Fe_3O_4$ | 56.2 | 100 | $Fe^{3+}$ |
| $Fe_{2.9}Sn_{0.1}O_4$ | 54.3 | 47 | $Fe^{2+}$ |
| | 56.2 | 53 | $Fe^{3+}$ |
| $Fe_{2.8}Sn_{0.2}O_4$ | 54.3 | 62 | $Fe^{2+}$ |
| | 56.2 | 38 | $Fe^{3+}$ |

***Table 4.6 - Fe 3p binding energy values and assignments for $Fe_3O_4$, $Fe_{2.9}Sn_{0.1}O_4$ and $Fe_{2.8}Sn_{0.2}O_4$***

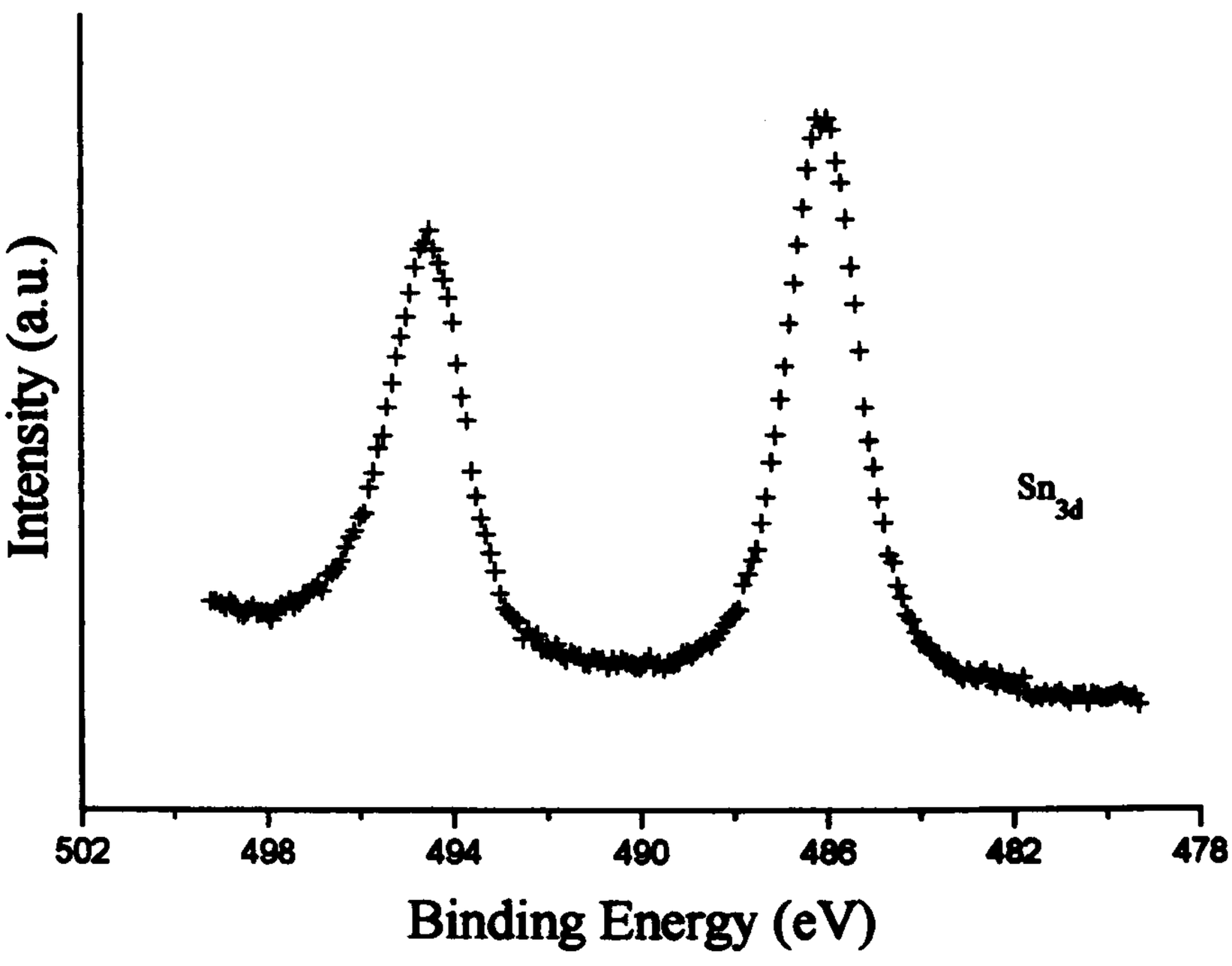


***Figure 4.14 - Sn 3d spectrum recorded from $Fe_{2.8}Sn_{0.2}O_4$***

### 4.2.5 Mössbauer spectra recorded from $Fe_{3-x}Sn_xO_4$

#### 4.2.5.1 $^{57}Fe$ Mössbauer spectra recorded at 298K

The $^{57}Fe$ Mössbauer spectra recorded at 298K from $Fe_{3-x}Sn_xO_4$, where $0.05 \leq x \leq 0.4$, Figure 4.15, were similar in appearance to that recorded for stoichiometric magnetite except that the B site peaks were considerably broadened. A fitting procedure which

combined the results of earlier work, Section 4.1, with the findings of Häggström et al[3] and Tanaka et al[7] was used to account for the broadened $^{57}Fe$ Mössbauer spectra. For pure magnetite the $^{57}Fe$ Mössbauer spectrum is best interpreted[3] in terms of one magnetic component being due to the $Fe^{3+}$ ions on tetrahedral A sites and another two magnetic components arising from the $Fe^{2+}/Fe^{3+}$ ions on magnetically non-equivalent octahedral B sites, Section 4.1.

In the titanomagnetite the spectra have been fitted to 3 sextets.[7] In this case the outer component is assigned to $Fe^{3+}$ ions on the tetrahedral A site, as in pure magnetite, with the second magnetic component attributed to the $Fe^{2+}/Fe^{3+}$ ions on the B site in conflict with the distribution envisaged by Häggström.[3] The third component in the spectrum was attributed to a superposition of components of varying hyperfine fields produced by the substitution of $Ti^{4+}$ onto the B sites. The ideas of Häggström[3] and Tanaka[7] have been combined in this work to produce a fit for the $^{57}Fe$ Mössbauer spectra recorded from tin-doped magnetite consisting of 4 components. The A-sextet was attributed to $Fe^{3+}$ ions on the tetrahedral A sites, as proposed by both Häggström[3] and Tanaka.[7] The second and third components, designated B1 and B2, were attributed to the $Fe^{2+}/Fe^{3+}$ ions on the non-equivalent octahedral B sites undergoing a hopping process as proposed by Häggström.[3] A fourth component, designated as the C-sextet, was attributed to the interaction of the $Sn^{4+}$ ions with the $Fe^{2+}$ and $Fe^{3+}$ ions on the B sites as envisaged by Tanaka.[7]

Fitting the spectra according to the above procedure gave the Mössbauer parameters collected in Table 4.7. The results showed that the introduction of $Sn^{4+}$ ions into the magnetite structure causes a reduction in the hyperfine field for each component. This effect has also been observed in the titanomagnetites.[7,8]

| x | A Sextet | | | B1 Sextet | | | B2 Sextet | | | C Sextet | | |
|---|---|---|---|---|---|---|---|---|---|---|---|---|
| | δ/mms$^{-1}$ ±0.03 | Δ/mms$^{-1}$ ±0.05 | H/Tesla ±0.2 | δ/mms$^{-1}$ ±0.03 | Δ/mms$^{-1}$ ±0.05 | H/Tesla ±0.2 | δ/mms$^{-1}$ ±0.03 | Δ/mms$^{-1}$ ±0.05 | H/Tesla ±0.2 | δ/mms$^{-1}$ ±0.03 | Δ/mms$^{-1}$ ±0.05 | H/Tesla ±0.2 |
| 0.05 | 0.33 | 0.03 | 50.8 | 0.58 | 0.03 | 47.0 | 0.69 | -0.01 | 46.1 | 0.68 | -0.04 | 42.8 |
| 0.1 | 0.41 | 0.02 | 50.2 | 0.72 | -0.01 | 47.1 | 0.78 | -0.01 | 45.3 | 0.77 | 0.00 | 42.5 |
| 0.2 | 0.39 | 0.03 | 49.5 | 0.69 | -0.03 | 46.8 | 0.82 | -0.03 | 44.3 | 0.84 | 0.01 | 40.5 |
| 0.3 | 0.35 | 0.06 | 46.4 | 0.62 | -0.02 | 43.4 | 0.79 | -0.04 | 40.9 | 0.79 | 0.01 | 37.1 |
| 0.4 | 0.30 | 0.03 | 45.5 | 0.63 | -0.10 | 42.9 | 0.69 | -0.05 | 39.9 | 0.68 | -0.09 | 35.8 |

***Table 4.7 - $^{57}Fe$ Mössbauer parameters for $Fe_{3-x}Sn_xO_4$ recorded at 298K***

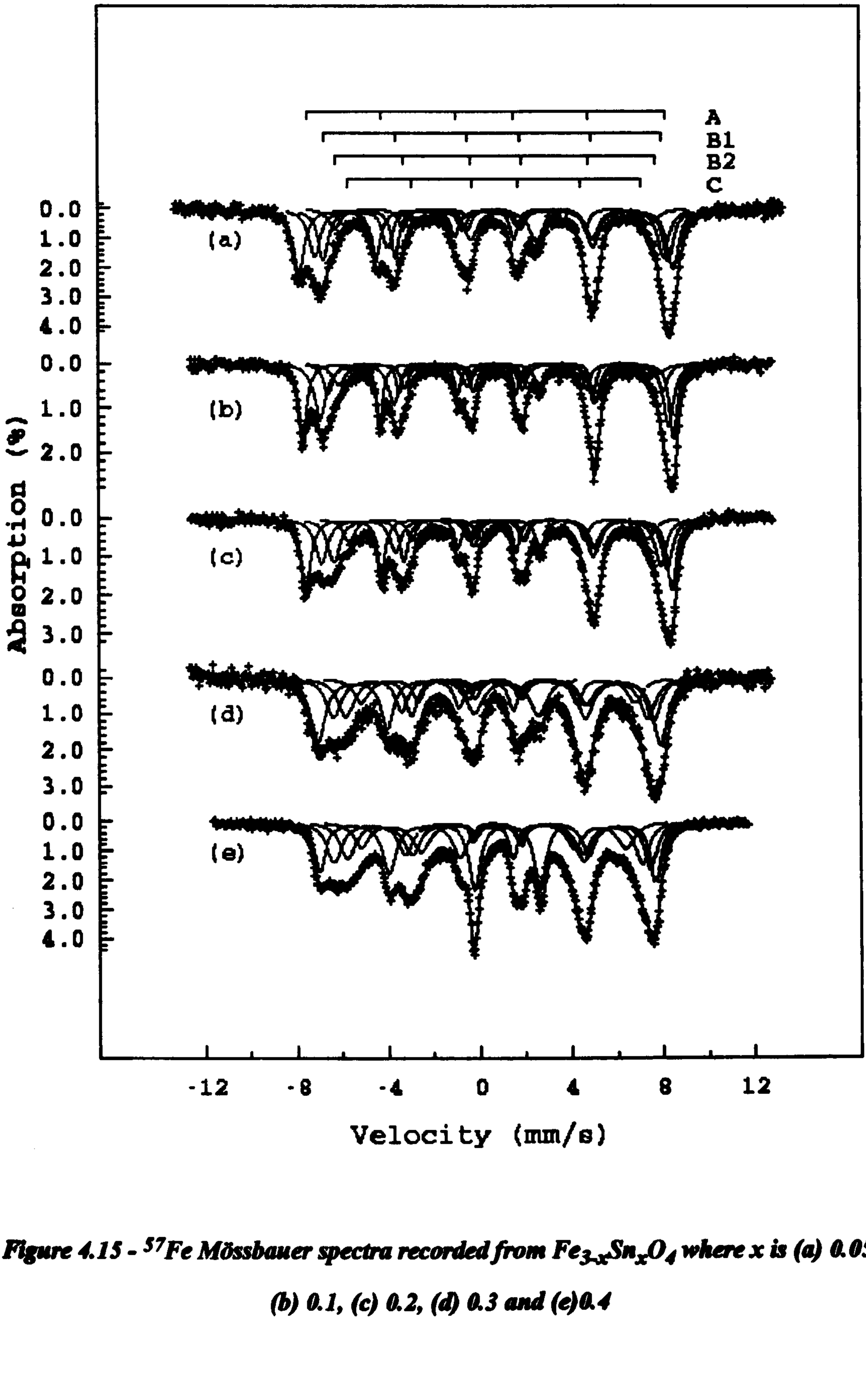


***Figure 4.15 - $^{57}Fe$ Mössbauer spectra recorded from $Fe_{3-x}Sn_xO_4$ where x is (a) 0.05, (b) 0.1, (c) 0.2, (d) 0.3 and (e)0.4***

The introduction of $Sn^{4+}$ ions into the $Fe_3O_4$ structure requires the maintenance of charge balance according to the relationship $2Fe^{3+} = Sn^{4+} + Fe^{2+}$ as suggested by the analogy with titanium-doped magnetite, Section 4.2.2. The reduction of $Fe^{3+}$ to $Fe^{2+}$ on introduction of $Sn^{4+}$ was established by XPS of tin-doped magnetite, Section 4.2.4. The change in the oxidation states of iron would be expected to have an effect on the ratio of the B site component to the A site component (B/A ratio) in the $^{57}Fe$ Mössbauer spectrum. In $Fe_3O_4$ the B/A ratio is 2 and on substituting $Sn^{4+}$ for B site $Fe^{3+}$ ions it would be expected that the B/A ratio would decrease. On examination of the $^{57}Fe$ Mössbauer spectra recorded from the tin-doped magnetite samples it was observed that the opposite was true, with an increase to 2.7 for the x = 0.2 sample, Table 4.8.

| x | B/A |
|---|---|
| 0.00 | 2.0 |
| 0.05 | 2.1 |
| 0.10 | 2.2 |
| 0.20 | 2.7 |

***Table 4.8 - B/A ratio for $Fe_{3-x}Sn_xO_4$ where $0 \leq x \leq 0.2$***

Maintenance of charge balance can occur through two routes a) the reduction of $Fe^{3+}$ to $Fe^{2+}$ on both the A and B sites[7,23] or b) reduction of $Fe^{3+}$ to $Fe^{2+}$ could be restricted to the B site only.[24] To envisage what the effects of a and b would be on the $^{57}Fe$ Mössbauer spectrum these effects have to be considered along with two possible magnetic interactions involving the A and B sites, i) a dominating magnetic hyperfine interaction (A-A or B-B interactions) inside the sublattices or ii) inter lattice interactions (A-B interactions). Combining these effects gives four possibilities, a-i, a-ii, b-i or b-ii which could explain the increase in the B/A ratio.

The a-i interaction would allow both ferrous and ferric ions on the A site. The ferrous component of the A site may then move into the area of the $^{57}Fe$ Mössbauer spectrum designated as the B site as this component would have a smaller hyperfine field than the

ferric component. This would explain the increase in the B/A ratio but it is possible that the sublattice interactions may not leave the A site component as sharp as has been observed. The a-ii interaction would mean that the field experienced by the ferric and the ferrous ions on the A site would be strongly dependent on the tin ion distribution on the B site. This interaction would probably cause broadening of the A site component and so this situation does not explain the observed increase in B/A ratio. The b-i interaction would not involve any change to the A site and the internal sublattice interactions would have a minimal effect on the spectrum and therefore this proposal may be less valid. Finally, the b-ii interaction may cause movement in the peak positions of the spectrum due to the ferric ions on the A site to the area of the spectrum designated as the B site as the ferric ions would experience a smaller hyperfine field due to the strong A-B interaction. This would produce a very similar spectrum to that produced by the a-i interaction, the only difference would be that the isomer shift of the ferrous and ferric components shifted onto the B site would differ. There is no conclusive evidence at the moment to distinguish between these two strong possibilities. It is envisaged that applied field Mössbauer spectroscopy may distinguish these two components and this will be the subject of subsequent study.

#### 4.2.5.2 $^{119}$Sn Mössbauer spectra recorded at 298K

The $^{119}$Sn Mössbauer spectrum recorded from $Fe_{2.9}Sn_{0.1}O_4$, Figure 4.16, showed a sextet pattern with a hyperfine field of 20.9T. As the level of tin in the magnetite structure was increased the internal hyperfine field decreased, to 18.8T for $Fe_{2.8}Sn_{0.2}O_4$. The magnetic field observed at the tin site occurs through a supertransfer of electron spin from the $Fe^{3+}$ ions on the tetrahedral A sites via oxygen to the $Sn^{4+}$ ions on the octahedral B sites by a superexchange mechanism.

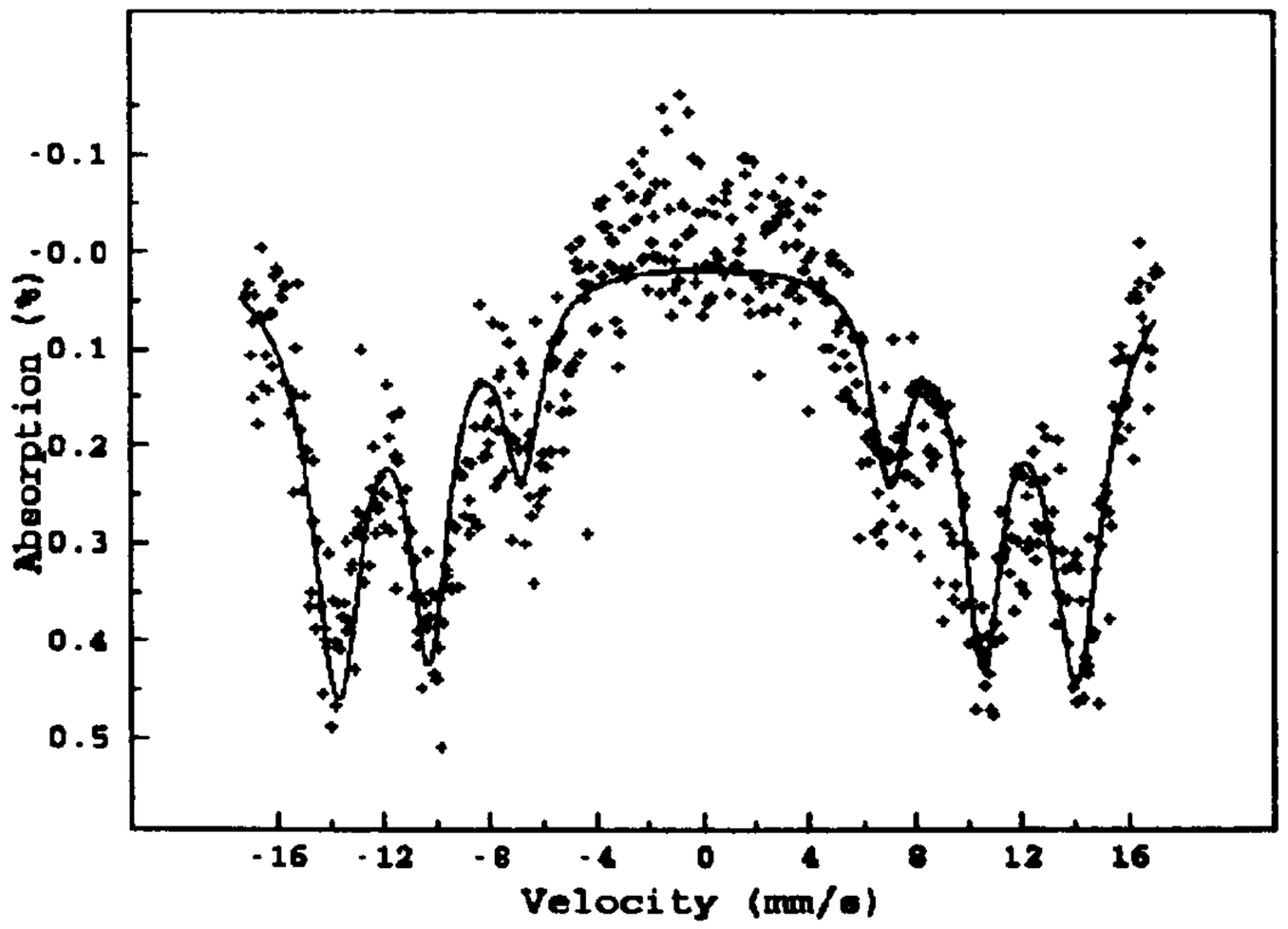


***Figure 4.16 - $^{119}Sn$ Mössbauer spectrum of $Fe_{2.9}Sn_{0.1}O_4$***

The lines in the $^{119}Sn$ Mössbauer spectra were seen to broaden considerably as the tin content increased to x = 0.3, Figure 4.17. The broadening of the spectra may be associated with a superposition of components of varying hyperfine field resulting from variations in the distribution of $Sn^{4+}$ throughout the B sites. As can be seen from Figure 4.17 the hyperfine field decreased as the tin content increased, Table 4.9, presumably because of a weakening of the Fe-O-Sn interaction.

| x | B / Tesla (±0.2) |
|---|---|
| 0.05 | 21.1 |
| 0.10 | 19.0 |
| 0.20 | 18.8 |
| 0.30 | 16.2 |

***Table 4.9 - Hyperfine field data determined from $^{119}Sn$ Mössbauer spectra recorded from $Fe_{3-x}Sn_xO_4$***

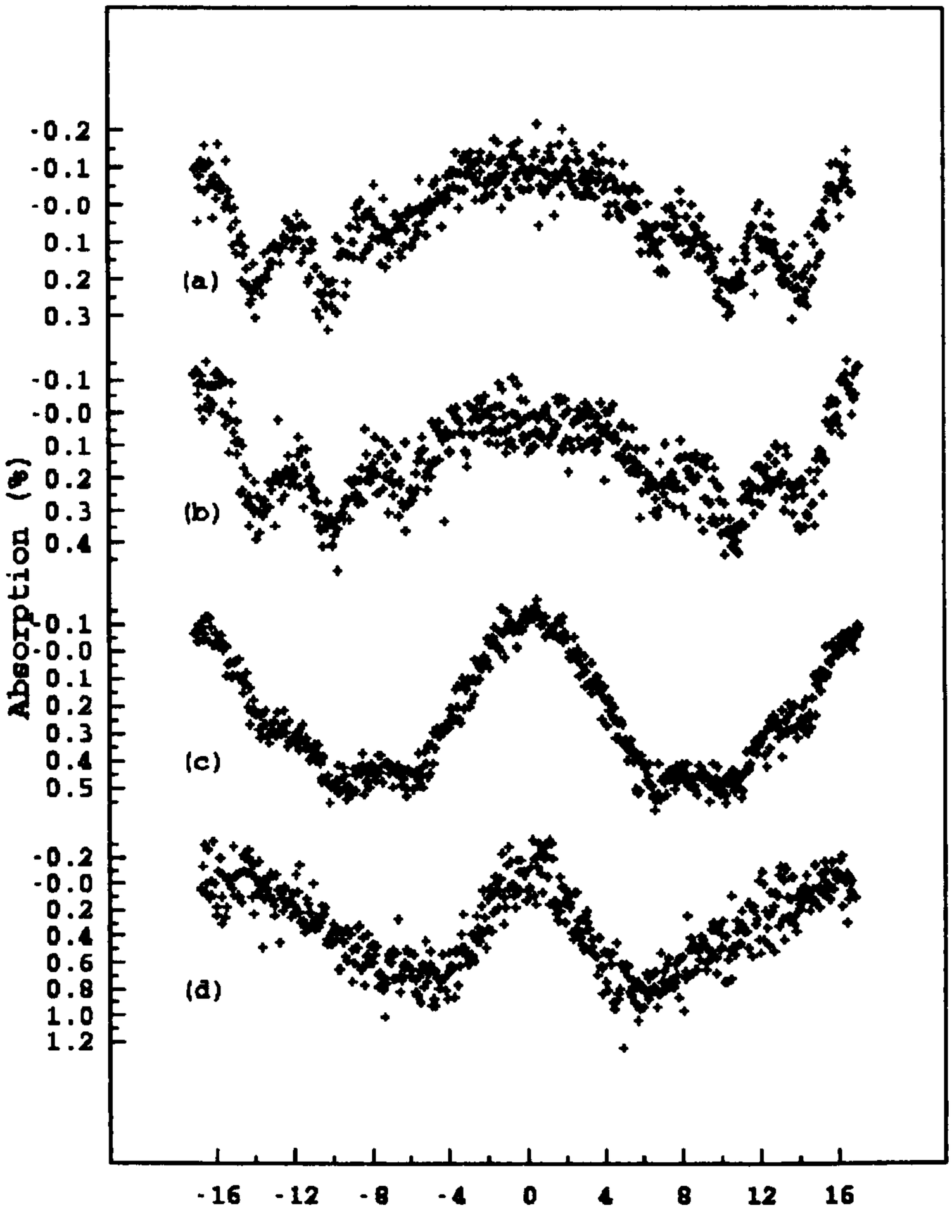


***Figure 4.17 - $^{119}Sn$ Mössbauer spectra recorded at 298K from $Fe_{3-x}Sn_xO_4$ where $x$ = (a) 0.05, (b) 0.1, (c) 0.2 and (d) 0.3***

#### 4.2.5.3 $^{57}$Fe Mössbauer spectra recorded at high temperature *in vacuo*

To establish the behaviour of $Fe_{3-x}Sn_xO_4$ at elevated temperatures *in vacuo* $^{57}$Fe Mössbauer spectra were recorded from samples of $Fe_{3-x}Sn_xO_4$ ($0.05 \leq x \leq 0.3$). The oxygen partial pressure in the evacuated furnace was estimated to be $10^{-6}$-$10^{-7}$ atm. $Fe_{3-x}Sn_xO_4$, $x = 0.1$, was heated to 480K over nine hours, the spectra being recorded *in situ*, then to 750K over nine hours, the spectra being recorded *in situ* and then to 770K, 780K and 790K each step over 9 hours and the Mössbauer spectra being recorded *in situ*.

In $Fe_{2.9}Sn_{0.1}O_4$ as the temperature was increased the magnetic hyperfine fields of the 4 magnetic components were seen to decrease, Figure 4.18.

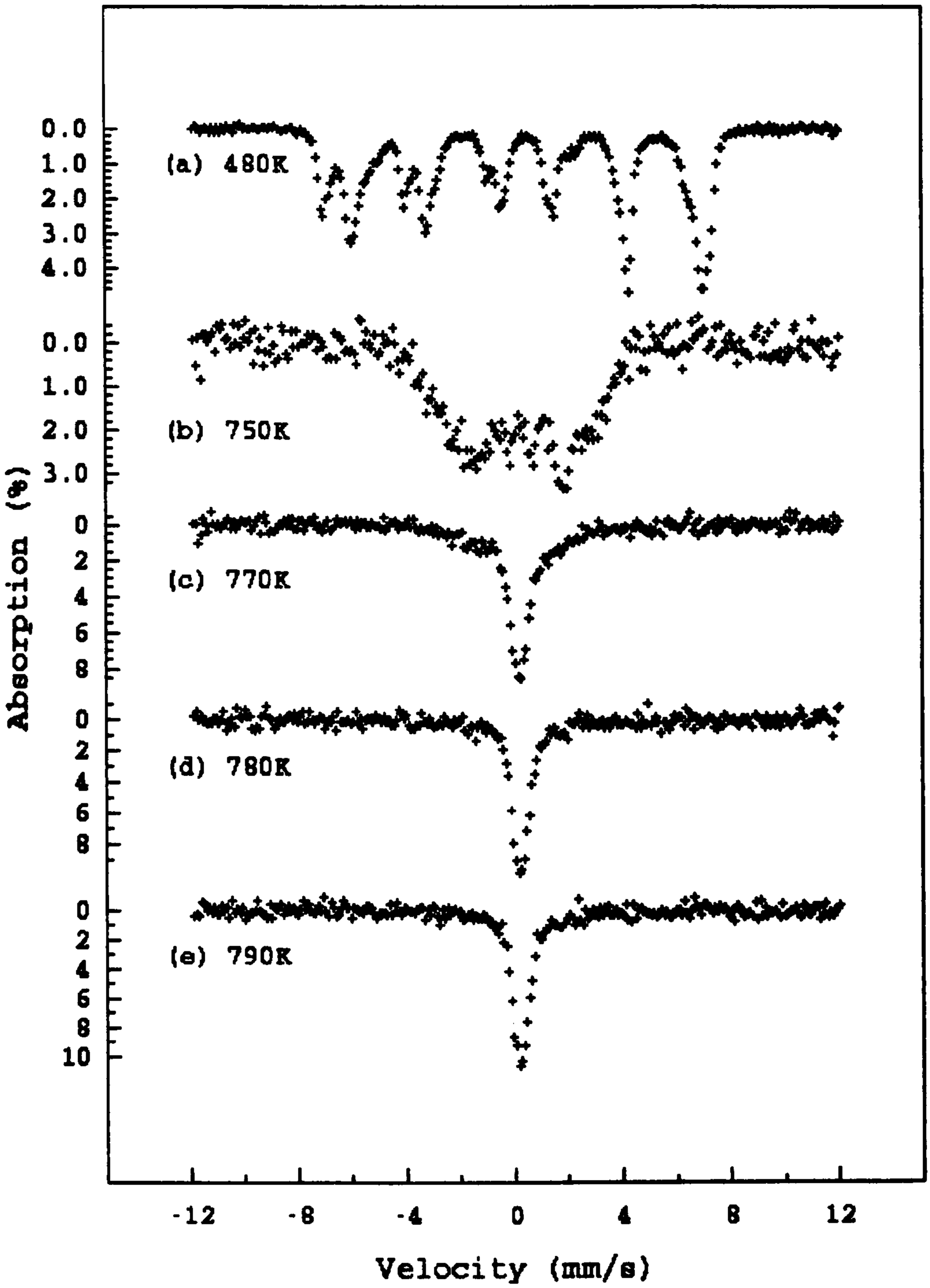


***Figure 4.18 - $^{57}Fe$ Mössbauer spectra recorded* in situ *from $Fe_{2.9}Sn_{0.1}O_4$ at (a) 480K, (b) 750K, (c) 770K, (d) 780K and (e) 790K in vacuo***

From Figure 4.18 it can be seen that the main change in the spectrum occurs between 750K and 770K. Closer inspection of the spectrum recorded at 770K indicated that there is still some magnetic character in the material at this temperature. Further heating to 780K caused this magnetic component to collapse completely. This allowed the Curie temperature to be determined as 770±15K. Using the relationship[3] $B(T) = B_0(1-T/T_c)^{\beta}$ where $\beta = 0.3$ and $B_0$ = the size of the hyperfine field at 0K, allowed the interval to be narrowed to 10K, and the $T_c$ was determined as 770±5K, 70K lower than for pure $Fe_3O_4$, Figure 4.19. Continued heating of the sample to higher temperatures did not induce any further change in the spectrum recorded *in situ*. The sharpness of the transition to the paramagnetic phase endorses the XRD findings that the sample is monophasic.

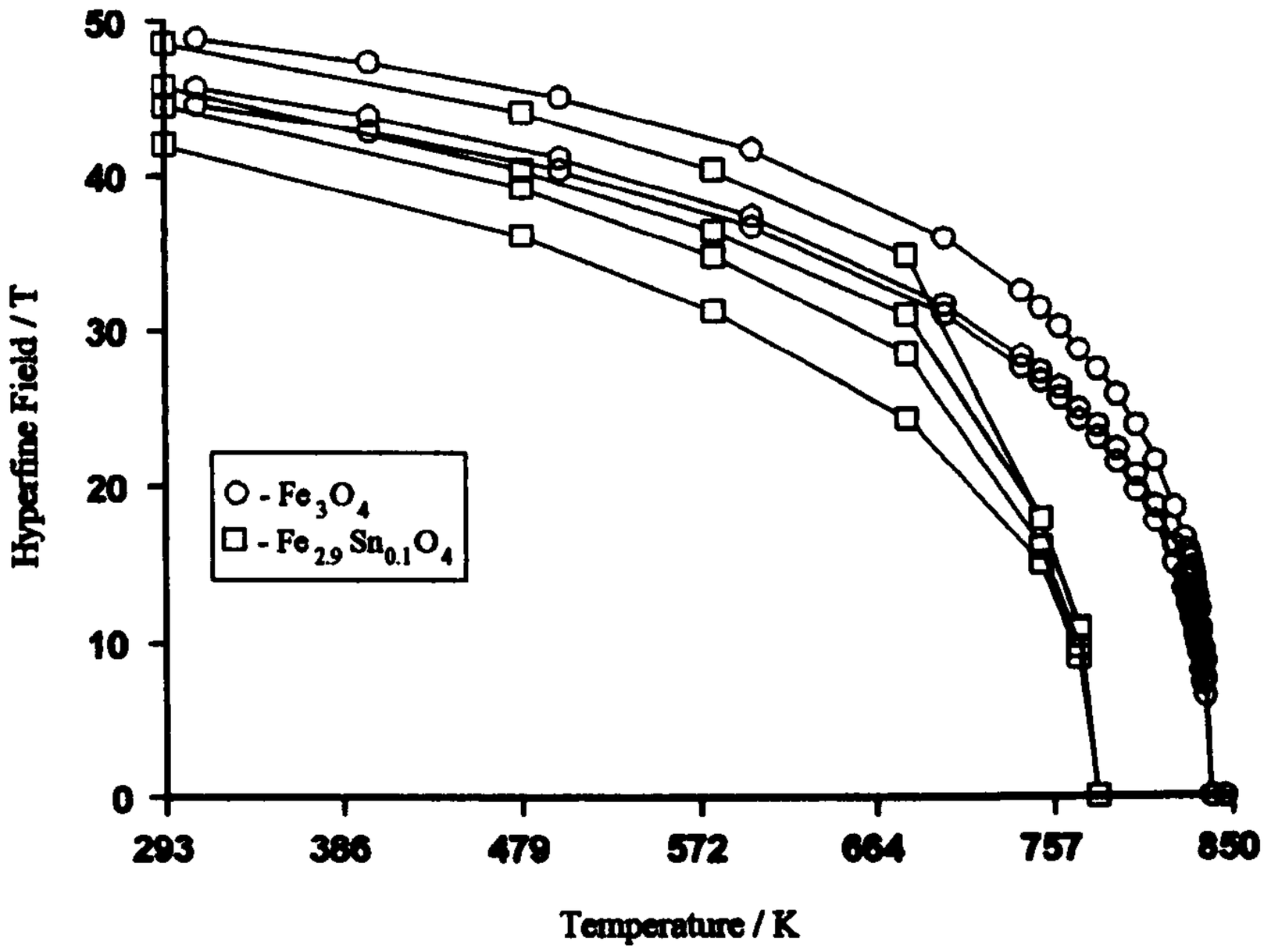


***Figure 4.19 - Plot of Hyperfine field vs Temperature indicating the lowering of Curie temperature with increased tin content. Each temperature is represented by three ($Fe_3O_4$) or four ($Fe_{2.9}Sn_{0.1}O_4$) components corresponding to the magnetic components present in the $^{57}Fe$ Mössbauer spectra***

For $Fe_{2.95}Sn_{0.05}O_4$ , Figure 4.20, a decrease of about 40K in $T_c$ to 800K was observed, Table 4.10. The $^{57}Fe$ Mössbauer spectra recorded from the x = 0.2, 0.3

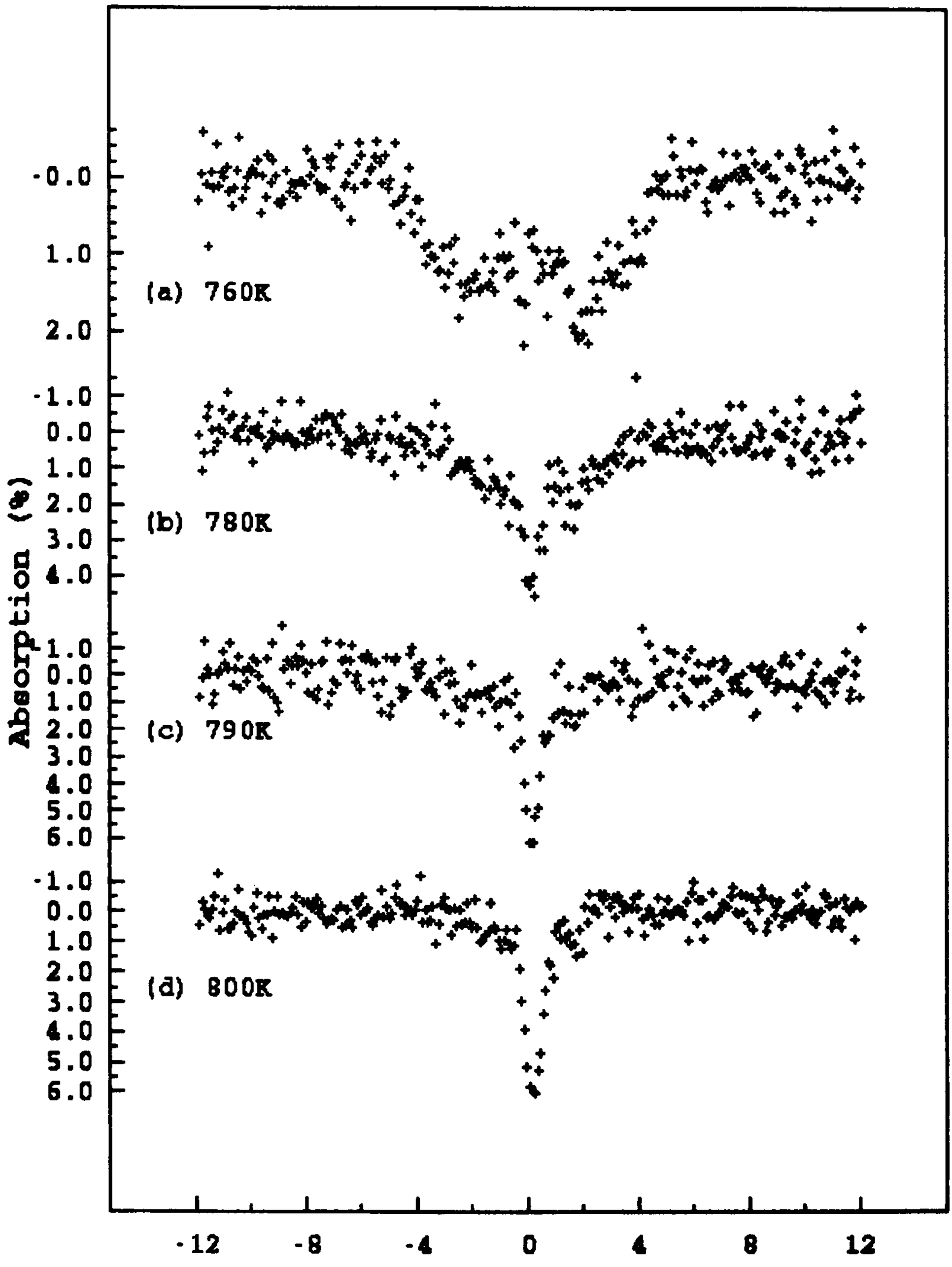


***Figure 4.20 - $^{57}Fe$ Mössbauer spectra recorded* in situ *from $Fe_{2.99}Sn_{0.05}O_4$ at (a) 760K, (b) 780K, (c) 790K and (d) 800K in vacuo***

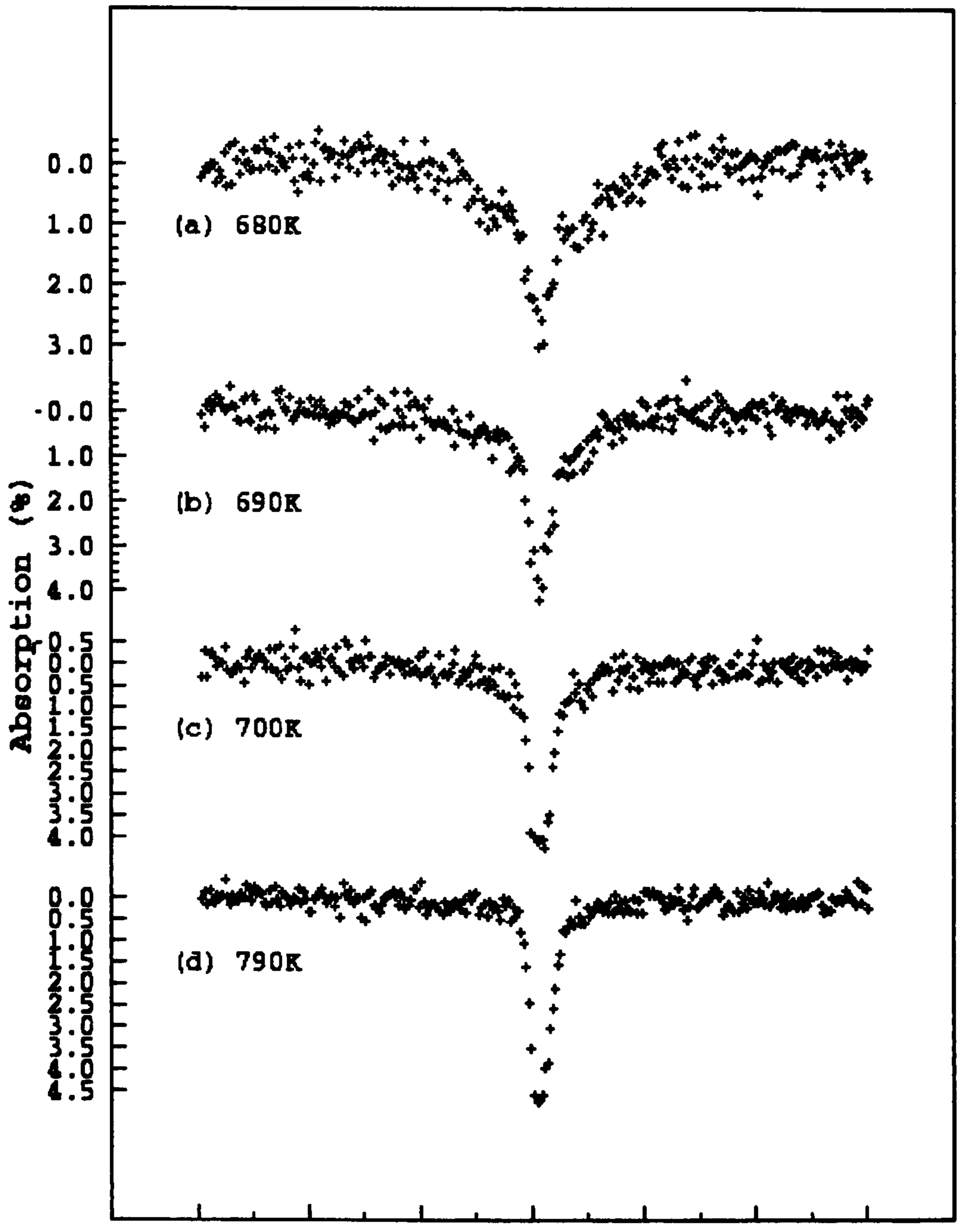


***Figure 4.21 - $^{57}Fe$ Mössbauer spectra recorded in situ from $Fe_{2.8}Sn_{0.2}O_4$ at (a) 680K, (b) 690K, (c) 700K and (d) 790K in vacuo***

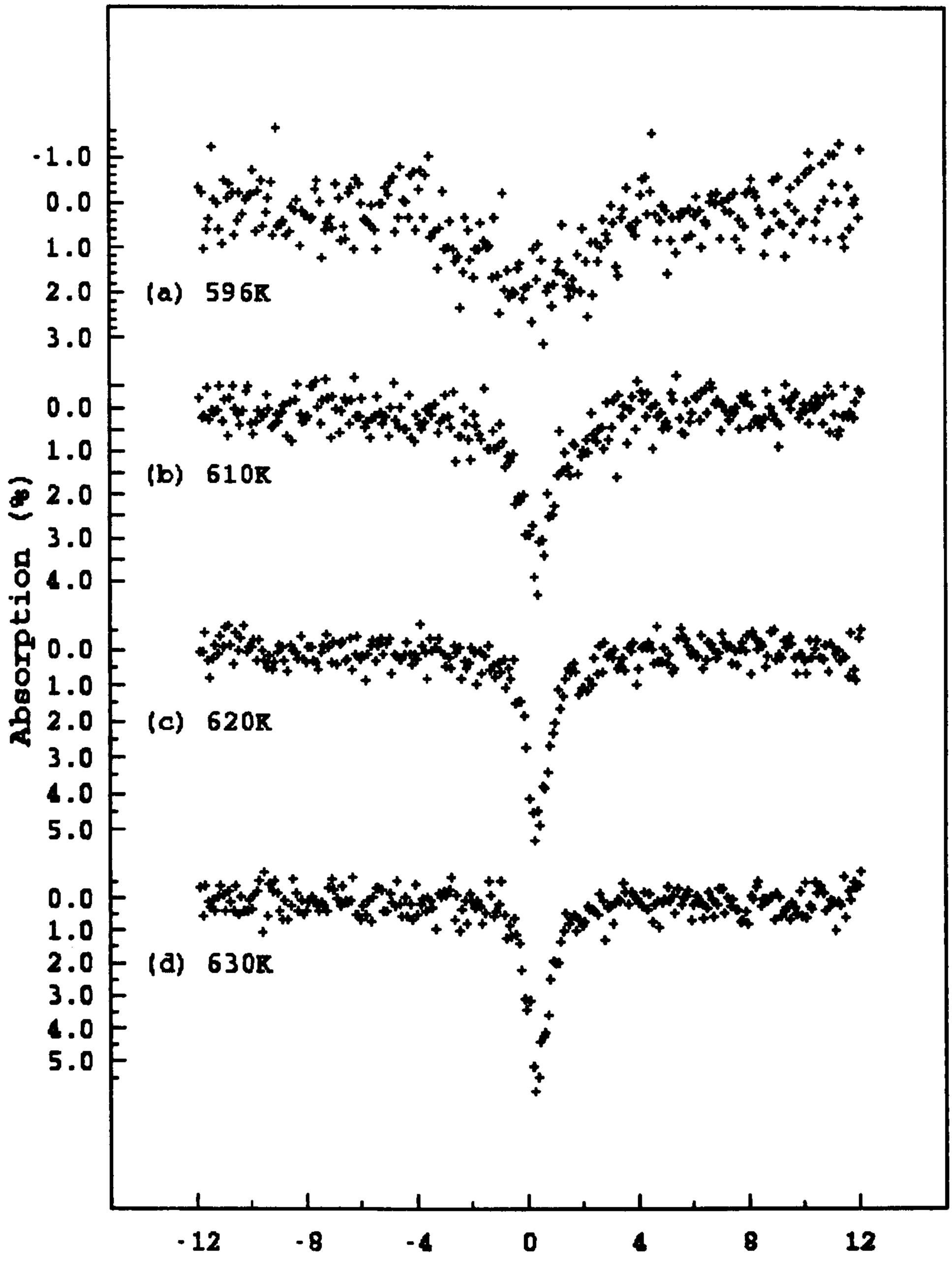


***Figure 4.22 - $^{57}Fe$ Mössbauer spectra recorded in situ from $Fe_{2.7}Sn_{0.3}O_4$ at (a) 596K, (b) 610K, (c) 620K and (d) 630K in vacuo***

samples are shown in Figures 4.21 and 4.22. A continued decrease in the $T_c$ was observed with increasing tin content, Table 4.11, and a plot of $T_c$ versus dopant concentration, Figure 4.23, indicated that the decrease was nearly linear.

| x | $T_o$ / K |
|---|---|
| 0.05 | 800 ± 5 |
| 0.10 | 770 ± 5 |
| 0.20 | 690 ± 5 |
| 0.30 | 630 ± 5 |

*Table 4.11 - Curie temperatures for $Fe_{3-x}Sn_xO_4$*

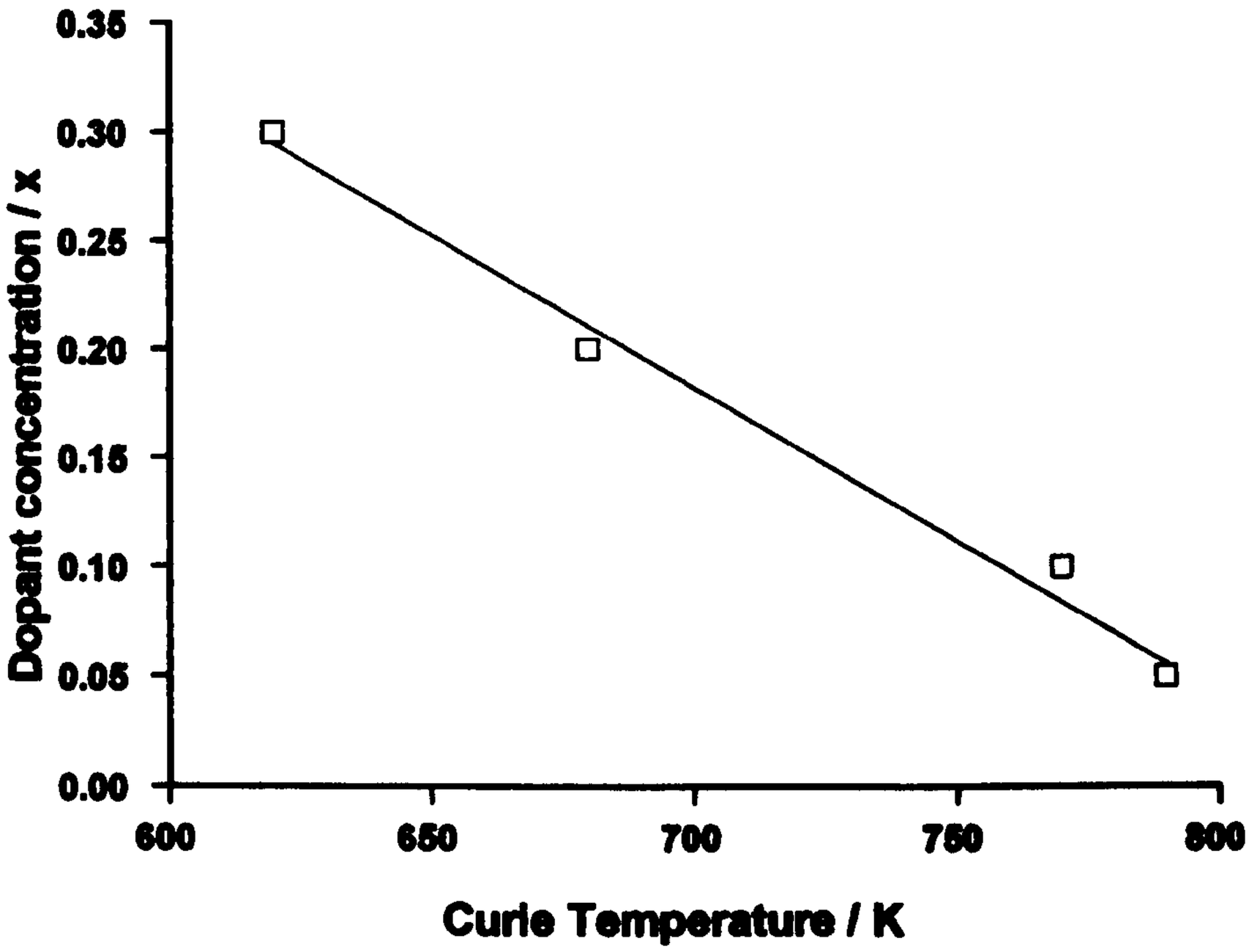


*Figure 4.23 - Variation of Curie temperature with tin content*

The slight deviation from linearity is indicative of compositional variations as indicated by EDX, Section 4.2.1. The observed depression of the Curie temperature in the tin-doped magnetite as compared to that in $Fe_3O_4$ was greater than the observed reduction in the Curie temperature for titanomagnetite.[25] The high Curie temperature in $Fe_3O_4$ has been[26] attributed to a strong interaction between the $Fe^{3+}$ ions on the A site and the $Fe^{3+}$ ions on the B site. Therefore introducing the $Sn^{4+}$ ions into the B sites is likely to weaken this interaction and hence cause a gradual lowering of $T_c$ as x is increased. The

introduction of $Sn^{4+}$ ions effectively reduces the $Fe^{3+}$ ion concentration on the B site through the substitution $2Fe^{3+} = Sn^{4+} + Fe^{2+}$ which is necessary to maintain charge balance. The reduction of $Fe^{3+}$ ion concentration will therefore weaken the A-B interaction. It is also possible that the substitution of $Sn^{4+}$ ions may produce $Fe^{2+}$ ions on the A site which would also weaken the A-B interaction further.

The $^{57}Fe$ Mössbauer spectra initially recorded *in situ* every 6 hours from $Fe_{2.9}Sn_{0.1}O_4$ heated at 760K *in vacuo*, Figure 4.24, showed that the outer components, A and B1, indicative of pure magnetite had increased in intensity whereas the B2 and C components had decreased in intensity. The $^{57}Fe$ Mössbauer spectrum recorded *in situ* from $Fe_{2.9}Sn_{0.1}O_4$ heated at 775K, Figure 4.25g, showed that the magnetic components in the spectrum had hyperfine fields of 25.8T and 21.4T for the A and B sites respectively. The Curie temperature for this material was determined as 770K, Section 4.2.5.3, and it would therefore be reasonable to expect that the Mössbauer spectrum would consist of a doublet component attributed to paramagnetic tin-doped magnetite. It was also observed that the values of the hyperfine fields in this spectrum were the same as those derived from the $^{57}Fe$ Mössbauer spectrum recorded from pure $Fe_3O_4$ at 790K. The result suggests that $Fe_{2.9}Sn_{0.1}O_4$, after heating *in vacuo* at elevated temperatures, contains less tin than the initial sample. This suggests that exsolution of $SnO_2$ leaving a nearly pure $Fe_3O_4$ phase, represented by the magnetic components, occurs. The remaining tin-doped magnetite represented by the doublet, Figure 4.25g, was paramagnetic with a $T_c$ above that of $Fe_{2.9}Sn_{0.1}O_4$ and coexisted with $Fe_3O_4$ with a lower tin content.

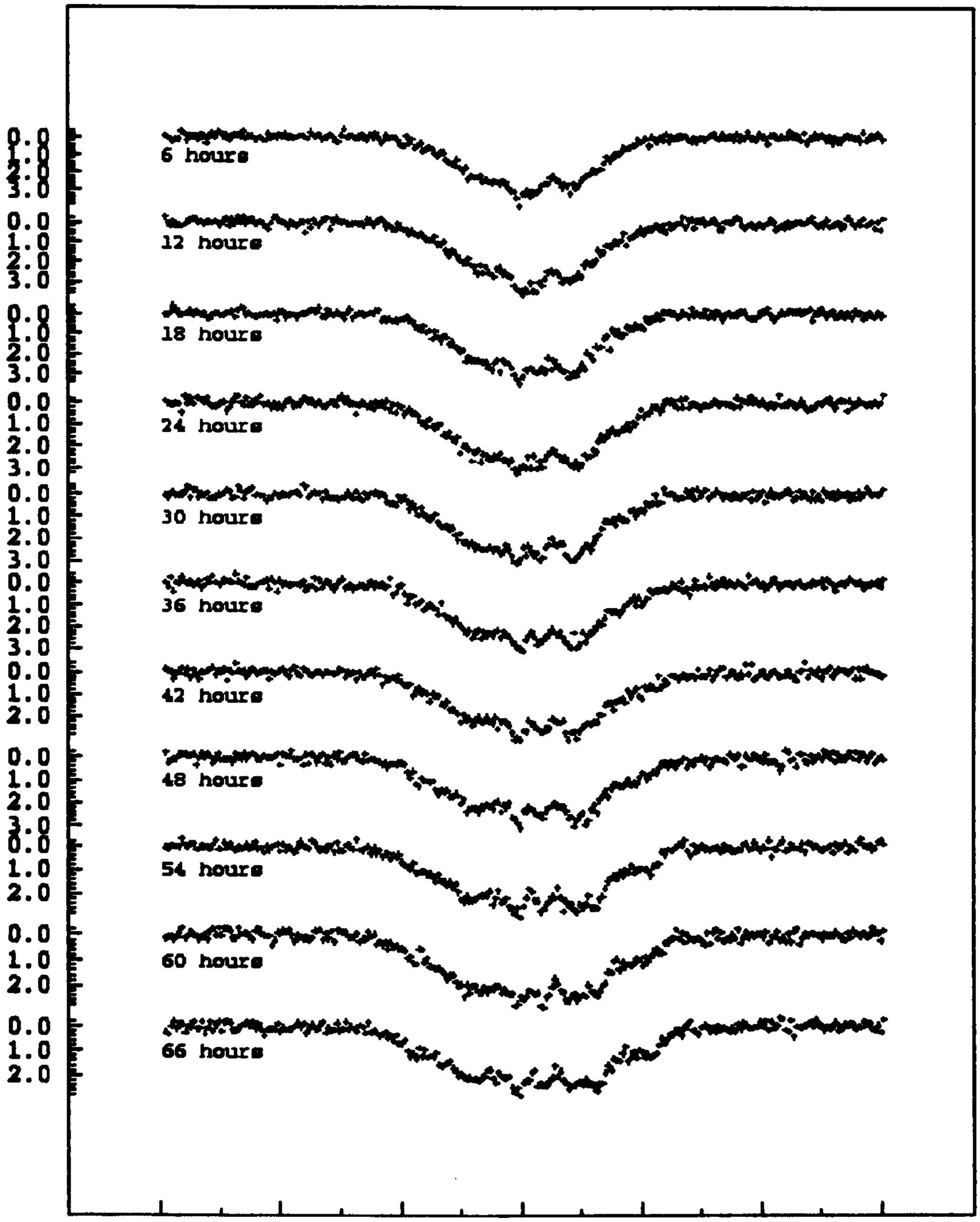


***Figure 4.24 - $^{57}Fe$ Mössbauer spectra recorded* in situ *from $Fe_{2.9}Sn_{0.1}O_4$ every 6 hours at 760K* in vacuo**

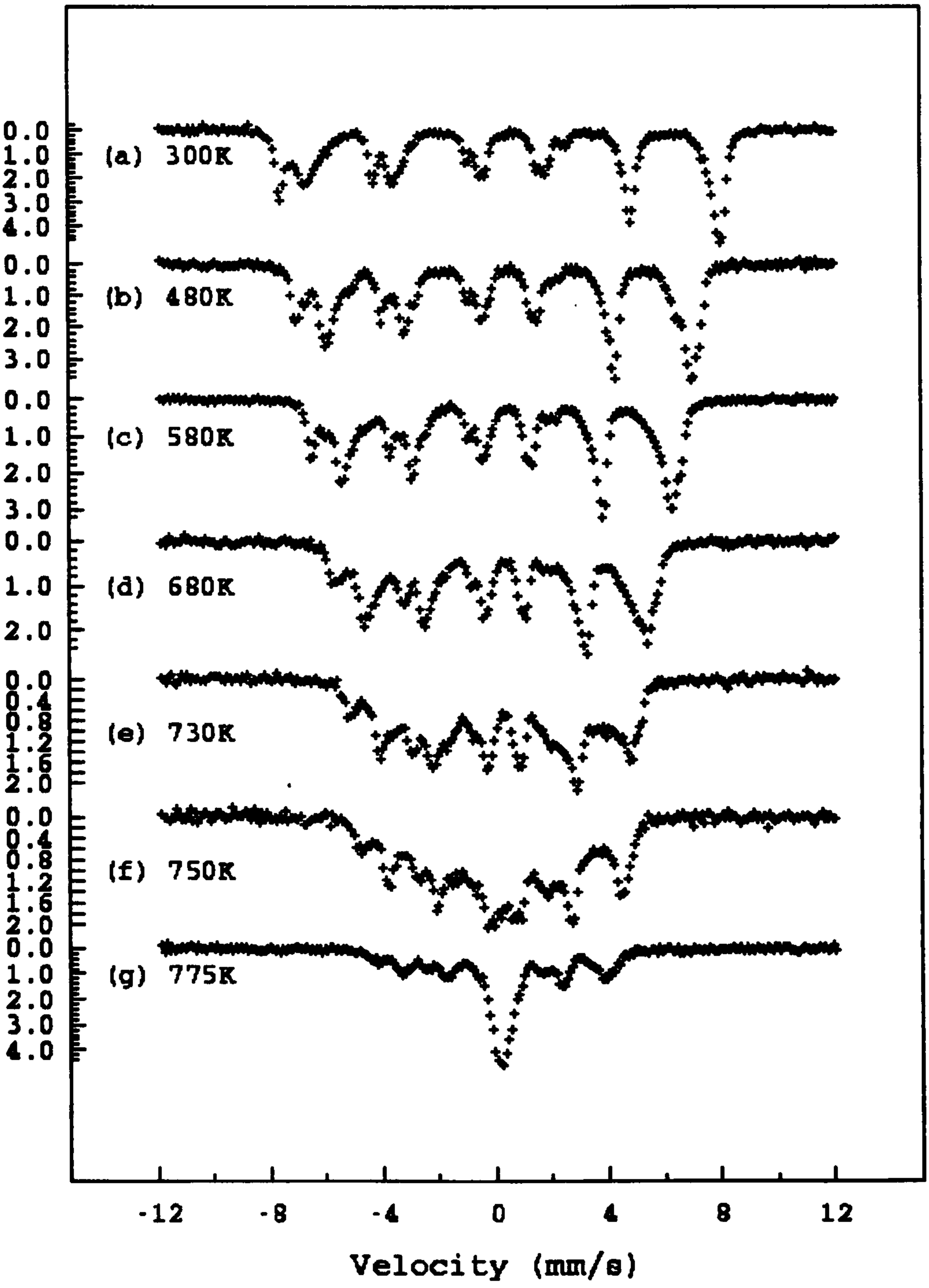


***Figure 4.25 - $^{57}Fe$ Mössbauer spectra recorded* in situ *at temperatures up to 775K from $Fe_{2.9}Sn_{0.1}O_4$***

The $^{57}Fe$ Mössbauer spectrum recorded from $Fe_{2.9}Sn_{0.1}O_4$ at 300K, Figure 4.26, after heating to 780K clearly indicated the formation of nearly pure magnetite as evidenced by the increase in the intensity of the outer peaks of the Mössbauer spectrum. The $^{119}Sn$

Mössbauer spectrum of the same sample, Figure 4.27, recorded at 300K consisted of two components. The large single peak was attributed to $SnO_2$ and the small magnetic component was attributed to residual tin-doped magnetite. The presence of the $SnO_2$ component confirmed that exsolution of $SnO_2$ from $Fe_{2.9}Sn_{0.1}O_4$ had occurred.

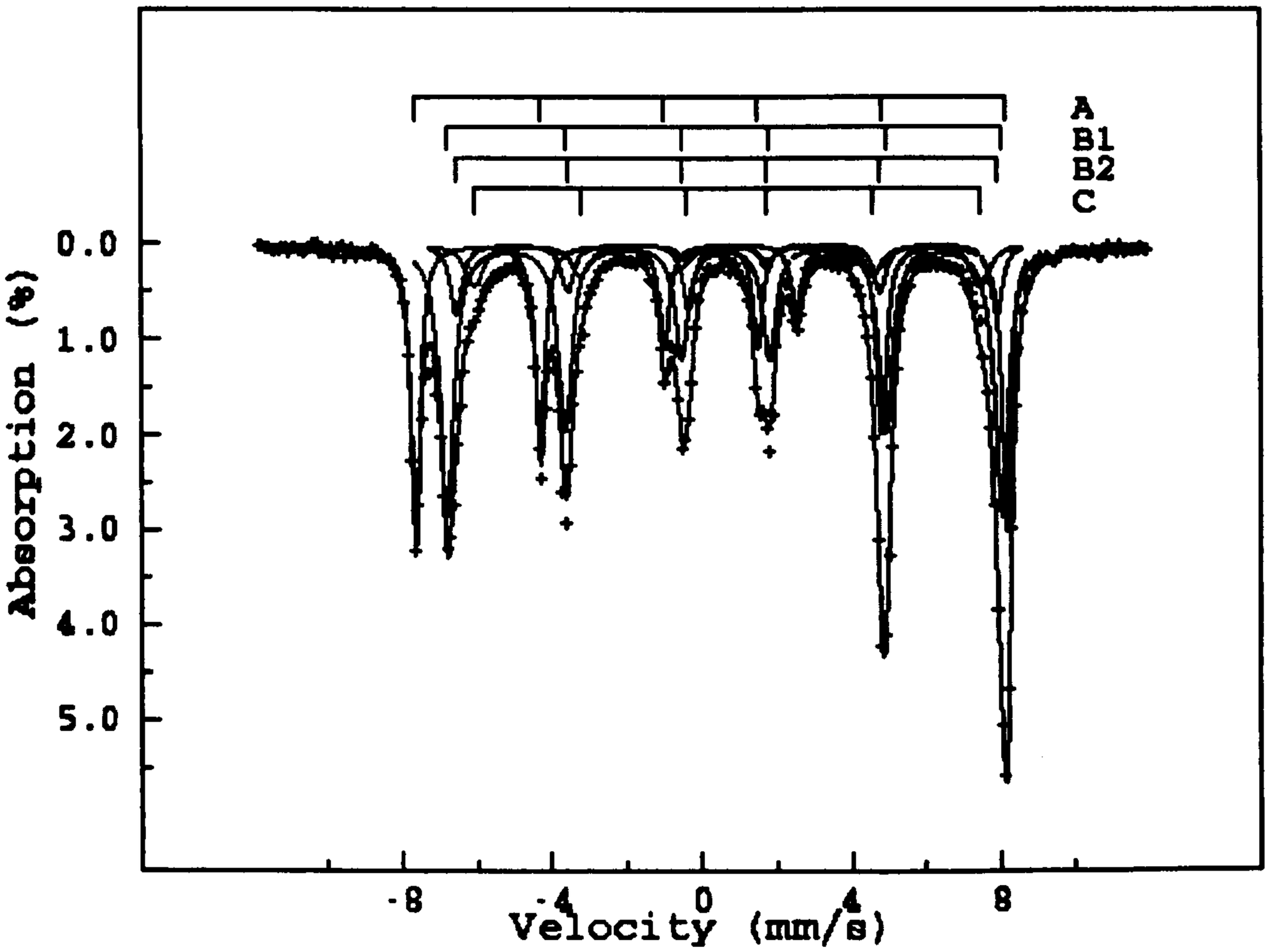


***Figure 4.26 - $^{57}Fe$ Mössbauer spectrum recorded from $Fe_{2.9}Sn_{0.1}O_4$ at 300K after heating to 780K* in vacuo**

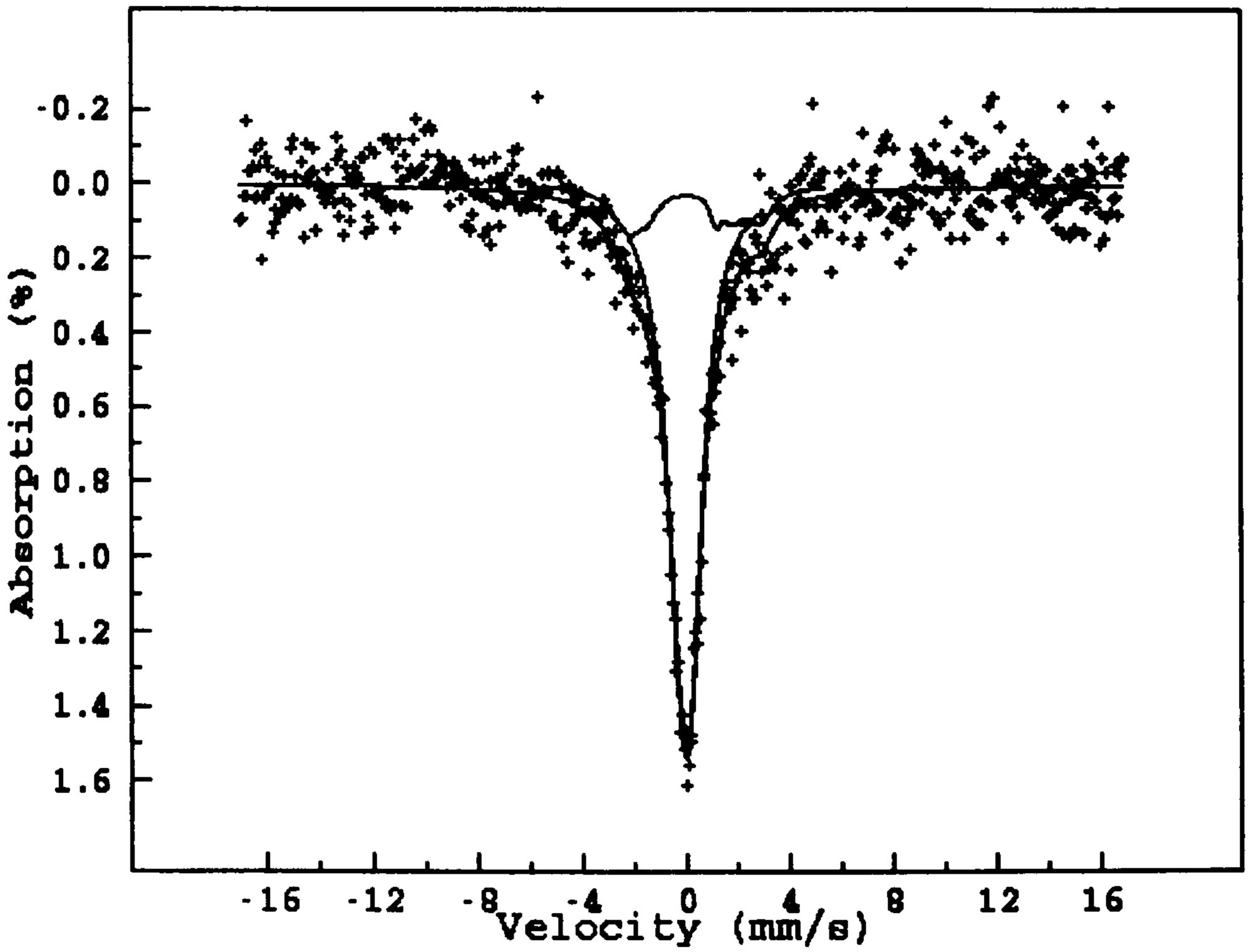


***Figure 4.27 - $^{119}Sn$ Mössbauer spectrum recorded from $Fe_{2.9}Sn_{0.1}O_4$ at 300K after heating to 780K in vacuo***

### 4.2.5.4 $^{57}Fe$ Mössbauer spectra recorded at high temperature in oxidising conditions

A sample of $Fe_{2.9}Sn_{0.1}O_4$ was heated in air at 680K for 21 hours. $^{57}Fe$ Mössbauer spectra were recorded *in situ* every 3 hours to follow the phase transformation. It would be expected that at high temperature in oxidising conditions tin-doped magnetite would be oxidised to tin-doped maghemite as it is known[27, 28] that magnetite is readily oxidised to maghemite. The results of this process as seen from the $^{57}Fe$ Mössbauer spectrum, Figure 4.28, Table 4.12, indicated that after 3 hours the tin-doped magnetite was oxidised to tin-doped maghemite. A second phase was also observed and identified as tin doped-hematite. As the material was heated for a longer period of time the evolution of the maghemite and hematite phase could be followed, Figure 4.28, and it was seen that the hematite component developed more rapidly than the maghemite component, Figure 4.29, Table 4.12.

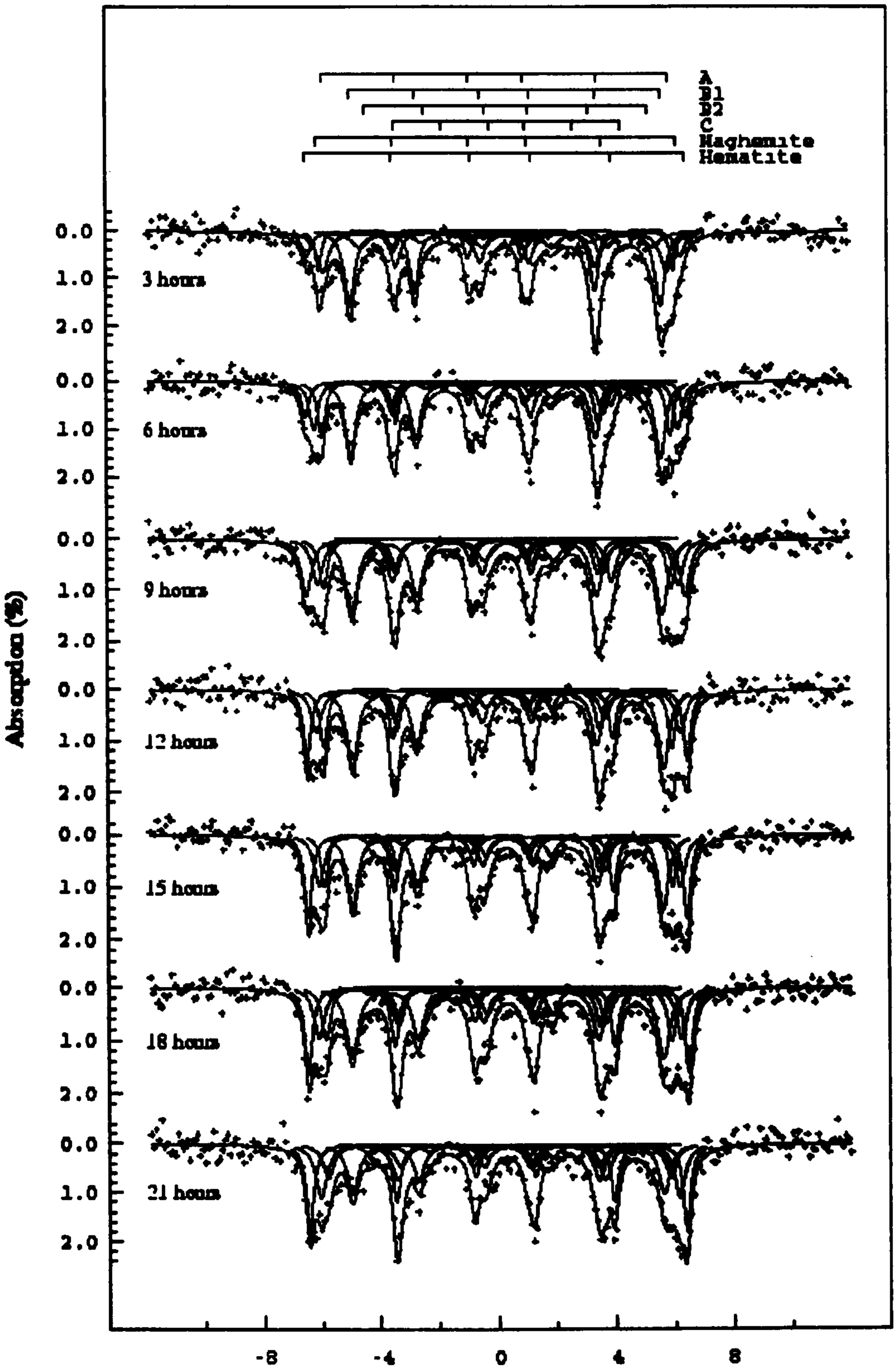


***Figure 4.28 - A sequence of $^{57}Fe$ Mössbauer spectra recorded every 3 hours in situ under oxidising conditions at 680K illustrating oxidation of tin-doped magnetite***

This was taken as further evidence for the oxidation of tin-doped magnetite to tin-doped maghemite followed by a structural transformation to tin-doped hematite.

| Period of oxidation at 680K / hours | Mössbauer Spectral Area (%) Tin-doped magnetite | Tin-doped maghemite | Tin-doped hematite |
|---|---|---|---|
| 3 | 77 | 11 | 12 |
| 6 | 66 | 21 | 14 |
| 9 | 60 | 22 | 27 |
| 12 | 61 | 20 | 24 |
| 15 | 57 | 22 | 27 |
| 18 | 60 | 22 | 29 |
| 21 | 51 | 28 | 30 |

***Table 4.12 - Development of oxidation products of $Fe_{2.9}Sn_{0.1}O_4$ as determined by $^{57}Fe$ Mössbauer Spectroscopy***

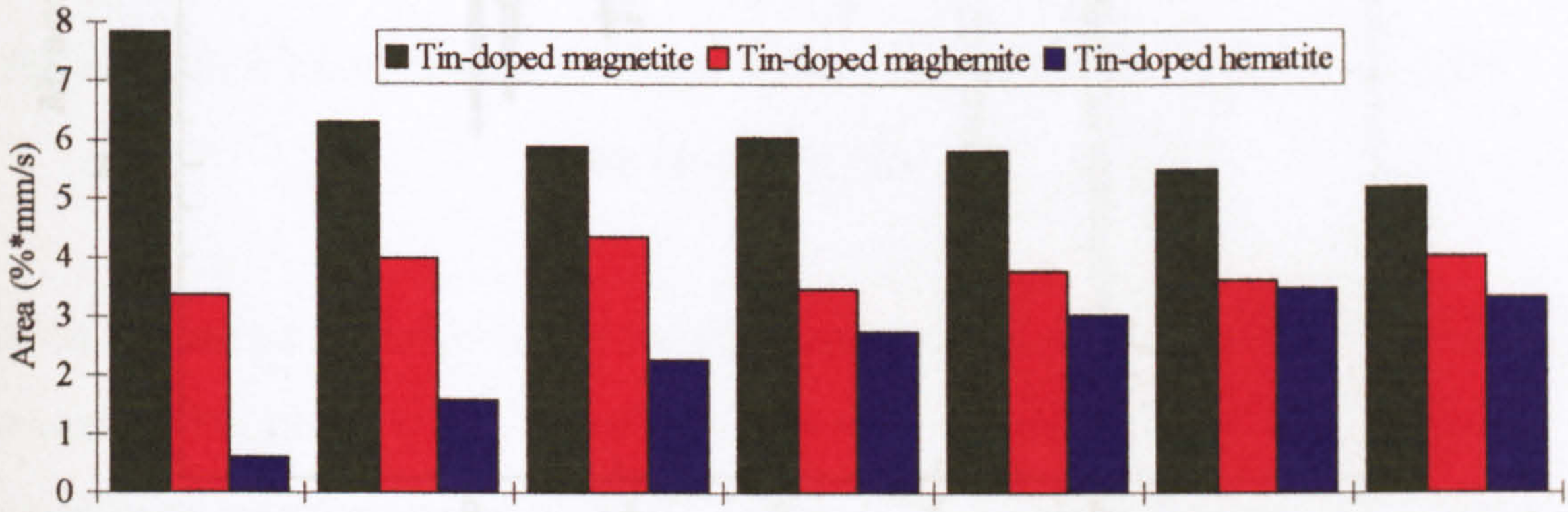


***Figure 4.29 - Development of magnetic components during oxidation***

The $^{57}Fe$ Mössbauer spectrum recorded *in situ* at 630K from $Fe_{2.8}Sn_{0.2}O_4$ after 47 hours of heating under oxidising conditions indicated that very little oxidation had taken place, Figure 4.30. The sample was then heated for 2.5 days at each temperature (580K, 630K and 680K) in an oxidising environment. The $^{57}Fe$ Mössbauer spectrum recorded at 300K after this heating process showed that the spectral area attributed to the oxidation products, tin-doped maghemite and tin-doped hematite, had increased, Figure

4.31. Increasing the temperature to 730K and then to 770K produced further oxidation and transformation of tin-doped-magnetite to tin-doped maghemite and tin-doped hematite, Table 4.13. The development of these components is evident from the $^{57}Fe$ Mössbauer spectrum recorded at 300K, Figure 4.32. It was apparent that the high tin content caused the oxidation/transformation process to be retarded compared to that of $Fe_{2.9}Sn_{0.1}O_4$.

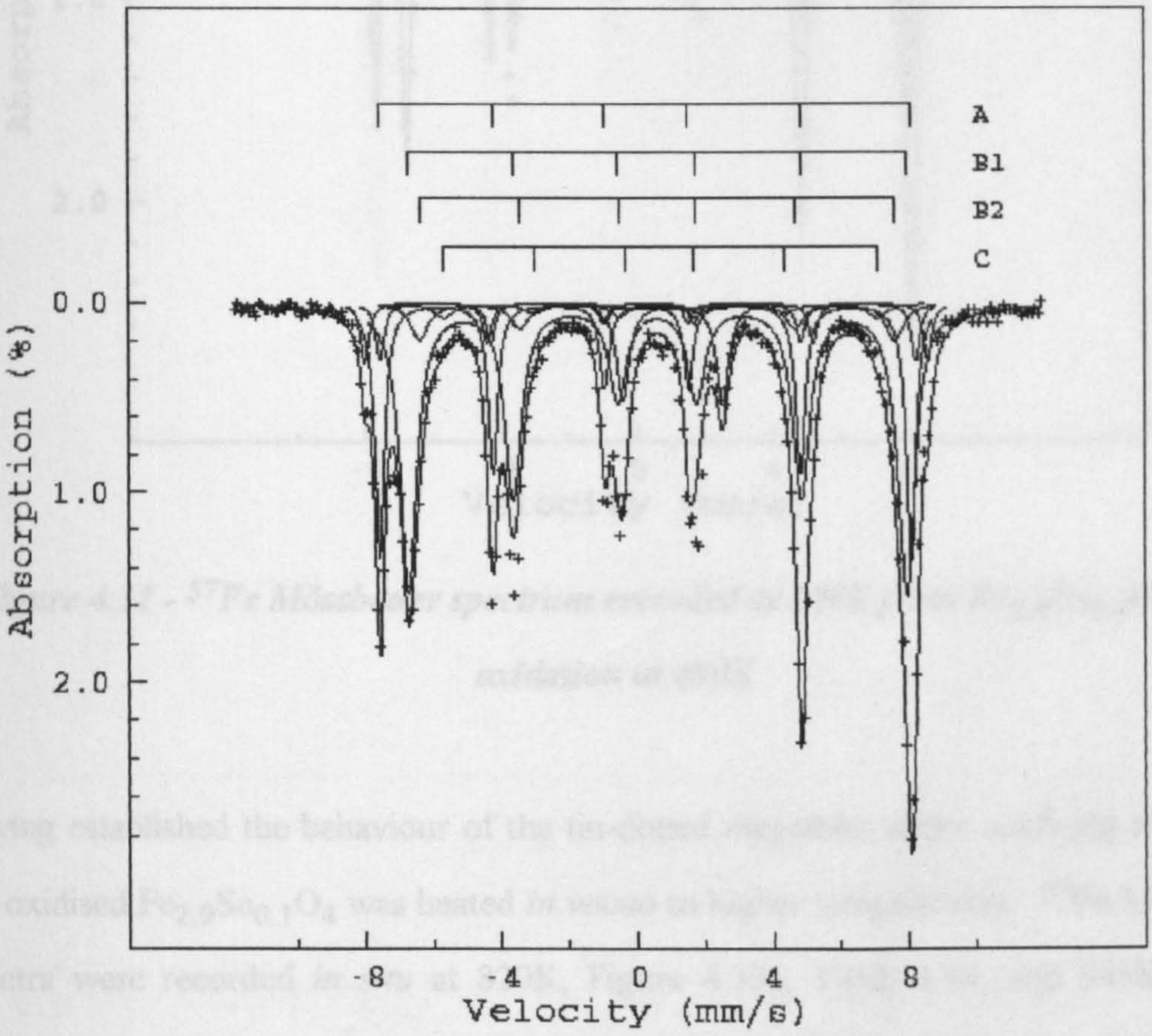


***Figure 4.30 $^{57}Fe$ Mössbauer spectrum recorded from $Fe_{2.8}Sn_{0.2}O_4$ at 300K after oxidation at 630K for 47 hours***

| Temp./K | Mössbauer spectral area / % | | |
|---|---|---|---|
| | Tin-doped magnetite | Tin-doped maghemite | Tin-doped hematite |
| 680 | 77 | 11 | 7 |
| 730 | 62 | 21 | 12 |
| 770 | 43 | 29 | 23 |

***Table 4.13 - Development of oxidation products of $Fe_{2.8}Sn_{0.2}O_4$ as determined by $^{57}Fe$ Mössbauer spectroscopy***

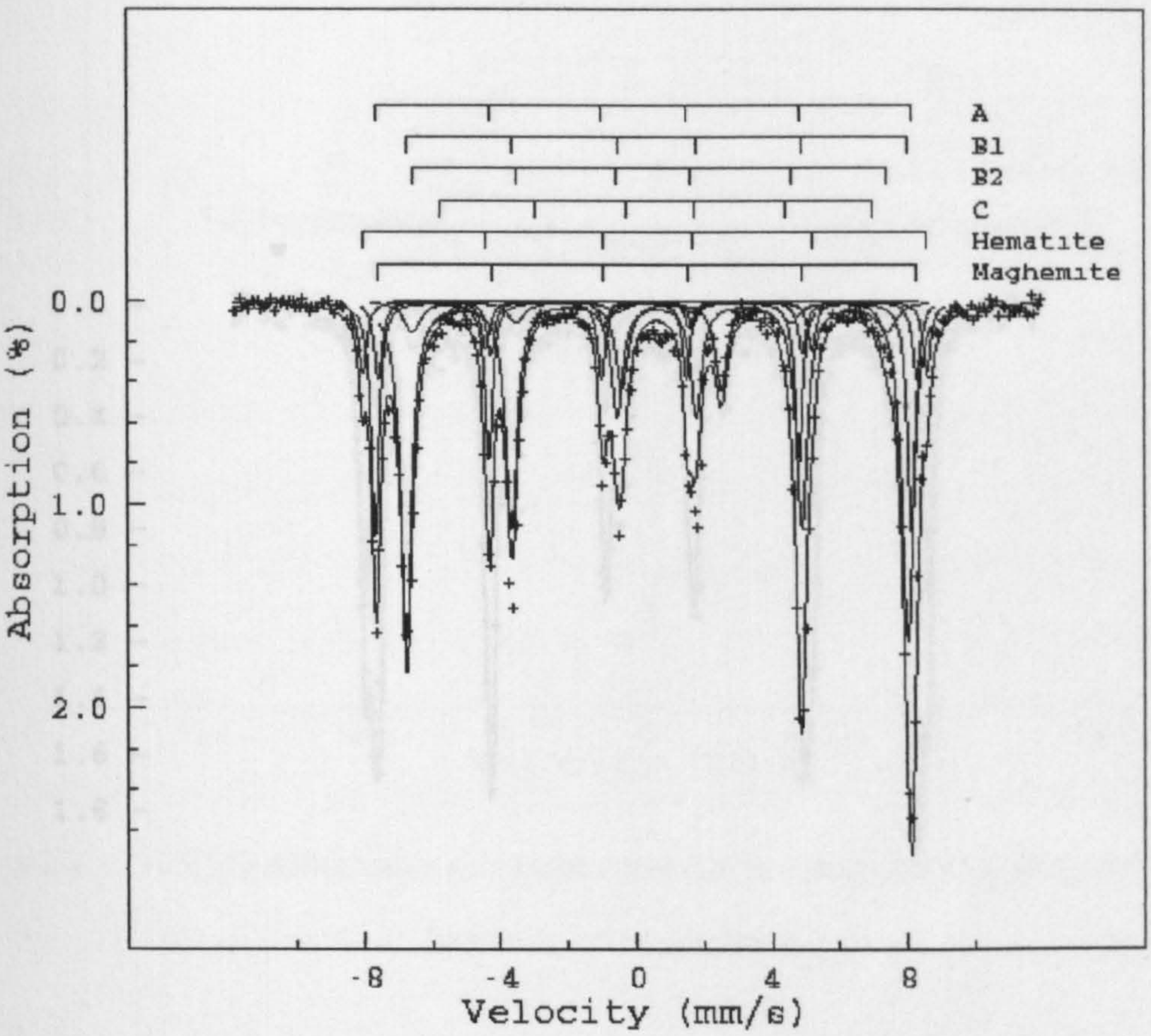


***Figure 4.31 - $^{57}Fe$ Mössbauer spectrum recorded at 300K from $Fe_{2.8}Sn_{0.2}O_4$ after oxidation at 680K***

Having established the behaviour of the tin-doped magnetite under oxidising conditions the oxidised $Fe_{2.9}Sn_{0.1}O_4$ was heated *in vacuo* to higher temperatures. $^{57}Fe$ Mössbauer spectra were recorded *in situ* at 820K, Figure 4.33a, Table 4.14, and 845K, Figure 4.33b, Table 4.15, over 18 and 24 hours respectively. The spectrum recorded at 820K consisted of components due to magnetite low in tin content as well as tin-doped hematite and tin-doped maghemite, all exhibiting magnetic splitting with the outer component having a field of 29.8T and another of 16.2T, which is far higher than expected for pure magnetite.

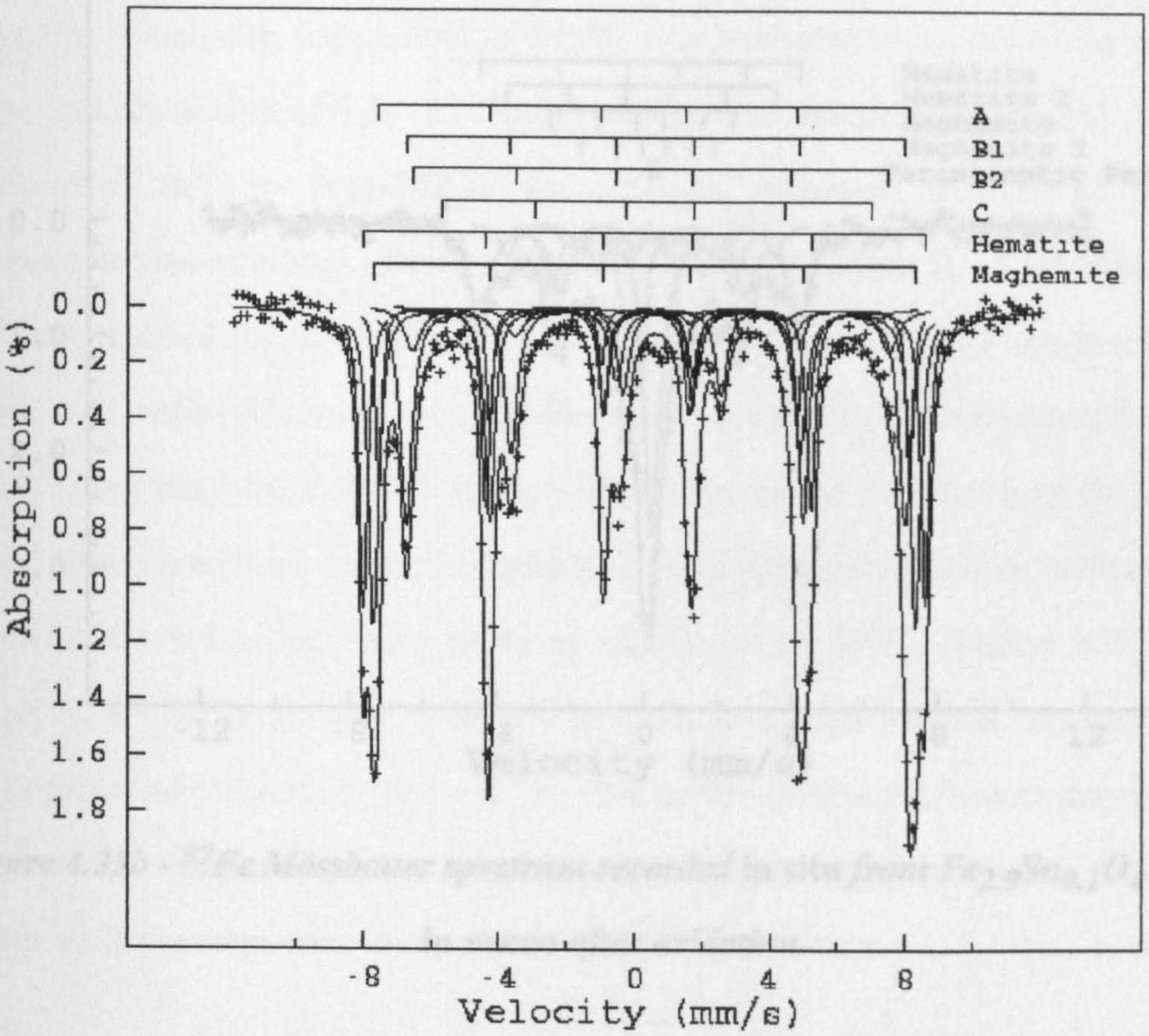


***Figure 4.32 - $^{57}Fe$ Mössbauer spectrum recorded at 300K from $Fe_{2.8}Sn_{0.2}O_4$ after oxidation at 770K***

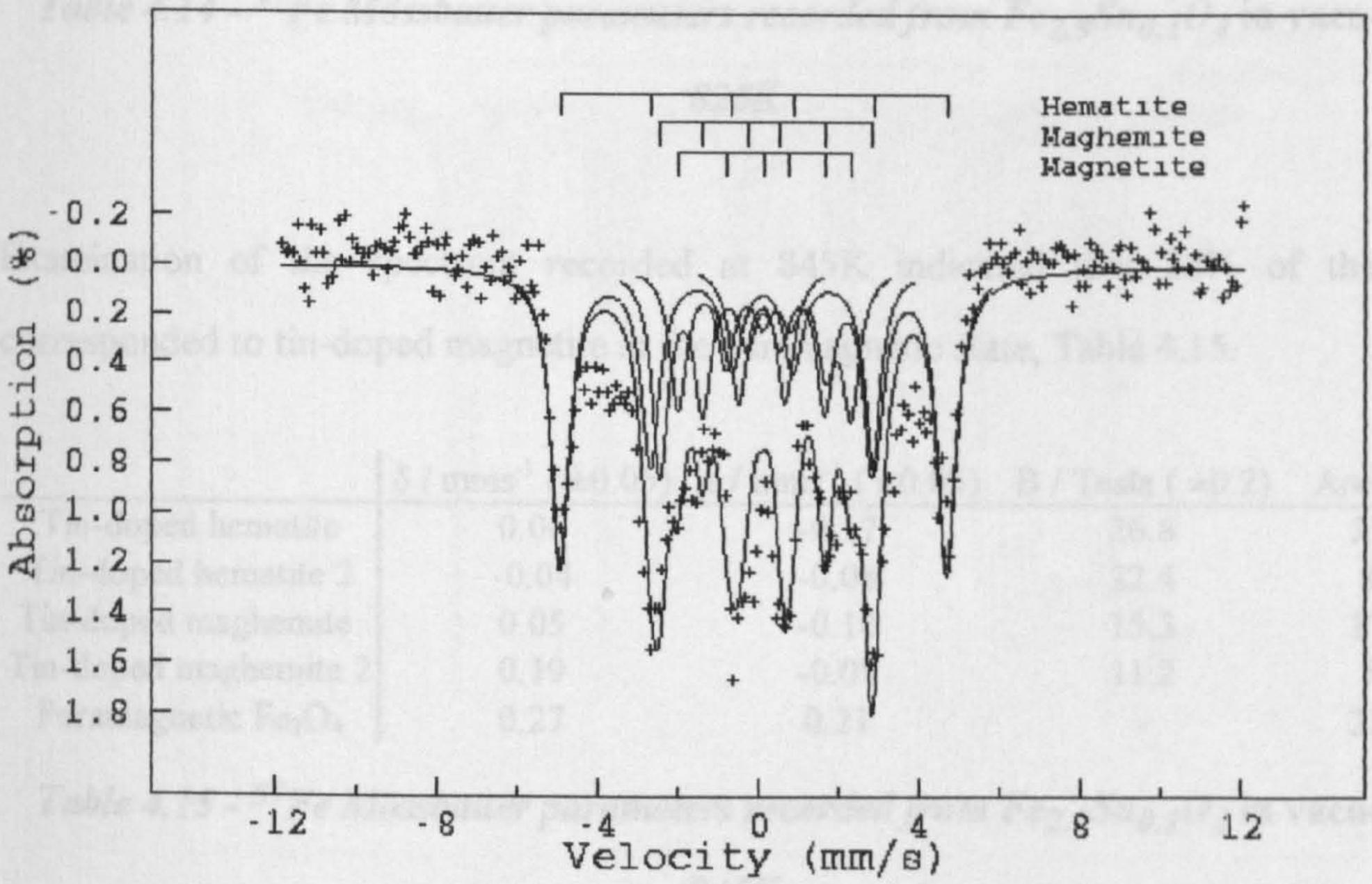


***Figure 4.33a - $^{57}Fe$ Mössbauer spectrum recorded* in situ *from $Fe_{2.9}Sn_{0.1}O_4$ at 820K* in vacuo *after oxidation***

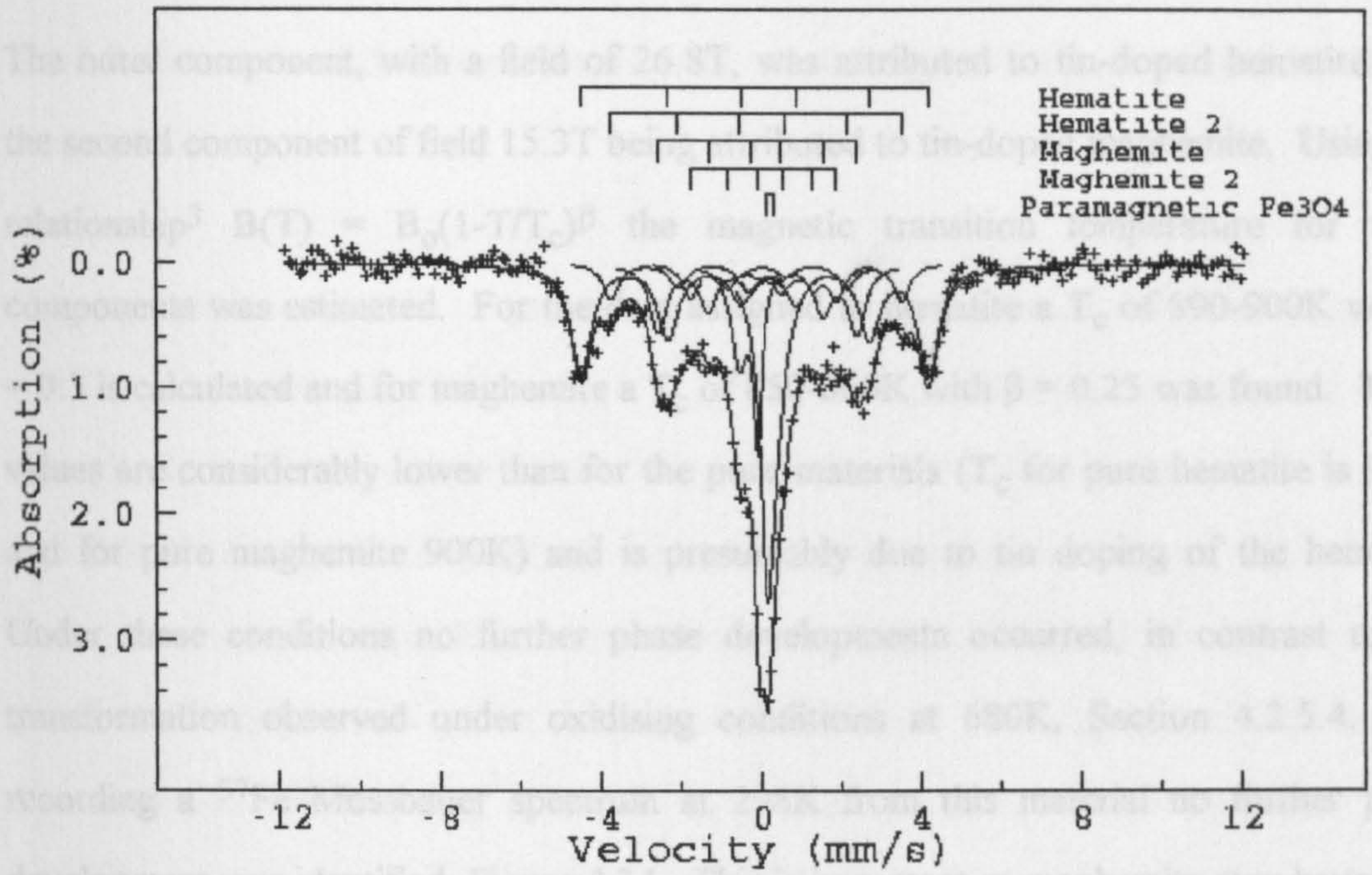


***Figure 4.33b - $^{57}Fe$ Mössbauer spectrum recorded* in situ *from $Fe_{2.9}Sn_{0.1}O_4$ at 845K in vacuo *after oxidation***

| | $\delta$ /mms$^{-1}$ ($\pm$0.05) | $\Delta$ / mms$^{-1}$ ($\pm$0.03) | B / Tesla ($\pm$0.2) | Area / % |
|---|---|---|---|---|
| Tin-doped hematite | 0.00 | -0.10 | 29.8 | 42.9 |
| Tin-doped maghemite | 0.16 | 0.14 | 16.2 | 33.7 |
| Tin-doped magnetite | 0.29 | -0.14 | 13.3 | 23.4 |

***Table 4.14 - $^{57}Fe$ Mössbauer parameters recorded from $Fe_{2.9}Sn_{0.1}O_4$* in vacuo *at 820K***

Examination of the spectrum recorded at 845K indicated that 22% of the area corresponded to tin-doped magnetite in the paramagnetic state, Table 4.15.

| | $\delta$ / mms$^{-1}$ ($\pm$0.05) | $\Delta$ / mms$^{-1}$ ($\pm$0.03) | B / Tesla ($\pm$0.2) | Area / % |
|---|---|---|---|---|
| Tin-doped hematite | 0.06 | -0.17 | 26.8 | 33.2 |
| Tin-doped hematite 2 | -0.04 | -0.08 | 22.4 | 8.6 |
| Tin-doped maghemite | 0.05 | -0.10 | 15.3 | 17.3 |
| Tin-doped maghemite 2 | 0.19 | -0.08 | 11.2 | 7.7 |
| Paramagnetic $Fe_3O_4$ | 0.27 | 0.21 | - | 22.0 |

***Table 4.15 - $^{57}Fe$ Mössbauer parameters recorded from $Fe_{2.9}Sn_{0.1}O_4$* in vacuo *at 845K***

The outer component, with a field of 26.8T, was attributed to tin-doped hematite with the second component of field 15.3T being attributed to tin-doped maghemite. Using the relationship[3] $B(T) = B_0(1-T/T_c)^{\beta}$ the magnetic transition temperature for these components was estimated. For the data assigned to hematite a $T_c$ of 890-900K with $\beta = 0.3$ is calculated and for maghemite a $T_c$ of 850-860K with $\beta = 0.25$ was found. These values are considerably lower than for the pure materials ($T_c$ for pure hematite is 960K and for pure maghemite 900K) and is presumably due to tin doping of the hematite. Under these conditions no further phase developments occurred, in contrast to the transformation observed under oxidising conditions at 680K, Section 4.2.5.4. On recording a $^{57}Fe$ Mössbauer spectrum at 298K from this material no further phase development was identified, Figure 4.34. This is important as maghemite may have been expected to transform to hematite under these conditions indicating that the tin impurities in the maghemite cause stabilisation of the structure.

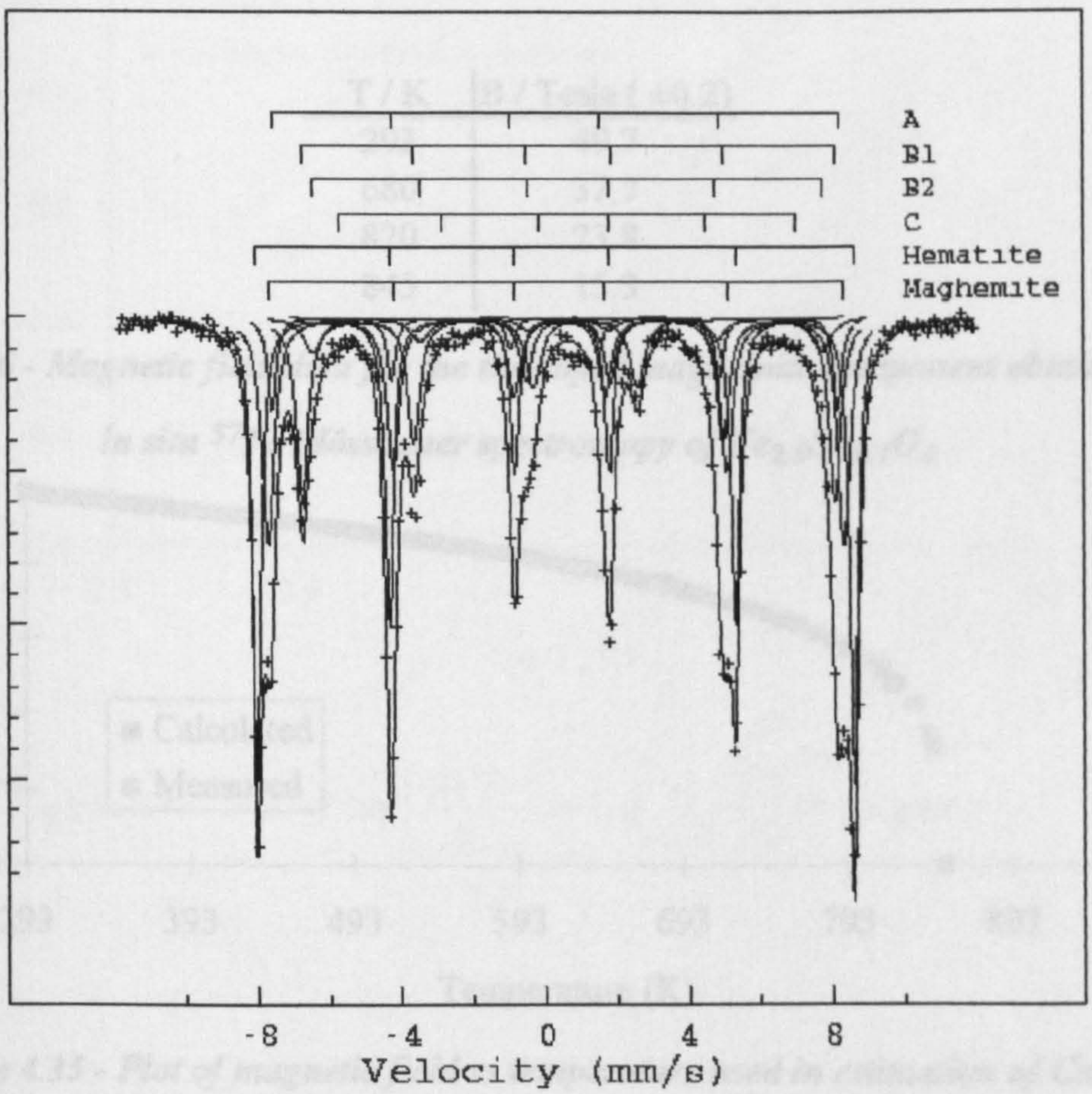


***Figure 4.34 - $^{57}Fe$ Mössbauer spectrum recorded from $Fe_{2.9}Sn_{0.1}O_4$ at 300K***

### 4.2.5.5 Estimation of Curie temperature of tin-doped maghemite and tin-doped hematite

Two methods were used to estimate the Curie temperature of tin-doped maghemite involving the relationship $B(T) = B_o(1-T/T_c)^{\beta}$ where $B_o$ is the magnetic hyperfine field at $T = 0K$, $T_c$ is the magnetic transition temperature and $\beta$ is less than 0.5. The first, and less reliable, method involved fitting the experimental magnetic field data, Table 4.16, to a magnetisation curve predicted from the above equation, Figure 4.35. To produce a predicted magnetisation curve magnetic field values were generated for various temperatures by substituting values of $T_c$, $\beta$ and $B_o$ into the above equation. These values were then varied until the theoretical curve became coincident with the experimental data. This process was repeated for various values of $T_c$, $B_o$ and $\beta$ for both tin-doped maghemite and tin-doped hematite and gave a $T_c$ of 850K for tin-doped maghemite and 900K for the tin-doped hematite phase.

| T / K | B / Tesla ( ±0.2) |
|---|---|
| 293 | 49.7 |
| 680 | 37.7 |
| 820 | 23.8 |
| 845 | 15.3 |

***Table 4.16 - Magnetic field data for the tin-doped maghemite component obtained by in situ $^{57}Fe$ Mössbauer spectroscopy of $Fe_{2.9}Sn_{0.1}O_4$***

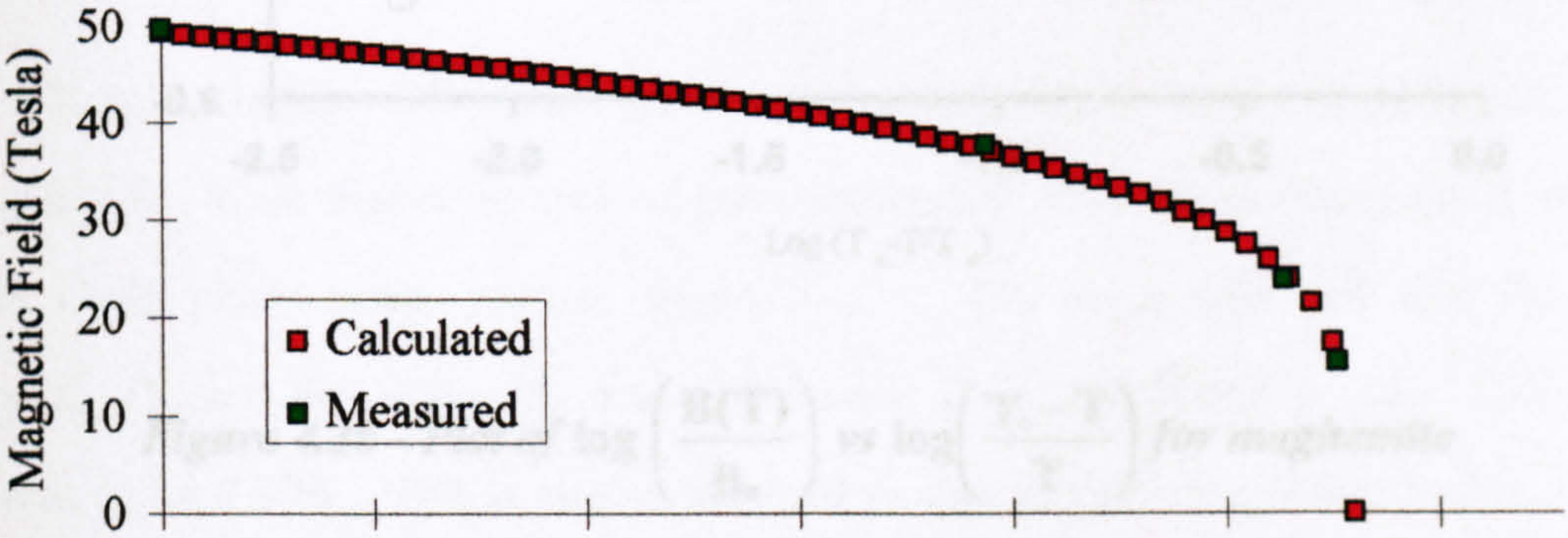


***Figure 4.35 - Plot of magnetic field vs temperature used in estimation of Curie temperature for tin-doped maghemite***

The second method involved rearranging the equation by taking logs of both sides to produce the following;

$$\log\left(\frac{B(T)}{B_o}\right) = \beta\left(\log\left(\frac{T_c - T}{T}\right)\right)$$

From this it is possible to plot $\log\left(\frac{B(T)}{B_o}\right)$ against $\log\left(\frac{T_c - T}{T}\right)$ and calculate β from the slope of the graph. It was anticipated that $T_c$ would be in the region of 850K for tin-doped maghemite and in the region of 900K for tin-doped hematite. Using $T_c$ values from the anticipated regions, several plots were obtained for both tin-doped maghemite and tin-doped hematite. By regression of each straight line plot the $T_c$ which gave the best regression value (r) i.e. that closest to unity, for tin-doped maghemite was found to be 850K, Figure 4.36, and for tin-doped hematite 900K.

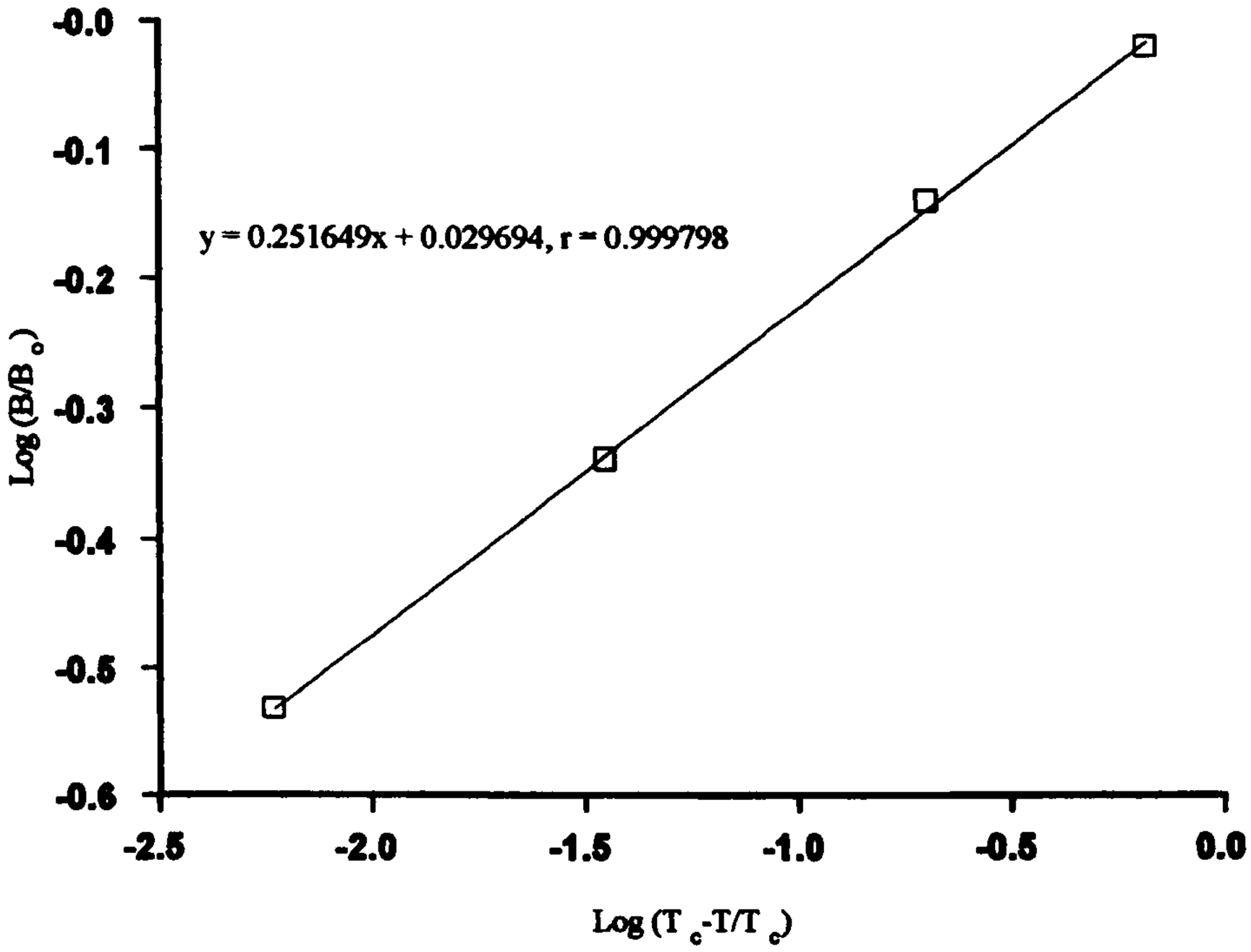


*Figure 4.36 - Plot of* $\log\left(\frac{B(T)}{B_o}\right)$ *vs* $\log\left(\frac{T_c - T}{T}\right)$ *for maghemite*

## 4.3 Cr and Ga doped magnetite

$Fe_3O_4$ was doped with $Cr^{3+}$ and $Ga^{3+}$ ions to investigate the effect of substituting paramagnetic and diamagnetic trivalent ions (as compared with tetravalent tin ions) on the magnetic properties of magnetite.

### 4.3.1 Energy Dispersive X-ray Microanalysis of $Fe_{3-x}M_xO_4$ (M = Cr, Ga)

In the case of Cr and Ga doped magnetite the use of EDX analysis was particularly useful for confirming the presence of the dopant ion in the magnetite structure. Whereas the presence of tin could be confirmed by $^{119}Sn$ Mössbauer spectroscopy, the Cr and Ga dopant ions are not Mössbauer active and so this technique could not be used. The results of the EDX analysis are shown in Table 4.17.

| Dopant ion | Nominal. At.% | Determined At.% |
|---|---|---|
| Cr | 3.4 | 3.6 |
| Ga | 3.4 | 5.8 |

*Table 4.17 - Energy Dispersive X-ray Microanalysis results for $Fe_{3-x}M_xO_4$ (M = Cr, Ga)*

### 4.3.2 X-ray powder diffraction

The X-ray powder diffraction patterns recorded from both $Fe_{2.9}Cr_{0.1}O_4$ and $Fe_{2.9}Ga_{0.1}O_4$ were similar to that of pure magnetite[5] with no evidence for a second metal oxide phase being present, Figure 4.37. The cubic unit cell size for both $Fe_{2.9}Cr_{0.1}O_4$ and $Fe_{2.9}Ga_{0.1}O_4$ was determined from the X-ray powder diffraction patterns to be 8.39Å. This is almost identical to that of pure magnetite, 8.40Å, and is not surprising given that the ionic radii of both $Cr^{3+}$ and $Ga^{3+}$ is 62pm.[6] As these ions are of similar size to $Fe^{3+}$ ions, 63pm, and of the same charge, there is no reduction of $Fe^{3+}$ to $Fe^{2+}$ and the associated change in unit cell size due to the difference between the ionic radii of $Fe^{3+}$ and $Fe^{2+}$.

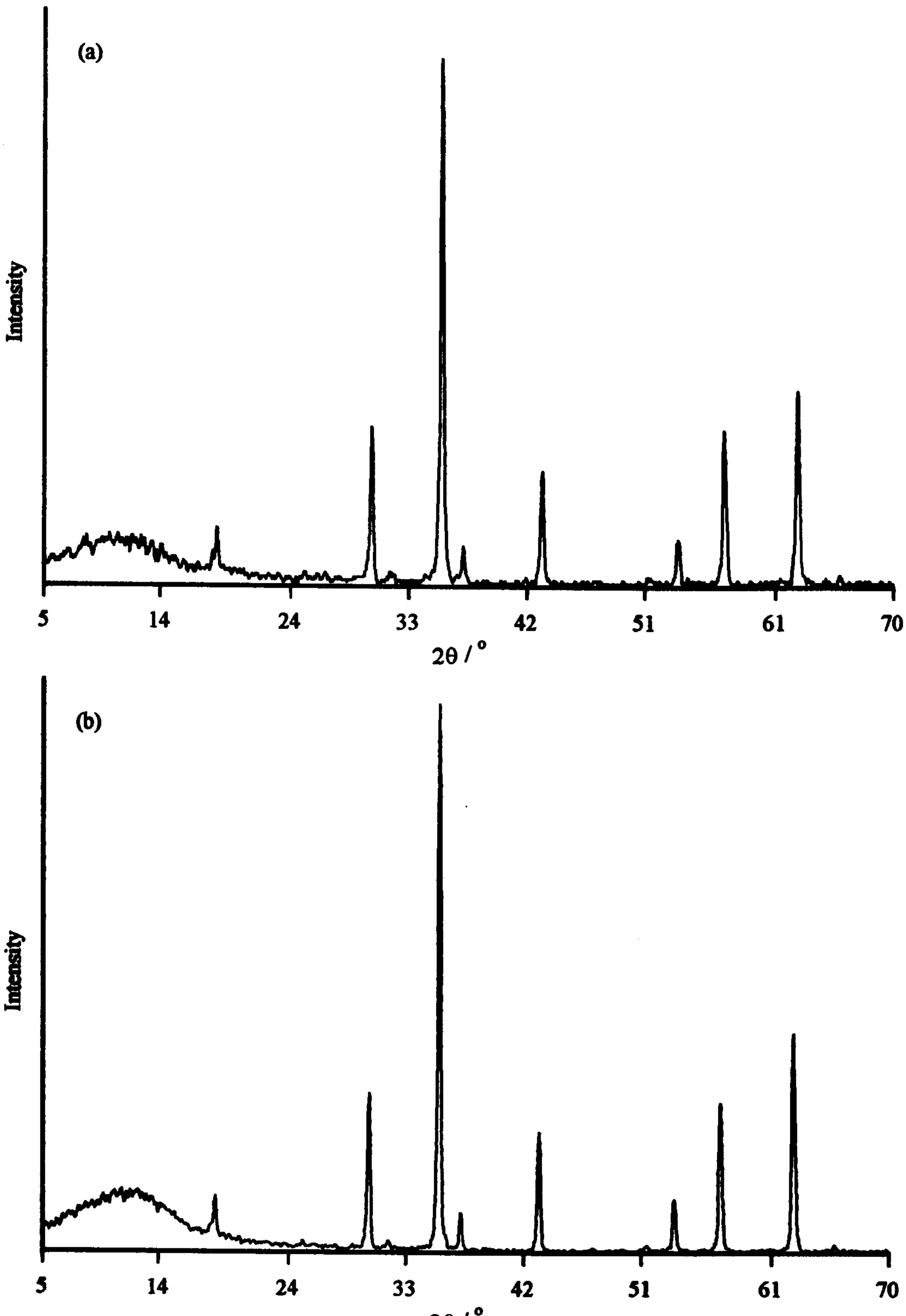


***Figure 4.37 - X-ray powder diffraction pattern recorded from (a) $Fe_{2.9}Cr_{0.1}O_4$ and (b) $Fe_{2.9}Ga_{0.1}O_4$***

### 4.3.3 $^{57}Fe$ Mössbauer spectra of $Fe_{3-x}M_xO_4$ ( M = Cr, Ga) recorded at 298K

The $^{57}Fe$ Mössbauer spectrum recorded from $Fe_{2.9}Cr_{0.1}O_4$, Figure 4.38a, consisted of 4 magnetic components. These components were interpreted in a similar fashion to that used for tin-doped magnetite i.e., one tetrahedral A site $Fe^{3+}$ ion, two $Fe^{2+}$-$Fe^{3+}$ sites (B1, B2) and finally one component due to the interaction of the $Cr^{3+}$ dopant with the B site iron ions. The size of the magnetic field for each component was very similar to that for pure $Fe_3O_4$, Table 4.18.

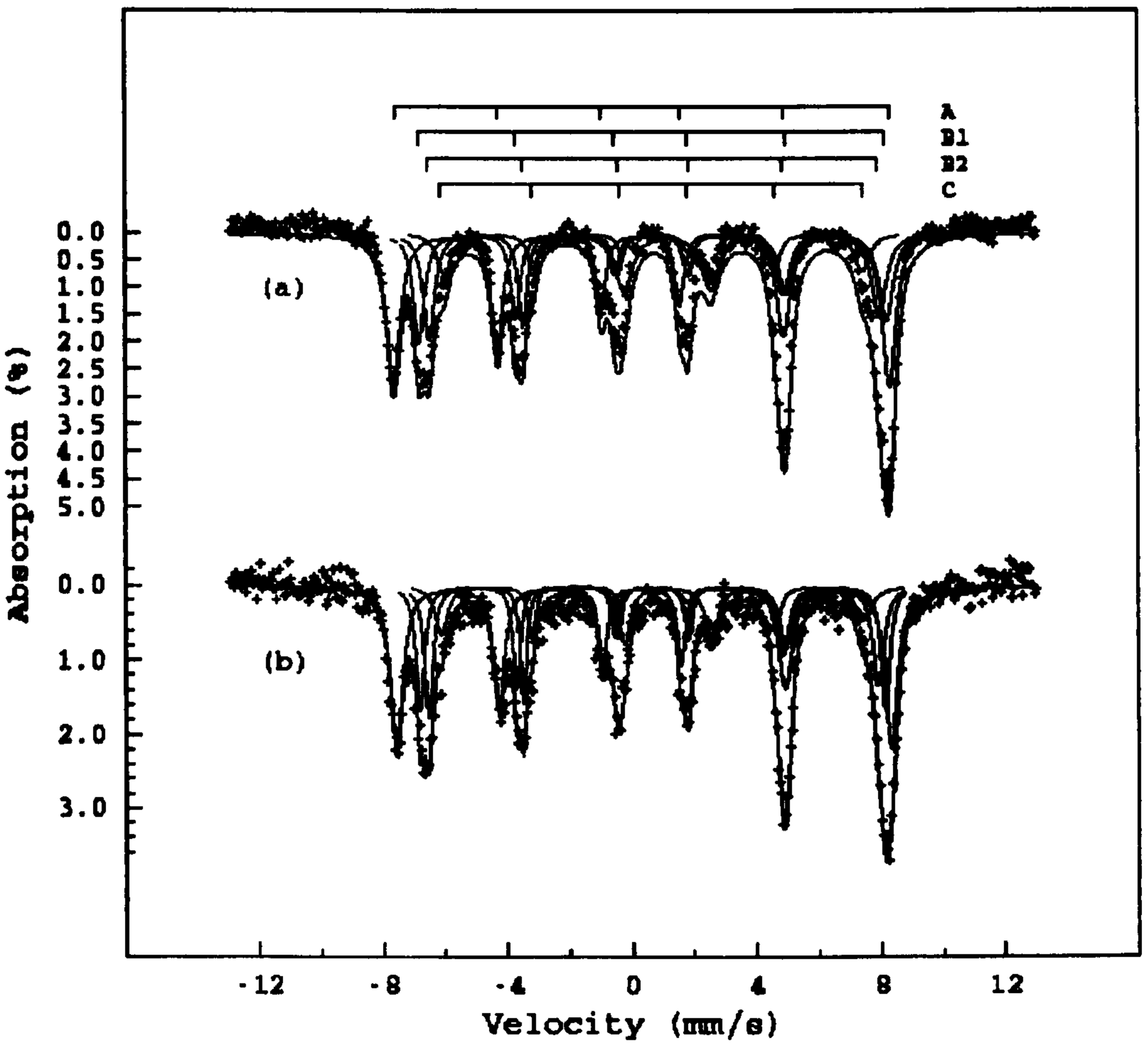


***Figure 4.38 - $^{57}Fe$ Mössbauer spectra recorded from $Fe_{3-x}M_xO_4$ where x = (a) Cr, (b) Ga***

The $^{57}Fe$ Mössbauer spectrum recorded from $Fe_{2.9}Ga_{0.1}O_4$, Figure 4.38b, was very similar to that recorded from the Cr doped magnetite. The $^{57}Fe$ Mössbauer parameters

| | A Sextet | | | B1 Sextet | | | B2 Sextet | | | C Sextet | | |
|---|---|---|---|---|---|---|---|---|---|---|---|---|
| Dopant | δ/mms$^{-1}$ ±0.03 | Δ/mms$^{-1}$ ±0.05 | H/Tesla ±0.2 | δ/mms$^{-1}$ ±0.03 | Δ/mms$^{-1}$ ±0.05 | H/Tesla ±0.2 | δ/mms$^{-1}$ ±0.03 | Δ/mms$^{-1}$ ±0.05 | H/Tesla ±0.2 | δ/mms$^{-1}$ ±0.03 | Δ/mms$^{-1}$ ±0.05 | H/Tesla ±0.2 |
| Fe | 0.31 | -0.01 | 49.3 | 0.69 | 0.00 | 46.5 | 0.81 | -0.09 | 44.6 | N/A | N/A | N/A |
| Cr | 0.35 | 0.03 | 49.3 | 0.64 | 0.02 | 46.4 | 0.69 | 0.00 | 44.8 | 0.68 | -0.03 | 42.1 |
| Ga | 0.31 | 0.01 | 49.4 | 0.67 | 0.03 | 46.7 | 0.72 | 0.02 | 44.9 | 0.73 | -0.01 | 41.9 |

***Table 4.18 - $^{57}$ Fe Mössbauer parameters for $Fe_{3-x}M_xO_4$ where M = Fe, Cr, Ga***

for both materials were very similar suggesting that use of $Ga^{3+}$ or $Cr^{3+}$ ions as dopants has very little effect on the magnetic properties of the materials, Table 4.18.

Examination of the ratio of the A and B subspectra in the $^{57}Fe$ Mössbauer spectrum of $Fe_{2.9}Cr_{0.1}O_4$ gave a value, 1.42, which was much lower than expected. For this sample a B/A ratio of ~1.9 would be expected, as the theoretical value for the B/A ratio of the subspectra in the $^{57}Fe$ Mössbauer spectrum of $Fe_3O_4$ is 2. A value of 1.42 suggested a Cr dopant level of ~0.62 which is far higher than the Cr content as determined by EDX, Section 4.3.2. An alternative argument is that there was an A site subspectrum arising from a $Fe^{2+}$ contribution which had been moved into the B site component making the B site contribution artificially high. This seems unlikely as there was no reason for any change in the $Fe^{2+}/Fe^{3+}$ distribution on either A or B sites as the substituting $Cr^{3+}$ ions were of the same oxidation state as the $Fe^{3+}$ being replaced in the host structure. The B/A ratio of 1.42 is also substantially different from that determined by Ok et al[29] who established a value of 1.75 for the B/A ratio for x = 0.125, very close to the expected value. A similar situation was observed with the B/A ratio in the $^{57}Fe$ Mössbauer spectrum of $Fe_{2.9}Ga_{0.1}O_4$. A slightly lower value of 1.38 was found which, as before, was unusually low. It was also unlikely that the dopant level was higher than anticipated as the results of the EDX analysis, Section 4.3.1, indicated that the dopant level was in good agreement with the nominal value. Further work on these samples is required to explain this anomaly.

### 4.3.4 $^{57}Fe$ Mössbauer spectra recorded at high temperature *in vacuo*

$^{57}Fe$ Mössbauer spectra recorded from the $Fe_{2.9}Cr_{0.1}O_4$ *in vacuo* with an oxygen partial pressure of $10^{-6}$-$10^{-7}$ atm at temperatures up to 810K are shown in Figure 4.39. The spectra indicate the Curie temperature to be 775±20K. This is similar to that observed in the tin-doped magnetite of composition $Fe_{2.9}Sn_{0.1}O_4$, $T_c$ = 780K, and is *ca.* 70K lower than the $T_c$ of pure $Fe_3O_4$ and similar to that obtained for Cr-doped magnetite by

Robbins et al.[26] The similarity of the value of the $T_c$ for the Cr doped magnetite to that determined by Robbins et al[26] does not help explain the very low B/A ratio calculated from the $^{57}Fe$ Mössbauer spectrum recorded at 298K and endorses the conclusion that the system requires further investigation.

$^{57}Fe$ Mössbauer spectra were recorded from $Fe_{2.9}Ga_{0.1}O_4$ at temperatures to 800K and are shown in Figure 4.40. From these spectra a $T_c$ of 785±10K was determined. The results indicated that the effects of both $Cr^{3+}$ and $Ga^{3+}$ ions on the magnetic properties of $Fe_3O_4$ are very similar to those of $Sn^{4+}$.

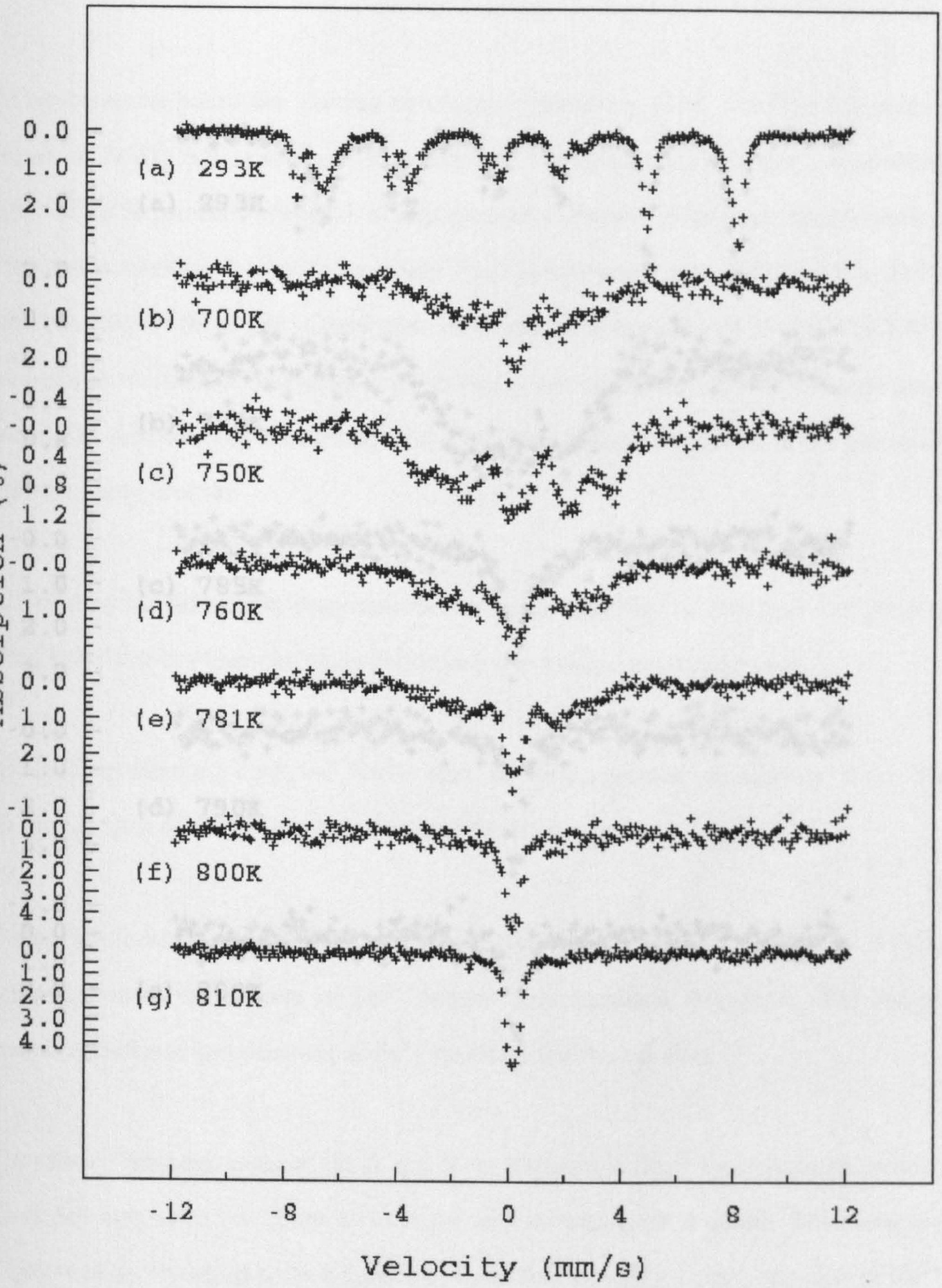


***Figure 4.39 - $^{57}Fe$ Mössbauer spectra recorded* in vacuo *from $Fe_{2.9}Cr_{0.1}O_4$***

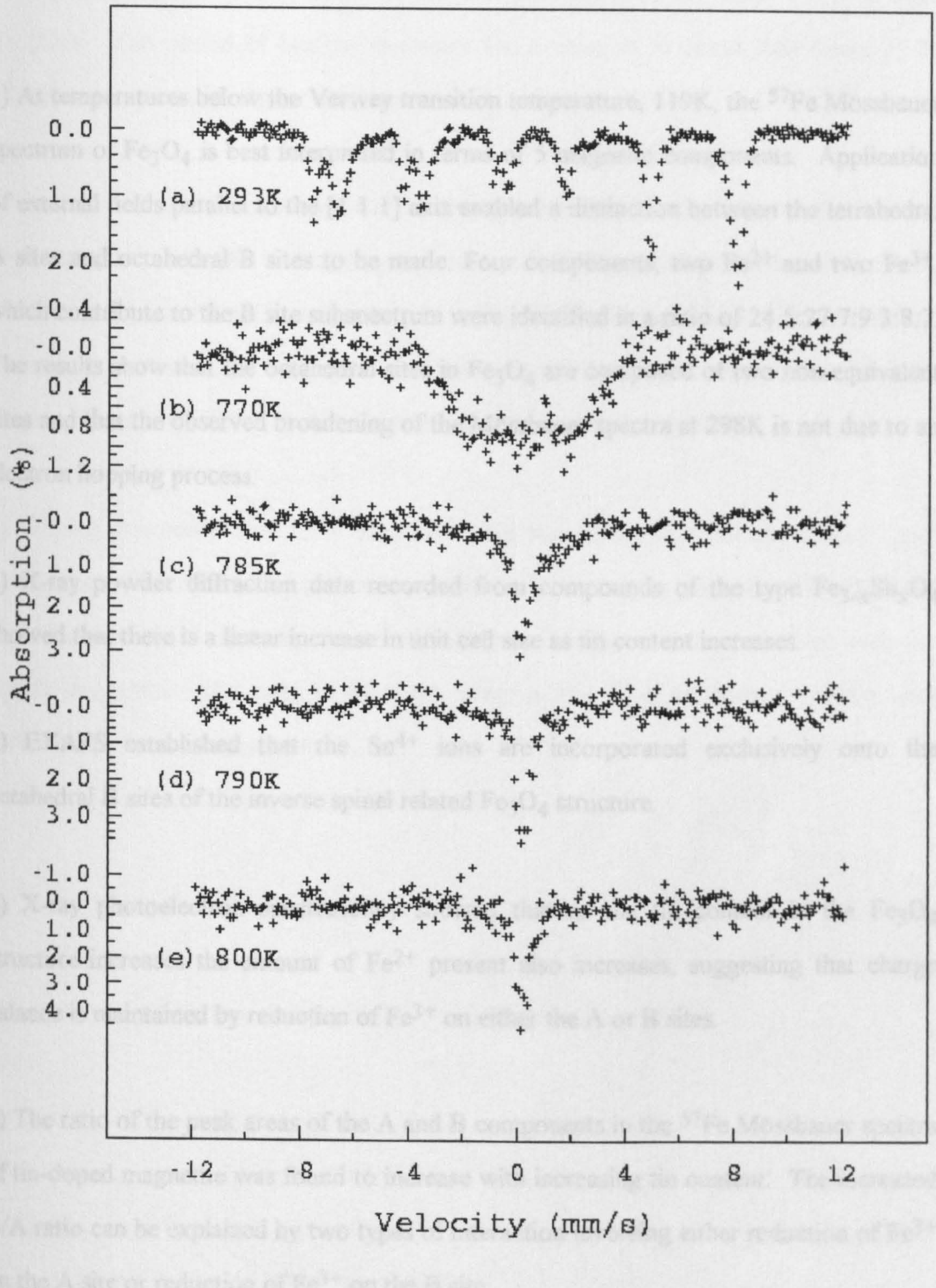


***Figure 4.40 - $^{57}Fe$ Mössbauer spectra recorded* in vacuo *from $Fe_{2.9}Ga_{0.1}O_4$***

## 4.4 Conclusions

1) At temperatures below the Verwey transition temperature, 119K, the $^{57}Fe$ Mössbauer spectrum of $Fe_3O_4$ is best interpreted in terms of 5 magnetic components. Application of external fields parallel to the [1 1 1] axis enabled a distinction between the tetrahedral A sites and octahedral B sites to be made. Four components, two $Fe^{2+}$ and two $Fe^{3+}$, which contribute to the B site subspectrum were identified in a ratio of 24.5:27.7:9.3:8.7. The results show that the octahedral sites in $Fe_3O_4$ are composed of two non-equivalent sites and that the observed broadening of the Mössbauer spectra at 298K is not due to an electron hopping process.

2) X-ray powder diffraction data recorded from compounds of the type $Fe_{3-x}Sn_xO_4$ showed that there is a linear increase in unit cell size as tin content increases.

3) EXAFS established that the $Sn^{4+}$ ions are incorporated exclusively onto the octahedral B sites of the inverse spinel related $Fe_3O_4$ structure.

4) X-ray photoelectron spectroscopy showed that as the tin content in the $Fe_3O_4$ structure increases the amount of $Fe^{2+}$ present also increases, suggesting that charge balance is maintained by reduction of $Fe^{3+}$ on either the A or B sites.

5) The ratio of the peak areas of the A and B components in the $^{57}Fe$ Mössbauer spectra of tin-doped magnetite was found to increase with increasing tin content. The increased B/A ratio can be explained by two types of interaction involving either reduction of $Fe^{3+}$ on the A site or reduction of $Fe^{3+}$ on the B site.

6) $^{57}Fe$ and $^{119}Sn$ Mössbauer spectroscopy showed that introduction of tin into the $Fe_3O_4$ structure causes a significant reduction in the Curie temperature of magnetite which is greater than that observed in the analogous titanomagnetite. Further, prolonged

heating at elevated temperatures causes the exsolution of tin from the magnetite structure. The period of heating necessary for exsolution to occur was found to be greater in samples with higher tin content.

7) Tin-doped magnetite heated under oxidising conditions transformed initially into tin-doped maghemite before undergoing a structural transformation to tin-doped hematite. The transition occurred at temperatures well above that at which pure maghemite transforms to hematite. A significant lowering of the Curie temperature for both maghemite and hematite was also observed with increased tin content.

8) Doping magnetite with $Cr^{3+}$ and $Ga^{3+}$ did not cause any change in the lattice parameters. $^{57}Fe$ Mössbauer spectroscopy showed that doping magnetite with $Cr^{3+}$ and $Ga^{3+}$ lowered the Curie temperature of $Fe_3O_4$ to a similar extent as observed with tin-doped magnetite. The ratio of the peak areas in the $^{57}Fe$ Mössbauer spectra were considerably lower than expected.

# References


1 A.Ito, K.Ono and Y.Ishikawa, J.Phys.Soc.Jpn., 1963, 18, 1465

2 G.A.Sawatzky, J.M.D.Coey and A.H.Morrish, J.Appl.Phys.,1969, 40, 1402

3 L.Häggström, H.Annerstein, T.Ericsson, R.Wäppling, W.Karner and S.Bjarman, Hyp.Int., 1978, 5, 201

4 Ö.Helgason, H.P.Gunnlaugsson, S.Steinhorrson and S.Mørup, Hyp.Int., 1992, 70, 981

5 JCPDS pattern 19-0629

6 R.D.Shannon and C.T.Prewitt, Acta Crystallogr., 1969, B25, 925

7 H.Tanaka and M.Kono, J.Geomag.Geoelectr., 1987, 39, 463

8 B.A.Wechsler, D.H.Lindsley and C.T.Prewitt, Amer. Mineral., 1984, 69, 754

9 D.H.Lindsley, Rev.Min. 25, Mineralogical Society of America, Washington, D.C., U.S.A., 1991, Editor D.H.Lindsley

10 M.E.Fleet, Acta Crystallogr., 1981, B37, 917

11 W.H.Bauer and A.A.Khan, Acta Crystallogr., 1971, B27, 2133

12 C.Djega-Mariadassou, F.Basile, P.Poix and A.Michel, Ann.Chim.(Paris), 1973, 8, 15

13 E.Aksenova, E.L.Arinkina and Y.A.Mamalui, Ukr.Fiz.Zh.(Russian Ed.), 1983, 28,

14 G.Blasse, Philips Research Reports Supplement, 1964, 3, 1

15 R.Restori, D.Schwarzenbach and J.R.Schneider, Acta Crystallogr., 1987, B43, 251

16 C.J.Howard, T.M.Sabine and F.Dickson, Acta Crystallogr., 1991, B47, 462

17 I.D.Welsh and P.M.A.Sherwood, Phys.Rev. B, 1989, 40, 6386

18 C.S.Kuivala, J.D.Butt and P.C.Stair, Appl.Surf.Sci., 1988, 20, 99

19 G.C.Allen, P.M.Tucker and R.K.Wild, Philisophical Magazine B, 1982, 46, 411

20 G.C.Allen, M.T.Curtis, A.J.Cooper, and P.M.Tucker, J.Chem.Soc. Dalton Trans., 1974, 1525

21 T.Choundhury, S.O.Saied, J.L.Sullivan and A.M.Abbot, J.Phys. D: Appl.Phys, 1989, 22, 1185

22 A.W.C.Lin, N.R.Armstrong and T.Kuwana, Anal.Chem., 1977, 49, 1228

23 F.Basile, C.Djega-Mariadassou and P.Poix, Mat.Res.Bull., 1973, 8, 619

24 C.Boekema, F. van der Woude and G.A.Sawatsky, J.Phys. C: Solid State Phys., 1976, 9, 2439

25 S.Akimoto, T.Katsura and M.Yoshida, J.Geomag.Geoelectr., 1957, 9, 165

26 M.Robbins, G.K.Wertheim, R.C.Sherwood and D.N.E.Buchanan, J.Phys.Chem. Solids, 1971, 32, 717

27 N.V.Sidgwick, "The Chemical Elements and Their Compounds", 1951, Vol. II, Oxford University Press, Oxford

28 N.N.Greenwood and A.Earnshaw, "Chemistry of the Elements", 1990, Pergamon Press, Oxford

29 H.N.Ok, L.S.Pan and B.J.Evans, Phys.Rev. B, 1978, 17, 85

# CHAPTER FIVE

# Characterisation of Zirconium(IV) Oxide

## 5.1 Synthesis of zirconium(IV) oxide

The work reported here concerns an investigation of the effect of synthesis conditions, including pH, on the nature of zirconia produced from zirconium(IV) acetate by i) boiling under reflux and ii) hydrothermal processing.

### 5.1.1 Aqueous chemistry of zirconium

The aqueous chemistry of zirconium has been studied by examining the zirconium oxychloride species in solution.[1-8] It was established that at concentrations of less than $10^{-4}$ M the Zr(IV) species was monomeric.[1] As the concentration was increased, up to 0.02M Zr, polymerisation occurred producing both trimeric and tetrameric species,[2] although subsequent studies[3, 4] indicated that the major species present was the tetramer. At higher concentrations the zirconyl species in zirconyl halides was identified as a tetramer[5, 6], $[Zr(OH)_2.4H_2O]_4^{8+}$. Addition of base to Zr(IV) solutions was found to cause hydrolytic polymerisation[7] of the tetrameric species which gave gelatinous, amorphous precipitates commonly described as hydrous zirconia.[1] Hydrolytic polymerisation was also observed when a solution of zirconyl chloride was boiled under reflux.[7] The rate at which polymerisation occurred was found to affect the nature of the final product. Rapid addition of base to the Zr(IV) solution caused the formation of a random polymer, Figure 5.1a. Each of the tetramer groups contained a multiplicity of hydroxyl bridging sites which allowed simultaneous polymer growth in many directions. This produces the 2-dimensional sheet structure illustrated in Figure 5.1a which is based upon the tetrameric units which link through hydroxyl bridges. The slower reaction, involving boiling under reflux, produced an ordered polymer, Figure 5.1b. In the slower process the polymer has the ability to grow in a more orderly fashion as the reflux process increases the hydroxyl content producing 2-dimensional polymers approaching $[Zr(OH)_4]_n$. These 2-dimensional sheets aggregate into the 3-dimensional crystal structure by condensation of water from the hydroxyl groups in adjacent sheets.

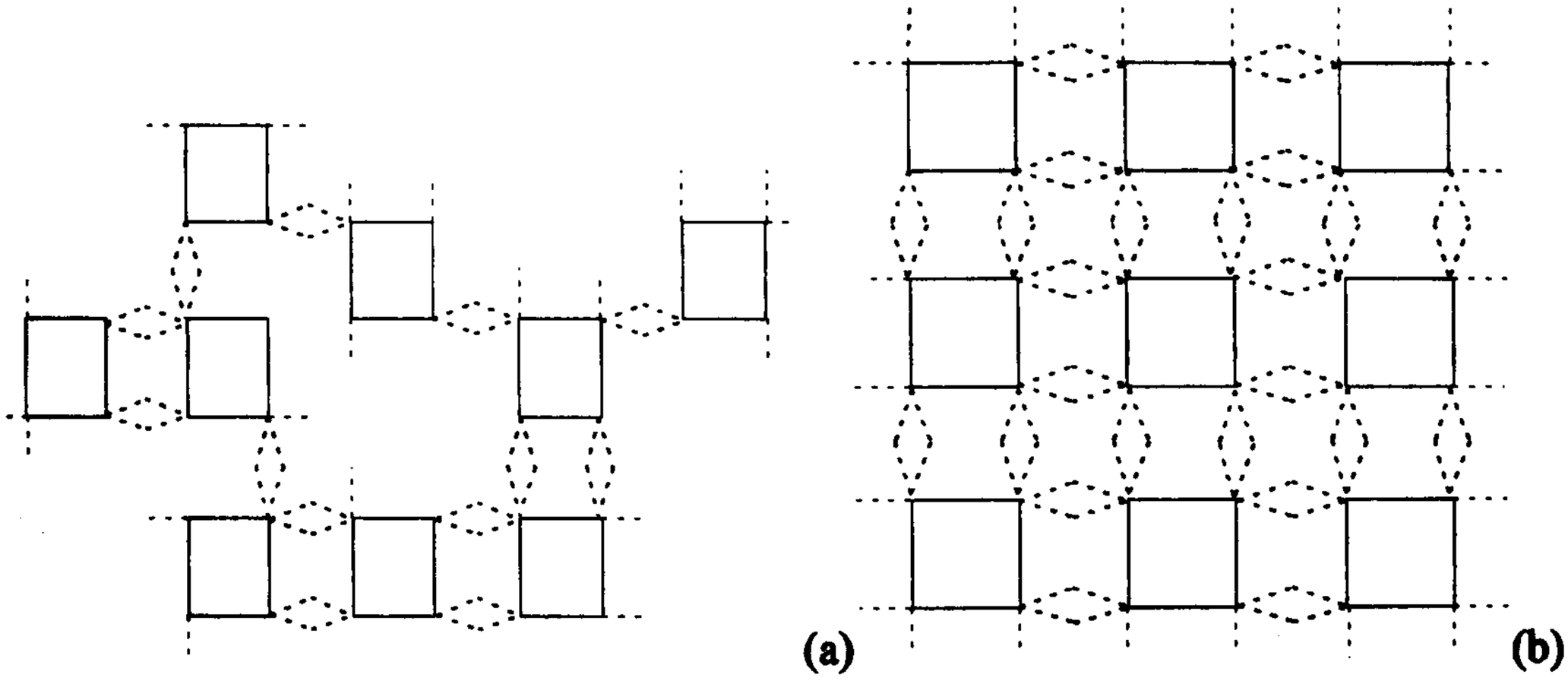


***Figure 5.1 - Two dimensional representation of the polymeric species formed from the aqueous Zr(IV) species on (a) addition of base and (b) under reflux conditions[1] where — — - OH group, ⌒ OH bridge, □ $Zr_4(OH)_8$ tetramers***

The coming together of these sheets under reflux conditions has been examined by electron microscopy[8] and the initial formation of a 2-dimensional structure was observed. After further calcination the formation of crystallites from these 2-dimensional sheets was detected. No evidence of sheet formation has been observed by electron microscopy in hydrothermally prepared zirconia.

### 5.1.2 Synthesis of $ZrO_2$ by boiling zirconium(IV) acetate under reflux

#### 5.1.2.1 Synthesis with $H_2O$

The X-ray powder diffraction pattern of the material dried under an infra red lamp showed it to be amorphous although a broad peak at *ca.* $2\theta = 30^o$ indicative of either cubic[9] or tetragonal[10] zirconia was identified, Figure 5.2a. Calcination in air at 200°C gave a material which X-ray powder diffraction showed to be similar to the dried material, Figure 5.2b, but, following calcination at 500°C the formation of a crystalline phase was observed, Figure 5.2c. Broadening of the X-ray powder diffraction pattern peaks made the distinction between the cubic and tetragonal phases difficult, as previously reported.[11]

Raman spectroscopy was used to distinguish between the cubic and tetragonal phases of zirconia as this technique has been found to distinguish clearly between the three common phases of zirconia.[12-14] The Raman spectrum recorded from monoclinic zirconia contains 16 bands[12] whereas that recorded from the tetragonal phase contains 6 bands.[13] Furthermore, the spectrum recorded from the cubic phase contains only one weak, broad band[14] at around 500cm$^{-1}$. Raman spectroscopy therefore has the advantage of being able to clearly distinguish between polymorphs which have coincident X-ray powder diffraction patterns. This is particularly useful when the material is poorly crystalline and consequently produces an X-ray powder diffraction pattern of broad peak width.

The Raman spectrum recorded from the material dried under an infra red lamp and subsequently calcined at 200°C, Figure 5.3, showed broad bands at 320cm$^{-1}$ and 490 cm$^{-1}$ similar to cubic zirconia,[14] whereas the spectrum recorded from the material calcined at 500°C, Figure 5.4, showed six bands characteristic of the spectrum recorded from tetragonal zirconia.[13] This suggests that the material calcined at 200°C is cubic zirconia and that, on calcination at 500°C, this transforms to the tetragonal phase. It was also found that laser irradiation of tetragonal zirconia at higher laser powers induced a transformation to the monoclinic phase.

The TGA trace recorded from the material calcined at 200°C indicated that there had been a 30% weight loss from the original mass, Figure 5.5. The decomposition products could not be identified but are likely to be hydroxide/oxide species. The TGA trace recorded from the material calcined at 500°C and identified by X-ray powder diffraction (Figure 5.2c) and Raman spectroscopy (Figure 5.4) as tetragonal zirconia showed a 1% weight loss, Figure 5.6.

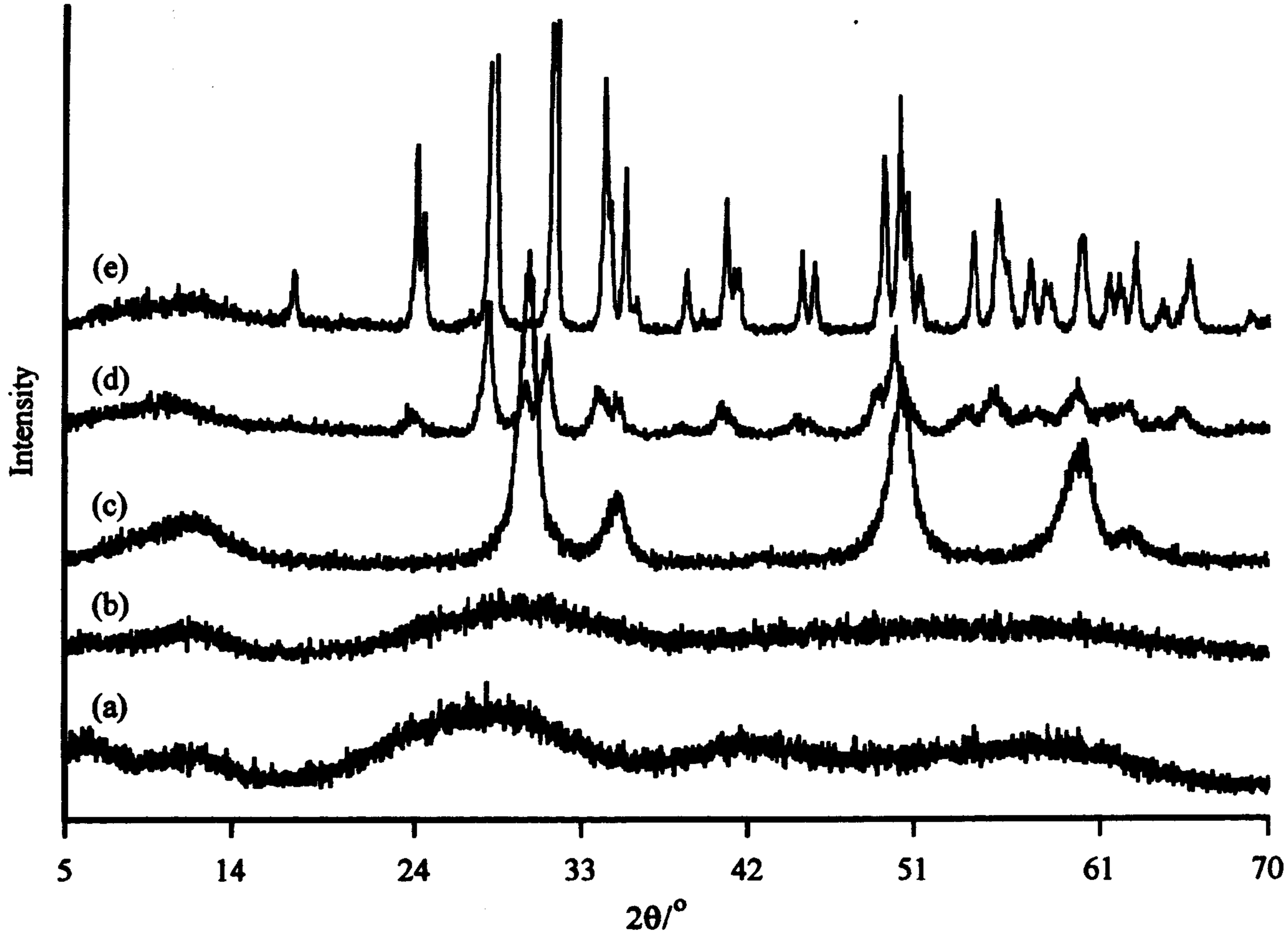


***Figure 5.2 - X-ray powder diffraction patterns recorded from the material produced by boiling zirconium(IV) acetate under reflux with $H_2O$ and (a) dried under an infra red lamp and calcined at (b) 200°C, (c) 500°C, (d) 900°C and (e) 1400°C***

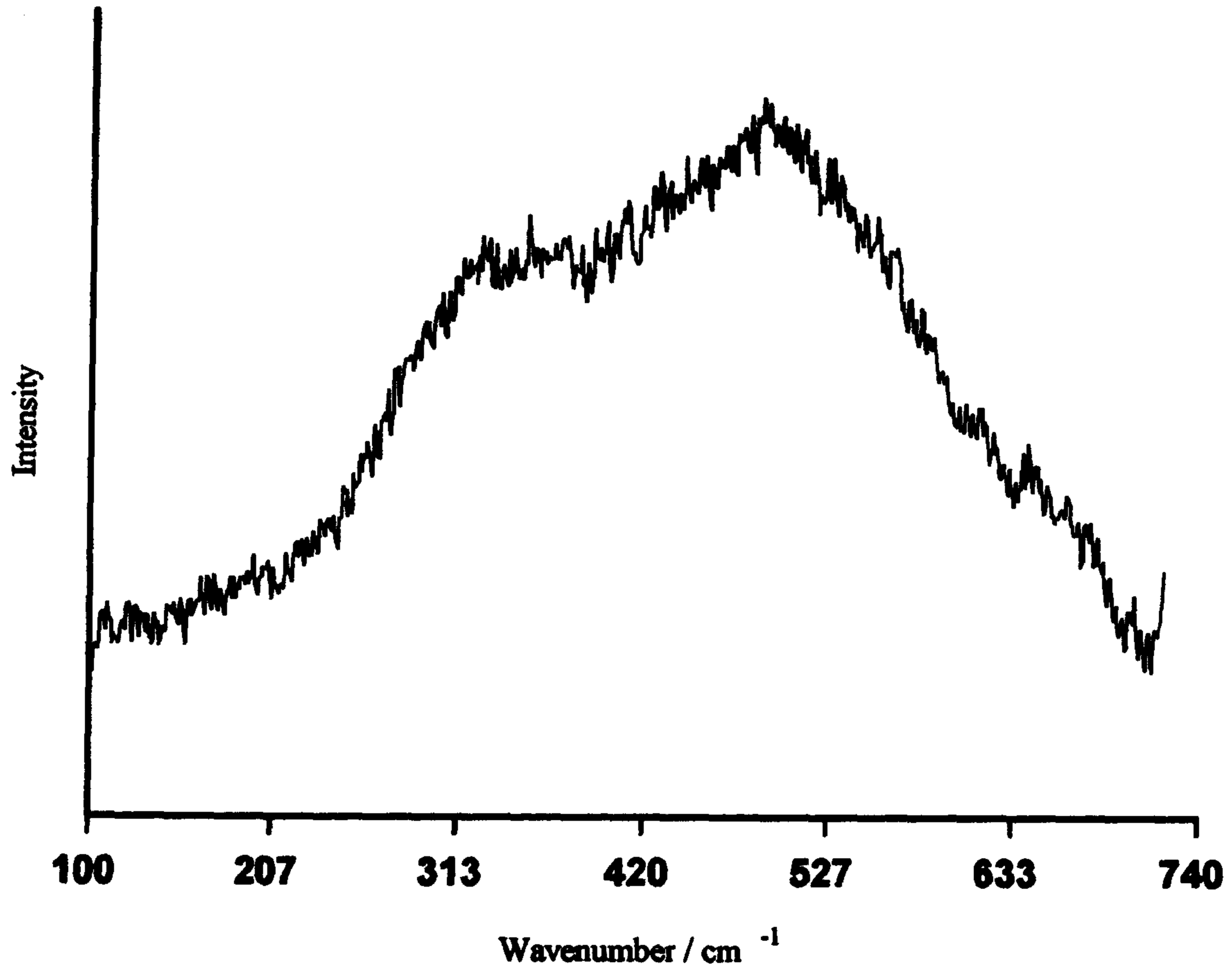


***Figure 5.3 - Raman spectrum recorded from $ZrO_2$ produced by boiling zirconium(IV) acetate under reflux in $H_2O$, drying under an infra red lamp, and subsequent calcination at 200°C***

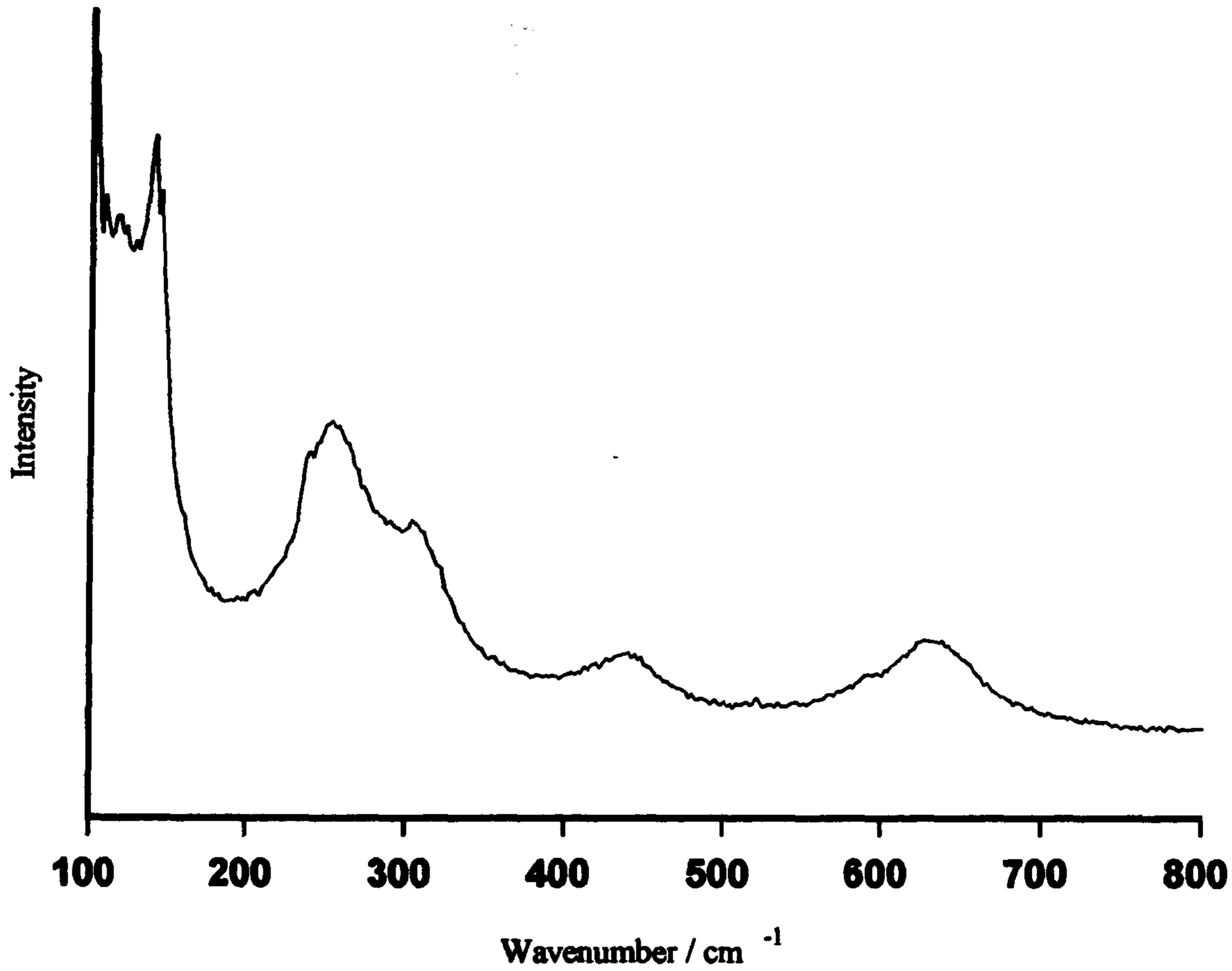


***Figure 5.4 - Raman spectrum recorded from $ZrO_2$ produced by boiling zirconium(IV) acetate under reflux in $H_2O$, drying under an infra red lamp, and subsequent calcination at 500°C***

This suggests that decomposition of the hydroxide/oxide species occurred on calcination, producing crystalline tetragonal zirconia. The spikes on the trace in Figure 5.6 are a result of the measurement being at the limit of detection of the equipment. Further TGA/DTA is required to identify the decomposition products and identify a crystallisation pathway.

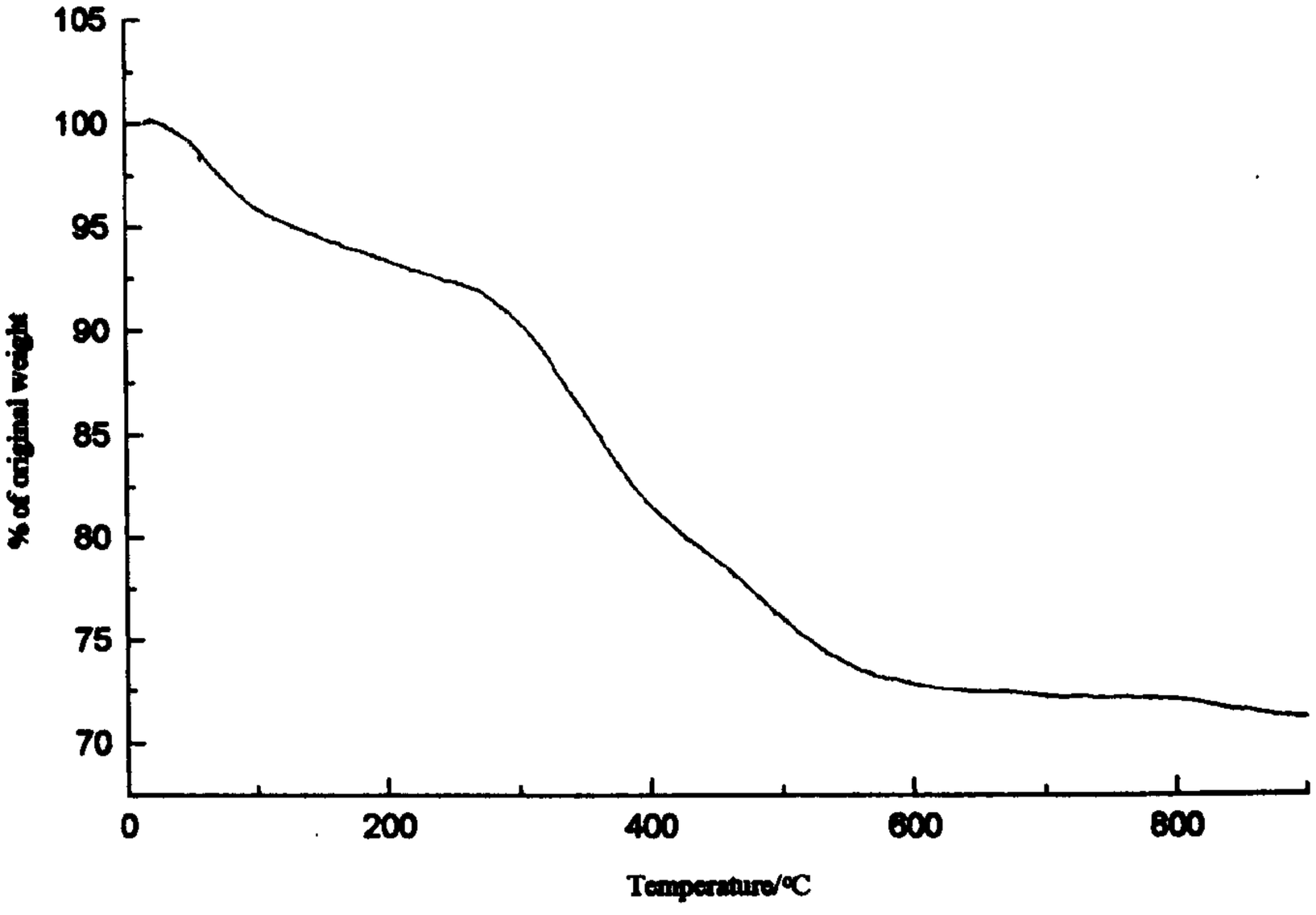


***Figure 5.5 - TGA trace recorded from zirconium(IV) acetate boiled under reflux in $H_2O$, dried under an infra red lamp, and calcined at 200°C***

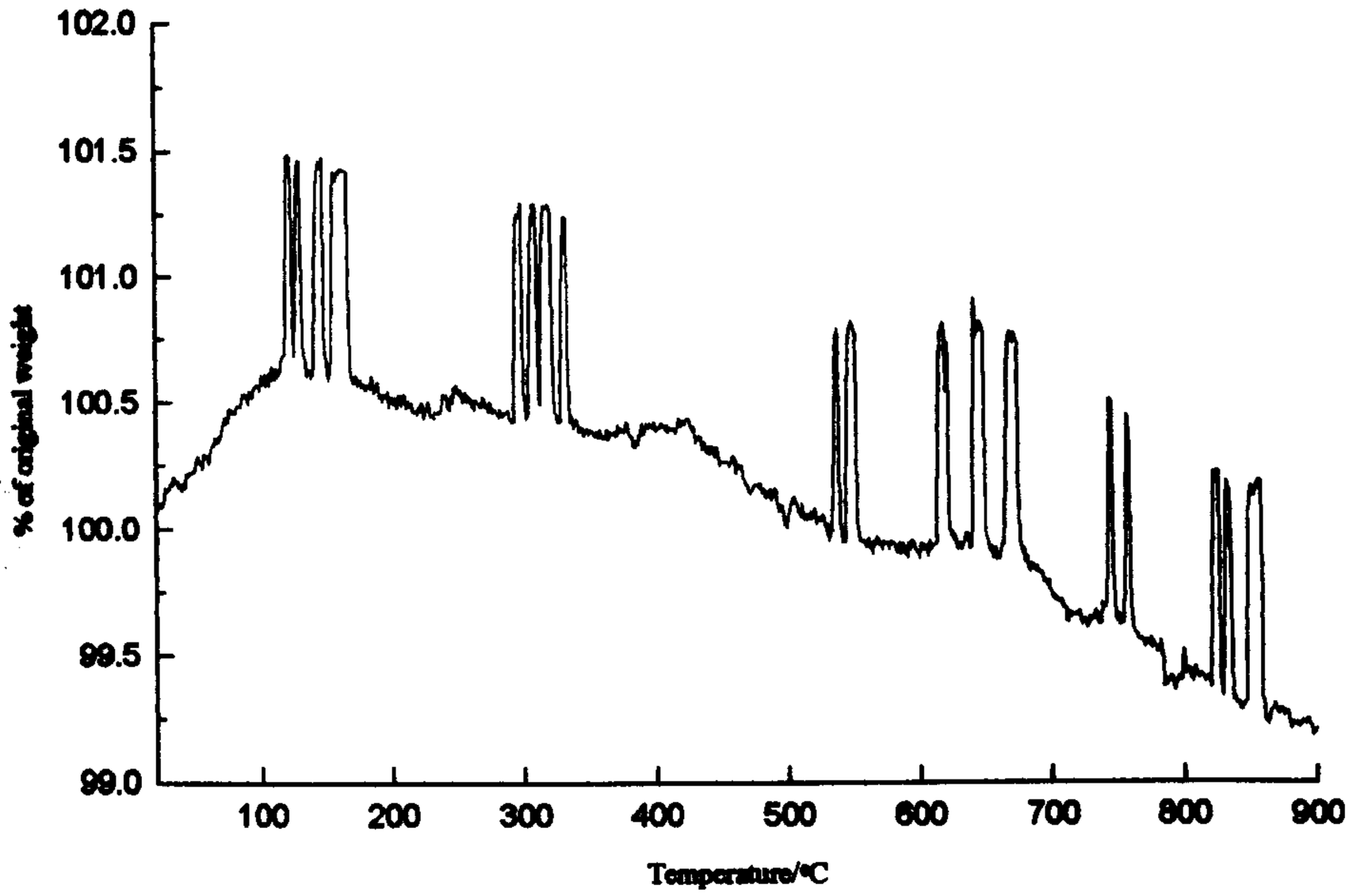


***Figure 5.6 - TGA trace recorded from zirconium(IV) acetate boiled under reflux in $H_2O$, dried under an infra red lamp, and calcined at 500°C***

The X-ray powder diffraction pattern recorded from the material calcined at 900°C showed there to be a second phase coexisting with the tetragonal phase which was characterised by peaks at $2\theta = 27^{o}$ and $31^{o}$. This was identified as monoclinic zirconia,[15] Figure 5.2d. After calcination at 1400°C the tetragonal phase had disappeared, Figure 5.2e. The amount of monoclinic $ZrO_2$ present in the samples, Table 5.1, was determined from the X-ray powder diffraction pattern using the method proposed by Suyama et al.[16] The intensities of the tetragonal [1 1 1] and monoclinic [1 1 $\bar{1}$] peaks were related to the fraction of the tetragonal phase present by the relationship

$$F_t = \frac{1}{1 + 2.2 I_m / I_t}$$

where $F_t$ = fraction of tetragonal zirconia, $I_m$ = intensity of the [1 1 $\bar{1}$] peak in the X-ray powder diffraction pattern of monoclinic $ZrO_2$, and $I_t$ = intensity of the [1 1 1] peak in the X-ray powder diffraction pattern of tetragonal $ZrO_2$. For the purposes of the determination of the amount of monoclinic $ZrO_2$ present the broadened tetragonal/cubic lines were regarded as a single phase of intensity $I_t$.

| Preparative Method | Amount (±5 %) of monoclinic $ZrO_2$ formed | | | | |
|---|---|---|---|---|---|
| | dried under IR lamp | 200°C | 500°C | 900°C | 1400°C |
| Reflux/$H_2O$ | 0 | 0 | 0 | 87 | 100 |
| Reflux/excess conc. HCl | 0 | 0 | 0 | 95 | 100 |
| /1M. HCl/pH 1.0 | 0 | 0 | 0 | 77 | 100 |
| /conc. HCl/pH 0.5 | 0 | 0 | 0 | 57 | 100 |
| Reflux/$NH_4OH$ | 0 | 0 | 0 | 3 | 100 |
| Precipitate with $NH_4OH$ | 0 | 0 | 0 | 92 | 100 |

*Table 5.1 - Amount of monoclinic zirconia formed by calcination in air as determined by X-ray powder diffraction*

Line broadening of X-ray powder diffraction patterns may be associated with either small particle size or poor crystallinity. The size of the particles present can be estimated from the peak width by using the Scherrer equation, Section 2.1.1. Using this equation gave a

particle size of the order of 10nm for the material produced by calcination at 500°C. After calcination at 1400°C the particle size had increased to 45nm.

Increasing calcination temperature also leads to improved crystallinity, giving sharper peaks in the X-ray powder diffraction pattern, Figure 5.2c-e. Electron diffraction patterns were recorded from a sample which X-ray powder diffraction had shown to be of broad peak width (i.e. the material calcined at 500°C). The electron diffraction pattern, Figure 5.7, showed rings indicative of poor crystallinity in contrast to a pattern of regular spots which would have been expected from a highly crystalline material. This indicated that the broadening of the X-ray powder diffraction pattern was due to poorly crystalline material rather than small particle size.

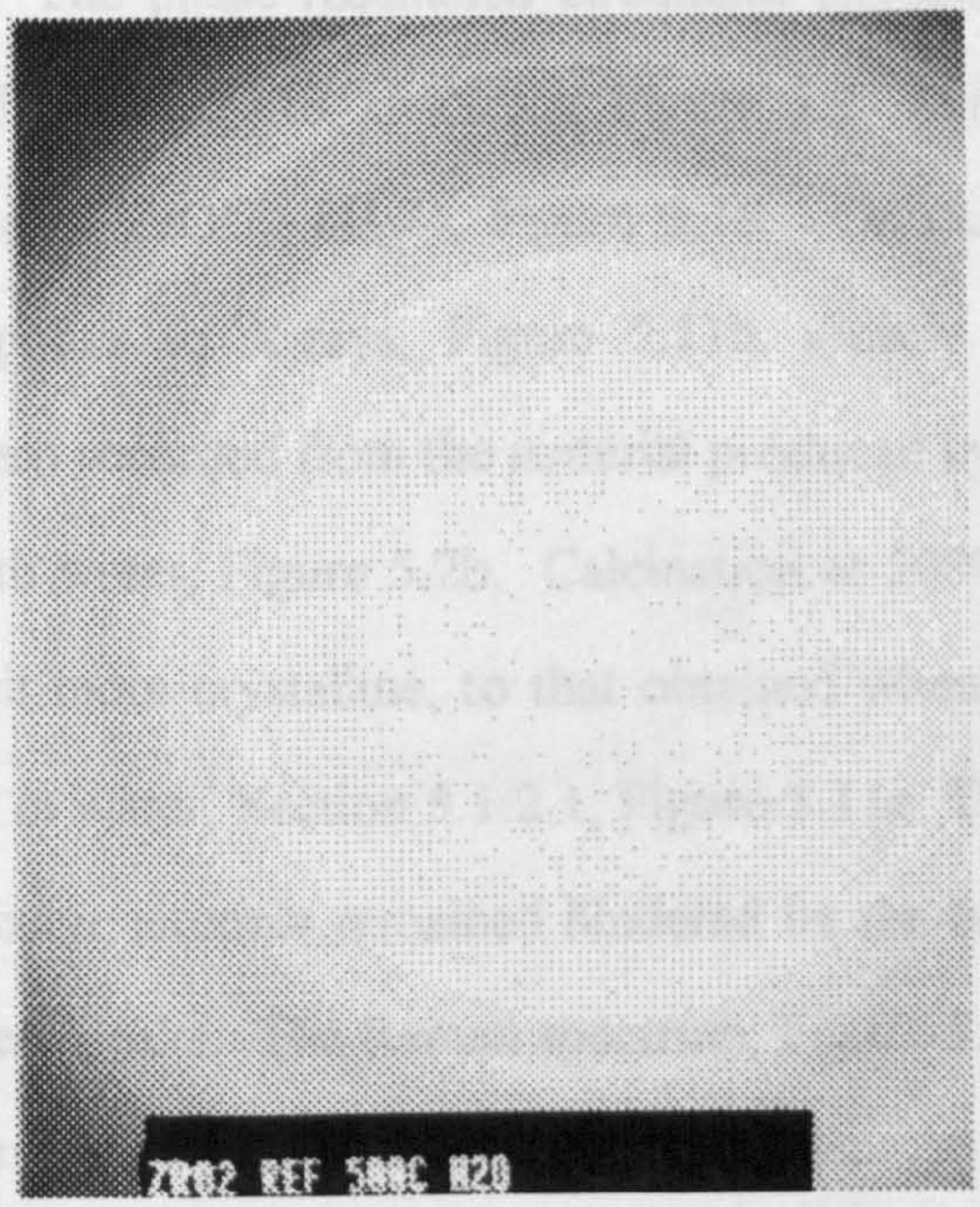

***Figure 5.7 - Electron diffraction pattern recorded from $ZrO_2$ synthesised by boiling zirconium(IV) acetate under reflux, dried under an infra red lamp and calcined at 500°C***

It may therefore be envisaged that by boiling zirconium(IV) acetate under reflux conditions there is a slow polymerisation of the aqueous tetrameric $[Zr(OH)_2.4H_2O]_4^{8+}$ species to amorphous zirconia. Drying under an infra red lamp causes the dehydration of

the polymeric species which form poorly crystalline cubic zirconia. As the calcination temperature is increased to 500°C there is a phase transformation to the fluorite related tetragonal phase. Heating to higher temperatures induces a further phase transformation to the stable monoclinic polymorph.

### 5.1.2.2 Synthesis with HCl

Hydrochloric acid was used to study the effect of low pH on the synthesis of zirconia. The X-ray powder diffraction pattern of the material dried under an infra red lamp, Figure 5.8, showed HCl to have a dramatic effect on the nature of the product. The phase produced could not be identified as a zirconia phase or the starting material, zirconium(IV) acetate. The phase resembled zirconium oxychloride,[17] $ZrOCl_2.xH_2O$, and this was confirmed by the FTIR spectrum, Figure 5.9, which was similar to that recorded from a sample of $ZrOCl_2.8H_2O$, Figure 5.10. On calcination at 200°C the material became amorphous to X-rays, Figure 5.11b, closely resembling the X-ray powder diffraction pattern recorded from the material produced by boiling zirconium(IV) acetate under reflux with water, Figure 5.2b. Calcination at 500°C produced a material which was similar, albeit more crystalline, to that obtained when zirconium(IV) acetate was boiled under reflux in water, Section 5.1.2.1, Figure 5.11c. The identification of this phase as tetragonal or cubic zirconia remained hindered by the broadening of the X-ray powder diffraction pattern peaks. The Raman spectrum, Figure 5.12, clearly consisted of 6 bands and showed that the material was tetragonal zirconia.

The TGA trace recorded from the material calcined at 500°C, Figure 5.13, showed a 3.5% weight loss from the original mass. The small weight loss indicates that any hydroxide/oxide phase present in the dried material had decomposed on calcination at 500°C leaving only the crystalline tetragonal zirconia. Further investigations of the thermal behaviour of this material are required.

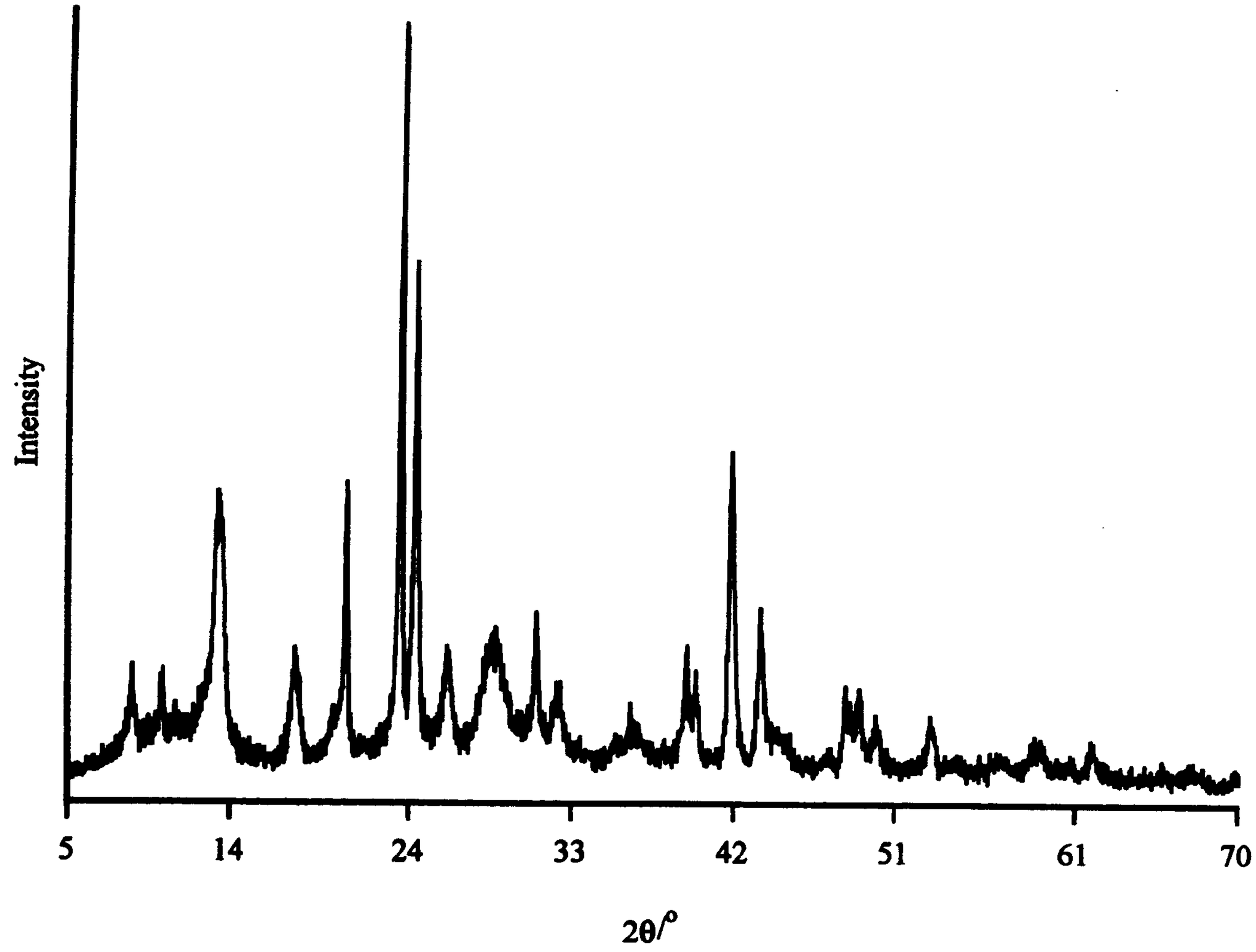


***Figure 5.8 - X-ray powder diffraction pattern recorded from zirconium(IV) acetate boiled under reflux with HCl and dried under an infra red lamp***

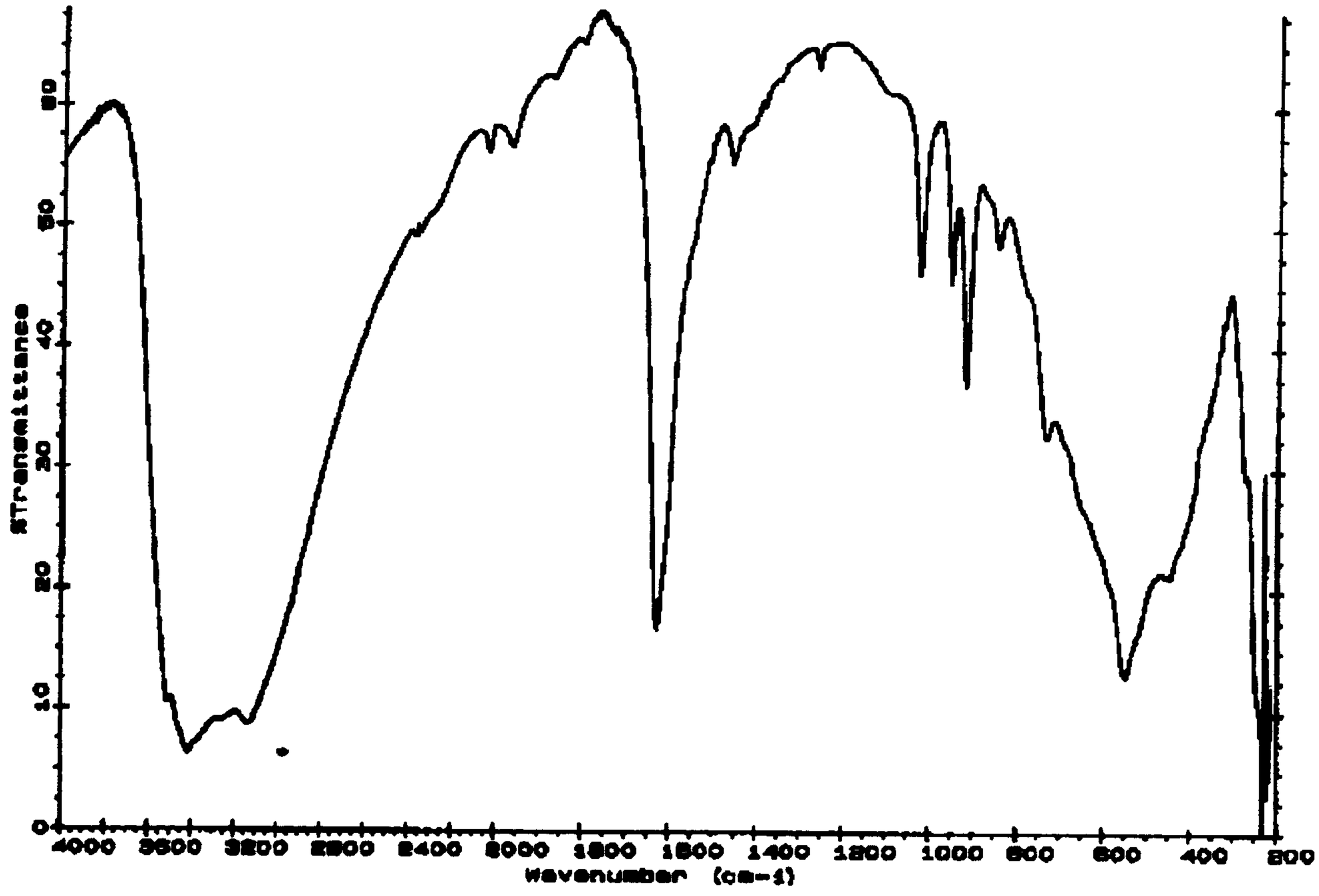


***Figure 5.9 - FTIR spectrum recorded from zirconium(IV) acetate boiled under reflux with HCl and dried under an infra red lamp***

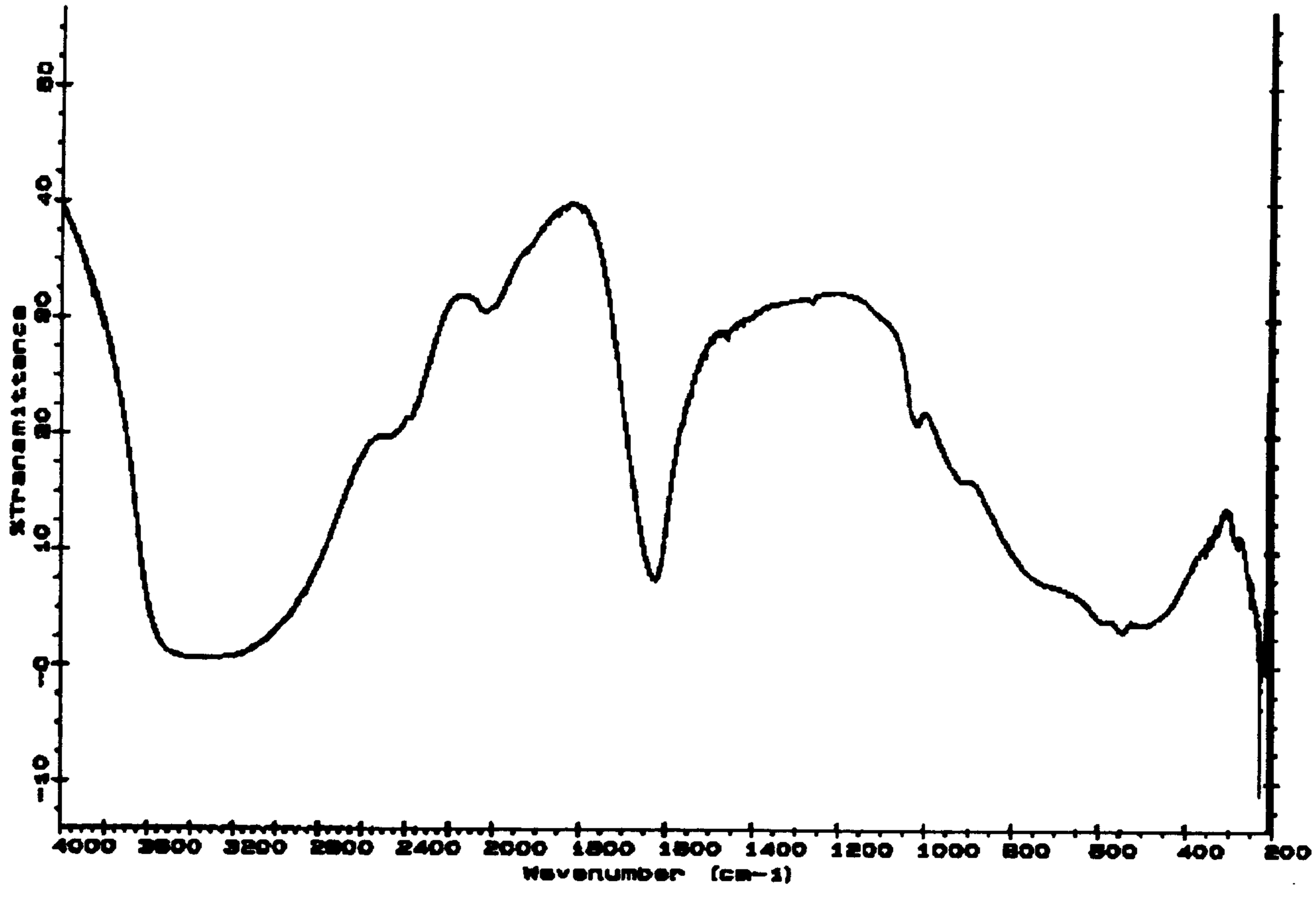


*Figure 5.10 - FTIR spectrum of $ZrOCl_2.8H_2O$*

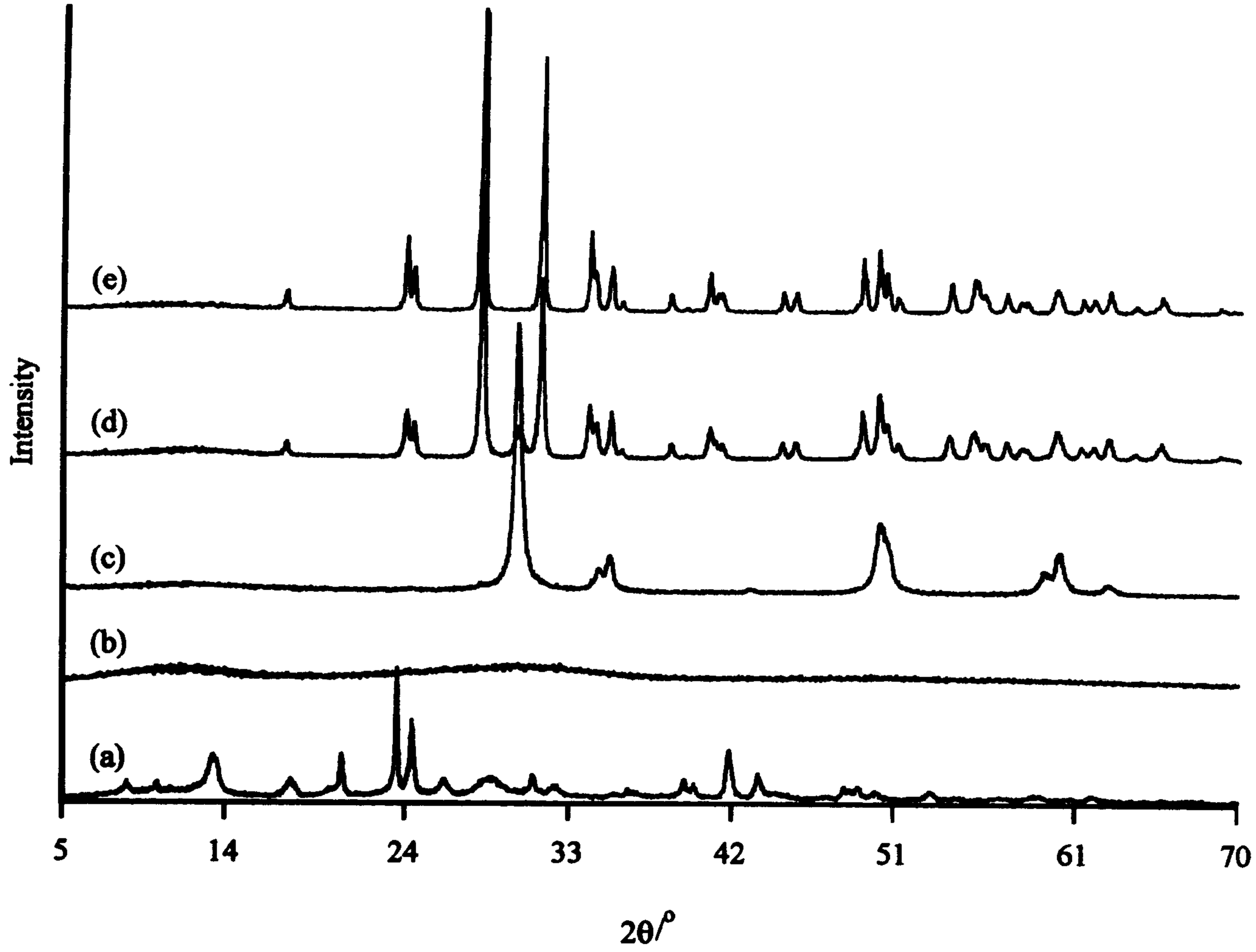


***Figure 5.11 - X-ray powder diffraction patterns recorded from zirconium(IV) acetate boiled under reflux with HCl and (a) dried under an infra red lamp and calcined at (b) 200°C, (c) 500°C, (d) 900°C and (e) 1400°C***

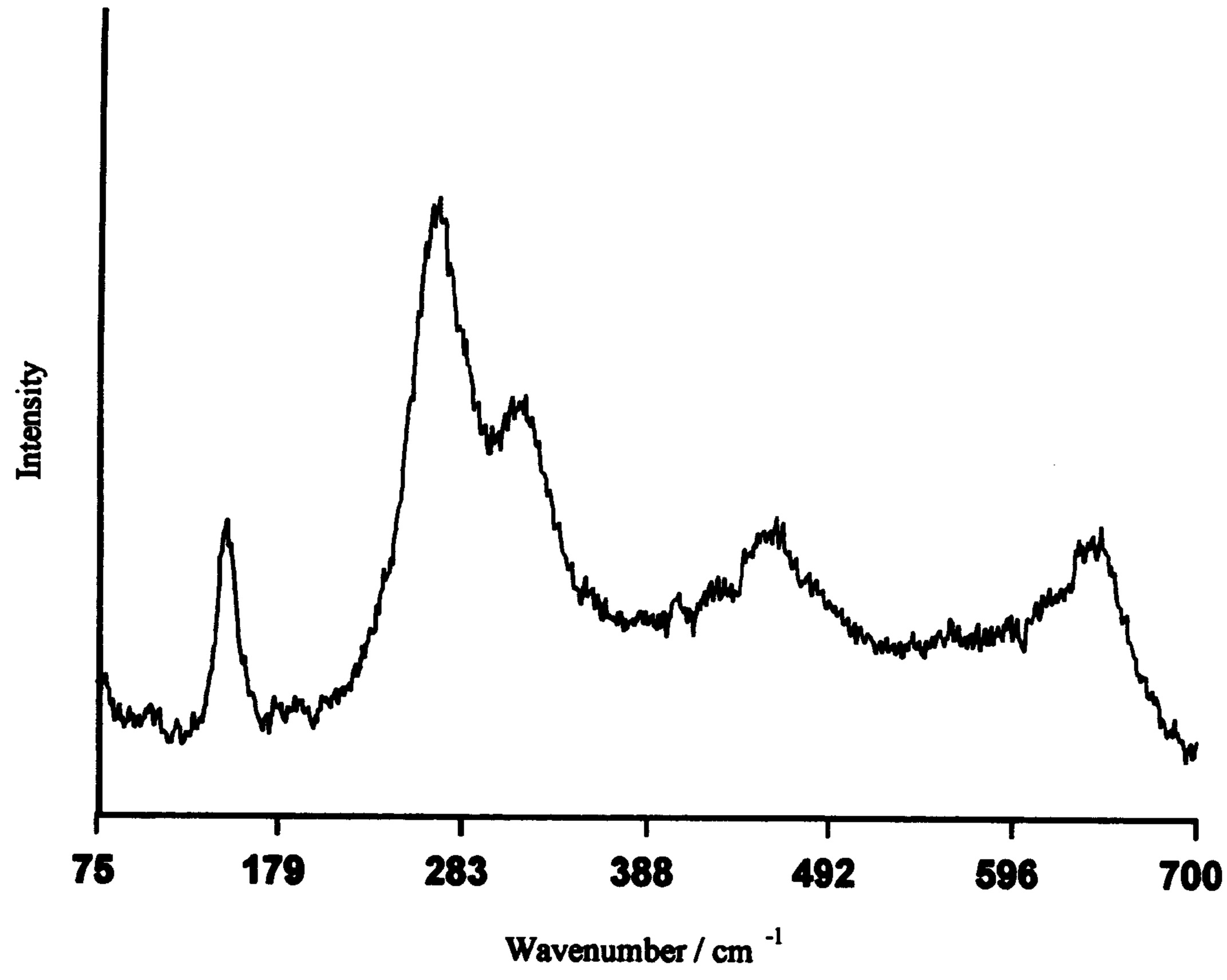


***Figure 5.12 - Raman spectrum recorded from zirconium(IV) acetate boiled under reflux with HCl, dried under an infra red lamp, and calcined at 500°C***

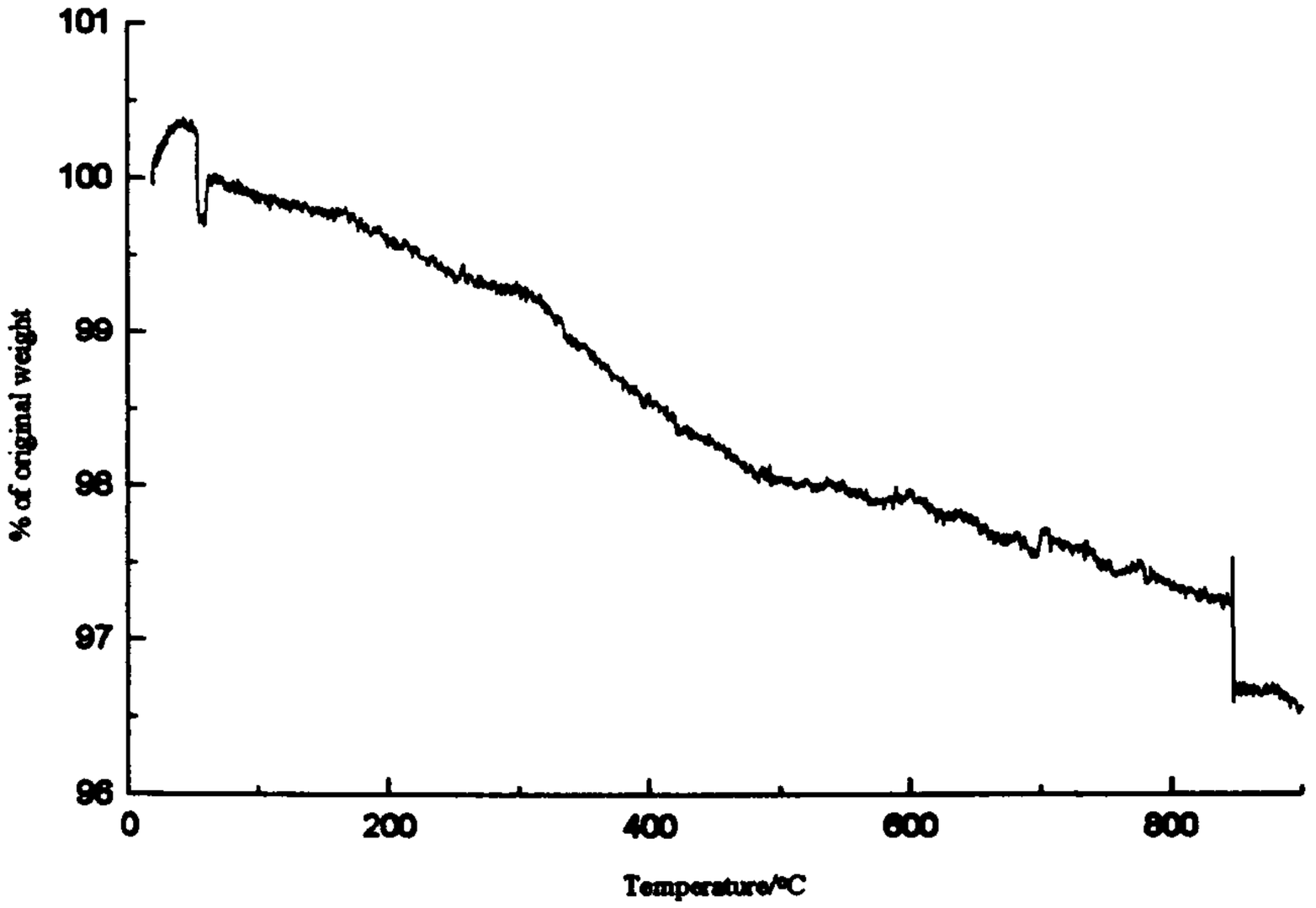


***Figure 5.13 - TGA trace recorded from zirconium(IV) acetate boiled under reflux in HCl, dried under an infra red lamp, and calcined at 500°C***

After calcination at 900°C the predominant phase was, as expected, the monoclinic polymorph, Figure 5.11d, but this phase was present in greater quantity than that produced at the same temperature from the material formed by boiling zirconium(IV) acetate with water, Table 5.1.

The X-ray powder diffraction pattern recorded from the material after calcination at 1400°C, Figure 5.11e, was indicative of monophasic, monoclinic material, in agreement with earlier observations.[15] Adjusting the pH of the zirconium(IV) acetate solution with HCl also affected the crystallinity of the zirconyl oxychloride phase produced before calcination, with the less crystalline sample being produced at higher pH, Figure 5.14. The amount of monoclinic $ZrO_2$ produced after calcination at 900°C was also affected by the pH of the initial zirconium(IV) acetate solution, Table 5.1. The zirconia produced from the solution of lowest pH, that in excess concentated HCl, produced more of the monoclinic phase after calcination at 900°C. The formation of a zirconyl oxychloride phase is indicative of the reaction of the $[Zr(OH)_2.4H_2O]_4^{8+}$ species with the chloride ions. The presence of chloride ions has been reported[18] to disrupt the polymerisation of this tetrameric species.

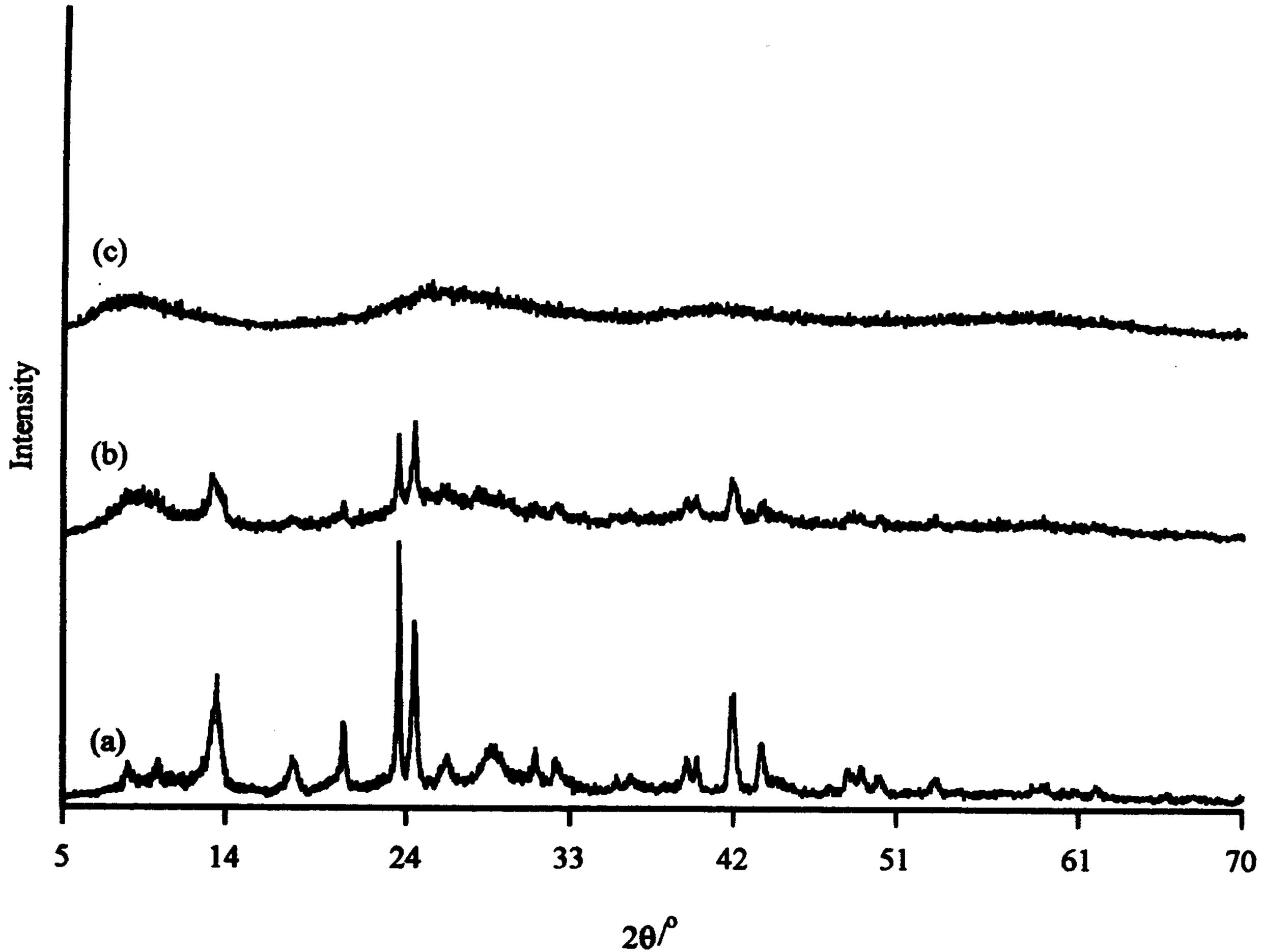


***Figure 5.14 - X-ray powder diffraction patterns recorded from the material produced by boiling zirconium(IV) acetate under reflux with (a) conc. HCl, (b) at pH = 0.5 and (c) at pH = 1.0***

Also the transformation of the $ZrOCl_2.xH_2O$ phase to tetragonal zirconia via an amorphous phase has been associated with initial dehydration processes.[19] It is therefore reasonable to assume that the phase produced by calcination at 200°C is a chloride-containing hydrous zirconia. The variation in the crystallinity of the oxychloride phase with pH also supports the findings that the presence of high concentrations of chloride ions disrupts the polymerisation process. Another factor which may influence the initial reaction process is the possible similarity between the structure of aqueous zirconium(IV) acetate and that of zirconyl oxychloride, as both are likely to contain the $[Zr(OH)_2.4H_2O]_4^{8+}$ species.

### 5.1.2.3 Synthesis with $NH_4OH$

The use of aqueous ammonia to adjust the pH of the zirconium(IV) acetate solution caused the formation of a white precipitate which has been described as hydrous zirconia,[1] and to result from hydrolytic polymerisation,[1, 20] discussed in Section 5.1.1.

The X-ray powder diffraction pattern recorded from the material dried under an infra red lamp was indicative of an amorphous phase, Figure 5.15a. A similar pattern was recorded from the material calcined at 200°C, Figure 5.15b. On calcination at 500°C a crystalline phase was produced, Figure 5.15c, which indicated that either the tetragonal or cubic phase had been formed. Peak broadening precluded the differentiation between these two phases. The Raman spectrum recorded from the material calcined at 500°C, Figure 5.16, indicated that the phase formed was tetragonal $ZrO_2$. After calcination at 900°C there was evidence for the formation of a small amount of monoclinic $ZrO_2$, Figure 5.15d, but considerably less than in the previous two cases, Sections 5.1.2.1 and 5.1.2.2, Table 5.1. The use of $NH_4OH$ in the synthesis appears to stabilise tetragonal zirconia against transformation to the monoclinic phase. Addition of $NH_4OH$ to the initial solution causes an increase in the number of $OH^-$ groups present in comparison to the methods described earlier, Sections 5.1.2.1 and 5.1.2.2..

This is consistent with the results of work by Srinivasan et al[11, 21] who found that the fraction of monoclinic $ZrO_2$ present in materials prepared by the calcination of precipitates of nitrate or chloride solutions was dependent on the time taken to attain a set pH, with the smaller amount of monoclinic phase being associated with rapid precipitation.

The amorphous nature of the material formed by calcination at 200°C reflects the random polymerisation of the $[Zr(OH)_2.4H_2O]_4^{8+}$ species as indicated in Section 5.1.1, Figure 5.1a. The conversion of this material to the tetragonal phase at 500°C is the result of a loss of $OH^-$ groups through condensation. Therefore it seems reasonable to attribute the stabilisation of the tetragonal phase to the presence of the ammonia in the reaction mixture. It should also be noted that rapid addition of ammonia to a zirconium(IV) acetate solution which was then dried under an infra red lamp gave an amorphous material, which on treatment at 500°C formed a crystalline phase, Figure 5.17, identified as tetragonal zirconia. The mechanism by which this occurred was presumably a condensation process similar to that observed with the material produced by boiling zirconium(IV) acetate under reflux in $NH_4OH$. A comparison of the relative amounts of monoclinic zirconia produced by these two methods, Table 5.1, indicates that boiling the precipitate under reflux stabilises the tetragonal phase against transformation to the monoclinic phase after calcination at 900°C. This may be due to the polymerisation of the tetrameric species occurring rapidly on precipitation but more slowly when boiled under reflux, allowing ordering to occur, Section 5.1.1.

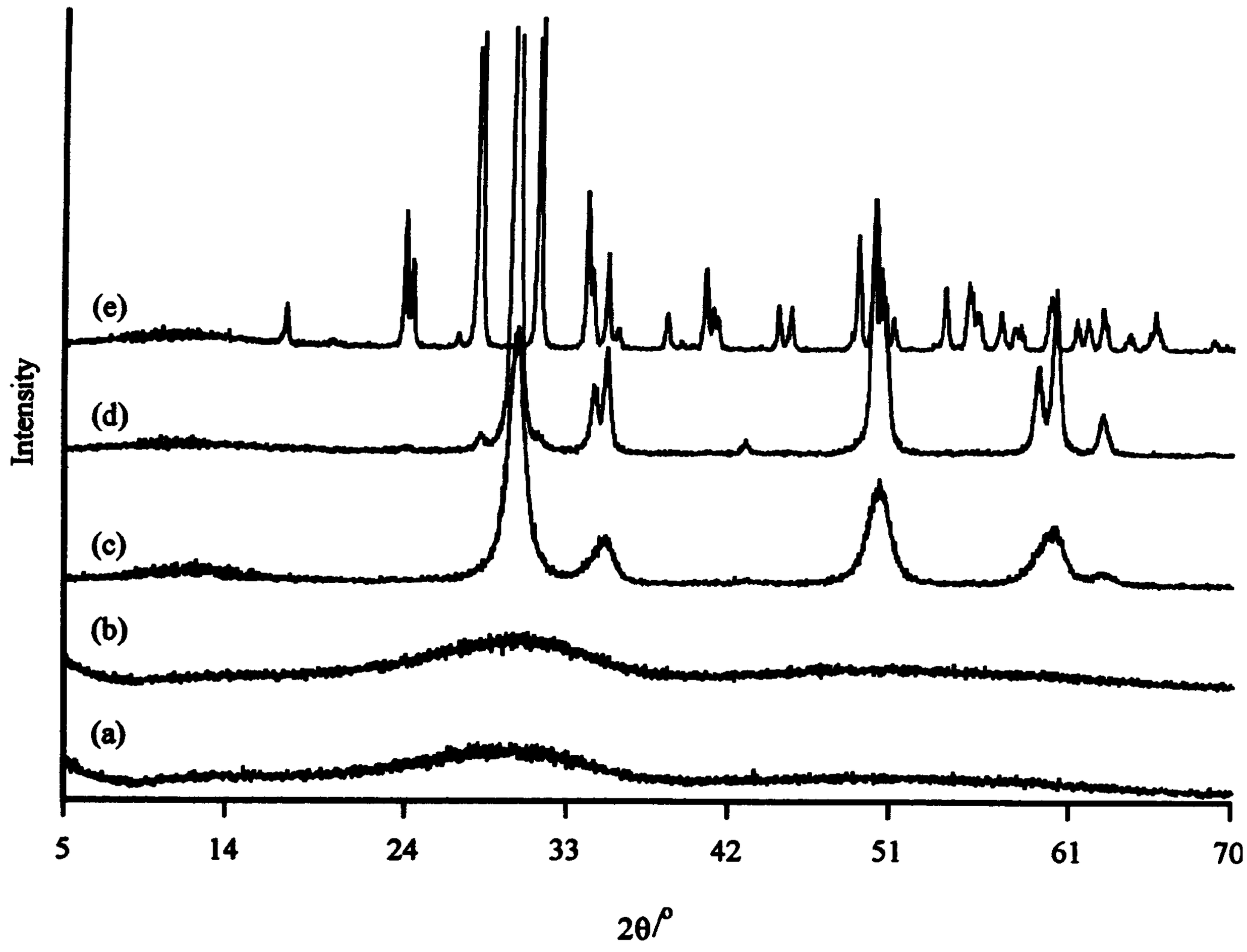


***Figure 5.15 - X-ray powder diffraction patterns recorded from zirconium(IV) acetate boiled under reflux with $NH_4OH$ and (a) dried under an infra red lamp and calcined at (b) 200°C, (c) 500°C, (d) 900°C and (e) 1400°C***

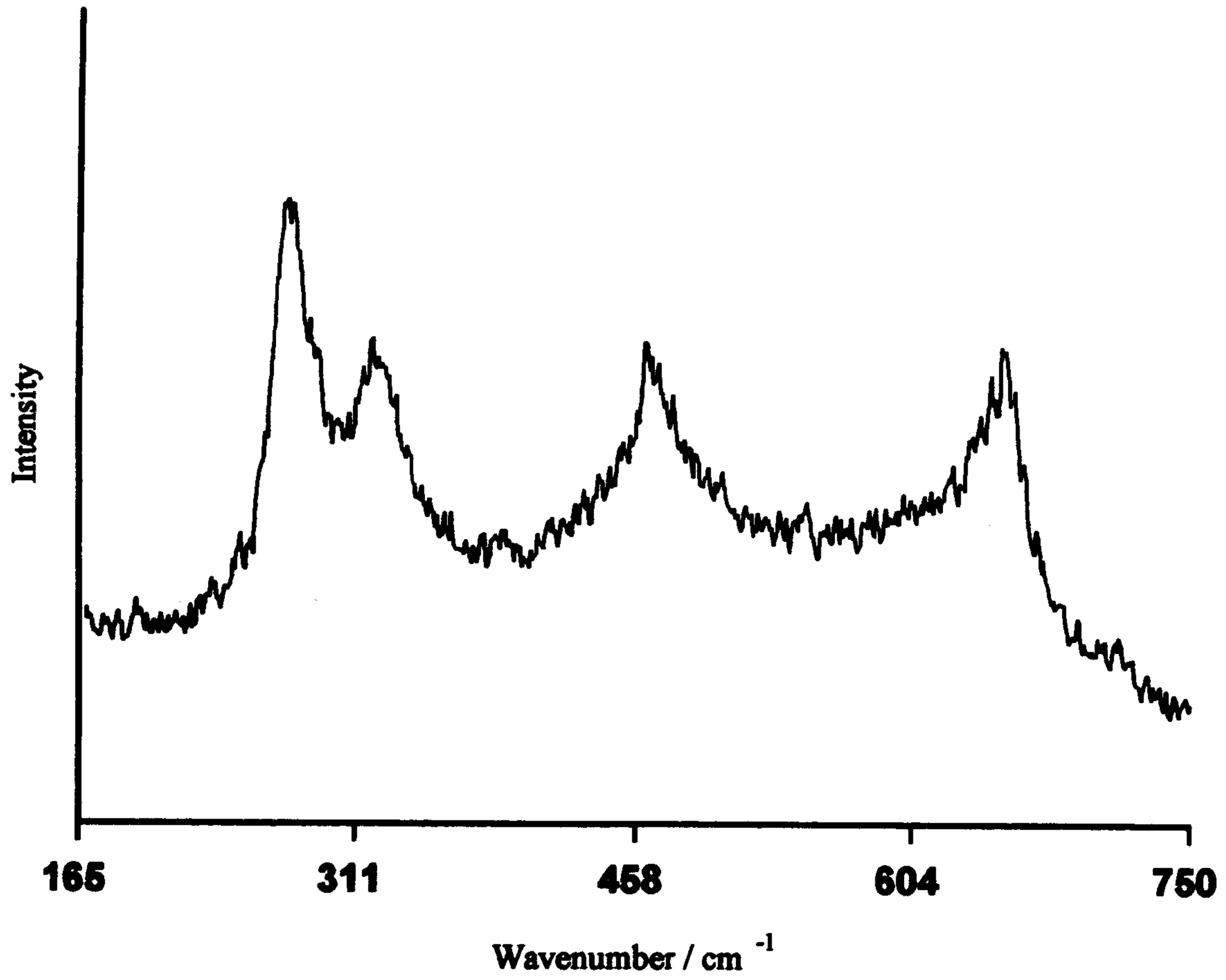


***Figure 5.16 - Raman spectrum recorded from $ZrO_2$ produced by boiling zirconium(IV) acetate under reflux with $NH_4OH$, dried under an infra red lamp, and subsequently calcined at 500°C***

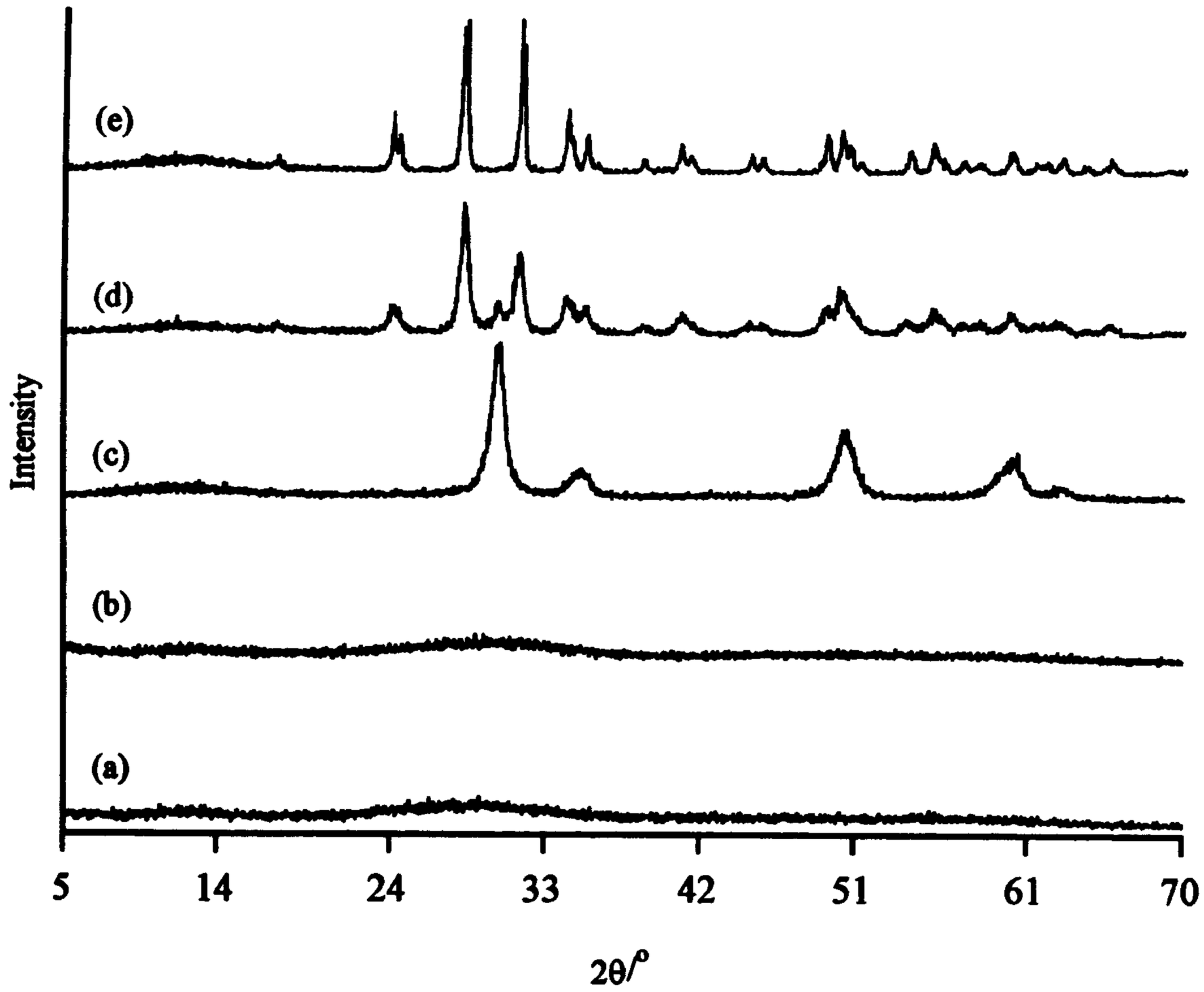


***Figure 5.17 - X-ray powder diffraction patterns recorded from zirconium(IV) acetate precipitated with $NH_4OH$ and (a) dried under an infra red lamp and calcined at (b) 200°C, (c) 500°C, (d) 900°C and (e) 1400°C***

### 5.1.3 Hydrothermal synthesis of $ZrO_2$

#### 5.1.3.1 Synthesis with $H_2O$

The X-ray powder diffraction pattern recorded from the material dried under an infra red lamp, Figure 5.18a, showed that the initial product was a mixture of two phases, identified as monoclinic zirconia[15] and either cubic[9] or tetragonal zirconia[10] with the major phase being the tetragonal/cubic phase, Table 5.2. Raman spectroscopy, Figure 5.19, indicated that the major phase present was the tetragonal zirconia. Calcination at 200°C induced no change in the phase composition, Table 5.2, Figure 5.18b. Calcination at 500°C was found by X-ray powder diffraction, Figure 5.18c, to have no influence on the relative amount of each phase present.

| | Amount (±5 %) of monoclinic $ZrO_2$ formed | | | | |
|---|---|---|---|---|---|
| Preparative Method | dried under IR lamp | 200°C | 500°C | 900°C | 1400°C |
| Hydrothermal/$H_2O$ | 45 | 45 | 42 | 92 | 100 |
| Hydrothermal/HCl | 100 | 100 | 100 | 100 | 100 |
| Hydrothermal/$NH_4OH$ | 20 | 26 | 28 | 57 | 100 |
| Hydrothermal/$(CH_3)_3N$ | 26 | 36 | 44 | 92 | 100 |
| Hydrothermal/$CH_3COOH$ | 100 | 100 | 100 | 100 | 100 |

***Table 5.2 - Amount of monoclinic zirconia formed by calcination in air after hydrothermal synthesis as determined by X-ray powder diffraction***

After calcination at 500°C the amount of monoclinic $ZrO_2$ present was found to have decreased in comparison to the amount present after calcination at 200°C, Table 5.2. However it is likely that the decrease of only 3% is within the errors introduced into the calculation of the peak intensities through the poor quality of the X-ray powder diffraction pattern, Figure 5.18c. Calcination at 900°C produced an increase in the amount of monoclinic $ZrO_2$ present, Figure 5.18d. Further calcination at 1400°C caused

the transformation of the remaining tetragonal phase to the monoclinic form, Figure 5.18e.

The coexistence of the tetragonal and monoclinic polymorphs may be explained by two different models. Yanwei et al[22] suggested that amorphous zirconia has a short range structure with a greater resemblance to monoclinic zirconia than to the tetragonal polymorph. It was proposed that the monoclinic nuclei in the amorphous $ZrO_2$ could undergo several crystallisation routes, one of which resulted in the coexistence of the tetragonal and monoclinic polymorphs. The monoclinic nuclei were observed to partially convert to the tetragonal polymorph depending on the kinetic conditions and chemical environments in which the nuclei were formed.

It is envisaged that the material removed from the autoclave after hydrothermal processing was essentially amorphous. This material could then crystallise according to the earlier proposed mechanism[22] producing both tetragonal and monoclinic zirconia. An alternative explanation is that the aqueous tetrameric $[Zr(OH)_2.4H_2O]_4^{8+}$ species undergoes a process of hydrolytic polymerisation,[20] in much the same way as occurs when zirconia was produced by boiling zirconium(IV) acetate under reflux in water. The polymerisation process would produce the relatively unstable tetragonal polymorph which on heating transforms to the stable monoclinic polymorph. Further work is required to enable a distinction between these two mechanisms to be made.

### 5.1.3.2 Synthesis with HCl

The hydrothermal processing of a zirconium(IV) acetate solution with hydrochloric acid at pH = 1 produced a suspension which, when dried under an IR lamp, gave a material which the X-ray powder diffraction pattern showed to be monoclinic $ZrO_2$, Figure 5.20a. The peaks in the X-ray powder diffraction pattern were considerably broadened.

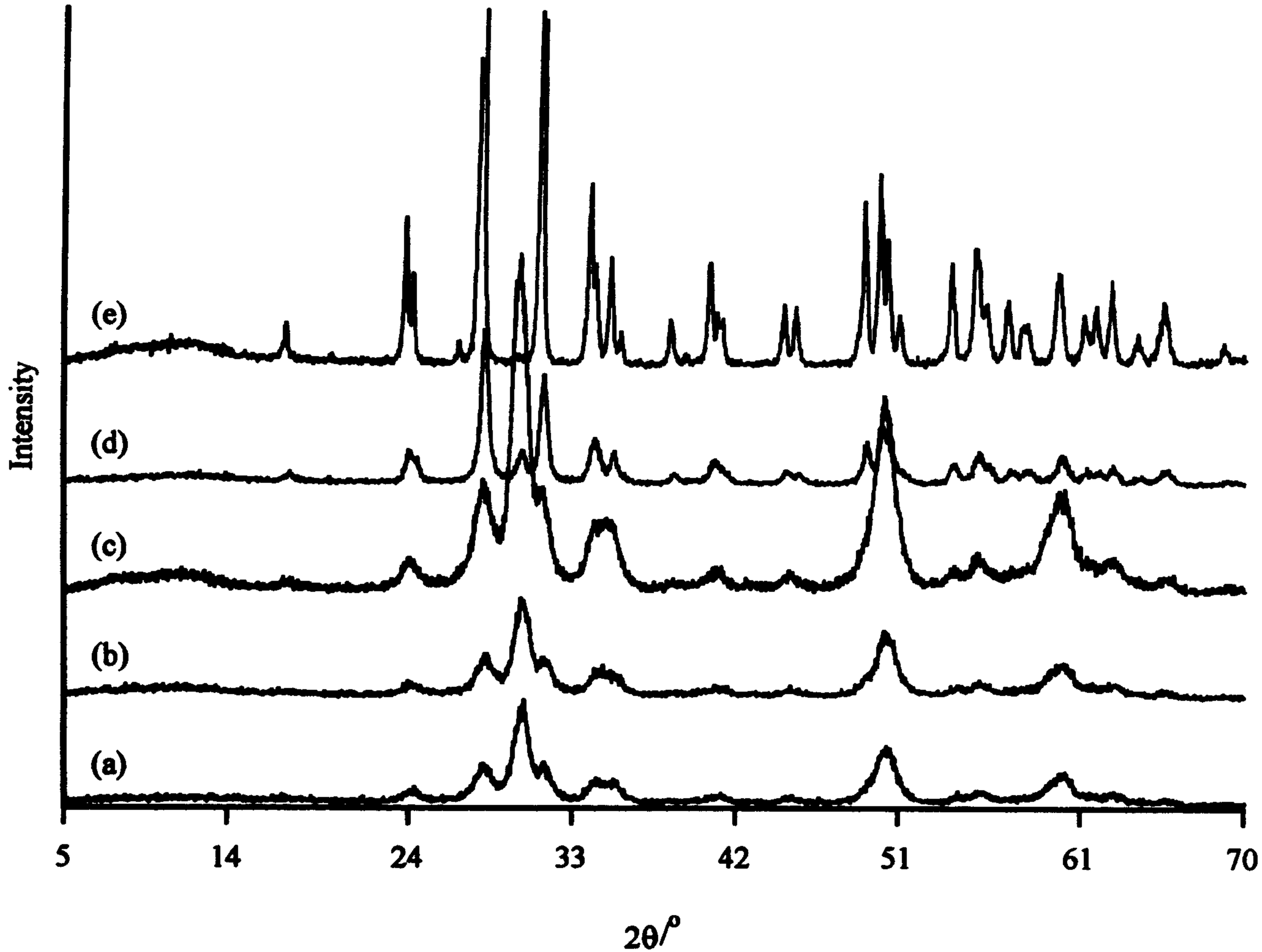


***Figure 5.18 - X-ray powder diffraction patterns recorded from zirconium(IV) acetate hydrothermally processed in $H_2O$ and (a) dried under an infra red lamp and calcined at (b) 200°C, (c) 500°C, (d) 900°C and (e) 1400°C***

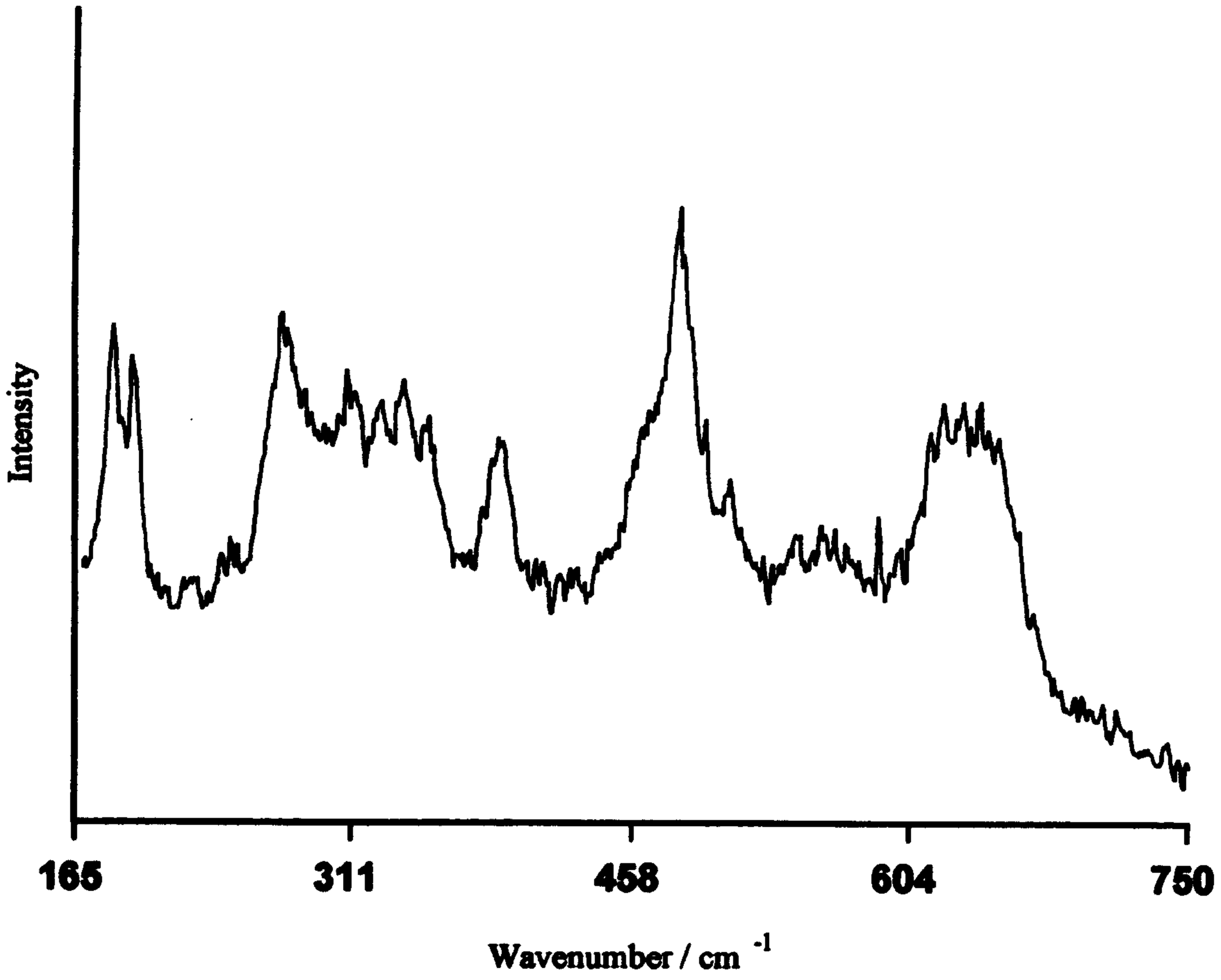


***Figure 5.19 - Raman spectrum recorded from zirconium(IV) acetate hydrothermally processed in $H_2O$ and dried under an infra red lamp***

On subsequent calcination at temperatures to 1400°C the width of the peaks decreased considerably, Figure 5.20b-e. The increasing sharpness of these peaks was found, by electron diffraction, Figure 5.21, to be due to increasing crystallinity rather than increasing particle size.

The formation of monophasic monoclinic zirconia under these conditions contrasts with the results obtained when zirconium(IV) acetate was boiled under reflux with HCl, Section 5.1.2.2, in which several stages of crystallisation occur, through an initial oxychloride phase until monoclinic $ZrO_2$ was produced at a calcination temperature of 900°C. To investigate whether a similar crystallisation process was occurring with the hydrothermal synthesis but proceeding at a faster rate due to the increased temperature and pressure, a sample of zirconium(IV) acetate in HCl was heated hydrothermally at 160°C at 2-3atm. pressure. The X-ray powder diffraction pattern of the dried material from this reaction, Figure 5.22, indicated that a zirconyl oxychloride phase had been produced.

The TGA trace recorded from the material produced by hydrothermal processing of zirconium(IV) acetate at 160°C and subsequently calcined at 500°C, Figure 5.23, showed a 3.5% weight loss from the original mass. The small weight loss indicates that any hydroxide/oxide phase present in the dried material had decomposed on calcination at 500°C leaving only the crystalline monoclinic zirconia. Further investigation of the thermal behaviour of this material is required.

It was also found that addition of zirconium(IV) acetate to HCl, followed by drying under an infra red lamp with no other processing, also produced an oxychloride phase. It is therefore reasonable to assume that in the hydrothermal processing of zirconium(IV) acetate in HCl the reaction proceeds via an oxychloride phase and that the use of hydrothermal processing causes the crystallisation pathway to proceed rapidly through the less stable polymorphs until monoclinic $ZrO_2$ is produced.

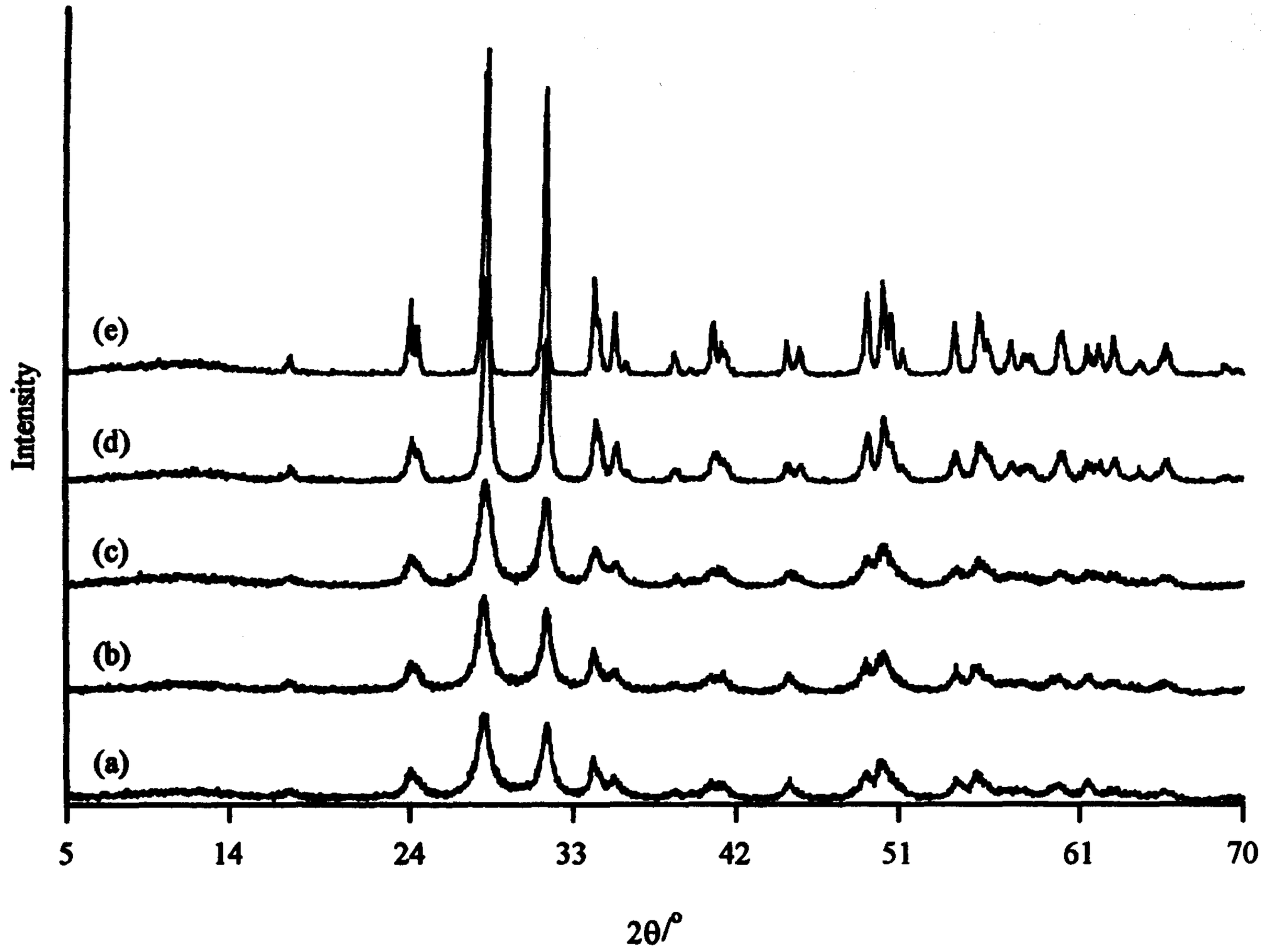


***Figure 5.20 - X-ray powder diffraction patterns recorded from zirconium(IV) acetate hydrothermally processed in HCl and (a) dried under an infra red lamp and calcined at (b) 200°C, (c) 500°C, (d) 900°C and (e) 1400°C***

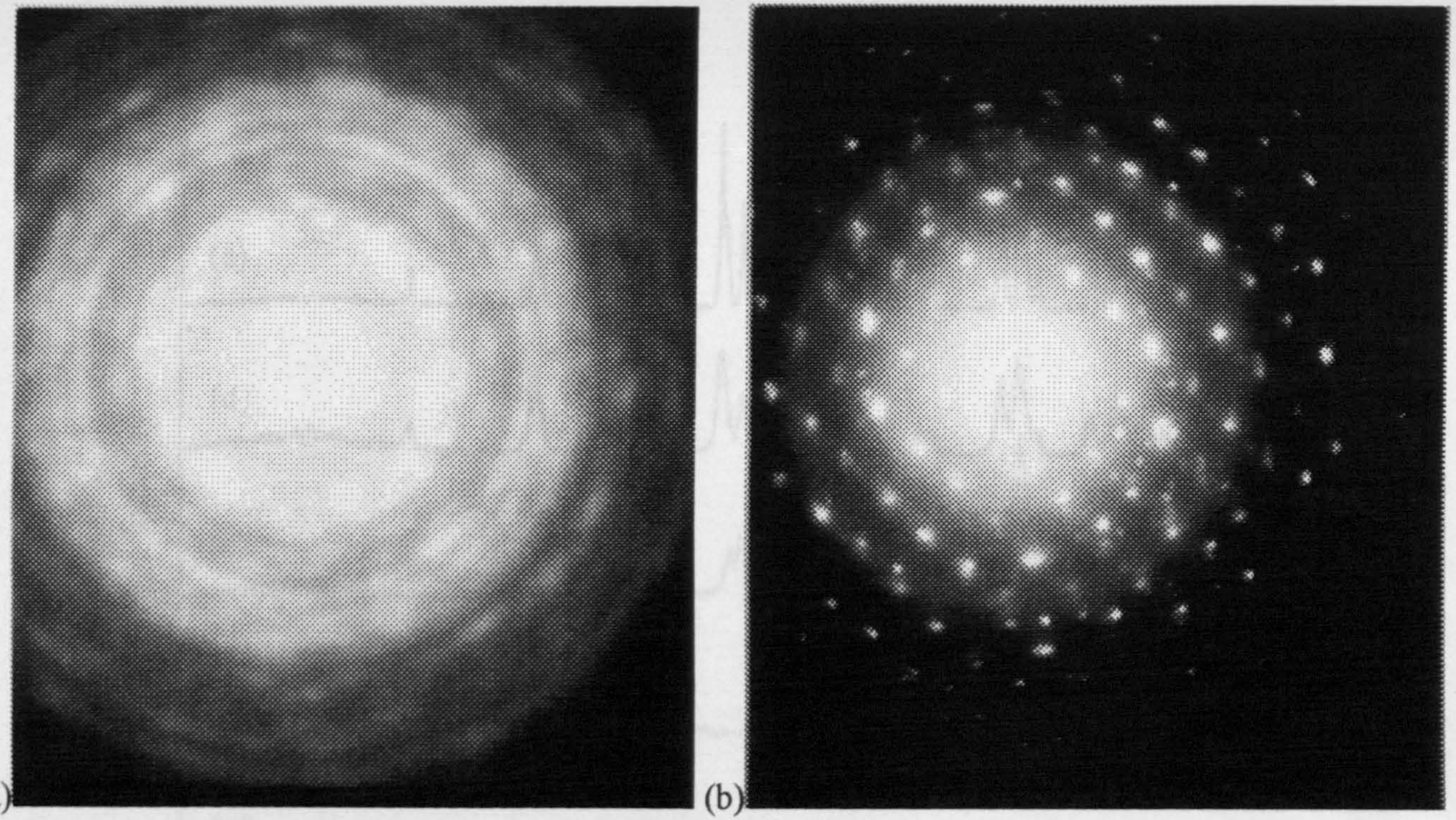

(a) (b)

***Figure 5.21 - Electron diffraction patterns recorded from $ZrO_2$ synthesised by hydrothermal processing in HCl (a) with no calcination and (b) calcined at 1400°C***

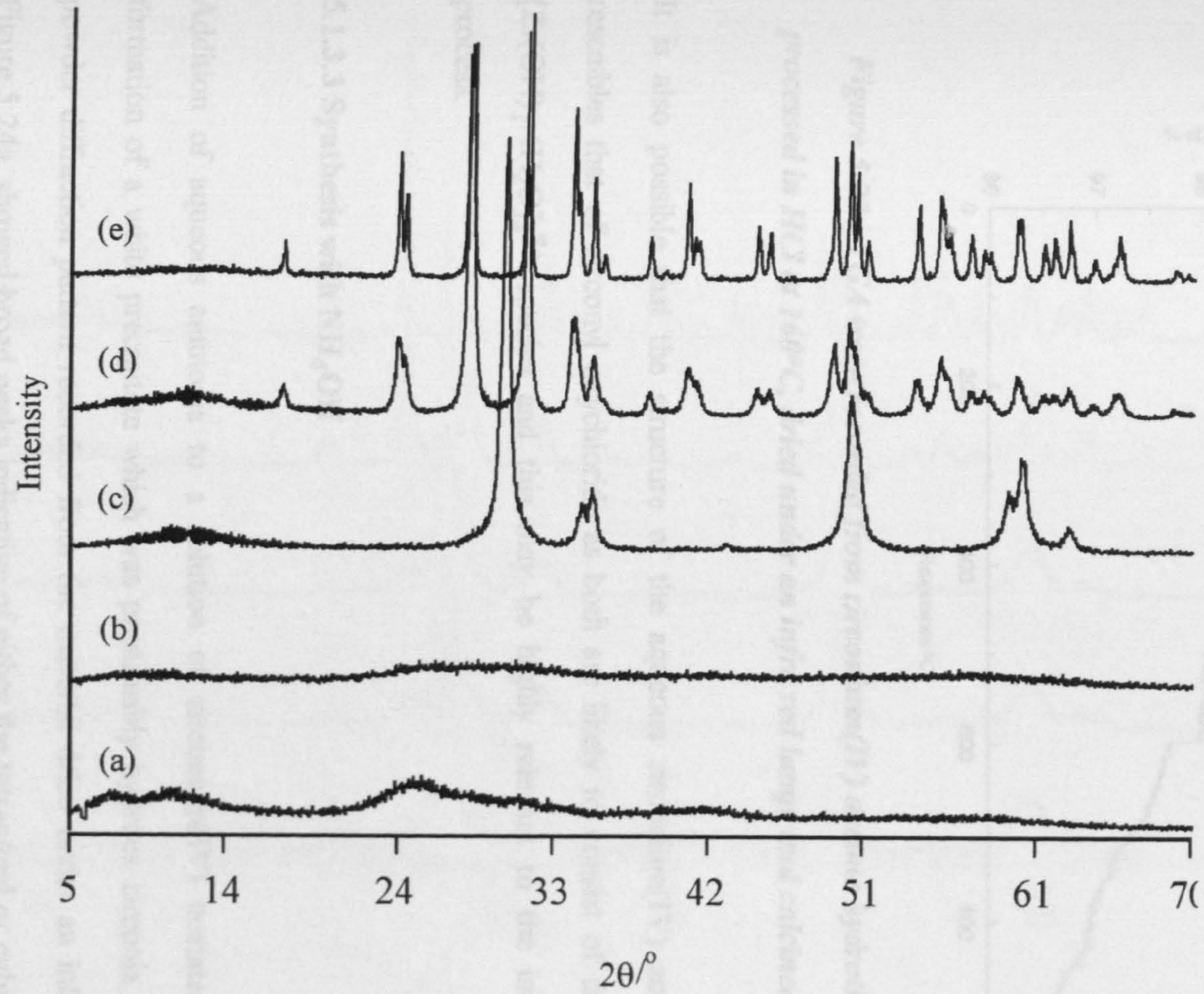


***Figure 5.22 - X-ray powder diffraction patterns recorded from zirconium(IV) acetate hydrothermally processed at 160°C in HCl and (a) dried under an infra red lamp and calcined at (b) 200°C, (c) 500°C, (d) 900°C and (e) 1400°C***

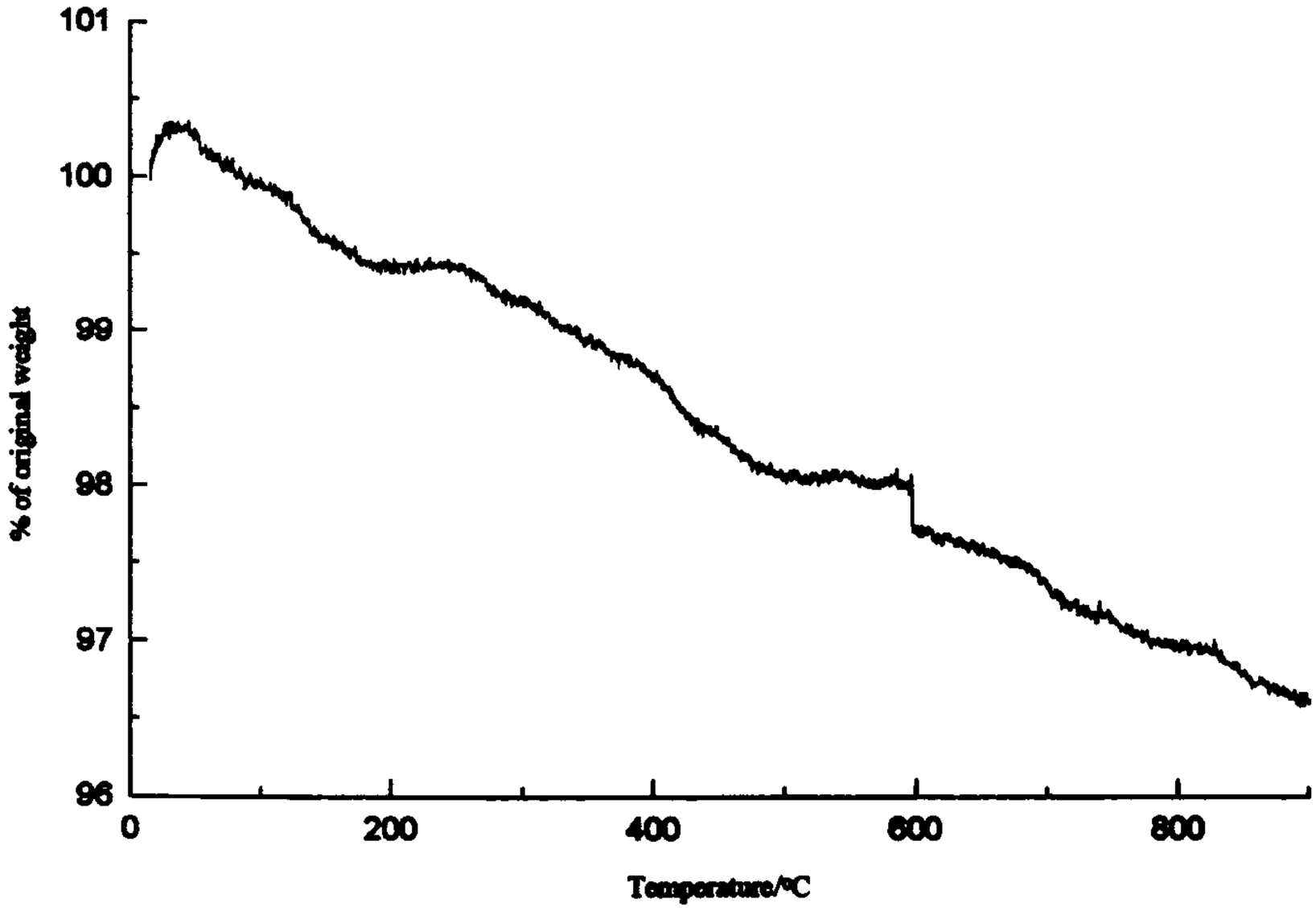


***Figure 5.23 - TGA trace recorded from zirconium(IV) acetate hydrothermally processed in HCl at 160°C, dried under an infra red lamp, and calcined at 500°C***

It is also possible that the structure of the aqueous zirconium(IV) acetate closely resembles that of zirconyl oxychloride as both are likely to consist of the tetrameric $[Zr(OH)_2.4H_2O]_4^{8+}$ species and this may be highly relevant to the initial reaction process.

### 5.1.3.3 Synthesis with $NH_4OH$

Addition of aqueous ammonia to a solution of zirconium(IV) acetate caused the formation of a white precipitate which was presumably hydrous zirconia. The X-ray powder diffraction pattern recorded from the material dried under an infra red lamp, Figure 5.24a, showed broad peaks indicative of either the tetragonal or cubic polymorph of $ZrO_2$ with evidence for a small amount of monoclinic $ZrO_2$, Table 5.2. The broad peak width precluded the determination of which polymorph of $ZrO_2$ was present as the majority phase. The Raman spectrum recorded from the dried material, Figure 5.25, showed peaks characteristic of both monoclinic and tetragonal $ZrO_2$.

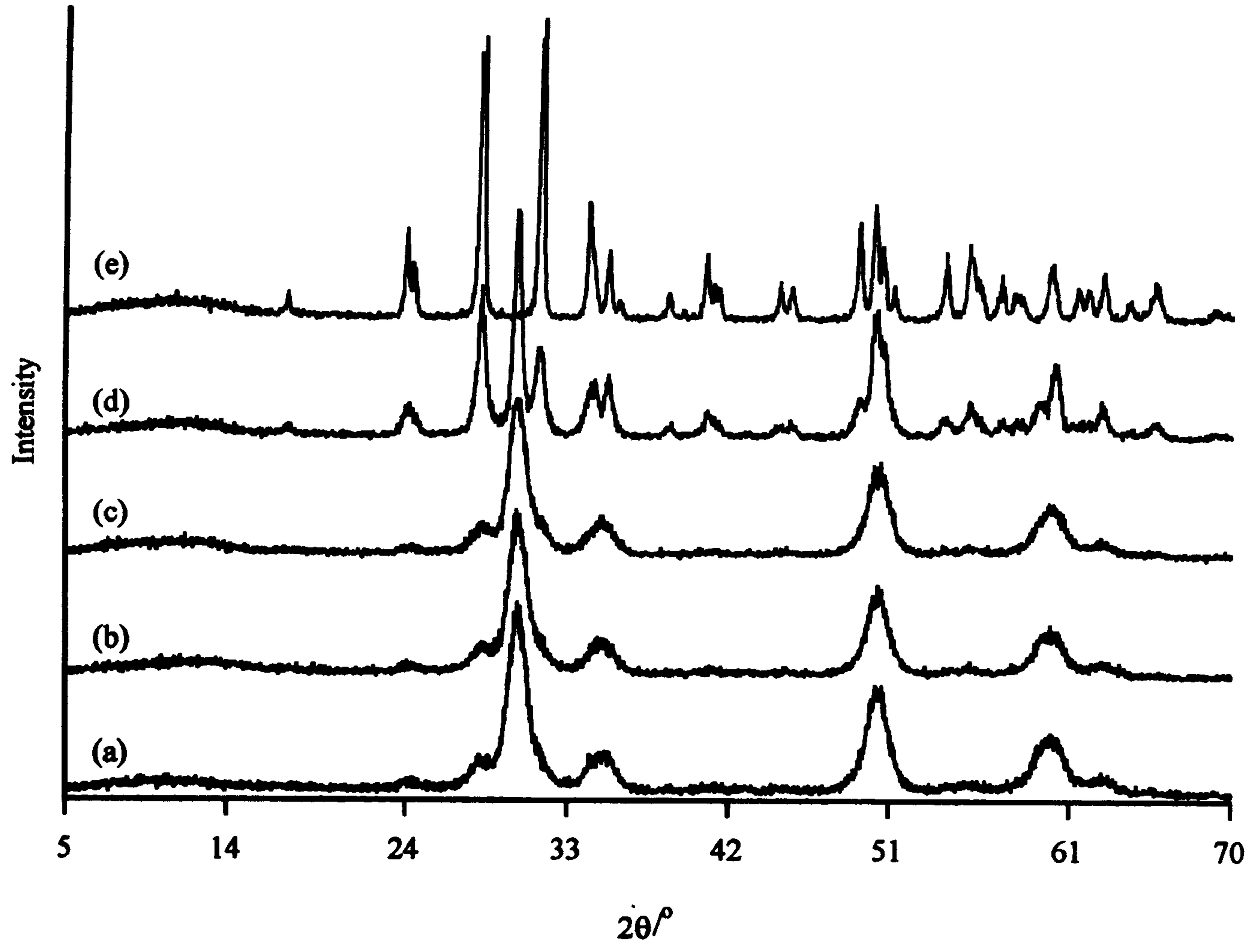


***Figure 5.24 - X-ray powder diffraction patterns recorded from zirconium(IV) acetate hydrothermally processed in $NH_4OH$ and (a) dried under an infra red lamp and calcined at (b) 200°C, (c) 500°C, (d) 900°C and (e) 1400°C***

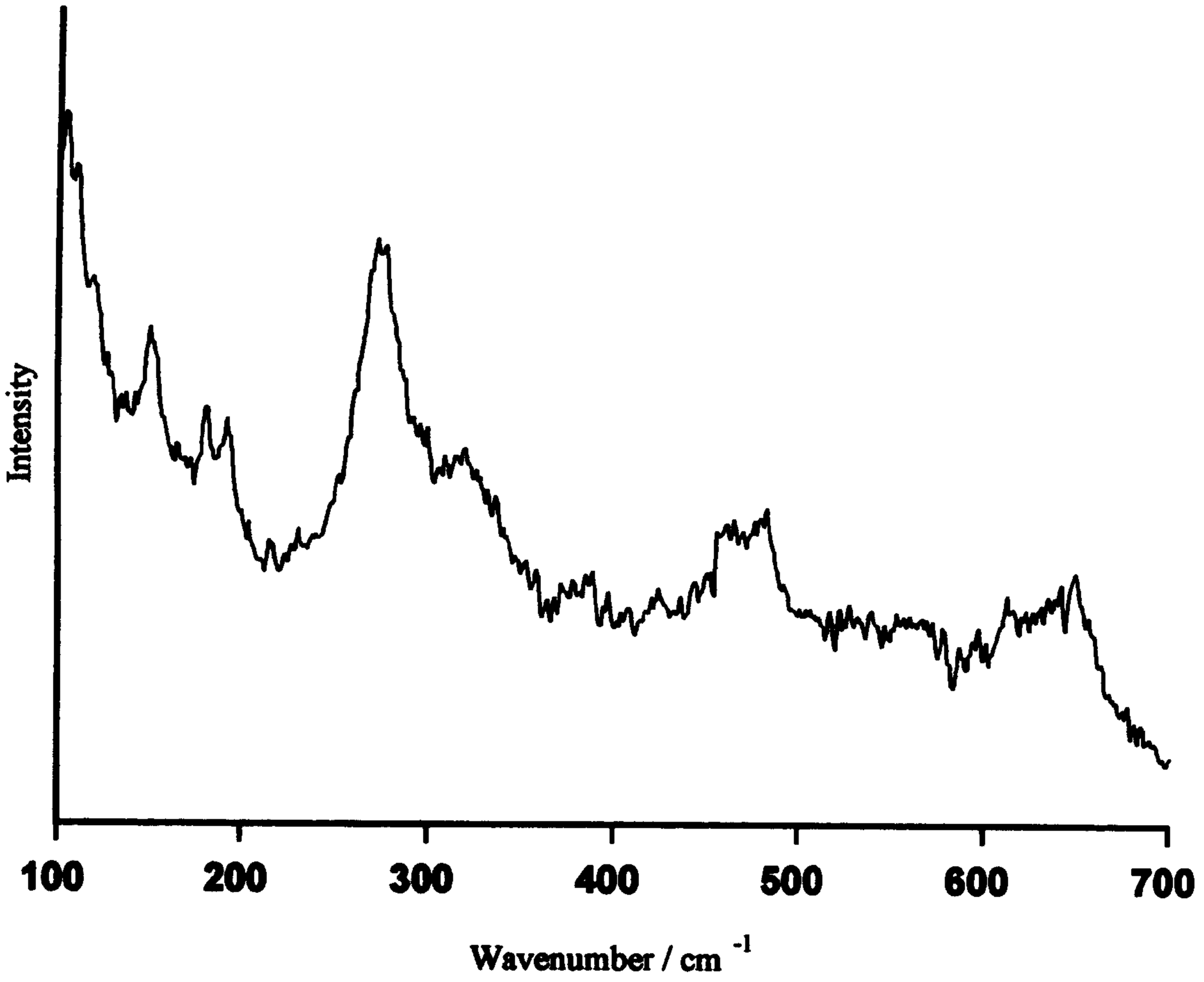


***Figure 5.25 - Raman spectrum recorded from zirconium(IV) acetate hydrothermally processed in $NH_4OH$ and dried under an infra red lamp***

The TGA trace recorded from the dried material, Figure 5.26, showed a 9% weight loss from the original mass. The small weight loss indicates that any hydroxide/oxide phase present in the dried material had decomposed either during the hydrothermal reaction or on drying leaving only crystalline tetragonal and monoclinic zirconia. The spikes on the trace in Figure 5.26 are a result of the measurement being at the limit of detection of the equipment. Further investigation of the thermal behaviour of this material is required.

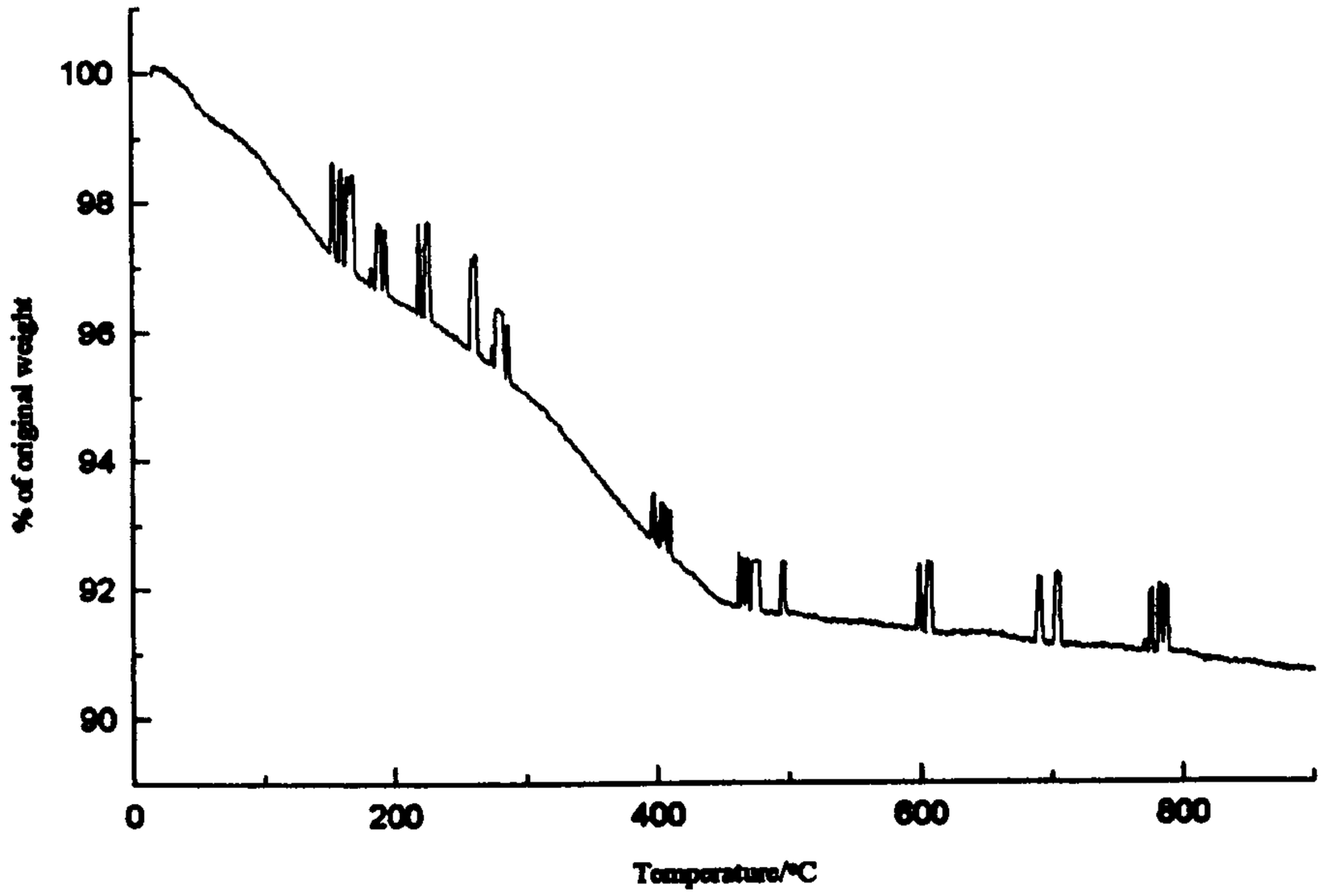


***Figure 5.26 - TGA trace recorded from zirconium(IV) acetate hydrothermally processed with $NH_4OH$ and dried under an infra red lamp***

Calcination at 200°C produced increasing amounts of monoclinic $ZrO_2$, Table 5.2, Figure 5.24b. The X-ray powder diffraction pattern of the material calcined at 500°C, Figure 5.24c, indicated that there had been no further phase development, Table 5.2.

The major change in the X-ray powder diffraction pattern was found to occur in the material formed by calcination at 900°C, Figure 5.24d, where the monoclinic polymorph became the major phase. The monoclinic polymorph was found exclusively after calcination at 1400°C, as in previous cases, Sections 5.1.3.1 and 5.1.3.2, Figure 5.24e.

The mechanism of formation is likely to be similar to that of the analogous reaction performed by boiling zirconium(IV) acetate under reflux in $NH_4OH$, but the precipitate was exposed to greater temperature and pressure which would promote the initial crystallisation of the tetragonal phase, and consequently the transformation to the monoclinic phase at lower temperatures.

### 5.1.3.4 Synthesis with $(CH_3)_3N$

The X-ray powder diffraction patterns of the material prepared with trimethylamine appeared similar to those produced by the reaction with $NH_4OH$, Figure 5.24. Initial reaction of trimethylamine with the zirconium(IV) acetate solution produced a white precipitate as obtained in the reaction with $NH_4OH$, Section 5.1.3.3. The X-ray powder diffraction pattern of the material dried under an infra red lamp, Figure 5.27a, was indicative of a mixture of the tetragonal and monoclinic phases. Peak intensity calculations, Table 5.2, showed that there was more monoclinic $ZrO_2$ present than in the corresponding sample produced with ammonia, Table 5.2. Calcination at 200°C did not cause any change in the X-ray powder diffraction pattern, Figure 5.27b, but on examining the peak intensities it was found that the proportion of the monoclinic polymorph had increased, Table 5.2. This situation continued on calcination at 500°C, Figure 5.27c, with a further increase of 8% in the amount of monoclinic phase present. The main change occurred on calcination at 900°C, where the major phase became monoclinic $ZrO_2$, Table 5.2. Further calcination at 1400°C resulted in the complete conversion of the tetragonal phase to the monoclinic phase, Figure 5.27e.

The differences in the relative amounts of monoclinic phase present in the samples produced with trimethylamine and those produced with $NH_4OH$ provides further evidence that the presence of $OH^-$ ions in the initial reaction mixture stabilises the tetragonal phase.

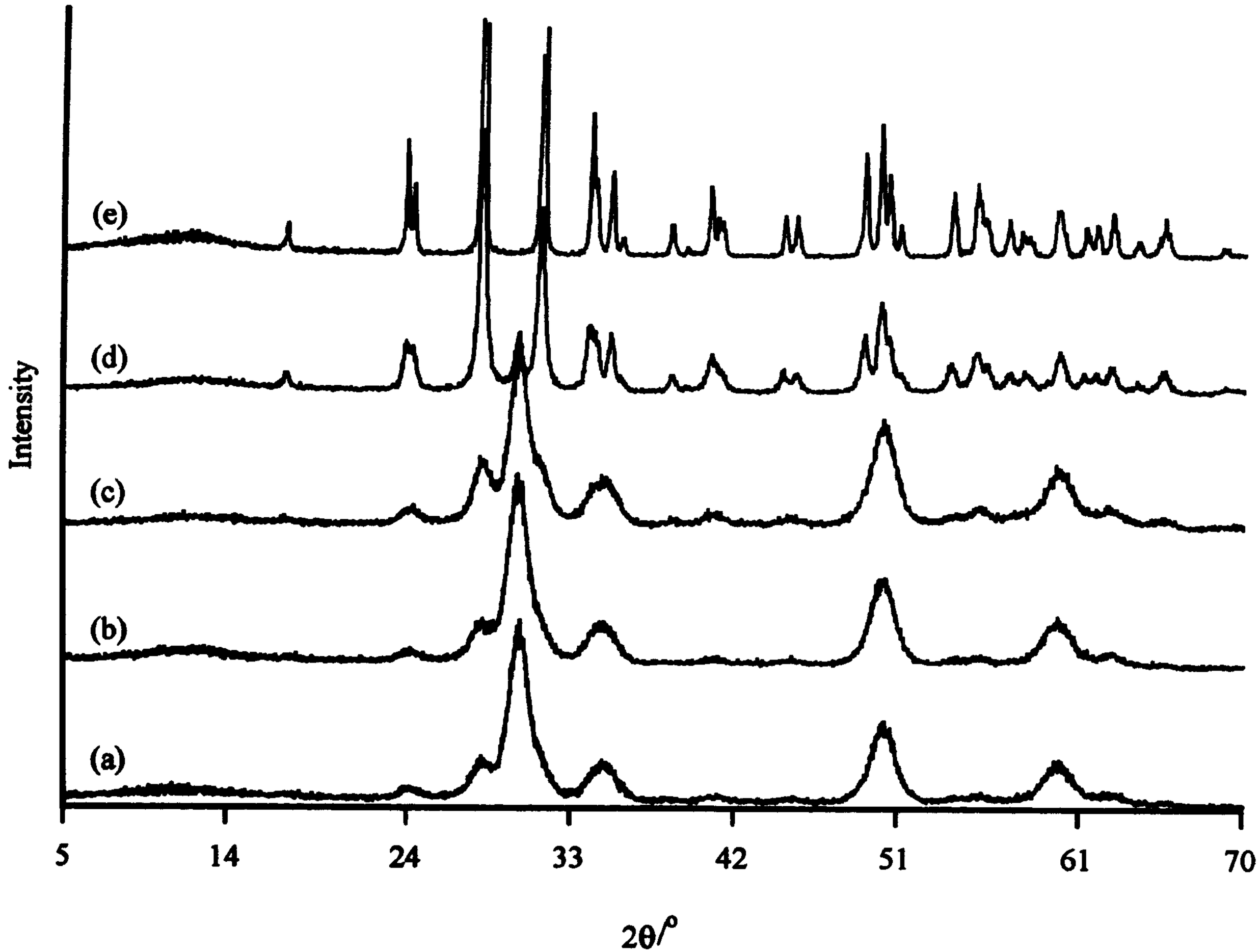


***Figure 5.27 - X-ray powder diffraction patterns recorded from zirconium(IV) acetate hydrothermally processed in $(CH_3)_3N$ and (a) dried under an infra red lamp and calcined at (b) 200°C, (c) 500°C, (d) 900°C and (e) 1400°C***

### 5.1.3.5 Synthesis with $CH_3COOH$

The X-ray powder diffraction pattern recorded from the dried material, Figure 5.28a, indicated that monophasic monoclinic $ZrO_2$ had been produced. Further calcination at 200°C also indicated that this phase was present, with no evidence for a tetragonal phase, Figure 5.28b. The peaks in the X-ray powder diffraction pattern of the dried material and of the material calcined at 200°C were broadened. At higher calcination temperatures (500°C - 1400°C) the diffraction peaks became gradually sharper, Figure 5.28c-e. The exclusive formation of monoclinic $ZrO_2$ at all calcination temperatures was similar to the situation observed with hydrothermal processing of zirconium(IV) acetate in hydrochloric acid, Section 5.1.3.2.

In this case there can be no influence from $Cl^-$ ions disrupting the polymerisation of the tetrameric species, and hence the production of monoclinic zirconia in acidic conditions may be influenced by the presence of $H^+$ ions, or conversely the absence of $OH^-$ ions. If indeed the presence of $OH^-$ ions strongly influences the stability of tetragonal $ZrO_2$, then it is reasonable to assume that a lack of $OH^-$ ions will allow preferential formation of the monoclinic phase. This also indicates that the formation of an oxychloride phase in the synthesis with HCl is an additional step in the crystallisation process peculiar to synthesis in HCl, but not necessarily a vital step in the formation of monoclinic $ZrO_2$ from zirconium(IV) acetate in acidic conditions.

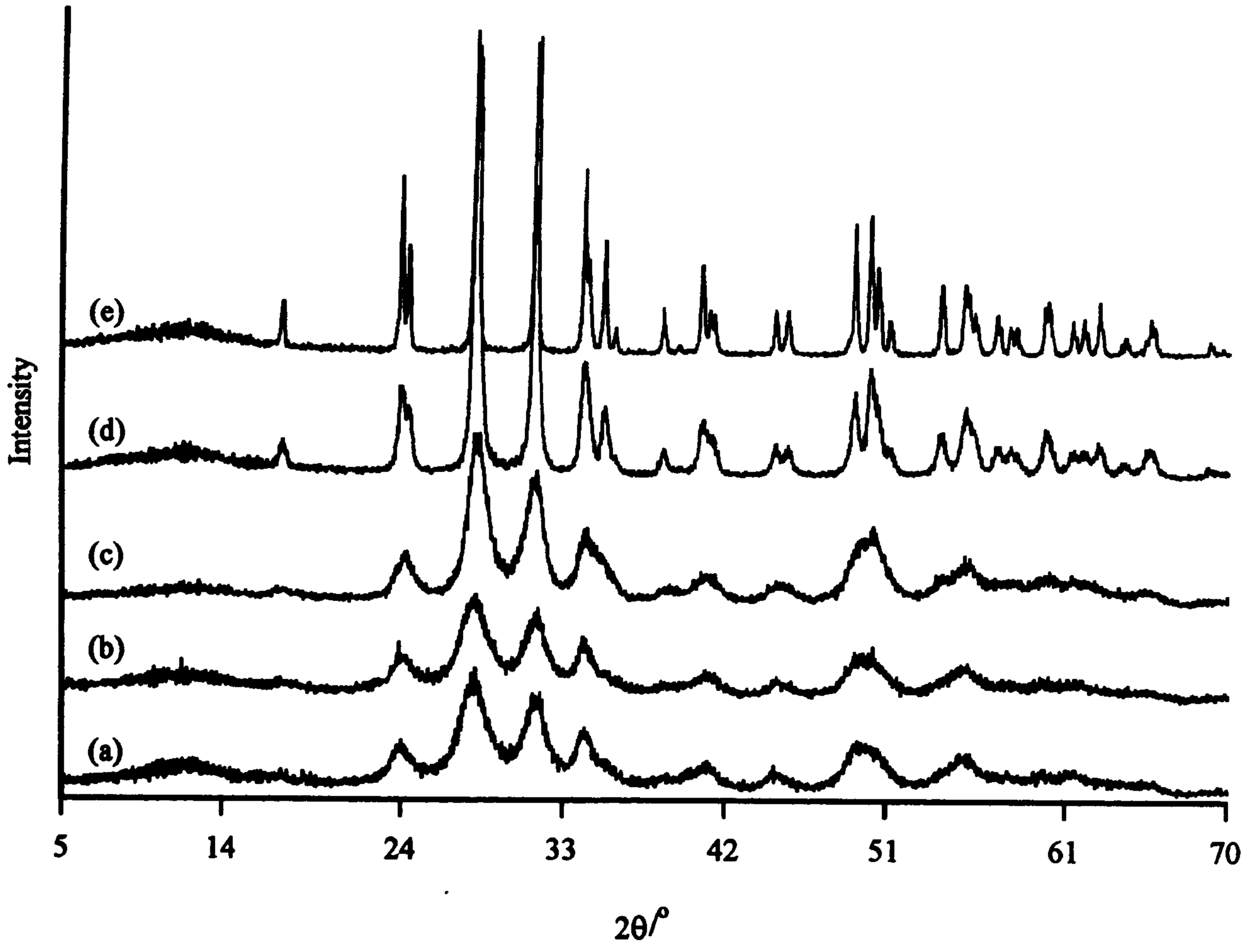


***Figure 5.28 - X-ray powder diffraction patterns recorded from zirconium(IV) acetate hydrothermally processed in $CH_3COOH$ and (a) dried under an infra red lamp and calcined at (b) 200°C, (c) 500°C, (d) 900°C and (e) 1400°C***

## 5.2 Conclusions

1) The preparation of zirconium(IV) oxide from solutions of zirconium(IV) acetate by boiling under reflux produced cubic, tetragonal and monoclinic polymorphs respectively with increasing calcination temperature.

2) The Raman spectra of tetragonal and cubic zirconia were found to differ considerably allowing the distinction between these phases to be made.

3) Addition of HCl to the zirconium(IV) acetate solution was found to suppress the formation of the cubic and tetragonal phases. Also the amount of monoclinic zirconia formed was found to be influenced by the pH of the reaction mixture with less being produced at a lower pH.

4) Addition of aqueous ammonia to the zirconium(IV) acetate solution produced tetragonal zirconia which was stabilised at calcination temperatures up to 900°C. At calcination temperatures above 900°C a phase transformation to monoclinic zirconia was observed.

5) The hydrothermal synthesis of zirconium(IV) oxide from a solution of zirconium(IV) acetate produced a powder which contained a mixture of both tetragonal and monoclinic polymorphs. As calcination temperature increased the tetragonal phase transformed to the monoclinic phase

6) The addition of HCl to the reaction mixture produced monoclinic zirconia via a zirconium oxychloride phase.

7) The addition of aqueous ammonia to the initial zirconium(IV) acetate solution was found to stabilise the tetragonal phase. Calcination at elevated temperatures caused the transformation to the monoclinic phase.

8) Thermogravimetric analysis showed that after calcination of dried materials at 500°C there was virtually no weight loss indicating that only crystalline zirconia was present at that temperature.

# References


1 A.Clearfield, Rev.Pure and Applied Chem., 1964, 14, 91

2 A.J.Zielen and R.E.Connick, J.Am.Chem.Soc., 1956, 78, 5785

3 K.A.Kraus and J.S.Johnson, J.Am.Chem.Soc., 1953, 75, 5769

4 J.S.Johnson and K.A.Kraus, J.Am.Chem.Soc., 1956, 78, 3937

5 A.Clearfield and P.A.Vaughan, Acta Crystallogr., 1956, 9, 555

6 G.M.Muha and P.A.Vaughan, J.Chem.Phys., 1960, 33, 194

7 A.Clearfield, Inorg.Chem., 1964, 3, 146

8 J.R.Fryer, J.L.Hutchinson and R.Paterson, J.Colloid Inter.Sci., 1970, 34, 238

9 JCPDS pattern number 27-0997

10 JCPDS pattern number 24-1164

11 R.Srinivasan, R.J.De Angelis, M.Harris, S.F.Simpson and B.H.Davis, J.Mat.Res., 1988, 3, 787

12 V.G.Keramidis and W.B.White, J.Am.Ceram.Soc., 1974, 57, 22

13 D-J.Kim, H-J.Jung and I-S.Yang, J.Am.Ceram.Soc., 1993, 76, 2106

14 C.M.Phillipi and K.S.Mazidiyasni, J.Am.Ceram.Soc., 1971, 54, 254

15 JCPDS pattern number 37-1484

16 Y.Suyama, T.Mizobe and A.Kato, Ceram.Int., 1977, 3, 141

17 JCPDS pattern number 32-1498

18 K.Matsui, H.Suzuki, M.Ohgai and H.Arashi, J.Am.Ceram.Soc., 1995, 78, 146

19 G.L.Clark and D.H.Reynolds, Ind.Eng.Chem., 1937, 29, 711

20 A.Clearfield, J.Mater.Res., 1990, 5, 161

21 R.Srinivasan, R.J.De Angelis and B.H.Davis, J.Mater.Res., 1986, 1, 583

22 Z.Yanwei, G.Fagherazzi and S.Polizzi, J.Mat.Sci., 1995, 30, 2153

# CHAPTER SIX

# Characterisation of Iron-Doped Zirconium(IV) Oxide

## 6.1 Synthesis of iron doped zirconium (IV) oxide

The use of dopant ions to stabilise the cubic and tetragonal polymorphs of zirconia is well known[1-5] and has normally been achieved by the calcination of precipitates. The work in this thesis reports on the synthesis of iron doped zirconia at varying pH by hydrothermal processing and compares the results with those obtained by calcination of precipitates formed by boiling suspensions under reflux.

### 6.1.1 Synthesis of iron doped zirconia by boiling under reflux

#### 6.1.1.1 Synthesis with $H_2O$

(i) 10 wt% iron doped zirconia

The X-ray powder diffraction pattern recorded from the nominally 10 wt% Fe doped material dried under an infra red lamp, Figure 6.1a, showed the material to be amorphous. The $^{57}Fe$ Mössbauer spectrum recorded from the material dried under an infra red lamp, Figure 6.2a, consisted of one doublet with an isomer shift, $\delta$, of 0.31 $mms^{-1}$, and quadrupole splitting, $\Delta$, of 0.65 $mms^{-1}$, consistent with $Fe^{3+}$ ions[6] being incorporated into the amorphous structure, Table 6.1. Calcination at 200°C caused no change to the material as evidenced by the X-ray powder diffraction pattern, Figure 6.1b. The $^{57}Fe$ Mössbauer spectrum recorded from this material, Figure 6.2b, also remained unchanged. The X-ray powder diffraction pattern recorded from the material calcined at 500°C showed evidence of the formation of a crystalline phase, Figure 6.1c, which was identified as tetragonal zirconia.[7] There was also a small peak at $2\theta = 28°$ which was attributed to the monoclinic phase, Table 6.2. The $^{57}Fe$ Mössbauer spectrum, Figure 6.2c, recorded from the material calcined at 500°C consisted of one doublet, $\delta$ = 0.30$mms^{-1}$, $\Delta$ = 1.13$mms^{-1}$. The increase in the quadrupole splitting, from 0.65$mms^{-1}$ after calcination at 200°C, coincided with the crystallisation of the tetragonal phase from the amorphous material.

An increase in the value of the quadrupole splitting indicates that the $Fe^{3+}$ ion, identified from the isomer shift value, is present in a more asymmetric environment. The asymmetric environment may arise because of the association of the dopant ions with oxygen vacancies, necessary to maintain charge balance. It has been proposed that in tetragonal zirconia[5] each oxygen vacancy is associated with 2 dopant ions, and each dopant ion is distorted towards the vacancy. Hence the asymmetry in the tetragonal phase, indicated by the large quadrupole splitting. It is therefore reasonable to associate the increase in quadrupole splitting, as observed for the material calcined at 500°C, with the formation of the tetragonal phase. After calcination at 900°C the X-ray powder diffraction pattern, Figure 6.1d, indicated that the material had increased in crystallinity. Calculations, using the method described in Section 5.1.2.1, on the intensities of the peaks attributed to each phase in the X-ray powder diffraction pattern, Table 6.2, indicated that the amount of monoclinic $ZrO_2$ present had decreased. The determination of the quantity of monoclinic $ZrO_2$ present after calcination at 500°C is likely to be less accurate because of the broad peak width observed in the X-ray powder diffraction pattern. Therefore the observed decrease in the quantity of monoclinic zirconia present may be attributed to errors in the calculation. The $^{57}Fe$ Mössbauer spectrum of the material calcined at 900°C consisted of two components, one sextet and one doublet. The sextet component had parameters, $\delta = 0.38 mms^{-1}$, $\Delta = -0.08 mms^{-1}$, $H = 51.6T$, consistent[8] with the presence of $\alpha$-$Fe_2O_3$ and the relative areas of the two components indicated that 72% of the iron in the sample was present as this phase, Table 6.1.

| Calcination Temperature | Doublet | | | Sextet | | |
|---|---|---|---|---|---|---|
| | $\delta$ / $mms^{-1}$ (±0.05) | $\Delta$ /$mms^{-1}$ (±0.03) | Area / % | $\delta$ / $mms^{-1}$ (±0.05) | $\Delta$ /$mms^{-1}$ (±0.03) | Area / % |
| Prefurnace | 0.31 | 0.64 | 100 | - | - | 0 |
| 200°C | 0.37 | 0.66 | 100 | - | - | 0 |
| 500°C | 0.30 | 1.13 | 100 | - | - | 0 |
| 900°C | 0.32 | 0.99 | 28 | 0.38 | -0.08 | 72 |
| 1400°C | 0.18 | 0.55 | 9 | 0.39 | -0.08 | 91 |

***Table 6.1 - $^{57}Fe$ Mössbauer spectral data for 10 wt% iron doped $ZrO_2$ synthesised by boiling zirconium acetate with iron(II) acetate under reflux with $H_2O$***

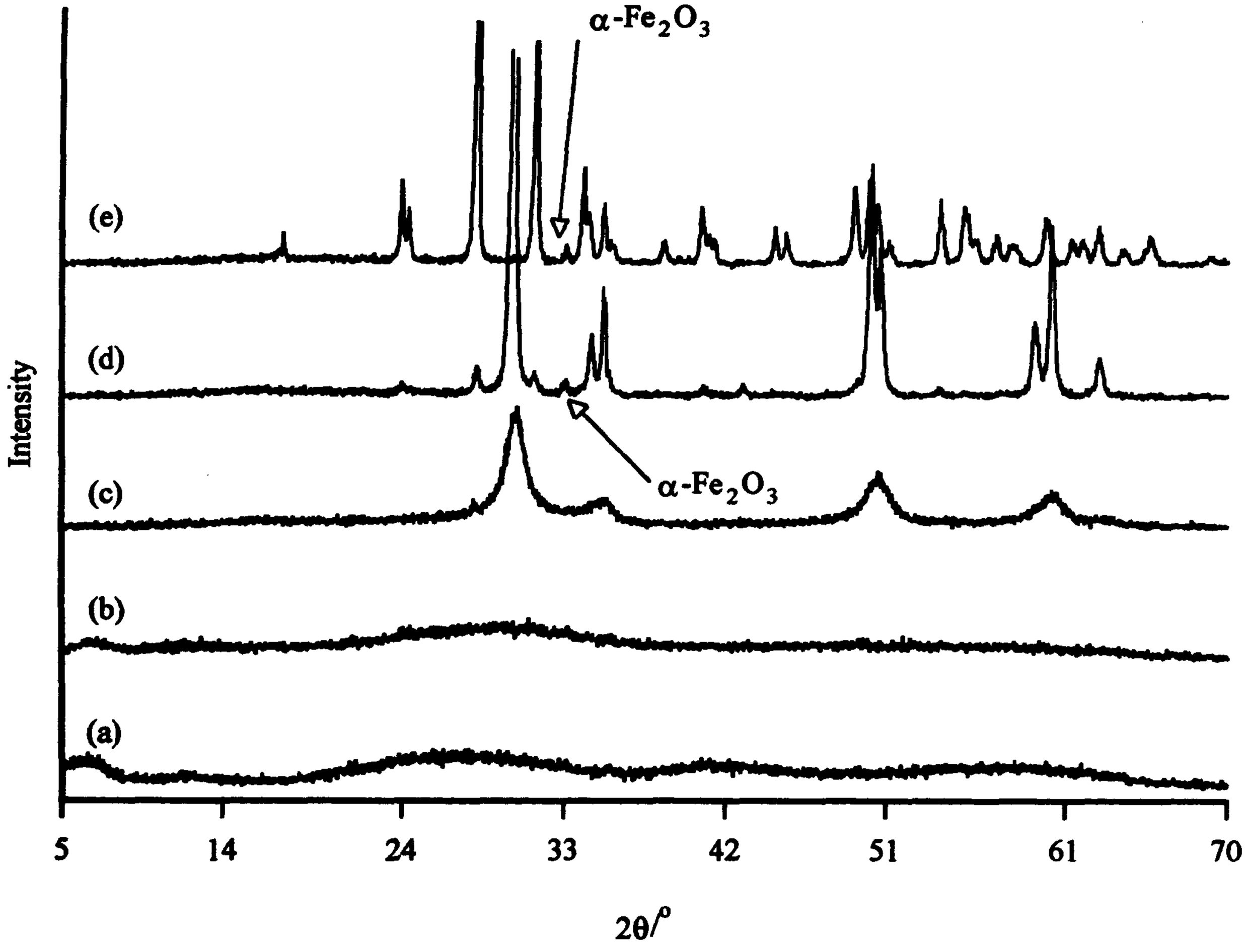


***Figure 6.1 - X-ray powder diffraction patterns recorded from iron doped zirconia produced by boiling zirconium(IV) acetate and 10 wt% iron(II) acetate under reflux with $H_2O$ and (a) dried under an infra red lamp and calcined at (b) 200°C, (c) 500°C, (d) 900°C and (e) 1400°C***

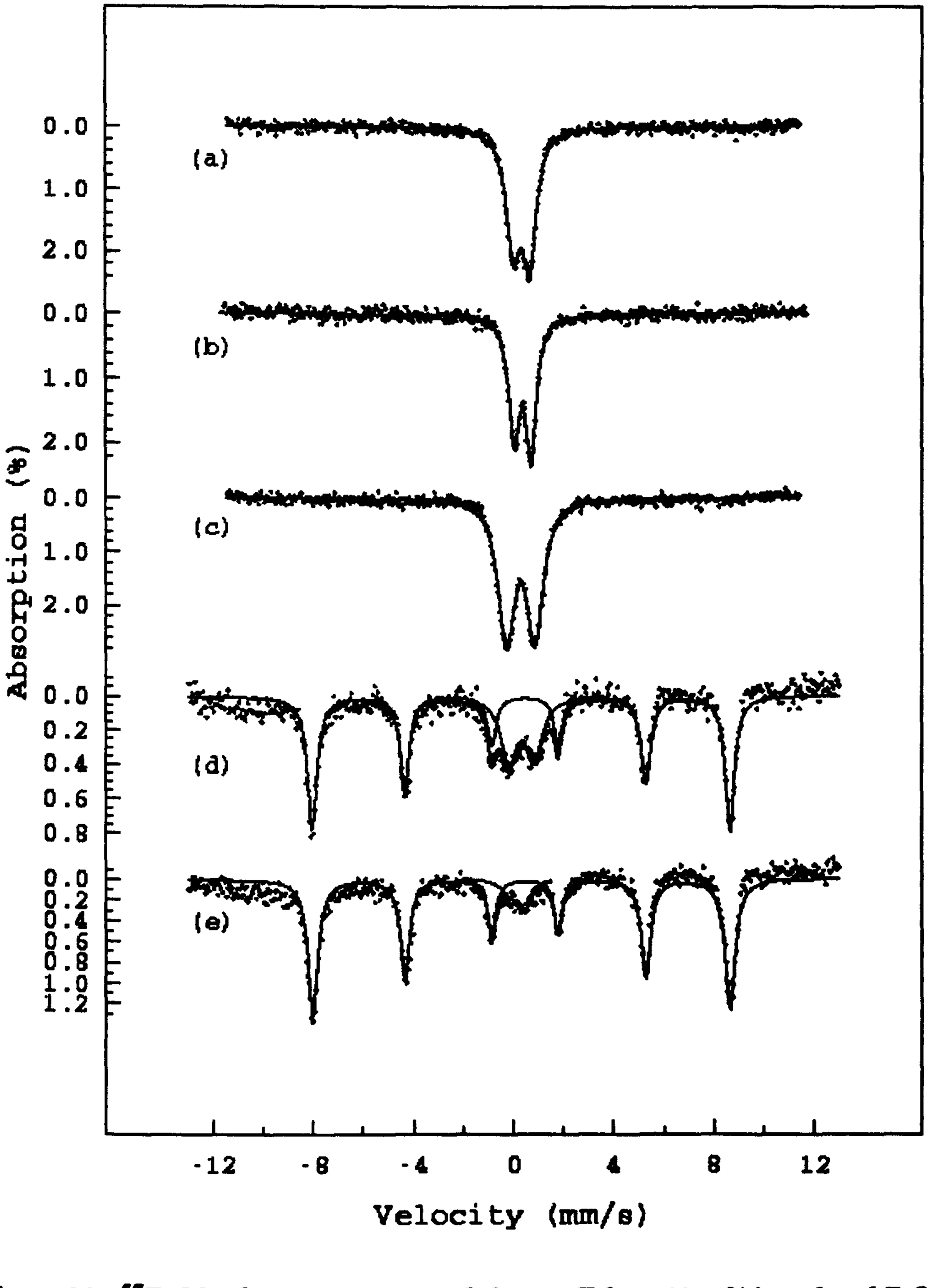


***Figure 6.2 - $^{57}Fe$ Mössbauer spectra recorded at 298K from 10 wt% iron doped $ZrO_2$ synthesised by boiling zirconium(IV) acetate and iron(II) acetate under reflux with $H_2O$ and (a) dried under an infra red lamp and calcined at (b) 200°C, (c) 500°C, (d) 900°C and (e) 1400°C***

| Preparative method | Amount (± 5%) of monoclinic zirconia | | | | |
|---|---|---|---|---|---|
| | Dried under IR lamp | 200°C | 500°C | 900°C | 1400°C |
| Reflux/10 wt%/$H_2O$ | 0 | 0 | 15 | 7 | 100 |
| Reflux/ 5 wt%/$H_2O$ | 0 | 0 | 0 | 76 | 100 |
| Reflux/10 wt%/HCl | 0 | 0 | 0 | 73 | 100 |
| Reflux/ 5 wt%/HCl | 0 | 0 | 0 | 19 | 100 |
| Reflux/10 wt%/$NH_4OH$ | 0 | 0 | 0 | 0 | 100 |
| Reflux/ 5 wt%/$NH_4OH$ | 0 | 0 | 0 | 0 | 100 |

***Table 6.2 - Amount of monoclinic zirconia formed by calcination in air of iron doped zirconia prepared by boiling iron(II) and zirconium(IV) acetates under reflux***

The X-ray powder diffraction pattern recorded from the material calcined at 1400°C, Figure 6.1e, showed that tetragonal $ZrO_2$ had transformed to the monoclinic phase. There was also evidence in the X-ray powder diffraction pattern for the presence of α-$Fe_2O_3$. The proportion of α-$Fe_2O_3$ present increased with calcination temperature, the $^{57}Fe$ Mössbauer spectrum indicating that 91% of the total iron content was present as α-$Fe_2O_3$ after calcination at 1400°C, Figure 6.2e and Table 6.1. This indicated that the $Fe^{3+}$ ions had segregated as the tetragonal zirconia converts to the monoclinic polymorph. The transformation of the tetragonal phase to the monoclinic phase on calcination at 1400°C was accompanied by a decrease in quadrupole splitting to 0.55mms$^{-1}$ and isomer shift to 0.18mms$^{-1}$, Table 6.1. The decrease in quadrupole splitting can be attributed to the $Fe^{3+}$ ion existing in a more symmetrical environment in the monoclinic structure when compared to the fluorite related tetragonal structure. This result endorses the suggestion that there is a relationship between magnitude of the quadrupole splitting and the zirconia phase present.

(ii) 5 wt% iron doped zirconia

The X-ray powder diffraction pattern recorded from the 5 wt% Fe doped material dried under an infra red lamp, Figure 6.3a, showed the material to be amorphous. The $^{57}Fe$ Mössbauer spectrum, Figure 6.4a, showed a doublet with an isomer shift of 0.31 mms$^{-1}$,

Table 6.3, indicative of $Fe^{3+}$ ions having been incorporated into the amorphous material. After calcination of the material at 200°C the X-ray powder diffraction pattern, Figure 6.3b, and the $^{57}Fe$ Mössbauer spectrum, Figure 6.4b, were unchanged. Calcination at 500°C caused the crystallisation of the material which X-ray powder diffraction, Figure 6.3c, identified as tetragonal $ZrO_2$. The $^{57}Fe$ Mössbauer spectrum, Figure 6.4c, consisted of one doublet with an isomer shift of 0.34mms$^{-1}$. The quadrupole splitting increased to 1.08mms$^{-1}$, Table 6.3. As proposed earlier, Section 6.1.1.1.(i), this increase in quadrupole splitting may be associated with the presence of $Fe^{3+}$ ions in the tetragonal phase.

| Calcination Temperature | Doublet | | | Sextet | | |
|---|---|---|---|---|---|---|
| | δ / mms$^{-1}$ (±0.05) | Δ /mms$^{-1}$ (±0.03) | Area / % | δ / mms$^{-1}$ (±0.05) | Δ /mms$^{-1}$ (±0.03) | Area / % |
| Prefurnace | 0.31 | 0.59 | 100 | - | - | 0 |
| 200°C | 0.35 | 0.66 | 100 | - | - | 0 |
| 500°C | 0.34 | 1.08 | 100 | - | - | 0 |
| 900°C | 0.32 | 1.11 | 58 | 0.36 | -0.07 | 42 |
| 1400°C | 0.11 | 0.57 | 13 | 0.35 | -0.08 | 87 |

***Table 6.3 - $^{57}Fe$ Mössbauer spectral data for 5 wt% iron doped $ZrO_2$ synthesised by boiling zirconium acetate and iron(II) acetate under reflux with $H_2O$***

After calcination at 900°C the X-ray powder diffraction pattern, Figure 6.3d, showed the material to be a mixture of two crystalline phases identified as tetragonal $ZrO_2$ and monoclinic $ZrO_2$ with the major phase being monoclinic zirconia, Table 6.2. The $^{57}Fe$ Mössbauer spectrum, Figure 6.4d, consisted of two components, one sextet and one doublet. The sextet component had a magnetic field of 51.3T with isomer shift and quadrupole splitting values consistent[8] with $\alpha$-$Fe_2O_3$, Table 6.3, although there was no evidence for this phase in the X-ray powder diffraction pattern. This is due to the small amount of iron present in the sample which is likely to be below the limit of detection of X-ray powder diffraction.

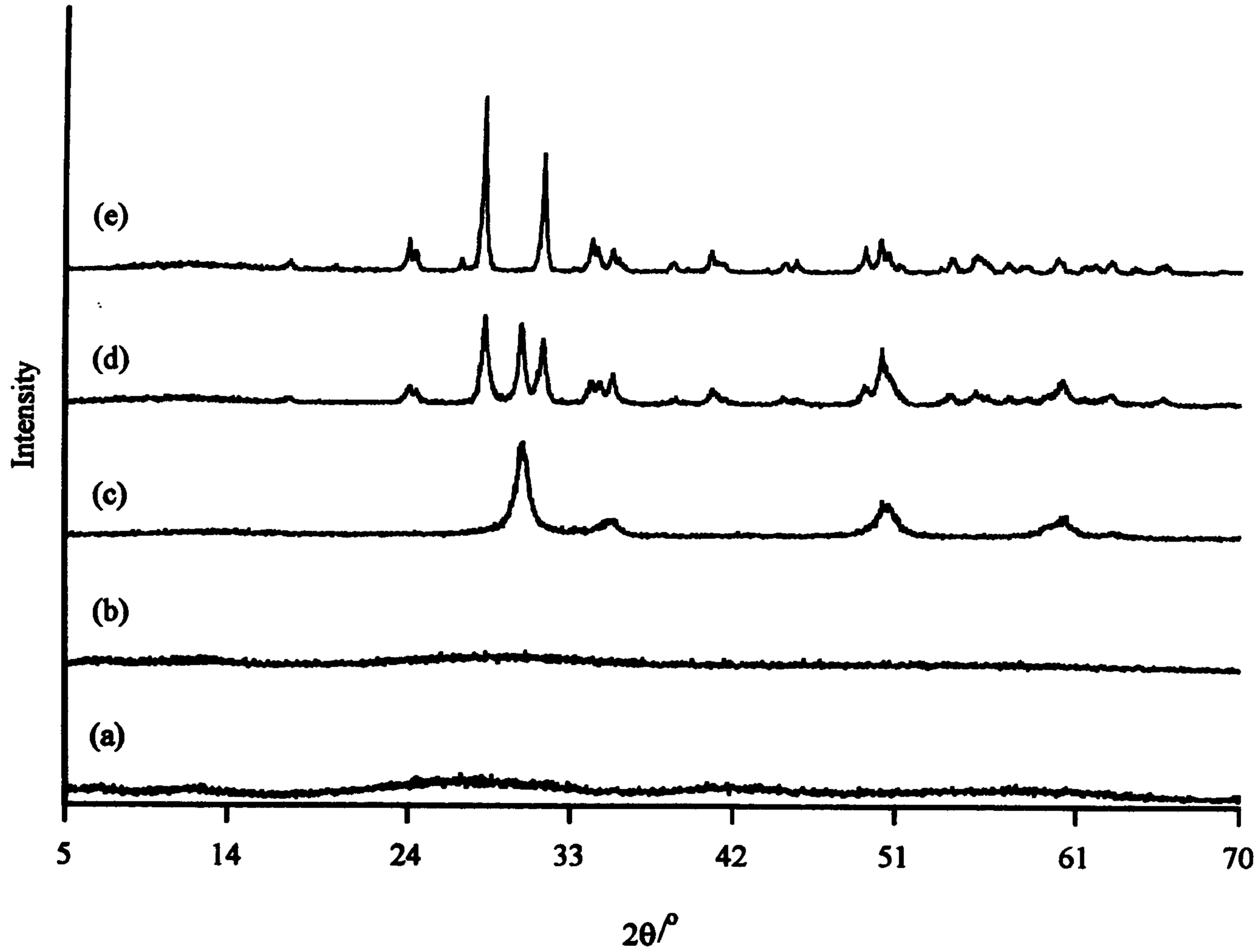


***Figure 6.3- X-ray powder diffraction patterns recorded from iron doped zirconia produced by boiling zirconium(IV) acetate and 5 wt% iron(II) acetate under reflux with $H_2O$ and (a) dried under an infra red lamp and calcined at (b) 200°C, (c) 500°C, (d) 900°C and (e) 1400°C***

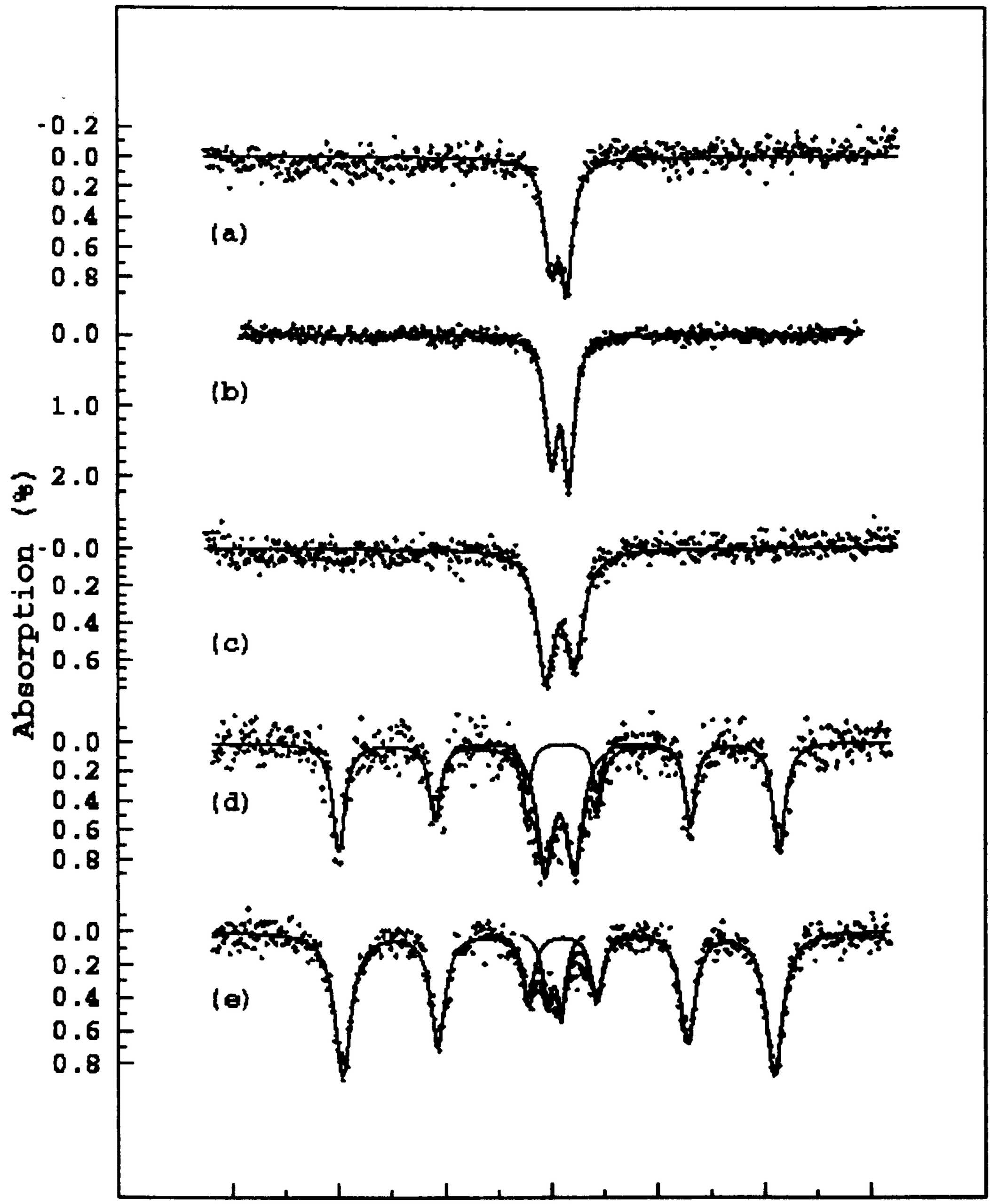


***Figure 6.4 - $^{57}Fe$ Mössbauer spectra recorded from 5 wt% iron doped $ZrO_2$ synthesised by boiling zirconium(IV) acetate and iron(II) acetate under reflux with $H_2O$ and (a) dried under an infra red lamp and calcined at (b) 200°C, (c) 500°C, (d) 900°C and (e) 1400°C***

Following calcination at 1400°C the X-ray powder diffraction pattern, Figure 6.3e, showed that the mixture of tetragonal and monoclinic zirconia had transformed to monophasic monoclinic $ZrO_2$. The $^{57}Fe$ Mössbauer spectrum, Figure 6.4e showed the amount of $\alpha$-$Fe_2O_3$ present in the sample to have increased from 42% after calcination at 900°C to 87% after calcination at 1400°C, Table 6.3, indicating that further segregation had taken place. Whether the segregation was due to increasing calcination temperature or was associated with phase transformation is not known.

The effect of the dopant ion on the phase composition of the calcined materials produced by boiling under reflux with $H_2O$ is shown in Figure 6.5. The amount of tetragonal $ZrO_2$ was seen to be the same in both the 0 and 5 wt% doped materials at temperatures to 500°C. The 10 wt% doped material appeared to have destabilised the tetragonal phase at 500°C, but this was dramatically reversed at 900°C where more tetragonal zirconia was produced. The results therefore show a pattern of increased stabilisation with increased dopant level above 900°C. The decrease in the amount of tetragonal phase present in the 10 wt% Fe doped zirconia after calcination at 900°C is unusual and requires further investigation.

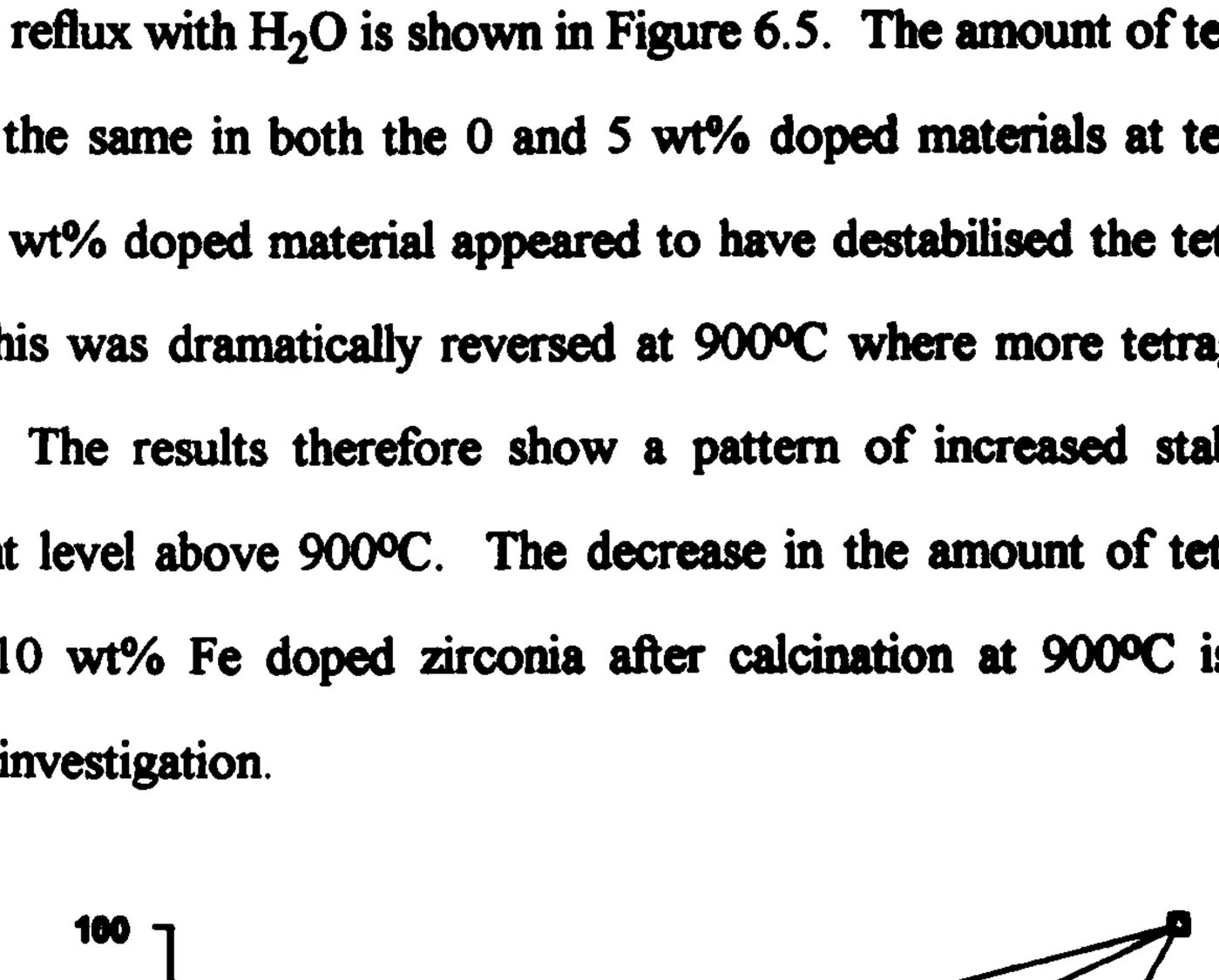


***Figure 6.5 - Comparison of the effects of iron dopant level on the formation of monoclinic zirconia by boiling under reflux in water***

### 6.1.1.2 Synthesis with HCl

(i) 10 wt% iron doped zirconia

The X-ray powder diffraction pattern, Figure 6.6a, recorded from the 10 wt% Fe doped material dried under an infra red lamp showed that a phase resembling $ZrOCl_2.xH_2O$ had been produced.[9] The $^{57}Fe$ Mössbauer spectrum recorded from this sample, Figure 6.7a, consisted of one doublet with an isomer shift of 0.16mms$^{-1}$ and a quadrupole splitting of 0.33mms$^{-1}$, Table 6.5. This suggests that the iron ions had doped the $ZrOCl_2.xH_2O$ phase as the $^{57}Fe$ Mössbauer parameters for the doublet were lower than observed for $Fe^{3+}$ ions incorporated into the amorphous material, Section 6.1.1.1(i). There was no evidence in the $^{57}Fe$ Mössbauer spectrum for any other phase which is in agreement with the X-ray powder diffraction pattern which indicated the presence of only one crystalline phase.

| Calcination Temperature | Doublet | | | Sextet | | |
|---|---|---|---|---|---|---|
| | δ / mms$^{-1}$ (±0.05) | Δ /mms$^{-1}$ (±0.03) | Area / % | δ / mms$^{-1}$ (±0.05) | Δ /mms$^{-1}$ (±0.03) | Area / % |
| Prefurnace | 0.16 | 0.33 | 100 | - | - | 0 |
| 200°C | 0.22 | 0.64 | 100 | - | - | 0 |
| 500°C | 0.32 | 1.09 | 100 | - | - | 0 |
| 900°C | 0.32 | 1.17 | 20 | 0.36 | -0.07 | 80 |
| 1400°C | 0.50 | 0.59 | 7 | 0.38 | -0.07 | 93 |

***Table 6.5 - $^{57}Fe$ Mössbauer spectral data for 10 wt % iron doped $ZrO_2$ synthesised by boiling zirconium(IV) acetate with iron (II) acetate under reflux with HCl***

Calcination at 200°C caused the oxychloride phase to become amorphous, Figure 6.6b, and the $^{57}Fe$ Mössbauer spectrum, Figure 6.7b, may be associated with the iron ions in the amorphous phase. The isomer shift and quadrupole splitting values of this sample had increased, Table 6.5, suggesting that the environment around the iron ions had altered. The X-ray powder diffraction pattern, Figure 6.6c, recorded from the material calcined at 500°C showed that a crystalline phase had been produced. Although the peaks in the X-ray powder diffraction pattern were broadened, this phase was identified

as tetragonal $ZrO_2$. The $^{57}Fe$ Mössbauer spectrum of this material, Figure 6.7c, showed one doublet with an isomer shift of $0.32mms^{-1}$ consistent with $Fe^{3+}$ ions incorporated into the zirconia structure. The quadrupole splitting of the doublet component, $1.09mms^{-1}$, indicated that this was tetragonal $ZrO_2$ and in agreement with observations made in Section 6.1.1.1. Following calcination at 900°C the X-ray powder diffraction pattern, Figure 6.6d, indicated that there were two phases present identified as monoclinic and tetragonal $ZrO_2$. Closer inspection of the X-ray powder diffraction pattern showed there to be evidence for the presence of $\alpha$-$Fe_2O_3$. The amount of monoclinic $ZrO_2$ present, Table 6.2, indicated that the majority of the tetragonal phase had transformed to the monoclinic polymorph after calcination at 900°C.

The $^{57}Fe$ Mössbauer spectrum, Figure 6.7d, showed two components, one sextet and one doublet, $\delta = 0.32mms^{-1}$, $\Delta = 1.17mms^{-1}$. The quadrupole splitting of the doublet was larger than expected given that the major phase present was monoclinic zirconia. The sextet component had parameters which were consistent[8] with $\alpha$-$Fe_2O_3$, Table 6.5. The presence of the $\alpha$-$Fe_2O_3$ phase indicates that segregation of iron from the zirconia structure had taken place with 80% of the total iron content being due to the $\alpha$-$Fe_2O_3$ phase. Calcination at 1400°C produced a complete transformation to the monoclinic phase with evidence in the X-ray powder diffraction pattern, Figure 6.6e, for the presence of $\alpha$-$Fe_2O_3$. The $^{57}Fe$ Mössbauer spectrum, Figure 6.7e, showed that the amount of $\alpha$-$Fe_2O_3$ had increased, Table 6.5, to 93%, consistent with iron being segregated on increasing calcination temperature. It has been suggested[1] that segregation of iron occurs as zirconia transforms to the monoclinic phase. As both tetragonal and monoclinic phases were present at both 900°C and 1400°C it was not possible to distinguish whether calcination at elevated temperature or phase transformation was responsible for the segregation.

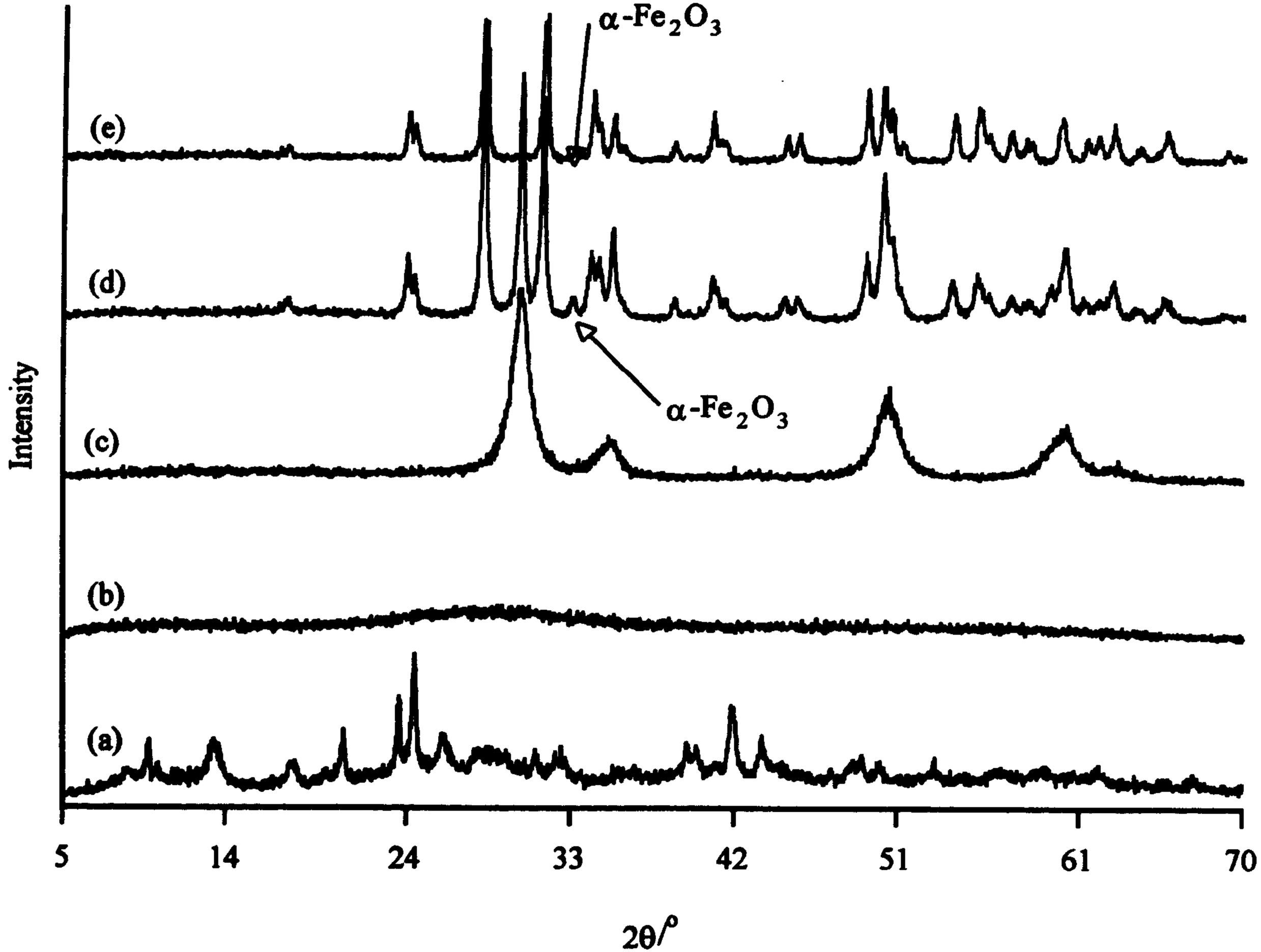


***Figure 6.6 - X-ray powder diffraction patterns recorded from iron doped material produced by boiling zirconium(IV) acetate and 10 wt% iron(II) acetate under reflux with HCl and (a) dried under an infra red lamp and calcined at (b) 200°C, (c) 500°C, (d) 900°C and (e) 1400°C***

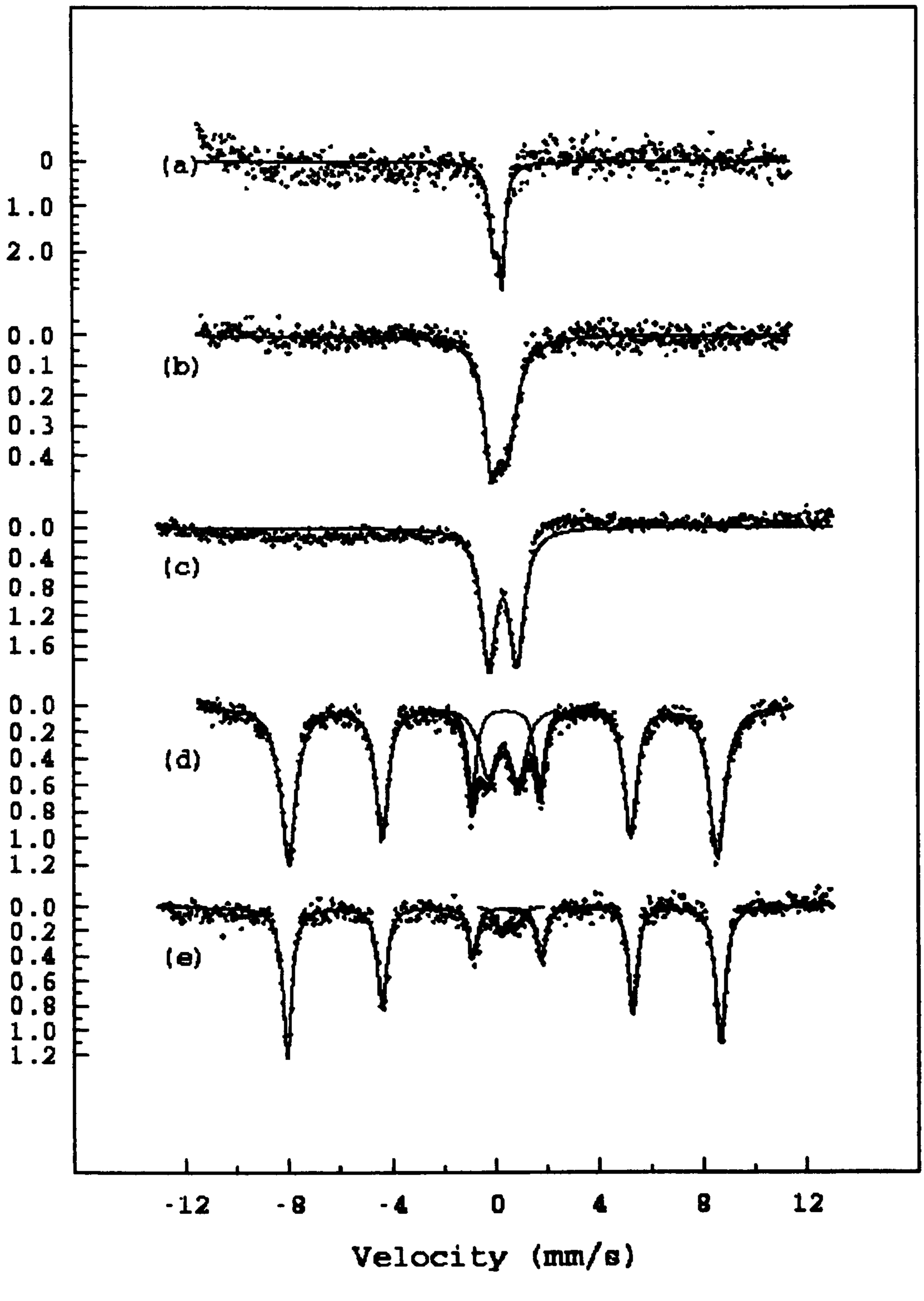


***Figure 6.7 - $^{57}Fe$ Mössbauer spectra recorded from 10 wt% iron doped $ZrO_2$ synthesised by boiling zirconium(IV) acetate and iron(II) acetate under reflux with HCl and (a) dried under an infra red lamp and calcined at (b) 200°C, (c) 500°C, (d) 900°C and (e) 1400°C***

(ii) 5 wt% doped zirconia

The 5 wt% Fe doped material dried under an infra red lamp was found by X-ray powder diffraction, Figure 6.8a, to be amorphous. The $^{57}Fe$ Mössbauer spectrum, Figure 6.9a, recorded from the material showed the iron species to be present in one environment, with an isomer shift of 0.31mms$^{-1}$, Table 6.6. The value of the isomer shift is consistent[4] with the presence of $Fe^{3+}$ ions and, since both X-ray powder diffraction and $^{57}Fe$ Mössbauer spectroscopy indicated the presence of only one phase, it is likely that the $Fe^{3+}$ ions were located in the amorphous material.

| Calcination Temperature | Doublet | | | Sextet | | |
|---|---|---|---|---|---|---|
| | δ / mms$^{-1}$ (±0.05) | Δ /mms$^{-1}$ (±0.03) | Area / % | δ / mms$^{-1}$ (±0.05) | Δ /mms$^{-1}$ (±0.03) | Area / % |
| Prefurnace | 0.31 | 0.39 | 100 | - | - | 0 |
| 200°C | 0.36 | 0.49 | 100 | - | - | 0 |
| 500°C | 0.33 | 1.05 | 100 | - | - | 0 |
| 900°C | 0.33 | 1.09 | 57 | 0.38 | -0.08 | 43 |
| 1400°C | 0.20 | 0.44 | 13 | 0.40 | -0.07 | 87 |

***Table 6.6 - $^{57}Fe$ Mössbauer spectral data for 5 wt % iron doped $ZrO_2$ synthesised by boiling zirconium(IV) acetate and iron(II) acetate under reflux with HCl***

Calcination of the material at 200°C resulted in no change to the X-ray powder diffraction pattern, Figure 6.7b, or the $^{57}Fe$ Mössbauer spectrum, Figure 6.8b, although the isomer shift and quadrupole splitting had increased, Table 6.6. Further calcination at 500°C caused crystallisation of the material, Figure 6.7c, producing tetragonal $ZrO_2$. The $^{57}Fe$ Mössbauer spectrum, Figure 6.8c, showed one doublet with an isomer shift of 0.33mms$^{-1}$ which indicated that $Fe^{3+}$ ions had been incorporated into the zirconia structure. The quadrupole splitting was found to increase to 1.05mms$^{-1}$ which is consistent with the proposal that the magnitude of the quadrupole splitting is indicative of the polymorph of zirconia produced, Section 6.1.1.1(i). After calcination at 900°C the X-ray powder diffraction pattern, Figure 6.7d, indicated that the tetragonal polymorph had begun to transform to the monoclinic phase, producing 19% of this phase, Table 6.2.

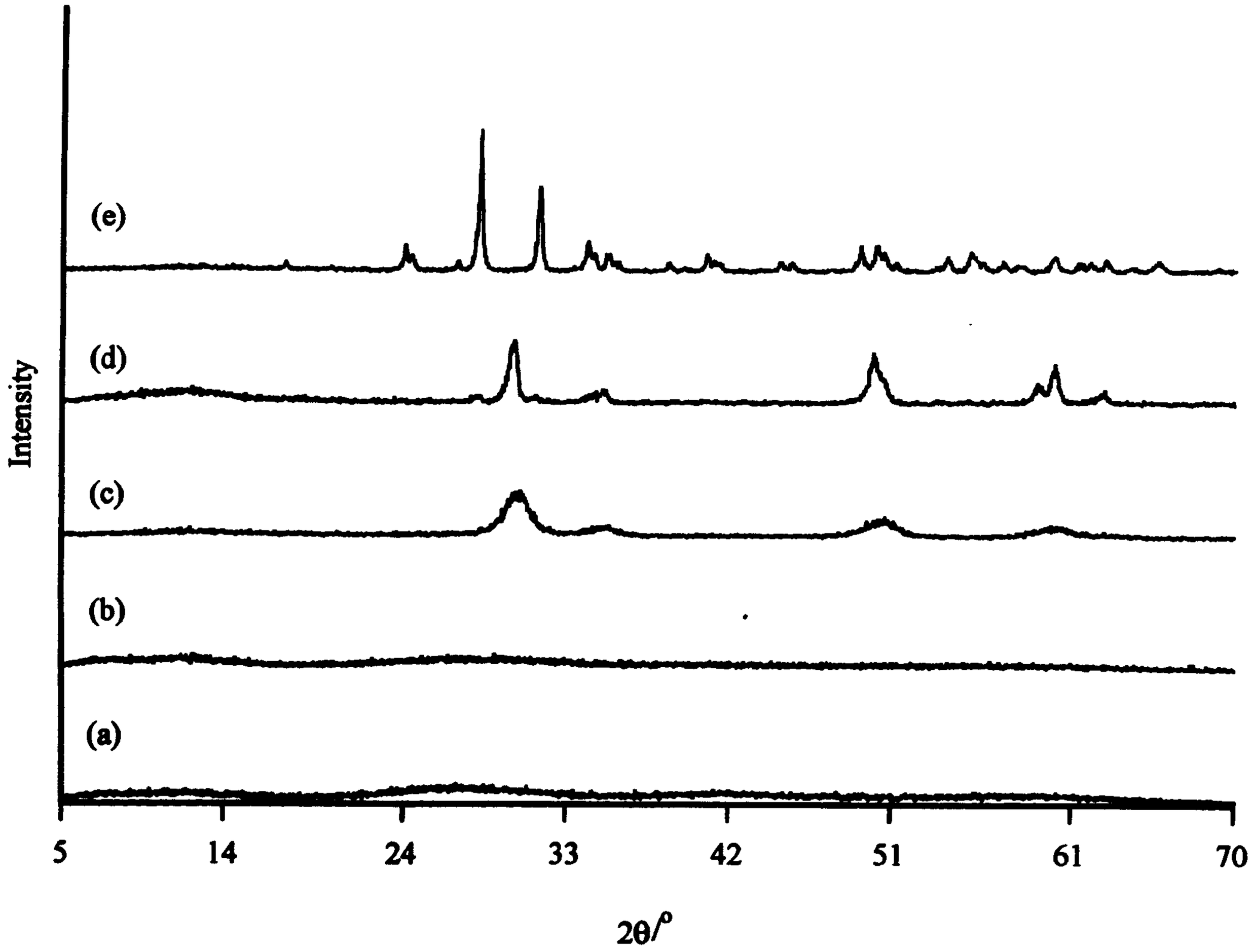


***Figure 6.7 - X-ray powder diffraction patterns recorded from iron doped zirconia produced by boiling zirconium(IV) acetate and 5 wt% iron(II) acetate under reflux with HCl and (a) dried under an infra red lamp and calcined at (b) 200°C, (c) 500°C, (d) 900°C and (e) 1400°C***

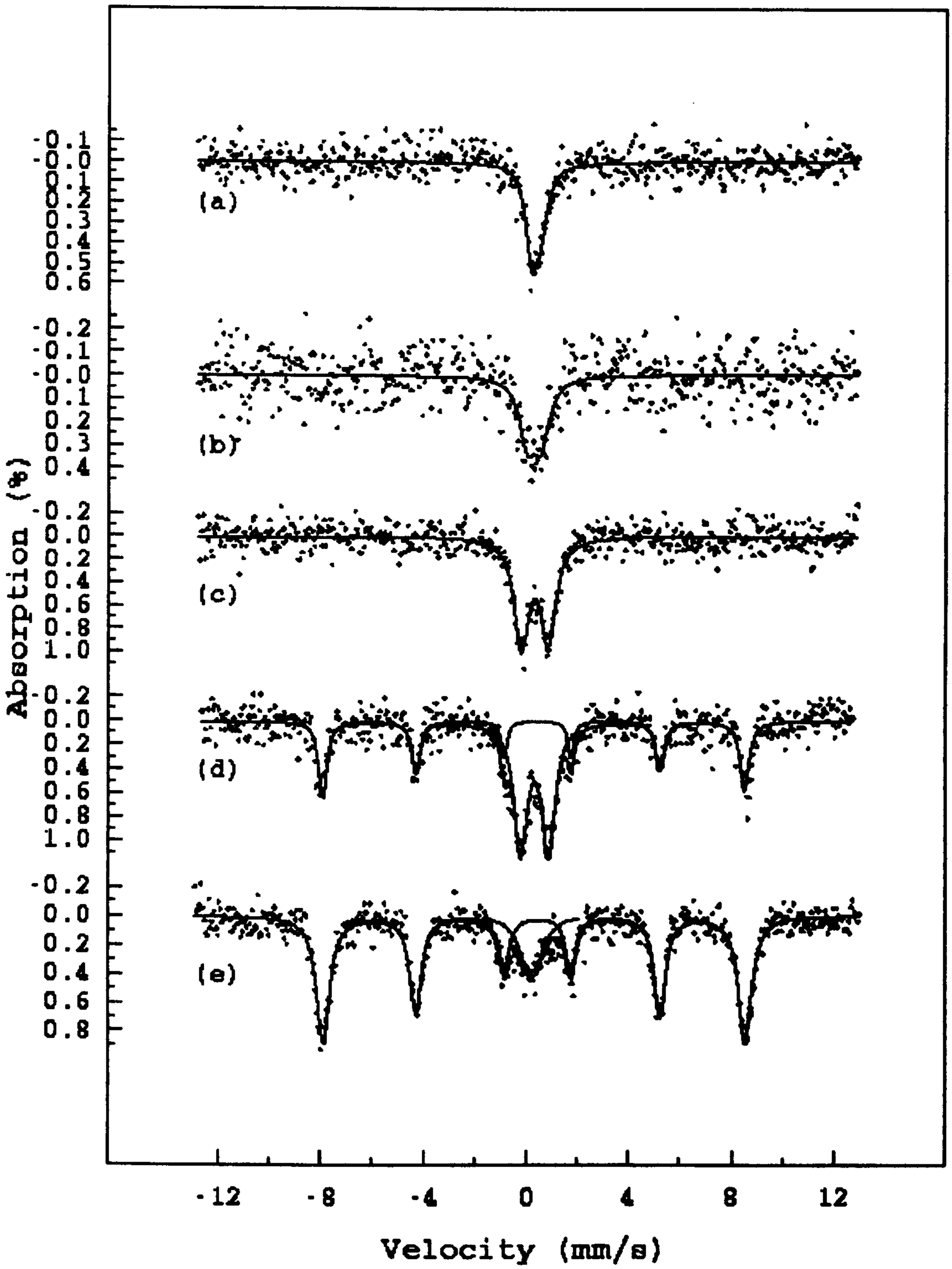


***Figure 6.8 - $^{57}Fe$ Mössbauer spectra recorded from 5 wt% iron doped $ZrO_2$ synthesised by boiling zirconium(IV) acetate and iron(II) acetate under reflux with HCl and (a) dried under an infra red lamp and calcined at (b) 200°C, (c) 500°C, (d) 900°C and (e) 1400°C***

The $^{57}Fe$ Mössbauer spectrum, Figure 6.8d, indicated that there was a second iron containing phase present representing 43% of the total iron content present, Table 6.6. This sextet component was identified[8] as $\alpha$-$Fe_2O_3$ with a magnetic field of 51.0T. Calcination at 1400°C caused the tetragonal phase to continue its transformation to monophasic monoclinic zirconia as observed in the X-ray powder diffraction pattern, Figure 6.7e. The $^{57}Fe$ Mössbauer spectrum, Figure 6.8e, consisted of two components, with the sextet component being attributed to $\alpha$-$Fe_2O_3$, contributing 87% of the total spectral area.

The effect of the dopant ions on the stabilisation of the tetragonal phase is illustrated in Figure 6.9. The 5 wt% iron doped material was found to have stabilised the largest quantity of tetragonal zirconia. The 0 and 10 wt% iron doped zirconia samples produced similar amounts of tetragonal zirconia. As a larger quantity of dopant ion would be expected to stabilise the tetragonal phase further against transformation to the monoclinic phase, the difference between the 5 wt% and 10 wt% doped samples is unusual and requires further investigation.

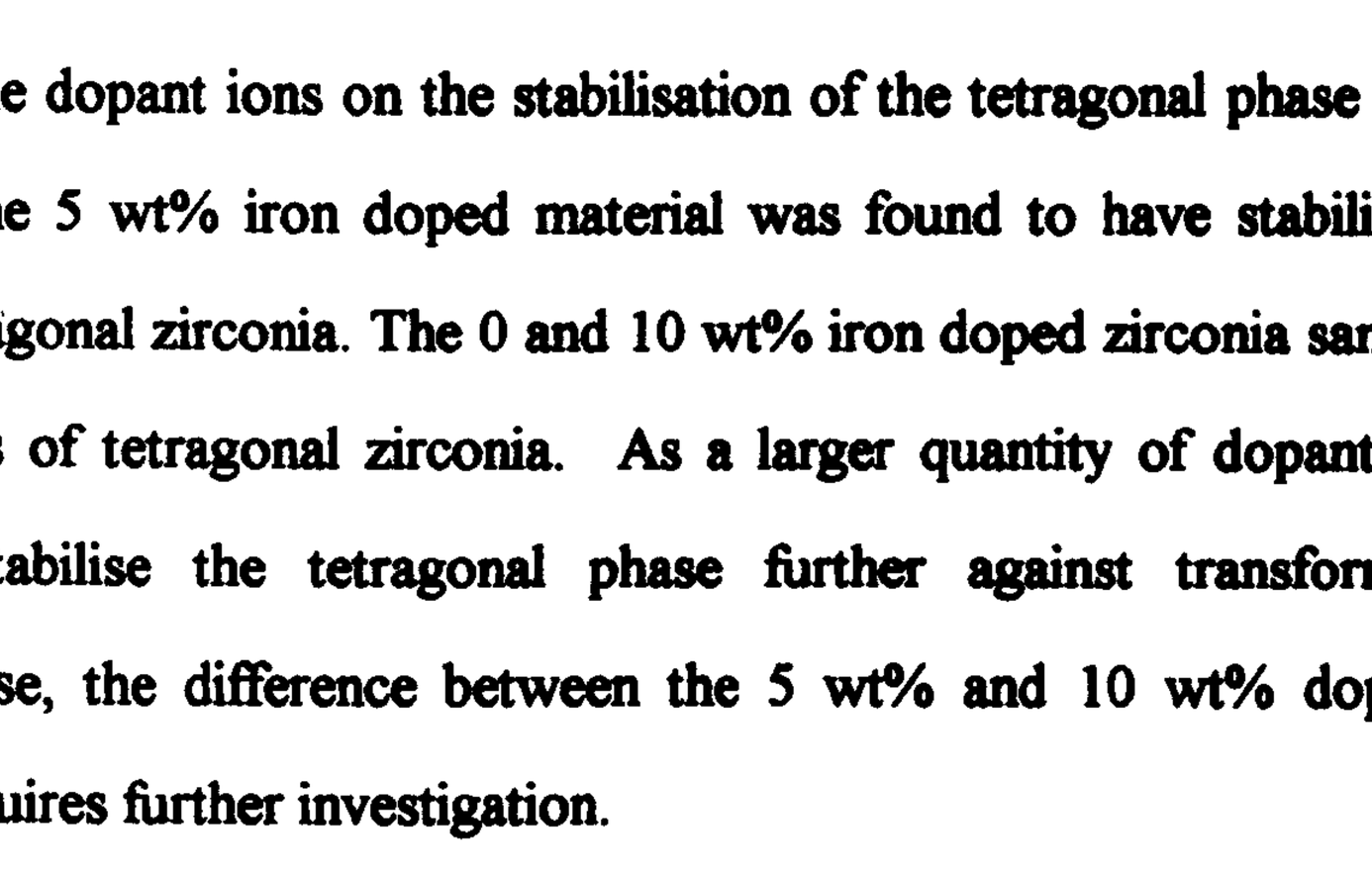


***Figure 6.9 - Comparison of the effects of iron dopant level on the formation of monoclinic zirconia by boiling under reflux in HCl***

### 6.1.1.3 Synthesis with $NH_4OH$

(i) 10 wt% iron doped zirconia

The X-ray powder diffraction pattern recorded from the 10 wt% Fe doped material dried under an infra red lamp, Figure 6.10a, showed the material to be amorphous. The $^{57}Fe$ Mössbauer spectrum, Figure 6.11a, consisted of one doublet component, $\delta = 0.27 mms^{-1}$, $\Delta = 0.78 mms^{-1}$, Table 6.7. These values are indicative[4] of $Fe^{3+}$ ions being present in the amorphous material. After calcination of the material at 200°C no change in either the X-ray powder diffraction pattern, Figure 6.10b, or the $^{57}Fe$ Mössbauer spectrum, Figure 6.11b, was observed. It was found that the quadrupole splitting of the material calcined at 200°C increased to $0.88 mms^{-1}$, Table 6.7. Crystallisation of the material occurred on calcination at 500°C with one phase, identified as tetragonal $ZrO_2$, being observed in the X-ray powder diffraction pattern, Figure 6.10c. The $^{57}Fe$ Mössbauer spectrum, Figure 6.11c, of this material consisted of one doublet, $\delta = 0.33 mms^{-1}$, $\Delta = 1.00 mms^{-1}$, Table 6.7.

| Calcination Temperature | Doublet | | | Sextet | | |
|---|---|---|---|---|---|---|
| | $\delta$ / $mms^{-1}$ (±0.05) | $\Delta$ /$mms^{-1}$ (±0.03) | Area / % | $\delta$ / $mms^{-1}$ (±0.05) | $\Delta$ /$mms^{-1}$ (±0.03) | Area / % |
| Prefurnace | 0.27 | 0.78 | 100 | - | - | 0 |
| 200°C | 0.27 | 0.88 | 100 | - | - | 0 |
| 500°C | 0.33 | 1.00 | 100 | - | - | 0 |
| 900°C | 0.35 | 1.07 | 32 | 0.41 | -0.09 | 68 |
| 1400°C | 0.11 | 0.63 | 7 | 0.40 | -0.08 | 93 |

***Table 6.7 - $^{57}Fe$ Mössbauer spectral data recorded from 10 wt% iron doped $ZrO_2$ synthesised by boiling zirconium(IV) acetate and iron(II) acetate under reflux with $NH_4OH$***

The increase in quadrupole splitting is in agreement with the suggestion, Section 6.1.1.1(i), that a high quadrupole splitting indicates the presence of tetragonal $ZrO_2$. Calcination of the material at 900°C produced an X-ray powder diffraction pattern in which the peaks had sharpened, Figure 6.10d, clearly indicating that the zirconia phase present was the tetragonal phase.

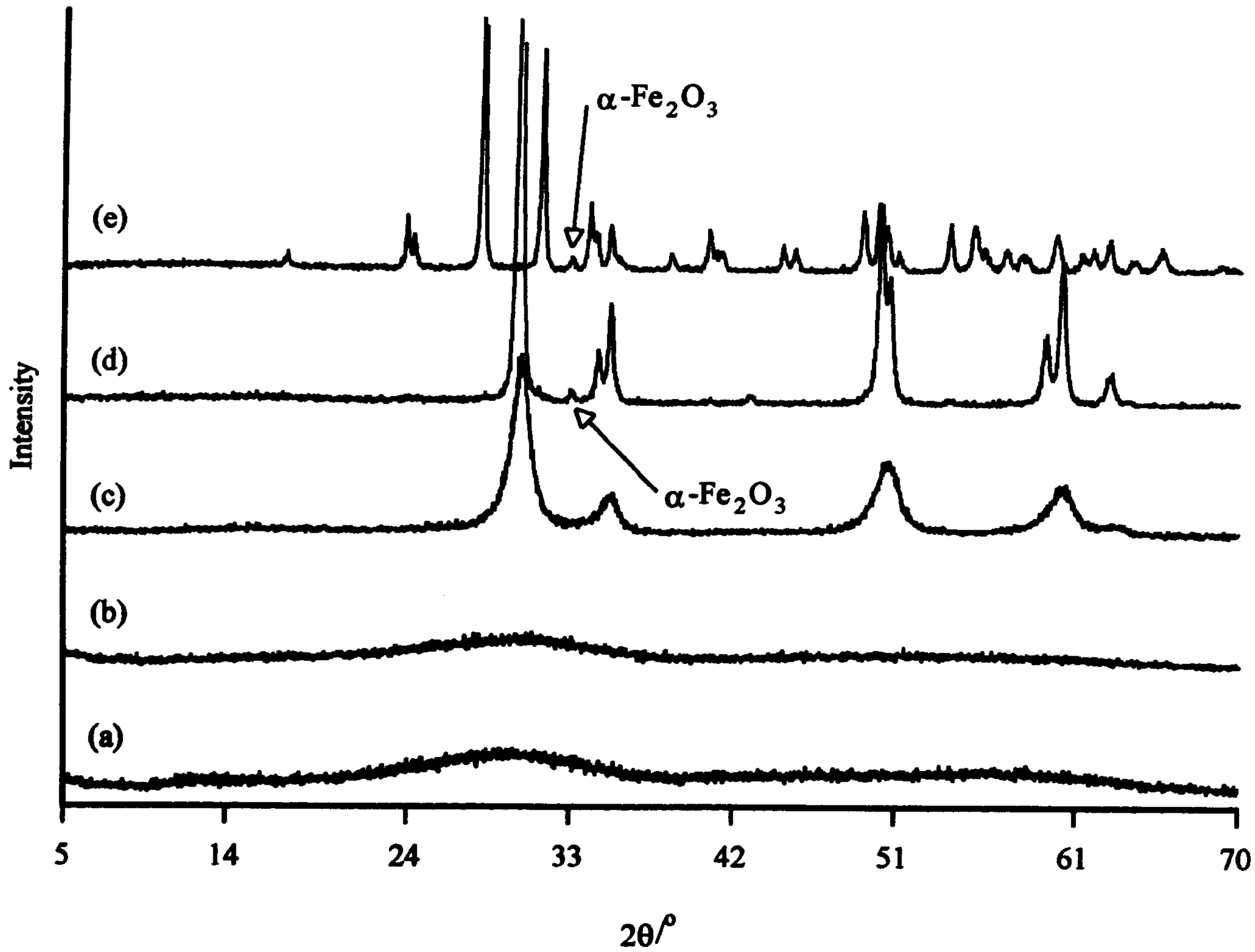


***Figure 6.10 - X-ray powder diffraction patterns recorded from the iron doped material produced by boiling zirconium (IV) acetate and 10 wt% iron(II) acetate under reflux with $NH_4OH$ (a) dried under an infra red lamp and calcined at (b) 200°C, (c) 500°C, (d) 900°C and (e) 1400°C***

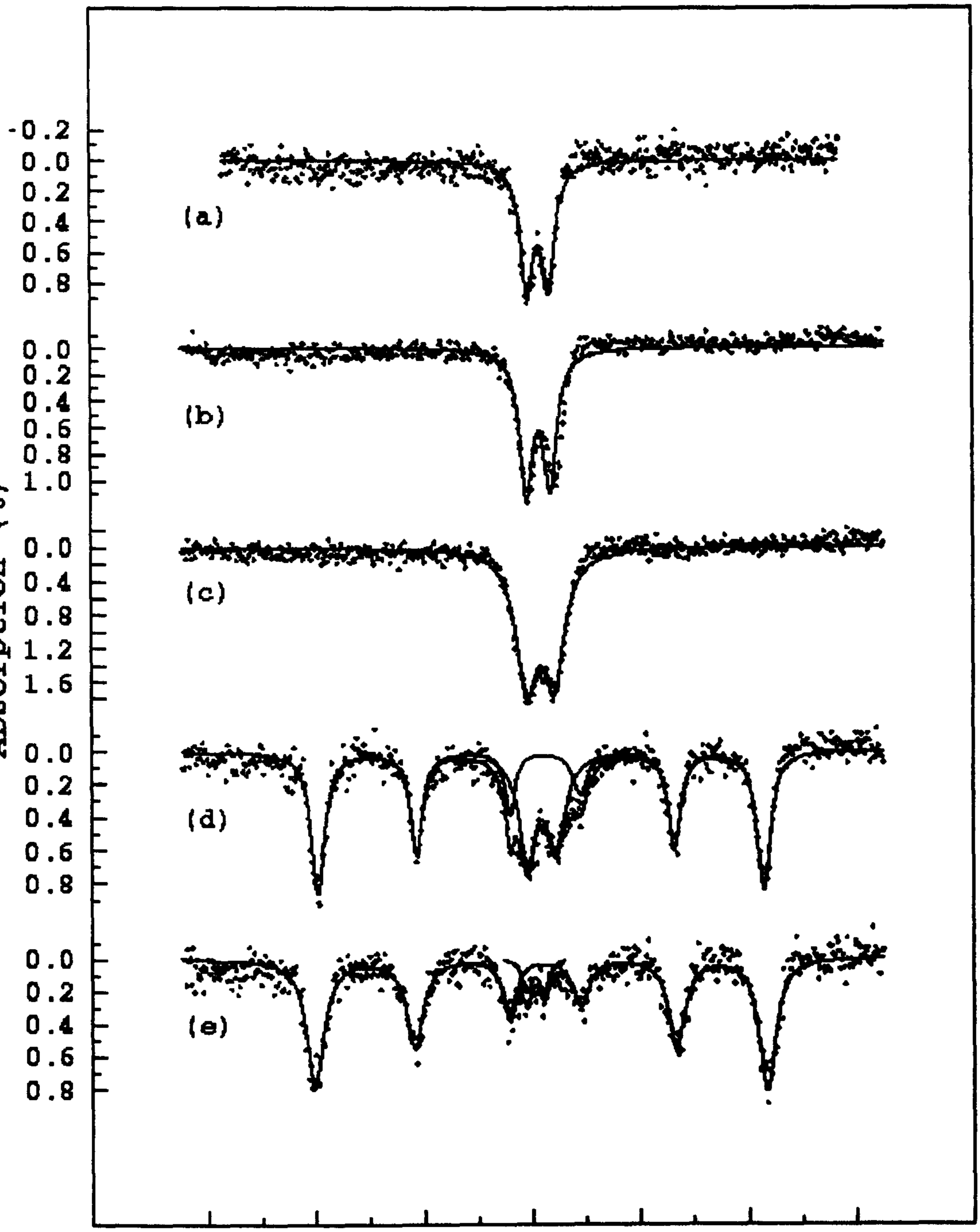


***Figure 6.11 - $^{57}Fe$ Mössbauer spectra recorded from 10 wt% iron doped $ZrO_2$ synthesised by boiling zirconium(IV) acetate and iron(II) acetate under reflux with $NH_4OH$ and (a) dried under an infra red lamp and calcined at (b) 200°C, (c) 500°C, (d) 900°C and (e) 1400°C***

A second phase, identified as $\alpha$-$Fe_2O_3$, was also observed in the X-ray powder diffraction pattern. The $^{57}Fe$ Mössbauer spectrum of the material calcined at 900°C, Figure 6.11d, consisted of two components, one sextet and one doublet. The sextet component had parameters indicative of $\alpha$-$Fe_2O_3$, contributing to 68% of the spectral area. The segregation of iron, forming $\alpha$-$Fe_2O_3$, was not associated with a phase transformation, Table 6.7, and therefore the suggestion that segregation of iron occurred with increased calcination temperature, Section 6.1.1.2, is reinforced. Calcination at 1400°C caused the complete transformation of the tetragonal phase to the monoclinic phase, Figure 6.10e. The $^{57}Fe$ Mössbauer spectrum of this material, Figure 6.11e, consisted of two components, one sextet indicative of $\alpha$-$Fe_2O_3$ contributing to 93% of the spectral area and one doublet, $\delta = 0.11 mms^{-1}$, $\Delta = 0.63 mms^{-1}$, Table 6.7. The increase in the spectral area of the component attributed to the $\alpha$-$Fe_2O_3$ phase is consistent with the segregation of iron from the zirconia structure. The variation of the quadrupole splitting with increasing calcination temperature is in agreement with the suggestion that magnitude of the quadrupole splitting is indicative of the zirconia phase produced.

(ii) 5 wt% iron doped zirconia

The X-ray powder diffraction pattern recorded from the 5 wt% Fe doped material dried under an infra red lamp, Figure 6.12a, showed the material to be amorphous. The $^{57}Fe$ Mössbauer spectrum, Figure 6.13a, showed that the iron was present as $Fe^{3+}$, $\delta = 0.28 mms^{-1}$, $\Delta = 0.75 mms^{-1}$, in one environment.

Calcination of the material at 200°C induced no change in the X-ray powder diffraction pattern, Figure 6.12b. The $^{57}Fe$ Mössbauer spectrum, Figure 6.13b, consisted of one doublet with an increased quadrupole splitting, Table 6.8. The X-ray powder diffraction pattern recorded after calcination at 500°C showed the material to have crystallised as the tetragonal modification, Figure 6.12c. The $^{57}Fe$ Mössbauer spectrum, Figure 6.13c,

consisted of one doublet component, $\delta$ = 0.35mms$^{-1}$, $\Delta$ = 0.97mms$^{-1}$, Table 6.8, consistent with $Fe^{3+}$ in tetragonal zirconia.

| Calcination Temperature | Doublet | | | Sextet | | |
|---|---|---|---|---|---|---|
| | $\delta$ / mms$^{-1}$ (±0.05) | $\Delta$ /mms$^{-1}$ (±0.03) | Area / % | $\delta$ / mms$^{-1}$ (±0.05) | $\Delta$ /mms$^{-1}$ (±0.03) | Area / % |
| Prefurnace | 0.28 | 0.75 | 100 | - | - | 0 |
| 200°C | 0.35 | 0.91 | 100 | - | - | 0 |
| 500°C | 0.35 | 0.97 | 100 | - | - | 0 |
| 900°C | 0.30 | 1.08 | 73 | 0.41 | -0.11 | 27 |
| 1400°C | 0.28 | 0.46 | 12 | 0.38 | -0.08 | 88 |

***Table 6.8 - $^{57}Fe$ Mössbauer spectral data recorded from 5 wt% iron doped $ZrO_2$ synthesised by boiling zirconium(IV) acetate and iron(II) acetate under reflux with $NH_4OH$***

The similarity between the quadrupole splitting of the materials calcined at 200°C and 500°C suggests that the material calcined at 200°C had undergone ordering prior to crystallisation. Calcination at 900°C did not induce any phase change which could be detected in the X-ray powder diffraction pattern, Figure 6.12d, although it was apparent from the sharpness of the peaks that the material had increased in crystallinity. The $^{57}Fe$ Mössbauer spectrum, Figure 6.13d, indicated that a second, magnetic iron containing phase was present which, due to the small amount of iron in the sample, was not observed in the X-ray powder diffraction pattern.

The magnetic component was identified from the $^{57}Fe$ Mössbauer parameters, Table 6.8 as the iron oxide[8] $\alpha$-$Fe_2O_3$ which represented 27% of the total iron content. Further calcination at 1400°C caused the complete transformation of the tetragonal phase to the monoclinic phase and in the X-ray powder diffraction pattern, Figure 6.12e, $\alpha$-$Fe_2O_3$ was observed. The $^{57}Fe$ Mössbauer spectrum, Figure 6.13e, indicated that the amount of $\alpha$-$Fe_2O_3$ had increased to 88% of the total iron content present, indicating that further segregation of iron had taken place. The value of the quadrupole splitting had also decreased, Table 6.8, to 0.46mms$^{-1}$, which is consistent with the view that a high quadrupole splitting is indicative of tetragonal $ZrO_2$, Section 6.1.1.1(i).

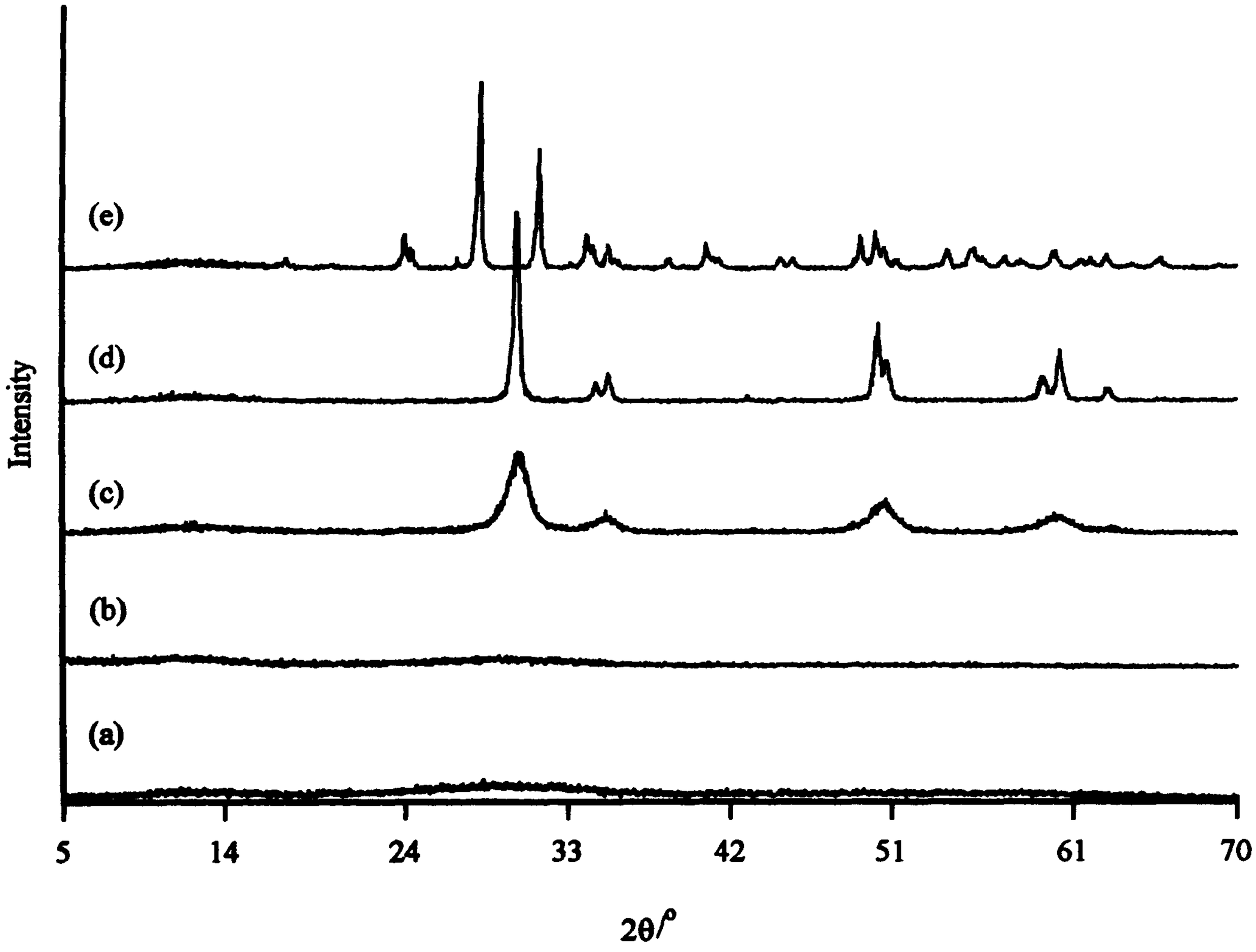


***Figure 6.12 - X-ray powder diffraction patterns recorded from iron doped zirconia produced by boiling zirconium(IV) acetate and 5 wt% iron(II) acetate under reflux with $NH_4OH$ and (a) dried under an infra red lamp and calcined at (b) 200°C, (c) 500°C, (d) 900°C and (e) 1400°C***

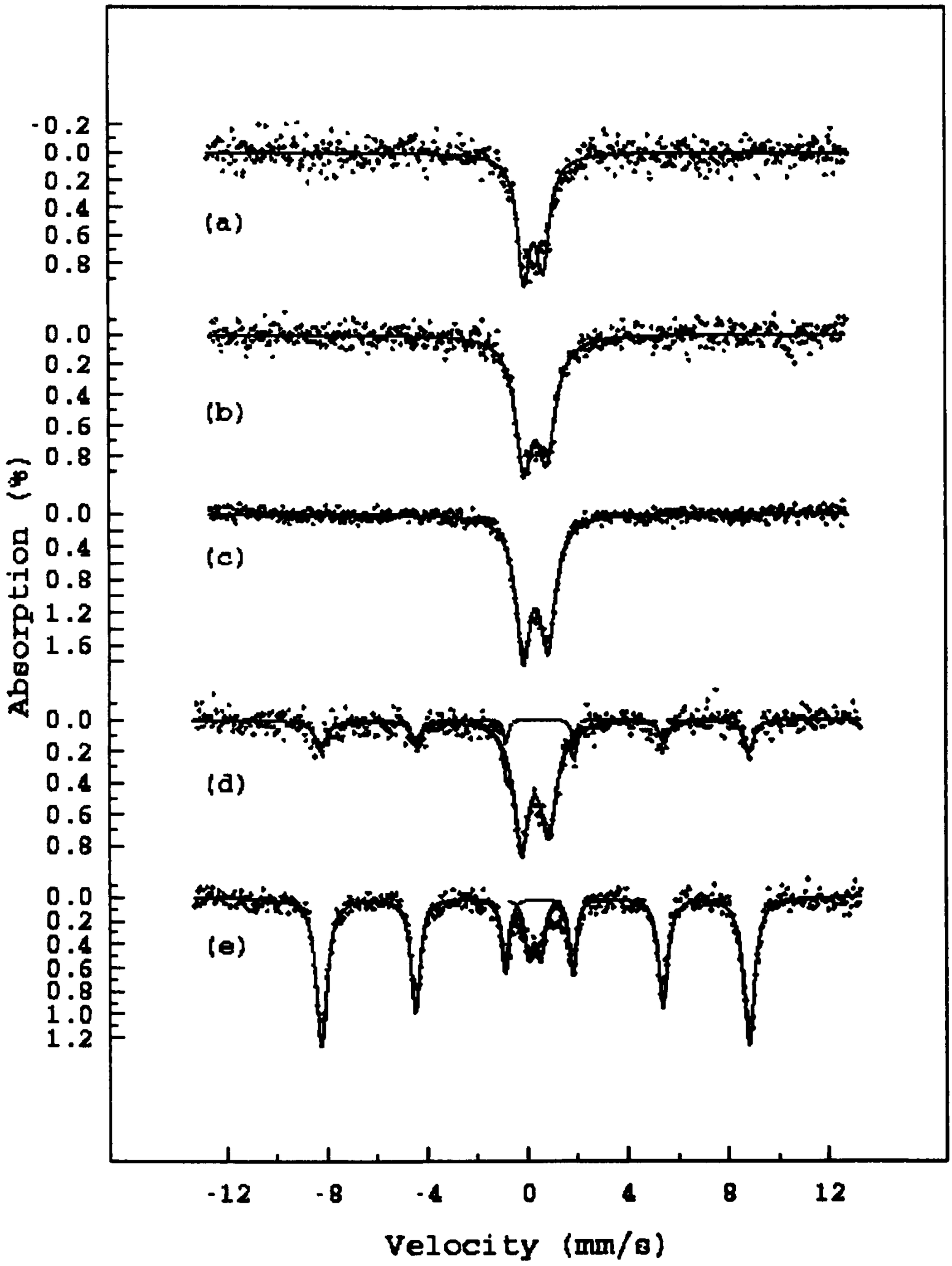


***Figure 6.13 - $^{57}Fe$ Mössbauer spectra recorded from 5 wt% iron doped $ZrO_2$ synthesised by boiling zirconium(IV) acetate and iron(II) acetate under reflux with $NH_4OH$ and (a) dried under an infra red lamp and calcined at (b) 200°C, (c) 500°C, (d) 900°C and (e) 1400°C***

The plot of the amount of monoclinic $ZrO_2$ present versus calcination temperature, Figure 6.14, indicated that the effect of the dopant on the stabilisation of the tetragonal phase was negligible at calcination temperatures up to 900°C. It was found that after calcination at 900°C the 5 and 10 wt% iron-doped samples produced monophasic tetragonal zirconia whereas with no dopant present 3% of the monoclinic phase was detected. However apparent stabilisation of the tetragonal phase is within the experimental error.

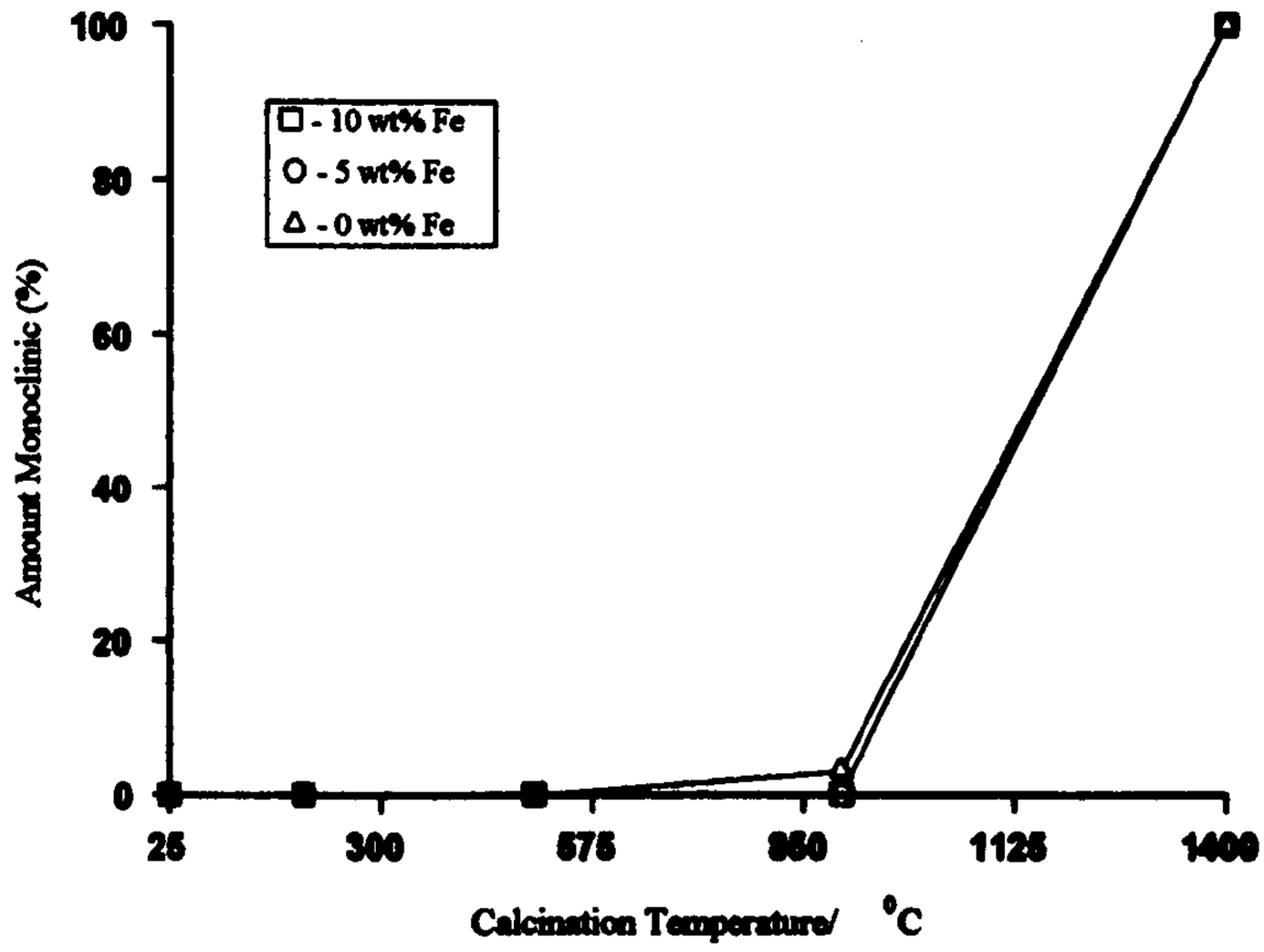


***Figure 6.14 - Comparison of the effects of iron dopant level on the formation of monoclinic zirconia by boiling under reflux in $NH_4OH$***

## 6.1.2 Hydrothermal synthesis of iron-doped $ZrO_2$

### 6.1.2.1 Synthesis with $H_2O$

(i) 10 wt% iron doped zirconia

The X-ray powder diffraction pattern recorded from the 10 wt% Fe doped material prior to calcination, Figure 6.15a, indicated that two phases were present, identified as monoclinic and tetragonal zirconia. The $^{57}Fe$ Mössbauer spectrum, Figure 6.16a, comprised one doublet component with an isomer shift of 0.38mms$^{-1}$, Table 6.9, characterising the $Fe^{3+}$ ions which had been incorporated into the zirconia structure.

Calcination of the material at 200°C produced little change in the X-ray powder diffraction pattern, Figure 6.15b. Peak intensity calculations using the method detailed earlier, Section 5.1.2.1, indicated that the amount of monoclinic $ZrO_2$ present had increased, Table 6.10. The $^{57}Fe$ Mössbauer spectrum, Figure 6.16b, was similar to the spectrum recorded from the dried material, with both isomer shift and quadrupole splitting remaining constant, Table 6.9.

| Calcination Temperature | Doublet | | | Sextet | | |
|---|---|---|---|---|---|---|
| | $\delta$ / $mms^{-1}$ (±0.05) | $\Delta$ /$mms^{-1}$ (±0.03) | Area / % | $\delta$ / $mms^{-1}$ (±0.05) | $\Delta$ /$mms^{-1}$ (±0.03) | Area / % |
| Prefurnace | 0.38 | 0.84 | 100 | - | - | 0 |
| 200°C | 0.38 | 0.84 | 100 | - | - | 0 |
| 500°C | 0.38 | 1.11 | 100 | - | - | 0 |
| 900°C | 0.35 | 1.13 | 26 | 0.39 | -0.09 | 74 |
| 1400°C | 0.43 | 0.87 | 6 | 0.39 | -0.08 | 94 |

***Table 6.9 - $^{57}Fe$ Mössbauer spectral data recorded from 10 wt% iron doped $ZrO_2$ synthesised by hydrothermal processing of zirconium(IV) acetate and iron(II) acetate with $H_2O$***

Further calcination of the material at 500°C also produced little change in the X-ray powder diffraction pattern, Figure 6.15c, but from the relative intensities of the X-ray powder diffraction peaks, Table 6.10, a decrease in the amount of the monoclinic phase present was observed. The decrease in monoclinic $ZrO_2$ content may have been due to the presence of a small amount of amorphous material which only crystallised on calcination at 500°C. It is more likely that the poor quality of the X-ray powder diffraction data, Figure 6.15c, introduced errors into the calculation which produced anomalous relative intensity values. The $^{57}Fe$ Mössbauer spectrum, Figure 6.16c, was similar to those recorded from the dried material and from that calcined at 200°C, Figure 6.16a and b, with the exception that the quadrupole splitting had increased to 1.11$mms^{-1}$, Table 6.9. This large increase, based on previous observations, Section 6.1.1.1(i), might be reasonably associated with an increase in the amount of the tetragonal phase present.

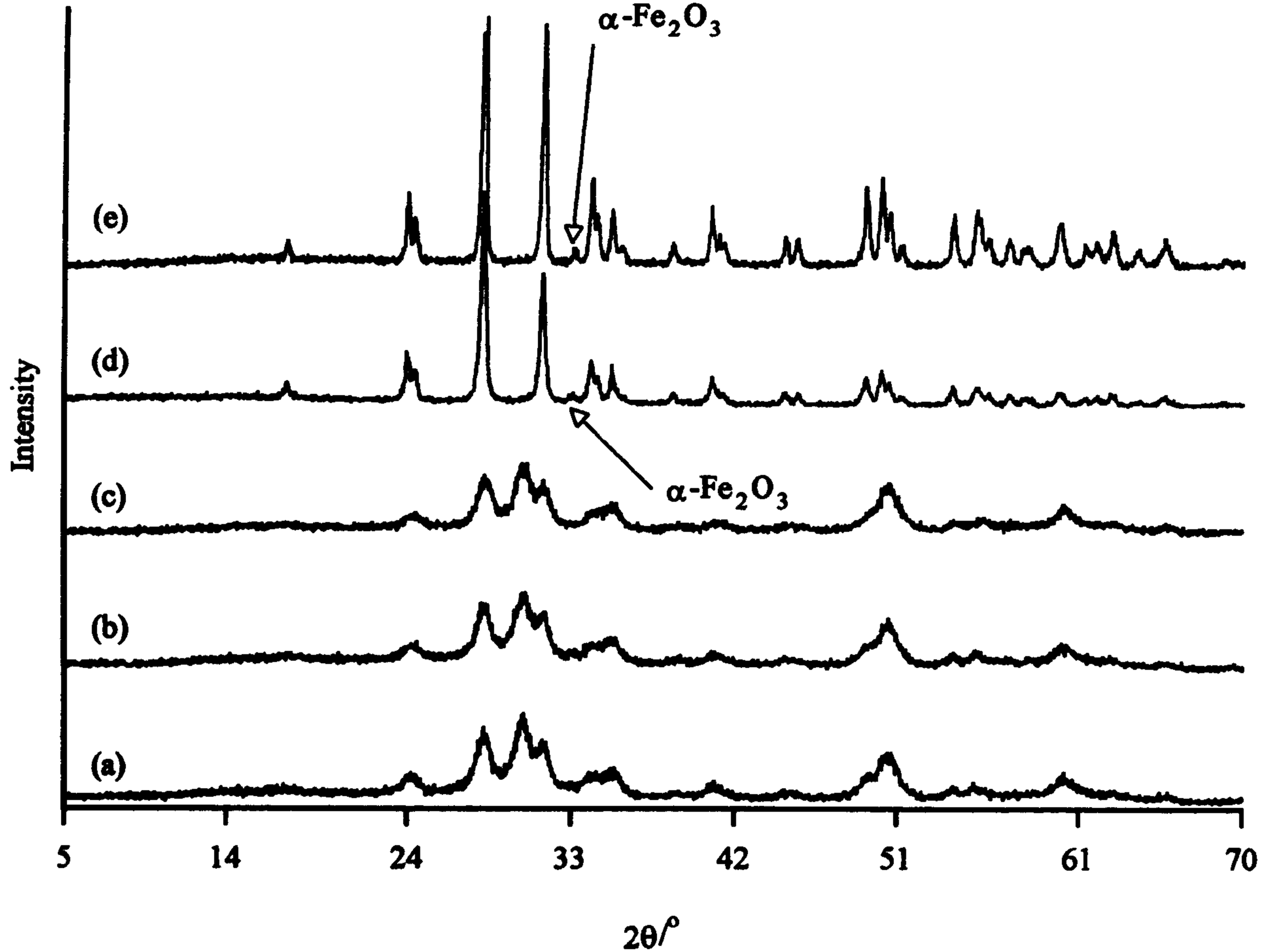


***Figure 6.15 - X-ray powder diffraction pattern recorded from iron doped zirconia synthesised by hydrothermal processing of zirconium(IV) acetate and 10 wt% iron(II) acetate with $H_2O$ and (a) dried under an infra red lamp and calcined at (b) 200°C, (c) 500°C, (d) 900°C and (e) 1400°C***

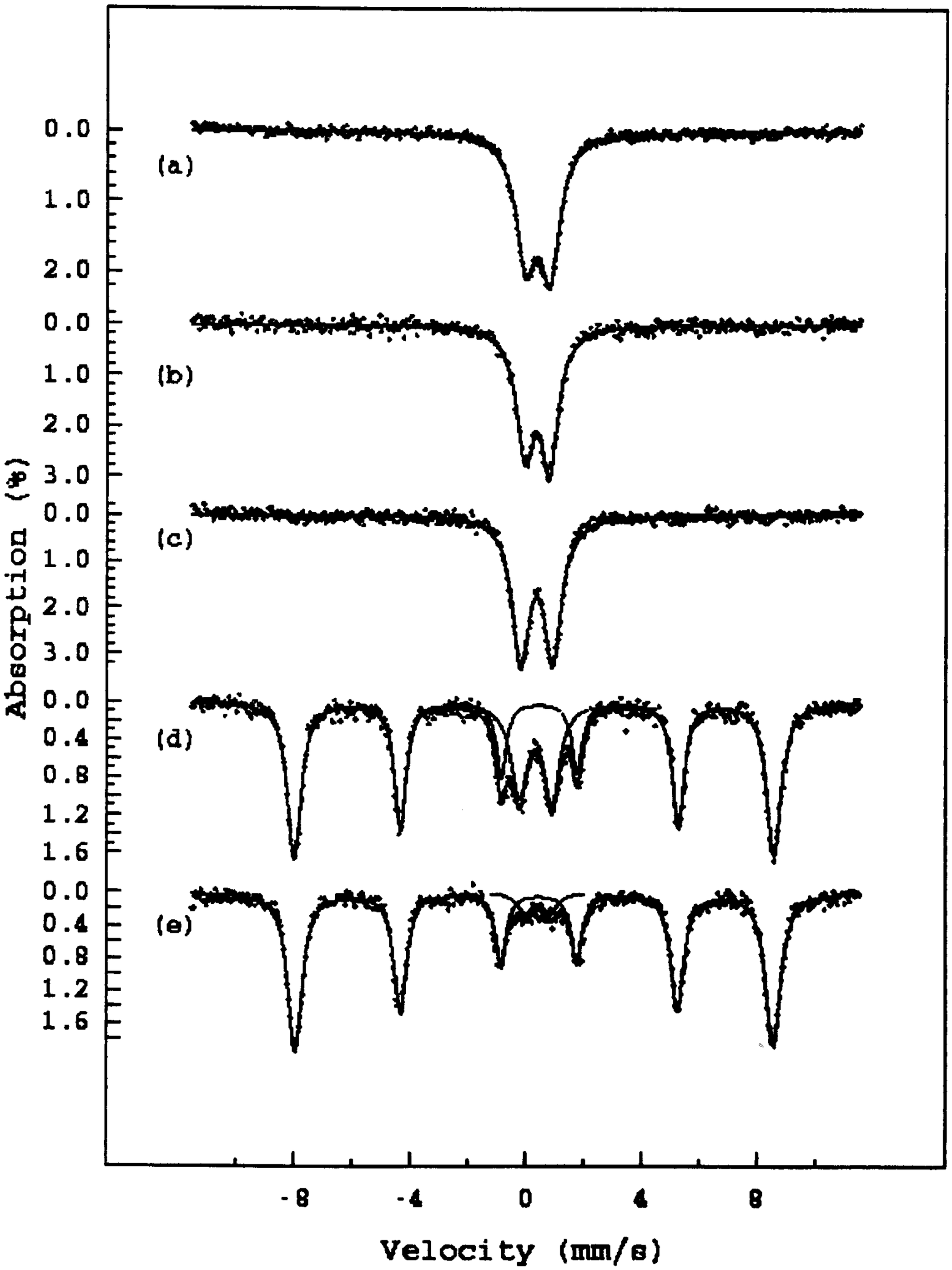


***Figure 6.16 - $^{57}Fe$ Mössbauer spectra recorded from 10 wt% iron doped $ZrO_2$ synthesised by hydrothermal processing of zirconium(IV) acetate and iron(II) acetate with $H_2O$ and (a) dried under an infra red lamp and calcined at (b) 200°C, (c) 500°C, (d) 900°C and (e) 1400°C***

However the results, Table 6.10, show that this is not the case and the observations require further investigation. The X-ray powder diffraction pattern recorded from the material calcined at 900ºC, Figure 6.15d, indicated that the tetragonal phase had transformed to the monoclinic phase and that iron had segregated from the zirconia structure as $\alpha$-$Fe_2O_3$. The $^{57}Fe$ Mössbauer spectrum recorded from this sample, Figure 6.16d, showed two components, one sextet and one doublet. The continued presence of the doublet in this spectrum was due to the segregation of the $Fe^{3+}$ species being incomplete at this temperature. Segregation was found to continue on calcination at 1400ºC where the peaks in the X-ray powder diffraction pattern, Figure 6.15e, attributed to $\alpha$-$Fe_2O_3$ were observed to increase in intensity. The process of calcination at increasing temperature, as well as inducing phase transformation, was seen to produce a more crystalline product. The increase in the spectral areas of each component of the $^{57}Fe$ Mössbauer spectrum, Figure 6.16e, indicated that the amount of hematite present in the sample had increased with calcination temperature, Table 6.9. This is consistent with $Fe^{3+}$ being segregated from the zirconia structure as temperature is increased.

(ii) 5 wt% iron doped zirconia

In contrast to the results obtained with the analogous reaction performed under reflux, Section 6.1.1.1(ii), the X-ray powder diffraction pattern, Figure 6.17a, recorded from the 5 wt% Fe doped material dried under an infra red lamp indicated the presence of both tetragonal and monoclinic $ZrO_2$. X-ray powder diffraction peak intensity calculations, Table 6.10, indicated that the predominant phase was monoclinic zirconia. The $^{57}Fe$ Mössbauer spectrum, Figure 6.18a, indicated that there were two components present, one sextet and one doublet. The sextet pattern had a field of 49.5T which is low for the expected $\alpha$-$Fe_2O_3$ phase, but may be due to small particles of $\alpha$-$Fe_2O_3$ being present.

| Preparative method | Amount (± 5%) of monoclinic zirconia | | | | |
|---|---|---|---|---|---|
| | Dried under IR lamp | 200°C | 500°C | 900°C | 1400°C |
| Hydrothermal/10 wt%/$H_2O$ | 64 | 67 | 62 | 100 | 100 |
| Hydrothermal/ 5 wt%/$H_2O$ | 54 | 53 | 57 | 100 | 100 |
| Hydrothermal/10 wt%/HCl | 100 | 100 | 75 | 90 | 100 |
| Hydrothermal/ 5 wt%/HCl | 100 | 100 | 100 | 100 | 100 |
| Hydrothermal/10 wt%/$NH_4OH$ | 10 | 13 | 11 | 93 | 100 |
| Hydrothermal/ 5 wt%/$NH_4OH$ | 23 | 14 | 15 | 100 | 100 |

***Table 6.10 - Amount of monoclinic zirconia formed by calcination in air of iron doped zirconia prepared by hydrothermal processing of zirconium(IV) acetate and iron(II) acetate***

Calcination of the material at 200°C caused no visible change to the X-ray powder diffraction pattern, Figure 6.17b, and there was no significant change in the relative amounts of each component present, Table 6.10. The $^{57}Fe$ Mössbauer spectrum, Figure 6.18b, showed that the relative amounts of the two iron containing phases remained constant, Table 6.11, and the size of the field in the sextet component remained constant at 49.6T.

| Calcination Temperature | Doublet | | | Sextet | | |
|---|---|---|---|---|---|---|
| | $\delta$ / $mms^{-1}$ (±0.05) | $\Delta$ /$mms^{-1}$ (±0.03) | Area / % | $\delta$ / $mms^{-1}$ (±0.05) | $\Delta$ /$mms^{-1}$ (±0.03) | Area / % |
| Prefurnace | 0.33 | 0.87 | 46 | 0.35 | -0.10 | 54 |
| 200°C | 0.33 | 0.87 | 46 | 0.35 | -0.08 | 54 |
| 500°C | 0.35 | 0.99 | 60 | 0.32 | -0.10 | 40 |
| 900°C | 0.36 | 1.13 | 56 | 0.44 | -0.07 | 44 |
| 1400°C | 0.14 | 0.52 | 12 | 0.42 | -0.07 | 88 |

***Table 6.11 - $^{57}Fe$ Mössbauer spectral data recorded from 5 wt% iron doped $ZrO_2$ synthesised by hydrothermal processing of zirconium(IV) acetate and iron(II) acetate with $H_2O$***

Calcination of the material at 500°C caused no change in the X-ray powder diffraction pattern and this was confirmed from calculations of the relative peak intensity ratios, Table 6.10. The $^{57}Fe$ Mössbauer spectrum of the material calcined at 500°C, Figure 6.18c, contained one doublet component, $\delta = 0.35 mms^{-1}$, indicating the presence of $Fe^{3+}$

ions in one of the crystalline phases present and one sextet component. The quadrupole splitting, of the doublet, 0.99mms$^{-1}$, Table 6.11, was higher than expected for a mixture of tetragonal and monoclinic $ZrO_2$. After calcination at 900°C the material had transformed to monophasic monoclinic $ZrO_2$ as evidenced by the X-ray powder diffraction pattern, Figure 6.17d. The $^{57}$Fe Mössbauer spectrum, Figure 6.18d, indicated that the sextet component present had a magnetic field of 52.3T, indicative of $\alpha$-$Fe_2O_3$. The size of the field indicated that the process of calcination had caused the $\alpha$-$Fe_2O_3$ particles to increase in size. The variation in the amount of $\alpha$-$Fe_2O_3$ present as calcination temperature increased, Table 6.11, appeared to be unusual and suggested that $Fe^{3+}$ ions moved into the zirconia structure after calcination at 500°C before segregating on calcination at 900°C. This point requires further investigation. Also, the quadrupole splitting of the doublet component had increased to 1.13mms$^{-1}$, Table 6.11, which contrasts with earlier findings, Section 6.1.1.1(i), which suggested that a large quadrupole splitting indicated the presence of the tetragonal phase. Subsequent calcination of the material at 1400°C showed there to be no further change in the X-ray powder diffraction pattern, Figure 6.17e, with the exception that a small peak attributable to $\alpha$-$Fe_2O_3$ was present. The increase in $\alpha$-$Fe_2O_3$ content was confirmed by the $^{57}$Fe Mössbauer spectrum, Figure 6.18e, which indicated that 88% of the total iron content was present as $\alpha$-$Fe_2O_3$, Table 6.11. Furthermore, the isomer shift for the doublet had decreased to 0.14mms$^{-1}$, but this is likely to be due to the poor quality of the spectrum and the size of the component to be fitted introducing inaccuracies to the fitting procedure. The quadrupole splitting had also decreased to 0.52mms$^{-1}$ which was as expected for monoclinic iron doped $ZrO_2$.

The effect of the dopant ion on the stabilisation of the tetragonal phase was substantial for the materials prepared by hydrothermal processing with water, Figure 6.19. The introduction of greater amounts of the dopant ion caused a destabilisation of the tetragonal phase.

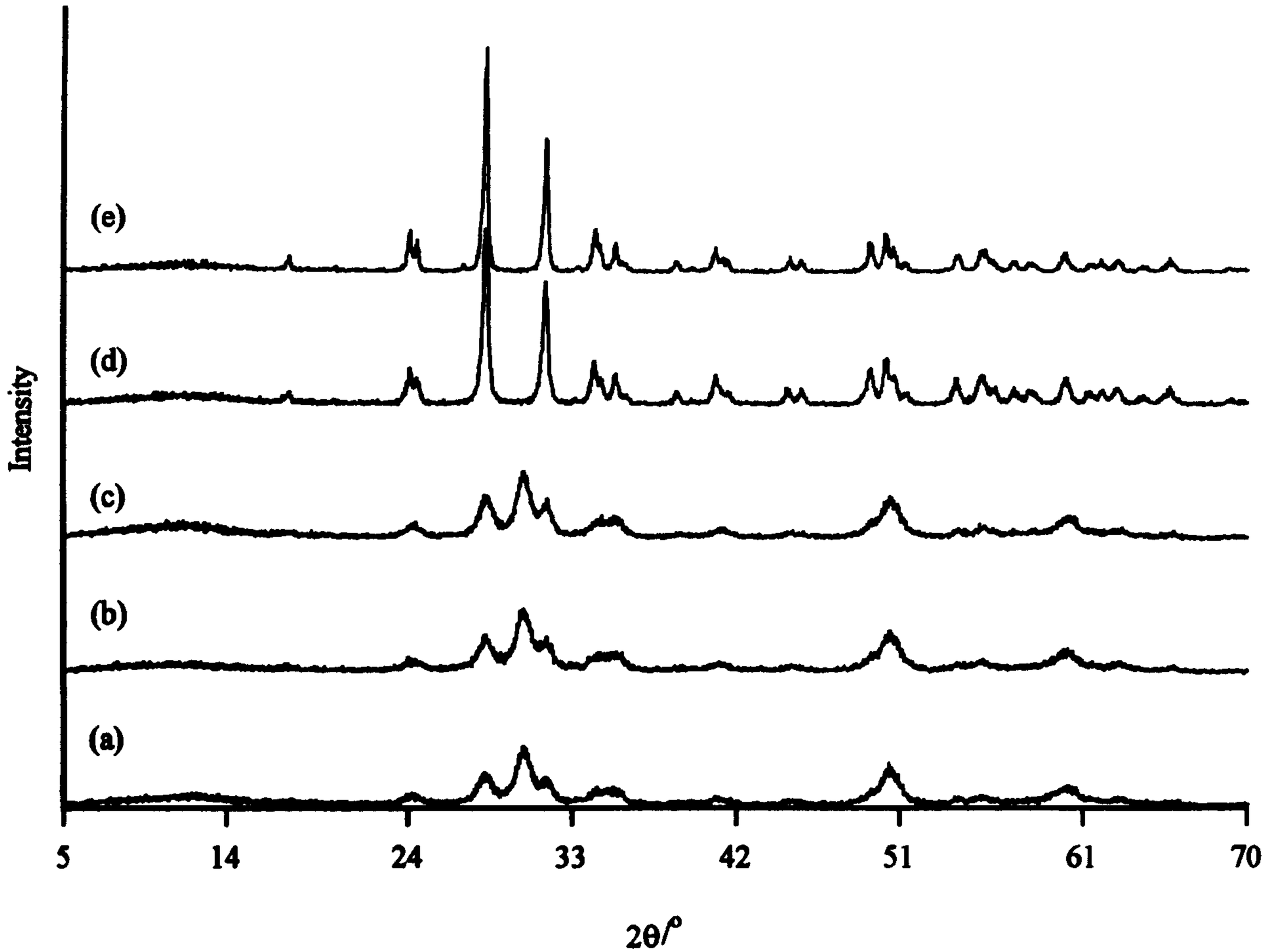


***Figure 6.17 - X-ray powder diffraction patterns recorded from iron doped zirconia synthesised by hydrothermal processing of zirconium(IV) acetate and 5 wt% iron(II) acetate with $H_2O$ and (a) dried under an infra red lamp and calcined at (b) 200°C, (c) 500°C, (d) 900°C and (e) 1400°C***

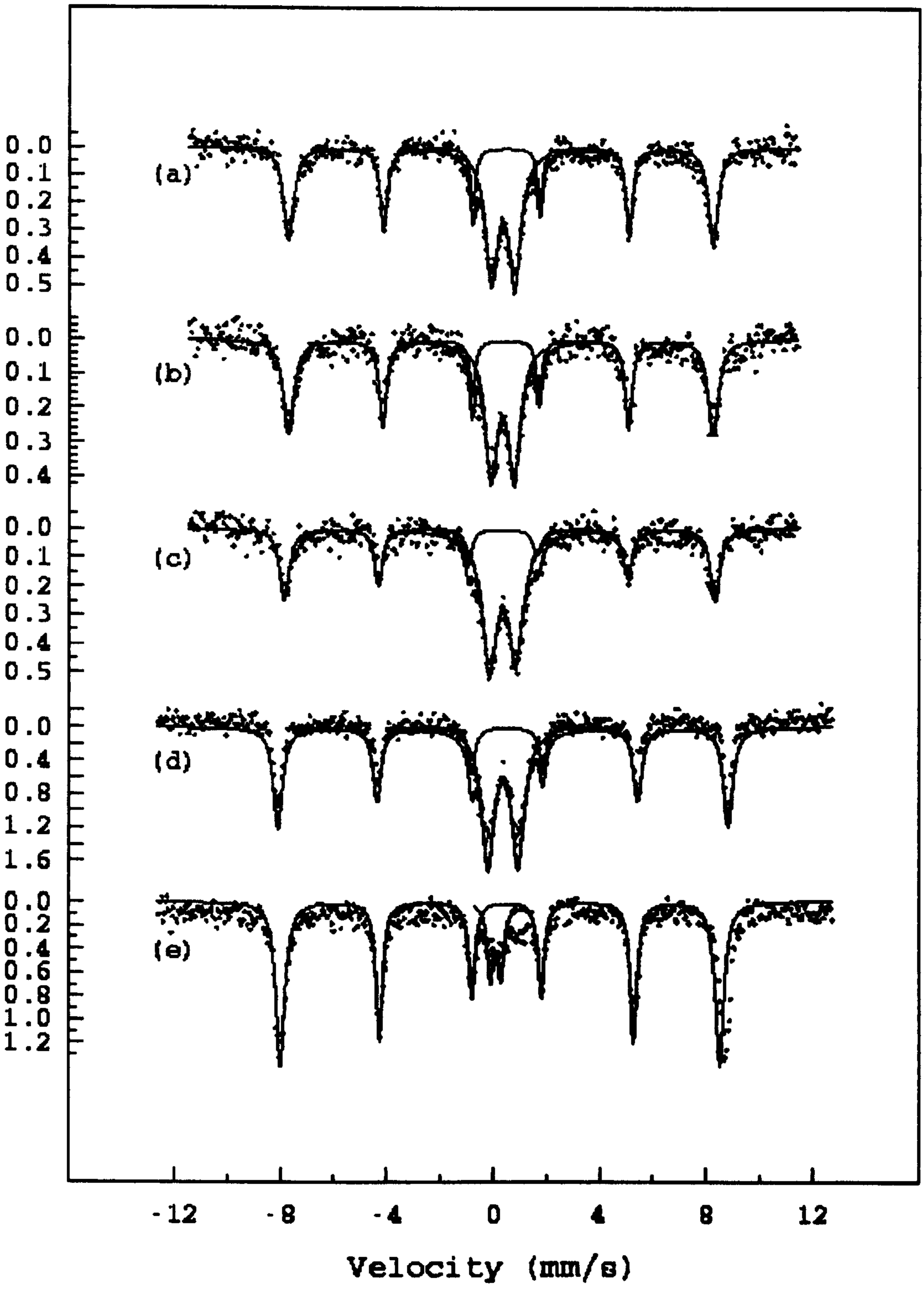


***Figure 6.18 - $^{57}Fe$ Mössbauer spectra recorded from 5 wt% iron doped $ZrO_2$ synthesised by hydrothermal processing of zirconium(IV) acetate and iron(II) acetate with $H_2O$ and (a) dried under an infra red lamp and calcined at (b) 200°C, (c) 500°C, (d) 900°C and (e) 1400°C***

These results differ from those obtained by boiling a zirconium(IV) acetate/iron(II) acetate solution under reflux, Section 6.1.1.1, where for 0 and 5 wt% iron-doped zirconia no monoclinic phase formed after calcination at 500°C. This suggests that synthesis route, as well as dopant level, has a marked effect on the phase of zirconia produced. The destabilisation of the tetragonal phase is in contrast to the findings of Li et al[5] who found that introduction of dopant ions caused the stabilisation of the tetragonal phase.

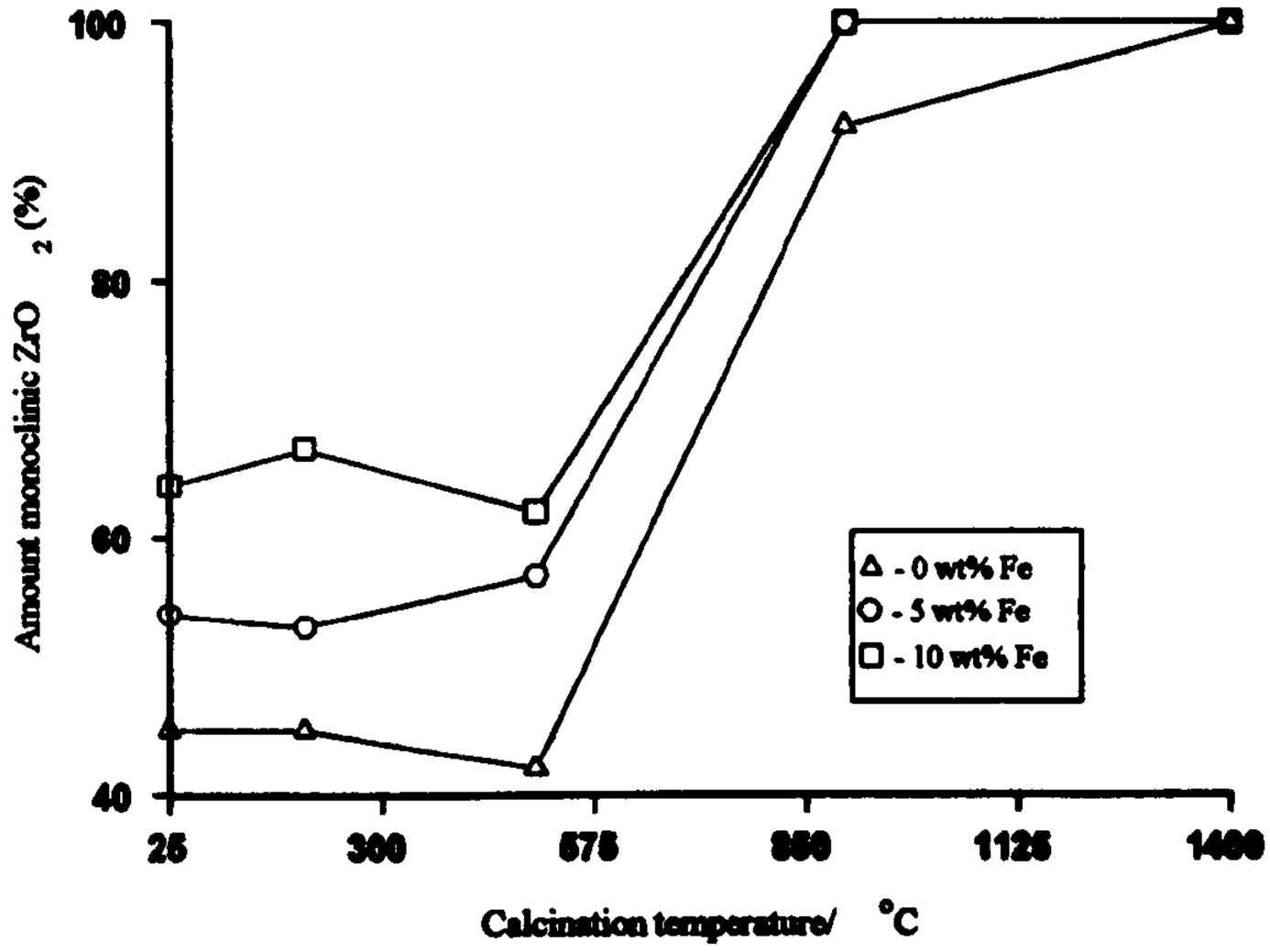


***Figure 6.19 - Comparison of the effects of iron dopant level on the formation of monoclinic zirconia by hydrothermal processing in water***

### 6.1.2.2 Synthesis with HCl

(i) 10 wt% iron doped zirconia

The X-ray powder diffraction pattern recorded from the 10 wt% Fe doped material dried under an infra red lamp indicated that monophasic monoclinic $ZrO_2$ had been produced, Figure 6.20a. After calcination of the material at 200°C the X-ray powder diffraction pattern, Figure 6.21b, was unchanged and the peaks attributed to monoclinic $ZrO_2$ remained broad. Calcination of the material at 500°C caused an unexpected change in the X-ray powder diffraction pattern, Figure 6.20c. As well as the monoclinic phase

being present a second phase appeared with the most intense peak occurring between the [1 1 1] and the [1 1 $\bar{1}$] peaks of the monoclinic phase at approximately $2\theta = 30^{o}$. Identification of this phase was not possible because of the broadness of the X-ray powder diffraction peaks of both phases, although it is likely that the phase would be either cubic or tetragonal $ZrO_2$. The $^{57}Fe$ Mössbauer spectra, Figure 6.21a-c, of the material calcined at temperatures to 500°C consist of one doublet with an isomer shift of $0.38 mms^{-1}$, Table 6.12, indicative of $Fe^{3+}$ ions having been incorporated into the zirconia structure. The X-ray powder diffraction pattern of the material calcined at 900°C, Figure 6.20d, showed considerably sharpened X-ray diffraction peaks indicating an increase in crystallinity and from this pattern it was possible to identify the unknown $ZrO_2$ phase as tetragonal. X-ray powder diffraction peaks indicative of the iron oxide phase, $\alpha$-$Fe_2O_3$, were also evident in the X-ray powder diffraction pattern, Figure 6.20d, indicating that segregation of iron from the $ZrO_2$ structure had occurred. Using the method described earlier, Section 5.1.2.1, the X-ray powder diffraction patterns, Figure 6.20c and d, enabled the maximum concentration of the tetragonal phase to be identified after calcination at 500°C. Calcination at 900°C transformed the remaining tetragonal phase to the monoclinic phase. This suggests that a substantial amount of amorphous zirconia was initially present which only crystallised as tetragonal $ZrO_2$ after calcination at 500°C.

The $^{57}Fe$ Mössbauer spectrum recorded from the sample after calcination at 900°C, Figure 6.21d, consisted of one doublet with an isomer shift of $0.36 mms^{-1}$ and one sextet with parameters consistent[8] with $\alpha$-$Fe_2O_3$, Table 6.12. Examination of the spectral area of the two components in the $^{57}Fe$ Mössbauer spectrum, Table 6.12, indicated that 75% of the iron present in the sample segregated upon calcination at 900°C, producing $\alpha$-$Fe_2O_3$. The X-ray powder diffraction pattern, Figure 6.20e, recorded from the material calcined at 1400°C showed that the tetragonal phase had transformed to the monoclinic phase.

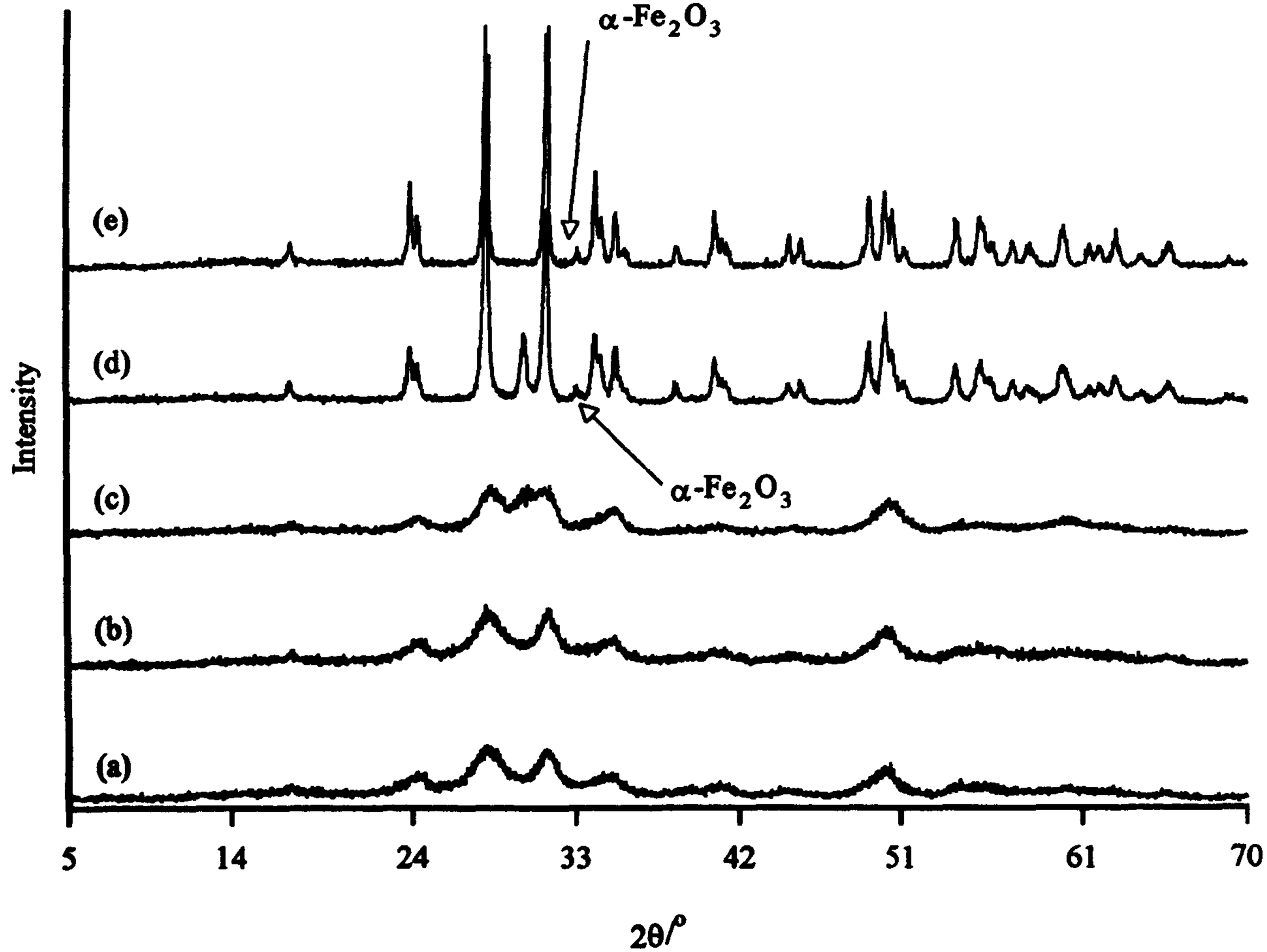


***Figure 6.20 - X-ray powder diffraction patterns recorded from iron doped zirconia synthesised by hydrothermal processing of zirconium(IV) acetate and 10 wt % iron(II) acetate with HCl and (a) dried under an infra red lamp and calcined at (b) 200°C, (c) 500°C, (d) 900°C and (e) 1400°C***

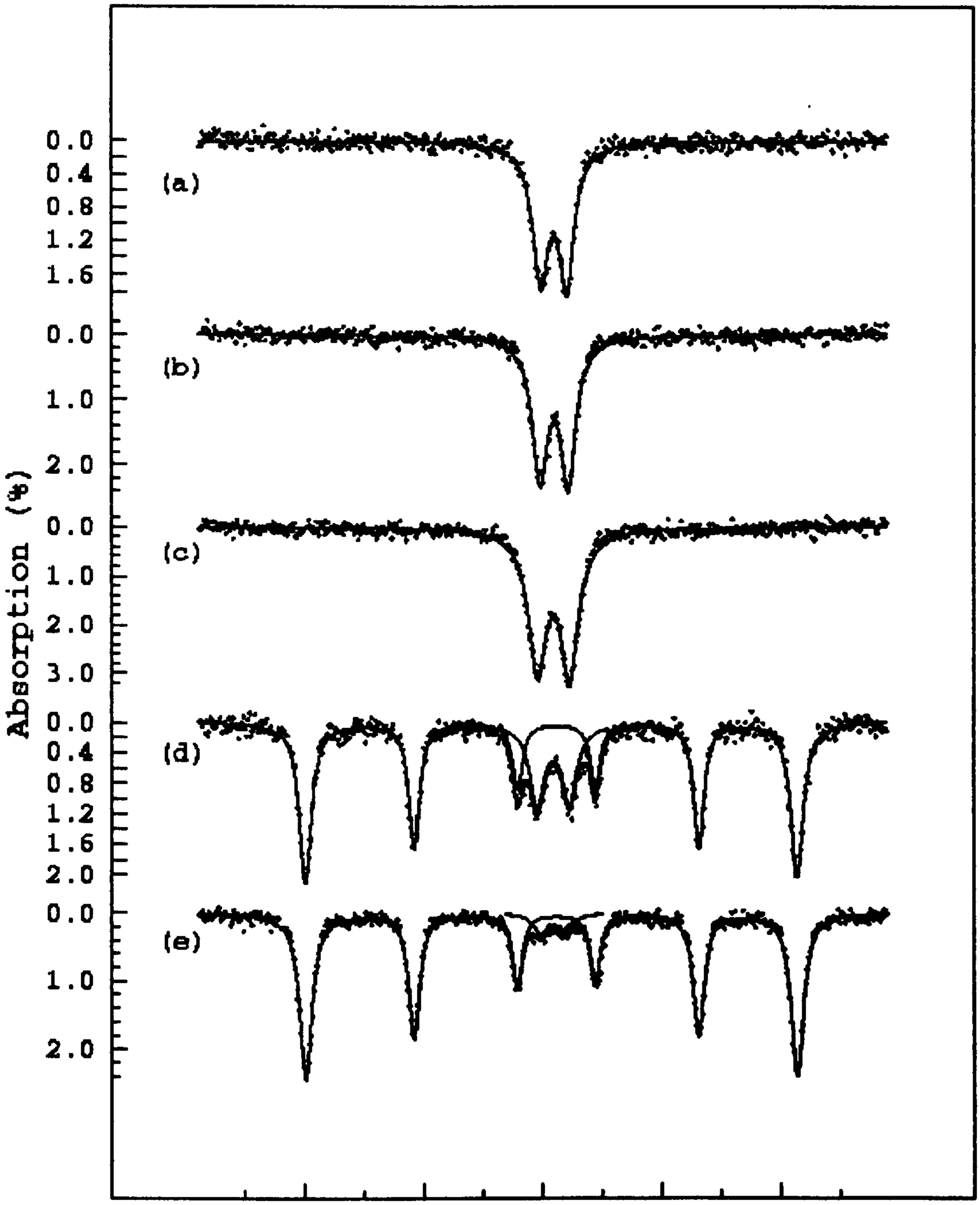


***Figure 6.21 - $^{57}Fe$ Mössbauer spectra recorded from 10 wt% iron doped $ZrO_2$ synthesised by hydrothermal processing of zirconium(IV) acetate and iron(II) acetate with HCl and (a) dried under an infra red lamp and calcined at (b) 200°C, (c) 500°C, (d) 900°C and (e) 1400°C***

The $^{57}Fe$ Mössbauer spectrum, Figure 6.21e, indicated that segregation of more of the remaining iron had taken place, with 93% of the total iron content being present as $\alpha$-$Fe_2O_3$ after calcination at 1400°C. The doublet component representing the iron remaining in the monoclinic structure had an isomer shift of $0.34mms^{-1}$ consistent with $Fe^{3+}$ ions being present in the zirconia structure.

| Calcination Temperature | Doublet | | | Sextet | | |
|---|---|---|---|---|---|---|
| | $\delta$ / $mms^{-1}$ (±0.05) | $\Delta$ /$mms^{-1}$ (±0.03) | Area / % | $\delta$ / $mms^{-1}$ (±0.05) | $\Delta$ /$mms^{-1}$ (±0.03) | Area / % |
| Prefurnace | 0.38 | 0.87 | 100 | - | - | 0 |
| 200°C | 0.38 | 0.94 | 100 | - | - | 0 |
| 500°C | 0.37 | 1.08 | 100 | - | - | 0 |
| 900°C | 0.36 | 1.09 | 24 | 0.38 | -0.09 | 75 |
| 1400°C | 0.34 | 0.82 | 7 | 0.38 | -0.08 | 93 |

***Table 6.12 - $^{57}Fe$ Mössbauer spectral data recorded from 10 wt% iron doped $ZrO_2$ synthesised by hydrothermal processing of zirconium(IV) acetate and iron(II) acetate with HCl***

(ii) 5 wt% iron doped zirconia

The X-ray powder diffraction pattern, Figure 6.22a, recorded from the 5 wt% Fe doped material dried under an infra red lamp indicated that the material produced was monophasic monoclinic $ZrO_2$. The $^{57}Fe$ Mössbauer spectrum, Figure 6.23a, consisted of one doublet component with an isomer shift of $0.34mms^{-1}$, Table 6.13, which indicated $Fe^{3+}$ ions present in the $ZrO_2$ structure. Calcination of the sample at 200°C caused the material to remain unchanged as observed in the X-ray powder diffraction pattern, Figure 6.22b. The $^{57}Fe$ Mössbauer spectrum, Figure 6.23b, showed the quadrupole splitting to increase from $0.66mms^{-1}$ to $0.86mms^{-1}$, Table 6.13. After calcination at 500°C the material, from the X-ray powder diffraction pattern, Figure 6.22c, appeared to have increased in crystallinity. Closer inspection of the pattern indicated that this material may have included a small amount of tetragonal $ZrO_2$, which could not be determined from the peak intensity calculations. If so, this would explain the observed increase in the quadrupole splitting of the doublet component in the $^{57}Fe$ Mössbauer spectrum, Figure

6.23c and Table 6.13. Calcination at 900°C produced a material which gave an X-ray powder diffraction pattern, Figure 6.22d, of increased peak intensity and sharpness, indicating that the tetragonal $ZrO_2$ had increased in crystallinity. The $^{57}Fe$ Mössbauer spectrum, Figure 6.23d, indicated that two iron containing phases were present. The sextet pattern had parameters indicative[8] of $\alpha$-$Fe_2O_3$, Table 6.13, and the doublet component had an isomer shift of $0.36 mms^{-1}$, indicative of $Fe^{3+}$ ions remaining in the tetragonal zirconia structure.

| Calcination Temperature | Doublet | | | Sextet | | |
|---|---|---|---|---|---|---|
| | $\delta$ / $mms^{-1}$ (±0.05) | $\Delta$ /$mms^{-1}$ (±0.03) | Area / % | $\delta$ / $mms^{-1}$ (±0.05) | $\Delta$ /$mms^{-1}$ (±0.03) | Area / % |
| Prefurnace | 0.34 | 0.66 | 100 | - | - | 0 |
| 200°C | 0.36 | 0.86 | 100 | - | - | 0 |
| 500°C | 0.38 | 1.04 | 100 | - | - | 0 |
| 900°C | 0.36 | 0.95 | 68 | 0.43 | -0.07 | 32 |
| 1400°C | 0.35 | 0.92 | 14 | 0.41 | -0.08 | 86 |

***Table 6.13 - $^{57}Fe$ Mössbauer spectral data recorded from 5 wt% iron doped $ZrO_2$ synthesised by hydrothermal processing of zirconium(IV) acetate and iron(II) acetate with HCl***

The doublet represented the majority phase in the $^{57}Fe$ Mössbauer spectrum, Table 6.13, contributing to 68% of the spectral area. The remaining 32% of the spectral area was attributed to the $\alpha$-$Fe_2O_3$ phase suggesting that calcination of the material at 900°C had induced a segregation process, resulting in the formation of the $\alpha$-$Fe_2O_3$ phase.

The X-ray powder diffraction pattern recorded from the material calcined at 1400°C, Figure 6.22e, showed that the calcination process had produced a material of increased crystallinity. Also evident in the pattern was a peak at $2\theta = 33.5°$ indicative of the $\alpha$-$Fe_2O_3$ phase. The $^{57}Fe$ Mössbauer spectrum, Figure 6.23e, indicated that there was an increase in the amount of $\alpha$-$Fe_2O_3$ present, from 32% of the spectral area to 86% of the spectral area, Table 6.13. The quadrupole splitting for the doublet component had decreased to $0.92 mms^{-1}$ from a maximum of $1.04 mms^{-1}$ after calcination at 500°C.

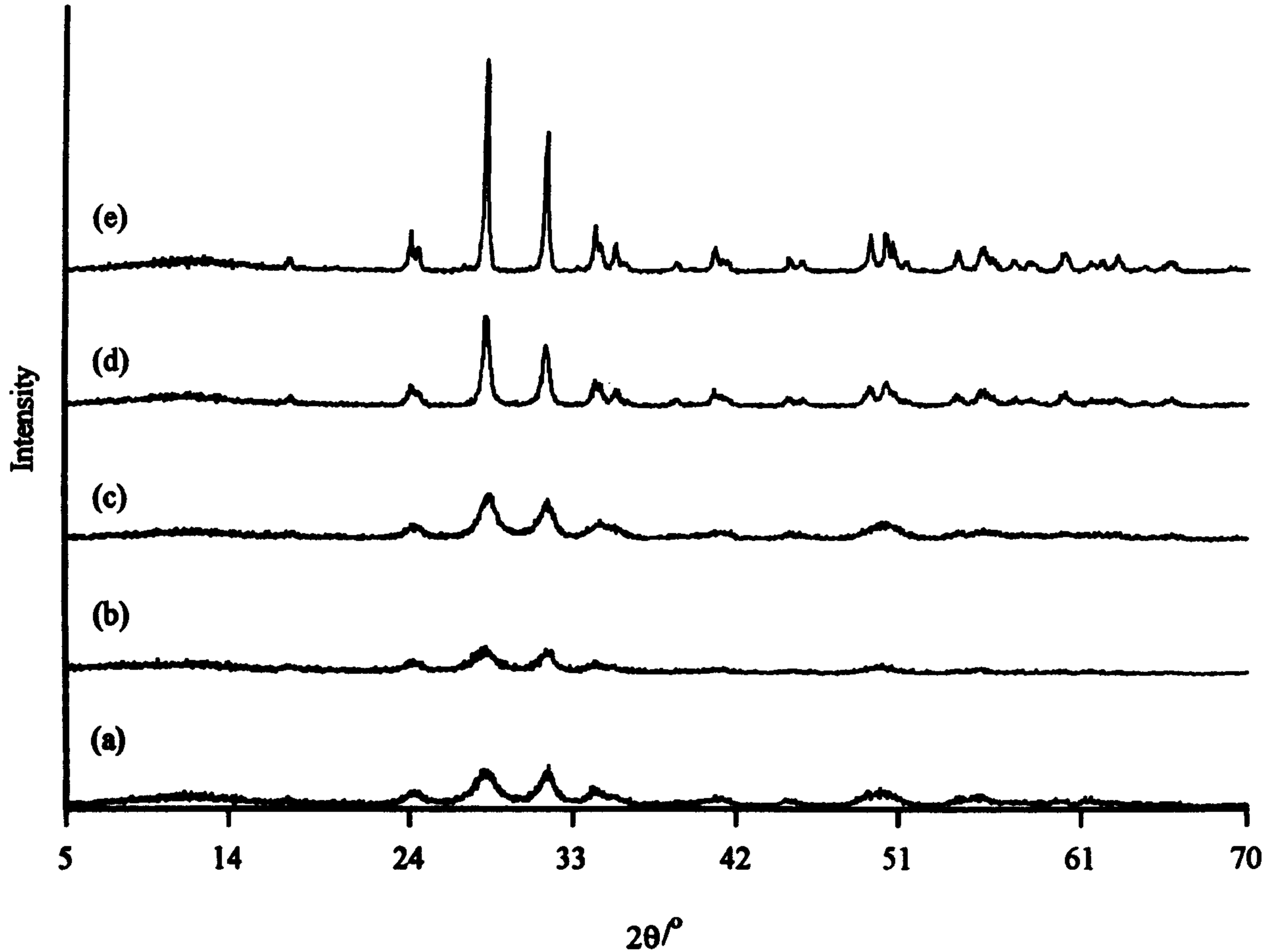


***Figure 6.22 - X-ray powder diffraction patterns recorded from iron doped zirconia produced by hydrothermal processing of zirconium(IV) acetate and 5 wt% iron(II) acetate with HCl and (a) dried under an infra red lamp and calcined at (b) 200°C, (c) 500°C, (d) 900°C and (e) 1400°C***

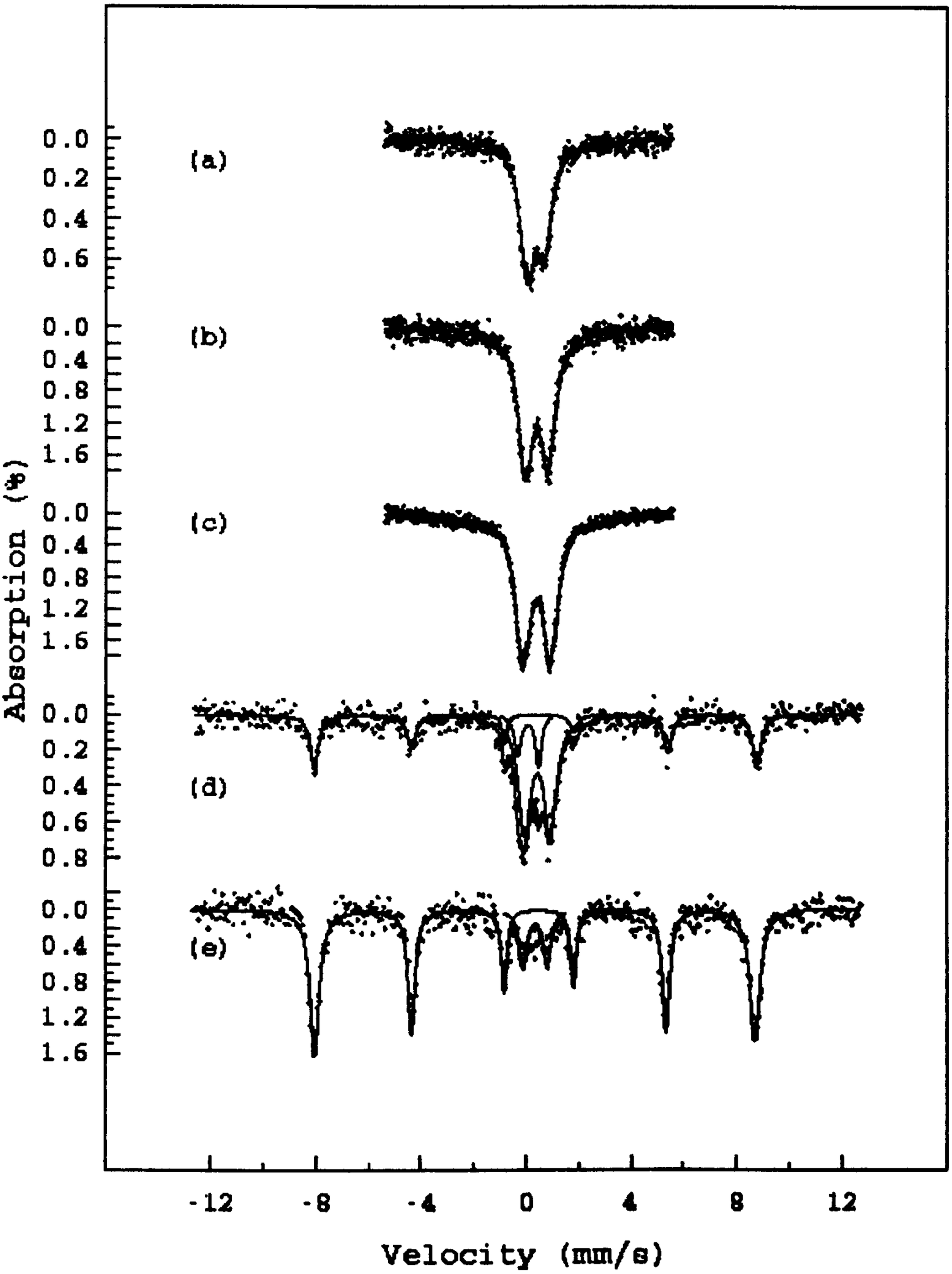


***Figure 6.23 - $^{57}Fe$ Mössbauer spectra recorded from 5 wt% iron doped $ZrO_2$ synthesised by hydrothermal processing of zirconium(IV) acetate and iron(II) acetate with HCl and (a) dried under an infra red lamp and calcined at (b) 200°C, (c) 500°C, (d) 900°C and (e) 1400°C***

This may be indicative of the transformation of a small amount of tetragonal $ZrO_2$ to monoclinic $ZrO_2$. Transformation of monoclinic zirconia to tetragonal zirconia with increasing calcination temperature is unusual and as the presence of the tetragonal phase could not be confirmed further investigation is required.

Examination of a plot of the amount of monoclinic $ZrO_2$ versus calcination temperature, Figure 6.24, for the materials produced by hydrothermal processing with HCl indicated that the dopant iron ion had no effect on the stability of the monoclinic phase. One exception to this was the production of tetragonal $ZrO_2$ with the 10 wt% doped sample after calcination at 500°C. This result is unusual and therefore warrants further investigation.

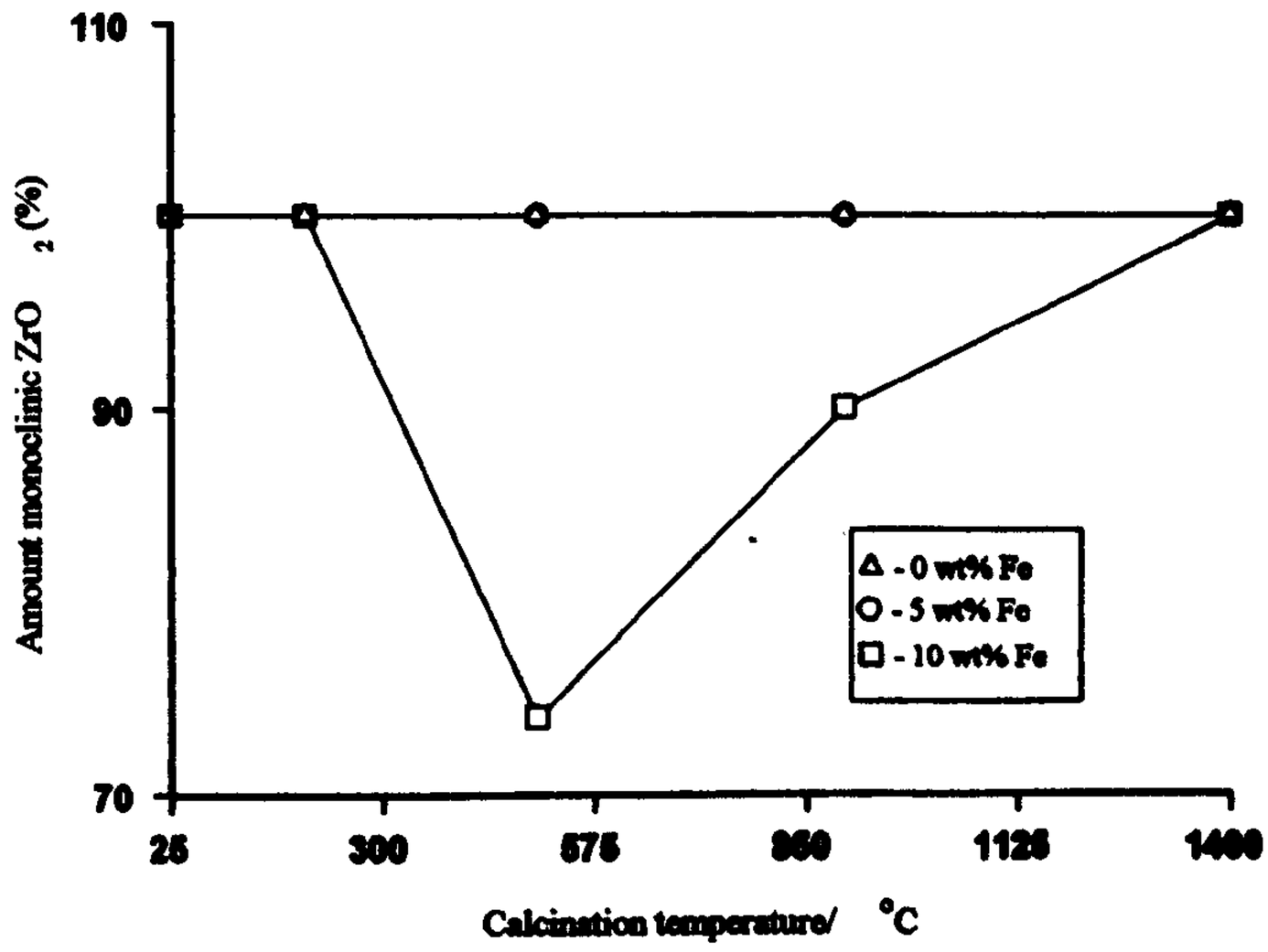


***Figure 6.24 - Comparison of the effects of iron dopant level on the formation of monoclinic zirconia by hydrothermal processing in HCl***

### 6.1.2.3 Synthesis with $NH_4OH$

(i) 10 wt% iron doped zirconia

The X-ray powder diffraction pattern of the material recorded from the 10 wt% Fe doped material dried under an infra red lamp, Figure 6.25a, indicated that two phases

were present, the major phase being the tetragonal phase with evidence for a small amount of the monoclinic phase, Table 6.10. The $^{57}Fe$ Mössbauer spectrum, Figure 6.26, consisted of one doublet with an isomer shift of 0.36mms$^{-1}$ and a quadrupole splitting of 1.04mms$^{-1}$, Table 6.14. The isomer shift indicated that $Fe^{3+}$ ions had been incorporated into the zirconia structure. The X-ray powder diffraction patterns, Figure 6.25b and c, of the material calcined at 200°C and 500°C appeared unchanged.

| Calcination Temperature | Doublet | | | Sextet | | |
|---|---|---|---|---|---|---|
| | δ / mms$^{-1}$ (±0.05) | Δ /mms$^{-1}$ (±0.03) | Area / % | δ / mms$^{-1}$ (±0.05) | Δ /mms$^{-1}$ (±0.03) | Area / % |
| Prefurnace | 0.36 | 1.04 | 100 | - | - | 0 |
| 200°C | 0.36 | 1.05 | 100 | - | - | 0 |
| 500°C | 0.36 | 1.08 | 100 | - | - | 0 |
| 900°C | 0.35 | 1.13 | 14 | 0.39 | -0.08 | 86 |
| 1400°C | 0.37 | 0.89 | 5 | 0.39 | -0.08 | 95 |

***Table 6.14 - $^{57}Fe$ Mössbauer spectral data for 10 wt% iron doped $ZrO_2$ synthesised by hydrothermal processing of zirconium(IV) acetate and iron(II) acetate with $NH_4OH$***

The $^{57}Fe$ Mössbauer spectra recorded from these samples, Figure 6.26b and c, both consisted of one doublet component with an isomer shift indicative of $Fe^{3+}$ ions in the zirconia structure, Table 6.14. The quadrupole splitting remained relatively constant, Table 6.14, and in agreement with the findings, Section 6.1.1.1(i), that tetragonal $ZrO_2$ resulted in a high quadrupole splitting value. The amount of the tetragonal phase present in the material was observed, Table 6.10, to vary over the calcination range (up to 500°C). This may be due to the presence of amorphous material or due to inaccuracies in the determination of the intensity of the X-ray powder diffraction peaks due to the poor quality of the X-ray powder diffraction pattern.

The X-ray powder diffraction pattern of the material calcined at 900°C, Figure 6.25d, showed that the increase in temperature had caused the onset of a phase transformation from tetragonal zirconia to monoclinic zirconia, and associated with this there was segregation of iron resulting in the formation of $\alpha$-$Fe_2O_3$. The $^{57}Fe$ Mössbauer

spectrum of the material calcined at 900°C, Figure 6.26d, consisted of two components, one doublet and one sextet. The sextet component had parameters which were indicative[8] of the $\alpha$-$Fe_2O_3$ phase. Further calcination of the material at 1400°C caused little change to the X-ray powder diffraction pattern, Figure 6.25e. The continued segregation of iron from the zirconia structure was illustrated by an increase in the area attributed to the sextet component in the $^{57}Fe$ Mössbauer spectrum, Figure 6.26e.

(ii) 5 wt% iron doped zirconia

The X-ray powder diffraction pattern recorded from the 5 wt% Fe doped material dried under an infra red lamp, Figure 6.27a, indicated that two phases identified as tetragonal $ZrO_2$ and monoclinic $ZrO_2$ were present, with the tetragonal phase being predominant, Table 6.10. The $^{57}Fe$ Mössbauer spectrum, Figure 6.28a, consisted of one doublet with an isomer shift of 0.36mms$^{-1}$ and a quadrupole splitting of 0.93mms$^{-1}$, Table 6.15. The value of the isomer shift indicated that $Fe^{3+}$ ions had been incorporated into the zirconia structure, while the large value of the quadrupole splitting endorsed earlier observations, Section 6.1.1.1(i), that a large quadrupole splitting could be associated with the tetragonal phase. After calcination of the material at 200°C the X-ray powder diffraction pattern, Figure 6.27b, appeared similar to that of the X-ray powder diffraction pattern of the material dried under an infra red lamp, Figure 6.27a. Examination of the X-ray powder diffraction pattern peak intensities showed that the amount of monoclinic $ZrO_2$ present had decreased, Table 6.15. This may have been due to inaccuracies in determining the relative peak intensities, particularly for the monoclinic [1 1 $\bar{1}$] peak. The $^{57}Fe$ Mössbauer spectrum, Figure 6.28b, consisted of one doublet, $\delta$ = 0.37mms$^{-1}$, $\Delta$ = 0.96mms$^{-1}$, indicative of the presence of $Fe^{3+}$ ions in one of the phases present. Calcination of the material at 500°C resulted in no further change to the X-ray powder diffraction pattern, Figure 6.27c, or to the $^{57}Fe$ Mössbauer spectrum, Figure 6.28c.

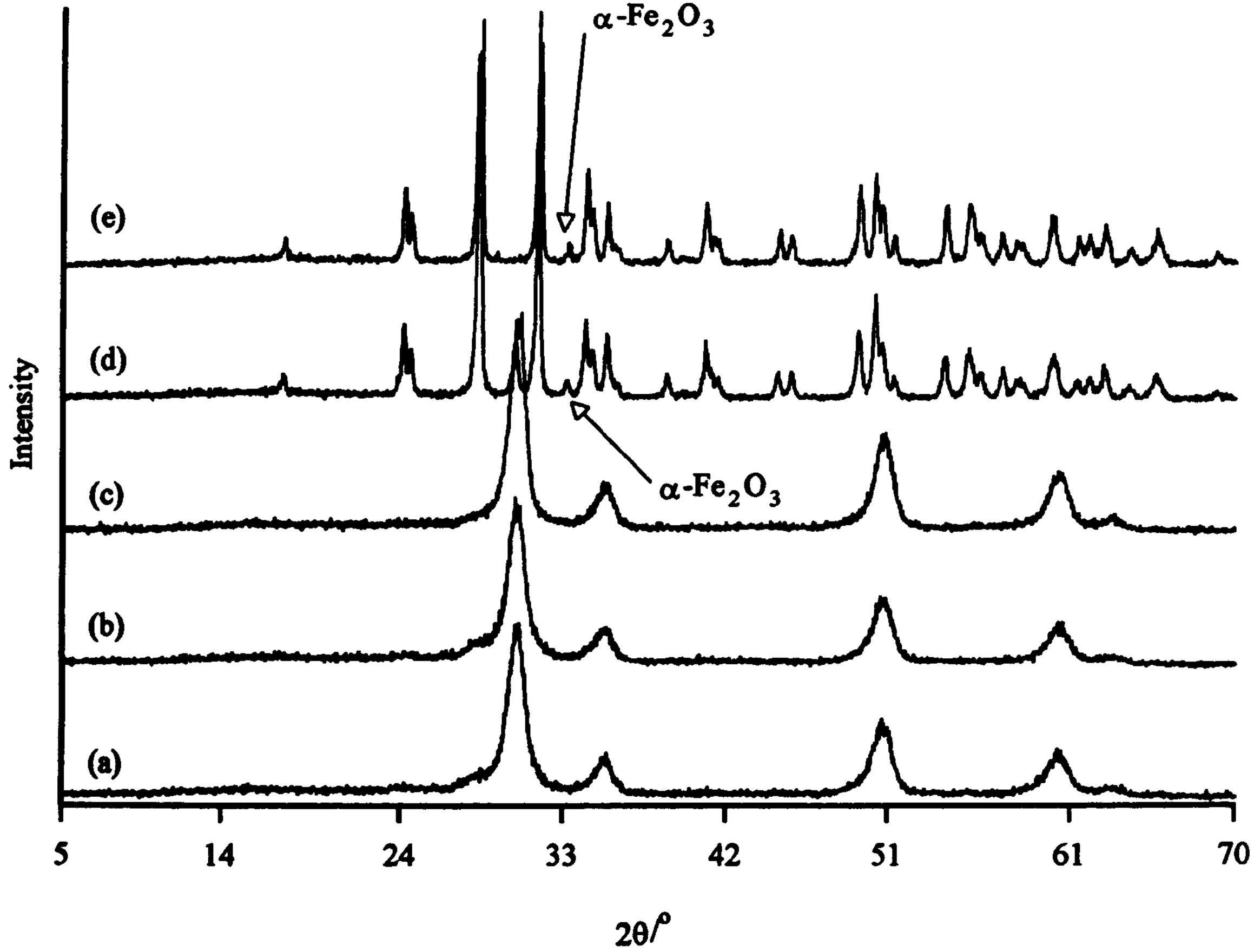


***Figure 6.25 - X-ray powder diffraction pattern recorded from the iron doped zirconia produced by hydrothermal processing of zirconium(IV) acetate and 10 wt% iron(II) acetate with $NH_4OH$ and (a) dried under an infra red lamp and calcined at (b) 200°C, (c) 500°C, (d) 900°C and (e) 1400°C***

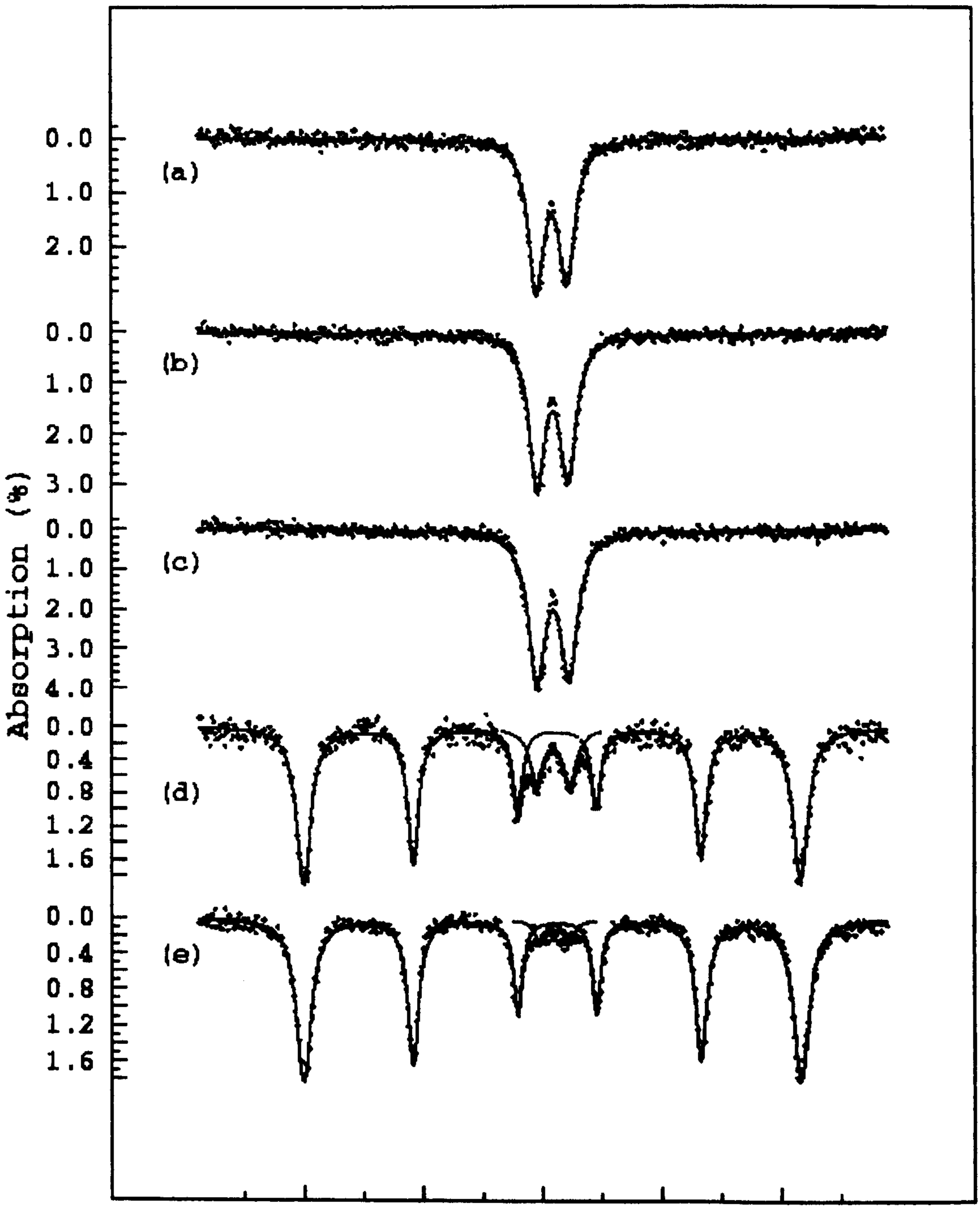


***Figure 6.26 - $^{57}Fe$ Mössbauer spectra recorded from 10 wt% iron doped $ZrO_2$ synthesised by hydrothermal processing of zirconium(IV) acetate and iron(II) acetate with $NH_4OH$ and (a) dried under an infra red lamp and calcined at (b) 200°C, (c) 500°C, (d) 900°C and (e) 1400°C***

| Calcination Temperature | Doublet | | | Sextet | | |
|---|---|---|---|---|---|---|
| | $\delta$ / $mms^{-1}$ (±0.05) | $\Delta$ /$mms^{-1}$ (±0.03) | Area / % | $\delta$ / $mms^{-1}$ (±0.05) | $\Delta$ /$mms^{-1}$ (±0.03) | Area / % |
| Prefurnace | 0.36 | 0.93 | 100 | - | - | 0 |
| 200°C | 0.37 | 0.96 | 100 | - | - | 0 |
| 500°C | 0.38 | 0.99 | 100 | - | - | 0 |
| 900°C | 0.32 | 1.13 | 70 | 0.38 | -0.11 | 30 |
| 1400°C | 0.37 | 0.99 | 9 | 0.40 | -0.10 | 91 |

***Table 6.15 - $^{57}Fe$ Mössbauer spectral data for 5 wt% iron doped $ZrO_2$ synthesised by hydrothermal processing of zirconium(IV) acetate and iron(II) acetate with $NH_4OH$***

Further calcination of the material at 900°C produced a complete phase transformation, as evidenced by the X-ray powder diffraction pattern, Figure 6.27d, from the tetragonal to the monoclinic phase. The $^{57}Fe$ Mössbauer spectrum, Figure 6.28d, showed that there were two phases present, one sextet component with parameters consistent[8] with $\alpha$-$Fe_2O_3$ and one doublet component with an isomer shift of 0.32$mms^{-1}$ and a quadrupole splitting of 1.13$mms^{-1}$. The $\alpha$-$Fe_2O_3$ phase constituted 30% of the total iron content present. This phase could not be detected in the X-ray powder diffraction pattern as the total iron content (5 wt%) is at the limit of detection of the diffractometer used. The high quadrupole splitting was inconsistent with previous findings, Section 6.1.1.1(i), which indicated a relationship between zirconia phase and the magnitude of the quadrupole splitting. Calcination at 1400°C produced an increase in crystallinity, indicated by an increase in the sharpness of the peaks in the X-ray powder diffraction pattern, Figure 6.27e. The $^{57}Fe$ Mössbauer spectrum, Figure 6.28e, indicated that the $\alpha$-$Fe_2O_3$ component had increased in area, to 91% of the total iron content, Table 6.15,. The isomer shift of the doublet component, Table 6.15, suggested that the remainder of the iron content was present as $Fe^{3+}$ ions in the $ZrO_2$ structure. The increase in the $\alpha$-$Fe_2O_3$ content was suggestive of segregation of $Fe^{3+}$ from the zirconia structure.

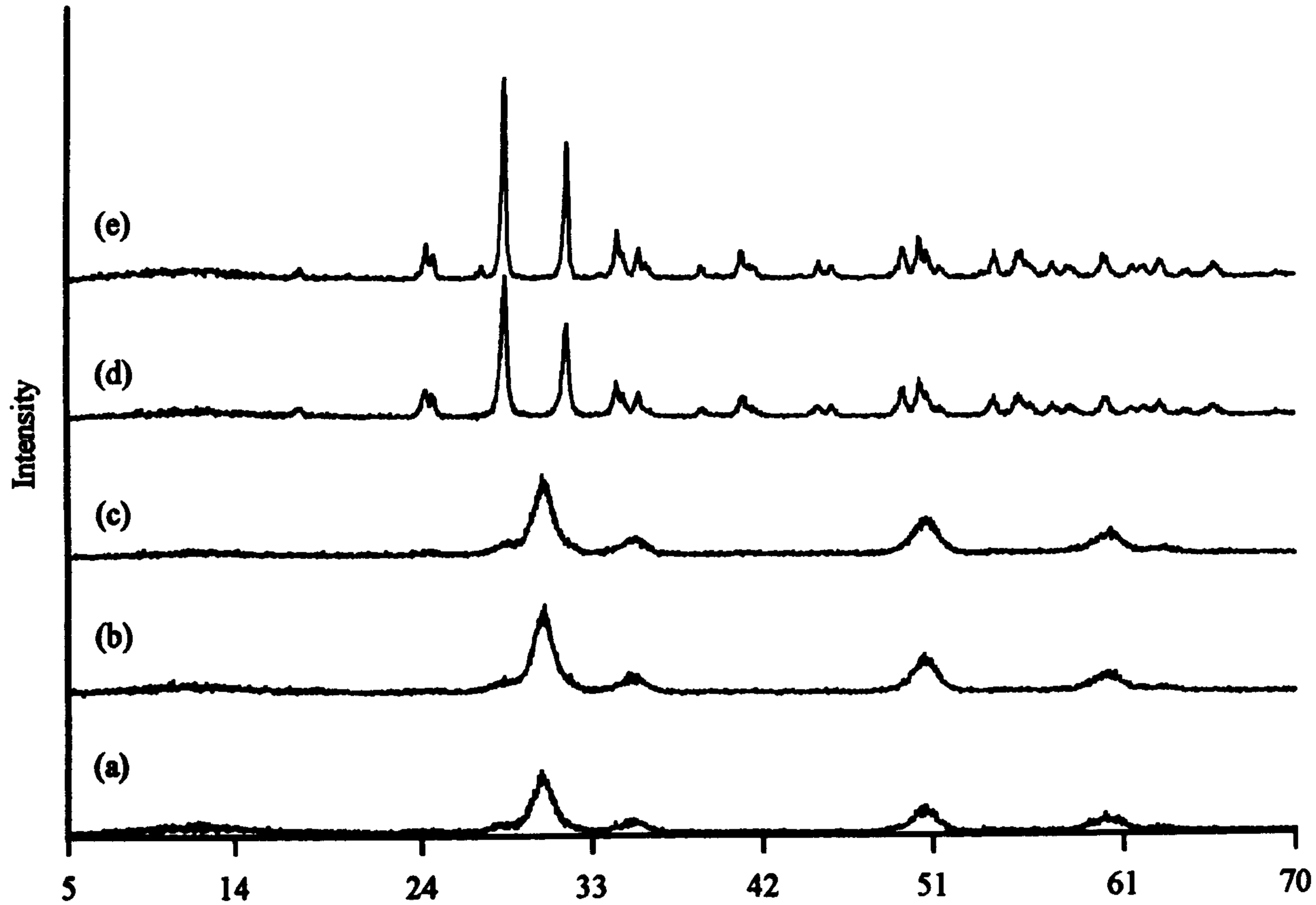


***Figure 6.27 - X-ray powder diffraction patterns recorded from the iron doped zirconia produced by hydrothermal processing of zirconium(IV) acetate and 5 wt% iron(II) acetate with $NH_4OH$ and (a) dried under an infra red lamp and calcined at (b) 200°C, (c) 500°C, (d) 900°C and (e) 1400°C***

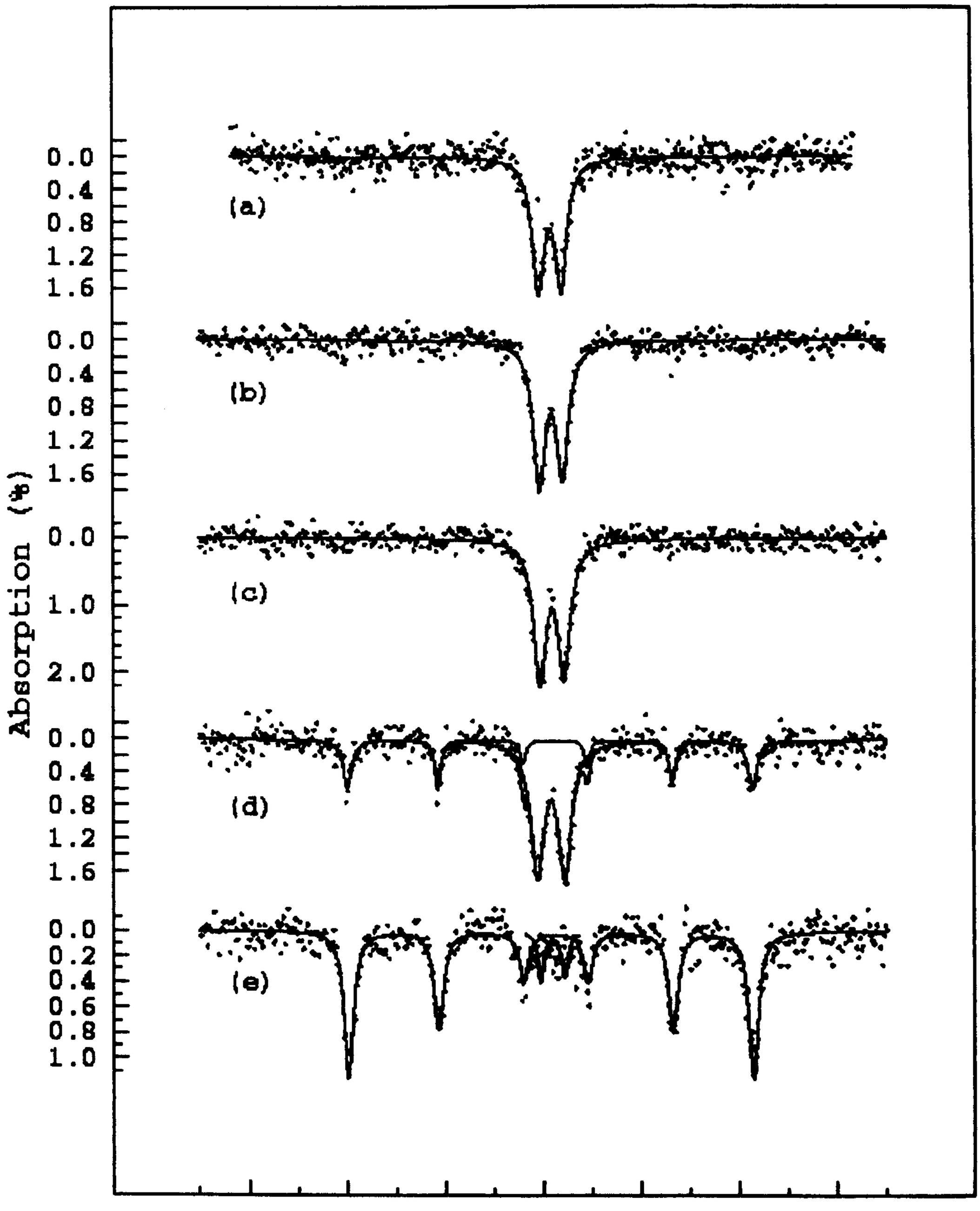


***Figure 6.28 - $^{57}Fe$ Mössbauer spectra recorded from 5 wt% iron doped $ZrO_2$ synthesised by hydrothermal processing of zirconium(IV) acetate and iron(II) acetate with $NH_4OH$ and (a) dried under an infra red lamp and calcined at (b) 200°C, (c) 500°C, (d) 900°C and (e) 1400°C***

In contrast to the results obtained with hydrothermal processing of zirconium(IV) and iron(II) acetates with water, Section 6.1.2.1, the dopant ions stabilised the tetragonal $ZrO_2$ phase at temperatures up to 500°C, Figure 6.29. On calcination of the material at 900°C there was virtually complete conversion to the monoclinic phase for both the 5 and 10 wt% iron doped samples, whereas the material with no iron present had 59% of the tetragonal phase present.

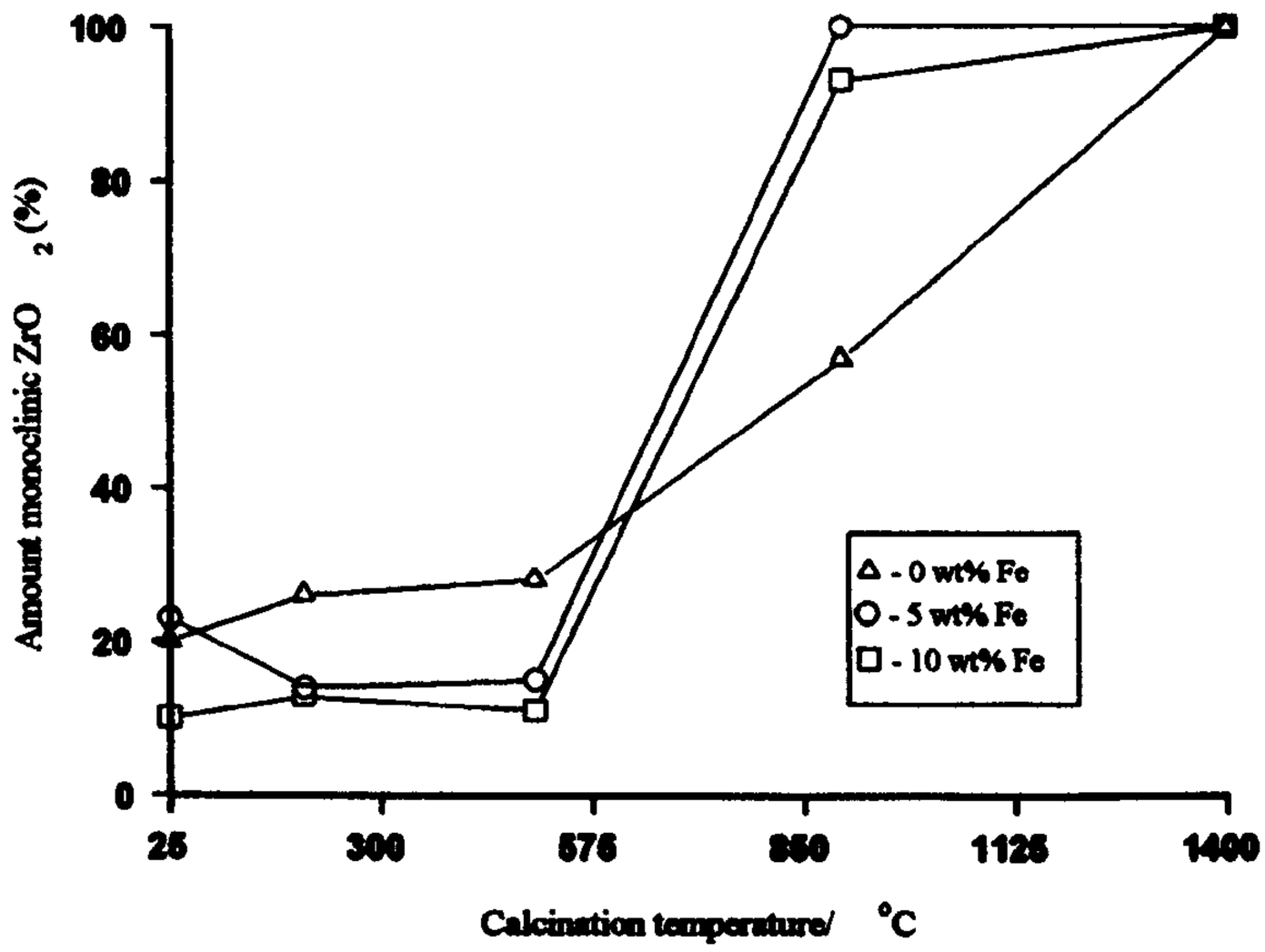


***Figure 6.29 - Comparison of the effects of iron dopant level on the formation of monoclinic zirconia by hydrothermal processing in ammonia***

## 6.2 Conclusions

1) X-ray powder diffraction indicated that the material produced by boiling zirconium(IV) and iron(II) acetates under reflux was, after calcination at 500°C tetragonal iron-doped zirconia. Increasing calcination temperatures caused the transformation of the tetragonal phase to the more stable monoclinic phase.

2) Increasing pH was found to stabilise the tetragonal phase against transformation to monoclinic zirconia for those materials produced by boiling zirconium(IV) and iron(II) acetates under reflux.

3) $^{57}$Fe Mössbauer spectroscopy showed that on calcination at temperatures of 900°C and above segregation of iron from zirconia occurred.

4) Introduction of HCl into the initial solution caused the formation of the zirconia phase to proceed via an oxychloride phase as observed in Chapter 5.

5) Stabilisation of the tetragonal polymorph occurred at all pH's. After calcination at 900°C conversion to the monoclinic polymorph was observed to differing degrees dependent on pH and dopant level.

6) Hydrothermal processing of zirconium(IV) and iron(II) acetates produced a mixture of tetragonal and monoclinic zirconia. Variation of dopant level produced differing effects dependent on pH.

7) $^{57}$Fe Mössbauer spectroscopy of the materials produced by hydrothermal processing showed that on calcination at 900°C and above segregation of iron occurred.

8) Large quadrupole splitting in the $^{57}$Fe Mössbauer spectra recorded from samples produced by both boiling under reflux and hydrothermal processing of zirconium(IV) and iron(II) acetates were found to be characteristic of tetragonal zirconia.

# References


1 F.J.Berry, M.H.Loretto and M.R.Smith, J.Solid State Chem., 1989, 83, 99

2 K.Chen, Y.Fan, Z.Hu, and Q.Yan, J.Mater.Chem., 1996, 6, 1041

3 J.F.Collins and I.F.Ferguson, J.Chem.Soc.(A), 1968 4

4 S.K.Srivastava and C.K.Jain, J.Mater.Sci., 1985, 20, 1079

5 P.Li, I-W.Chen and J.E.Penner-Hahn, J.Am.Ceram.Soc., 1994, 77, 118

6 "Mössbauer Spectroscopy", Cambridge University Press, Cambridge, Great Britain, 1986, Ed. D.P.E.Dickson and F.J.Berry

7 JCPDS pattern number 24-1164

8 O.C.Kistner and A.W.Sunyar, Phys.Rev.Lett., 1960, 4, 412

9 JCPDS pattern number 32-1498